PHD THESIS

Isomorph theory and extensions

Lorenzo Costigliola, *September 19, 2016*
supervisor: Jeppe Dyre

Abstract

This thesis has two main conceptual parts: in a first part the isomorph theory is discussed and used to describe the Lennard-Jones (LJ) system, following the path traced by previous works from the Roskilde group, while in the second part the theory is extended in different ways.

Chap. 2 and the starting sections of Chap. 3 correspond to the first conceptual part. Here the isomorph theory is presented and then used to describe the freezing and melting invariances and the empirical Andrade equation for the freezing viscosity (which can also be thought as an invariance), showing that the isomorph theory can justify why these invariances hold and that they are not peculiarities of the freezing and melting processes.

At the same time Chap. 3 is also the start of the second conceptual part because the isomorph theory is used here for the first time to formulate predictions not along an isomorph but in its proximity, allowing for a precise description of the freezing and melting line. These two works on freezing and melting have been published in the first two companion papers. In the end of the same chapter the first part of an unpublished work is also presented. In this work a connection is suggested between the generalized LJ system starting to behave Roskilde simply and a change in the behavior of the scaling exponent γ.

In Chap. 4 the isomorph theory is used to establish the temperature dependence of an isomorphic invariant quantity along an isochore, again 'going away from an isomorph' and investigating the connection between different isomorphs. This result has allowed the author to suggest a new equation describing the viscosity of the LJ system accurately in the whole Roskilde simple region.

Another extension of the theory is made by studying the LJ system (as prototype of Roskilde simple liquid) in 2d, 3d and 4d, verifying that the system conforms to hidden scale invariance (the symmetry consequence of isomorph theory) better in higher dimensions. These results have been published in the third companion paper and form the main matter of Chap. 5. In the same chapter the relation between the LJ system starting to behave Roskilde simple and the behavior of the scaling exponent γ is studied in 2d and 4d.

The thesis concludes with a work on a possible prototype non-simple system, the Gaussian core model. This study is presented in Chap. 6. The Gaussian core model exhibits strongly negative correlations and, for the first time, the existence of isomorphs with negative scaling exponent γ is reported, leading to a new application of the isomorph theory by including the Gaussian core system in the wide class of Roskilde simple systems.

Abstract in Danish

Denne afhandling falder i to konceptuelle dele: I den første del bliver isomorf-teorien diskuteret og anvendt til at beskrive Lennard-Jones (LJ) systemet i tråd med tidligere arbejde udført af gruppen fra Roskilde Universitet, mens den anden del udvider teorien på forskellige vis.

Kap. 2 og starten af Kap. 3 svarer til den første del. Her bliver isomorf-teorien præsenteret og derefter anvendt til at beskrive frysnings- og smelt-ningsinvarians samt den empiriske Andrade-ligning for frysningsviskositet (hvilket ligeledes kan betragtes som en invarians), hvilket viser, at isomorf-teorien kan belyse hvorfor disse invarianser holder og, at de ikke er særlige for frysning eller smeltning.

På samme tid er Kap. 3 også starten på den anden konceptuelle del fordi isomorfteorien bliver brugt her, for første gang, til at formulerer forudsigelser, der ikke er langs en isomorf, men i dennes omkreds, hvilket tillader en præ-cis beskrivelse af fryse- og smeltelinien. Disse to resultater om frysning og smeltning er blevet publiceret i de to første ledsagne artikler. I slutningen af samme kapitel bliver den første del af et upubliceret resultat præsenteret. Her antydes en sammenhæng mellem det, at det generaliserede Lennard-Jones system begynder at være Roskilde-simpelt og ændringen i opførslen af skaleringseksponenten γ.

I Kap. 4 bliver isomorfteorien brugt til at etablere temperaturafhængighe-den af en isomorft invariant størrelse langs en isokor, igen "ikke langs en isomorf", og undersøge sammenhængen mellem forskellige isomorfer. Dette resultat har gjort det muligt for forfatteren at fremsætte en ny formel, til nøjagtig beskrivelse af viskositeten for LJ systemet i hele den Roskilde-simple region.

En anden udvidelse af teorien kommer fra et studie af LJ systemet (som en prototype for en Roskilde-simple væske) i 2d, 3d og 4d, hvor det ver-ificeres at systemet overholder skjult skaleringsinvarians (den symmetriske konsekvens af isomorfteorien) bedre i højere dimensioner. Disse resultater er udgivet i den tredje ledsagne artikel og udgør hoveddelen af Kap. 5 sam-men med en udvidelse af undersøgelsen om sammenhængen mellem det, at LJ systemet begynder at opfører sig Roskilde-simpelt og opførslen af skaler-ingseksponenten γ i 2d og 4d.

Afhandlingen konkluderes med et studie af en mulig prototype på et ikke-simple system, Gaussian core-modellen. Dette studie er præsenteret i Kap. 6. Gaussian core-modellen udviser stærk negativ korrelation og for første gang rapporteres om eksistensen af isomorfer med negativ skaleringsekspo-nent γ, hvilket medfører en ny anvendelse af isomorfteorien ved inklusion af Gaussian core-systemet i den store klasse af Roskilde-simple systemer.

Preface

This doctoral thesis describes some of the work done during the three years of the Danish PhD program, between June 15st 2013 and June 14st 2016. The work has been supervised by Jeppe C. Dyre and was done in the *Glass and Time* group at Roskilde University.

Papers

The doctoral thesis has four companion papers which can be found in appendix D. The first paper has been published while the third one has been accepted for publication but was in the process of proof reading at the same time of this doctoral thesis submission. The second and forth papers have been submitted and are in the process of resubmission after receiving positive comments from referees.

Paper I *Freezing and melting line invariants of the Lennard–Jones system*
L. Costigliola, T. B. Schrøder, and J. C. Dyre,
Physical Chemistry Chemical Physics, **18**, 14678, 2016. Online

Paper II *Thermodynamics of freezing and melting*
U. R. Pedersen, L. Costigliola, N. P. Bailey, T. B. Schrøder,
and J. C. Dyre, submitted and under revision.

Paper III *Studies of the Lennard-Jones fluid in 2, 3, and 4 dimensions highlight the need for a liquid-state 1/d expansion*
L. Costigliola, T. B. Schrøder, and J. C. Dyre,
accepted in J. Chem. Phys. Communications, arXiv:1605.06007

Paper IV *RUMD: A general purpose molecular dynamics package optimized to utilize GPU hardware down to a few thousand particles*
N. P. Bailey, T. S. Ingebrigtsen, J. S. Hansen, A. A. Veldhorst,
L. Bøhling, C. A. Lemarchand, A. E. Olsen, A. K. Bacher,
L. Costigliola, U. R. Pedersen, H. Larsen, J. C. Dyre
and T. B. Schrøder, submitted and under revision. arXiv:1506.05094

Acknowledgements

I'll start by thanking Jeppe and Thomas for the kind and also often funny way they guided me through these years. An heartfelt thanks goes to Nick, Heine and Søren for the careful proofreading of this manuscript and to Andreas for the Danish translation of my abstract.

My last three years at Roskilde have been amazing and I'm sure it was not thanks to the typical *nice and welcoming* Danish weather but rather for the nice persons I met during these years. I would like to thank all my colleague of the *Glass and Time* group at Roskilde university and all the IMFUFA department for making my working time *hyggelig*.

I'm particularly in debt with the members of the simulations group who helped me in different aspects of my work: Nick, Lasse, Arno, Trond, Jesper, Heine, Claire, Andreas and Andreas, Ulf, Thomas, Jeppe and Søren.

I also want to thank all the members of the most envied club in the world, the cake seminar!

Thanks to Claire and Nick for sharing most of their working time with me and to Heine for acting as the department glue and for helping each new member to feel welcome in the IMFUFA group, or maybe better IMFUFA family.

A special thanks goes to Claire, Heine, Luna, Arno, Johanne, Jakub and Andreas for having been close to me and for their support in the happy and less happy moments of my last three years.

Contents

v

Chapter 1

Background

In this chapter some essential background on the liquid state is presented. Special attention is dedicated to the description of invariances in the liquid state. A section describing molecular dynamics (MD) is also included.

1.1 The liquid state

Among the four states of ordinary matter, the liquid state is most likely the worst defined. More than a proper definition, the liquid state is often described by what it is not. Plasmas are systems with a consistent number of charged particles, gasses are systems of mostly free particles (weakly interacting) and solids can be defined as systems not able to flow, at least on reasonable observation timescales, because of the strong interactions between particles. A liquid is a system of particles which strongly interact, similarly to solids, but can flow, as gasses. As with solids, the compression of liquids requires high pressures but, at the same time, they have the same structural symmetries as gasses. Many other examples of liquid properties shared with gasses or solids can be found. This 'problem of definition' is also evident in the not universally accepted definition of the liquid state from a physical point of view. According to the most common definition, a liquid can exist only below a well defined critical temperature T_C [1] (Fig. 1.1). For temperatures above T_C, the gas and the liquid of a given substance are termed fluid and are often considered to be indistinguishable. Different authors have questioned this definition of the liquid state [2–5]. It is possible, for example, to show that the structure and dynamics of several model liquids are the same, when expressed in proper units, along lines in the phase diagram "parallel" to the freezing line, as we will discuss in Chapter 2 and 3, even at temperatures well above the critical one.
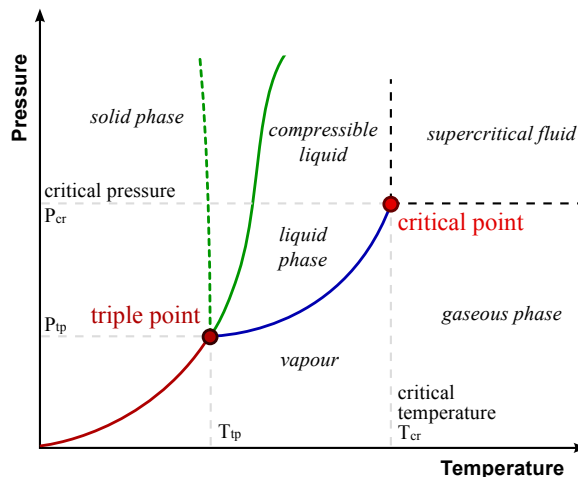
Figure 1.1: Phase diagram of a single-component system as function of pressure P and temperature T. The green line shows the melting line for a *normal* system while the dotted line shows an *anomalous* melting line [6], i.e. with negative slope, as, for example, the melting line of water [7]. The liquid phase is, according to the most common definition, restricted to the area delimited by the melting line, the vaporization line and the critical isobar, i.e. the line of constant pressure passing through the critical point. This figure is from Ref. [8]

Given the difficulties in finding an universal definition of the liquid state itself it is not surprising that a comprehensive theory of the liquid state does not exist yet. The main efforts in this direction through the last century have been in developing a theory for a subclass of liquids, called simple liquids. Simple liquids are usually defined as many-body systems interacting via radially symmetric pair potentials. Atoms and molecules in real systems present more complex interactions than pairwise ones but simple liquids are good model systems able to describe many features of common liquids. Not surprisingly the definition of simple liquid has also been a matter of debate [2, 9]. It is in fact well known that some molecular liquids, with quite complicated interactions, can behave more simply than systems interacting via peculiar pairwise interactions [2, 10]. This statement will become clearer in Chapter 2 and 6.

In the following three subsections we will describe some of the features of simple liquid theory and its applicability.

1.1.1   Theory of Simple liquids: The HS paradigm

The theory of simple liquids is based on the assumption that the liquid state is governed by the repulsive part of the interaction potential between its constituents [1]. In this perspective, the most interesting system to take into account is a system of hard spheres (HS). This system is described with a divergent repulsion at contact distance and a zero potential for greater distances. The interaction potential of HS is:

$$v(r) = \begin{cases} \infty & \text{if } r < r_{HS} \\ 0 & \text{if } r > r_{HS} \end{cases} \qquad (1.1)$$

where r_{HS} is the radius of the HS. The interests in studying this potential are many. For HS it is possible to solve the Percus-Yevick equation analytically [1] and obtain the phase diagram and the structure. The state of the system depends only on the packing fraction $\eta = (\pi/6)\rho r_{HS}^3$ and not on temperature as, in general, for real systems. It is intuitive that relating the properties of a real system with those of HS will require some sort of mapping. This mapping is hidden in the choice of the r_{HS} which, in general, depends on pressure (or density ρ) and temperature of the real system. From a simulation point of view, HS are less computationally expensive to simulate than continuous pair potentials and a specific kind of computer simulation, event driven simulations, has been developed for HS [11]. All interactions happen at the contact distance and therefore it is not necessary to simulate intermediate times between a collision and the following one.

Beyond these advantages, the HS paradigm of model liquid system has some important problematic aspects. The first one is that it cannot describe the liquid in regions close to the critical point or to the liquid-gas transition. This problem is due to the absence in the HS approach of any attraction between particles. Under this assumption, no transition between gas and liquid can take place [12]. Another open question is the proper way of defining the HS radius r_{HS} and the possibility of predicting, having chosen an interaction potential, if a model system will behave as a HS system or not, as it will be discussed in Chap. 2. This last problem is quite relevant because, while a wide class of system can be modelled in terms of HS, many exceptions are known. Two of these exceptions are water and the Gaussian core model liquid in a part of its phase diagram. This model liquid will be subject of Chapter 6. Liquids and model liquids which do not follow the HS paradigm are often called *anomalous* [6]. These liquids can have simple pair potentials, as the Gaussian core model liquid, and simple molecular structure, as water, but manifest uncommon behaviors as, for example, the decrease of melting temperature with increasing pressure [6].
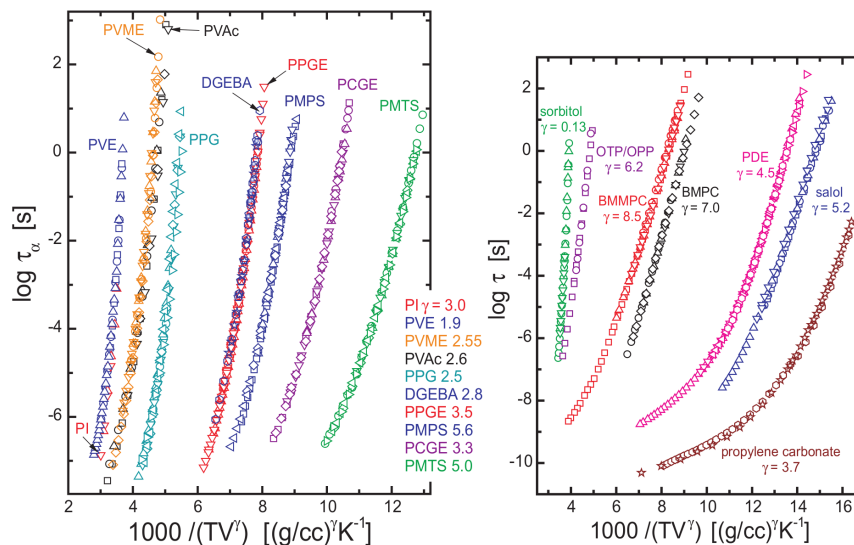
Figure 1.2: Power law density scaling. In these figures the dielectric relaxation time τ_α is shown to be a function of TV^γ and not independently of temperature T and volume V (or equivalently density). The scaling exponent γ is defined in the main text. Data for polymer melts and small molecular glass forming liquids are shown respectively in the left and right figure. These figures have been taken from Ref. [13], where also information on the different liquids studied can be found.

1.1.2 Density scaling : simple behavior of complex liquids

Starting from 1998 [14] several experimental works observed that it is possible to describe a wide class of liquids using density scaling. Density scaling consists in recognizing that the physical properties of a system, under some circumstances, do not depend independently on pressure (or density) and temperature but on a fixed combination of the two. This is similar to what happens in the case of HS described previously. Always under the hypothesis that only repulsive forces determine the behavior of the liquid phase, these invariances were explained using inverse power law potential (IPL) as model for particle interactions:

$$v_n^{IPL}(r) = \epsilon \left(\frac{\sigma}{r} \right)^n \tag{1.2}$$

For these potentials, the invariance curves are characterized by a fixed value of $\rho^{n/3}/T$. The system of particles interacting via IPLs is commonly named soft spheres; HS can be though as a limiting case of soft spheres when $n \to \infty$. If an IPL with $n = 12$ is considered, the scaling exponent $\gamma = n/3$ will be 4 and this scaling property is obeyed by several real liquids [13–16]. Data from Ref. [13] are shown in fig. 1.2. Different liquids will have different scaling exponents and are therefore associated with different IPLs [13, 16–18].

It is interesting to note that liquids obeying density scaling can have distinct molecular structure and real interactions rather more complex than IPLs, far away from the definition given above of simple liquids. Density scaling was first observed in *ortho*-terphenyl (OTP), then in polymers and ionic liquids. These systems are very different from rotationally invariant objects interacting via radially symmetric potentials, as HS or soft spheres. Density scaling has been confirmed also in computer simulations of generalized Lennard-Jones system [19, 20], i.e., a system of particles interacting via difference of two IPL potentials. In Chapter 2 we will discuss how these invariances can be understood without referring to HS or soft spheres.

1.1.3 Anomalous liquids: complex behavior of simple liquids

As introduced before, several liquids can be described through the HS paradigm but not all of them. There are two liquids which are worth mentioning in this context, i.e., water and the Gaussian core model liquid.

The first one is the system embedding the common idea of liquid itself in real life. Water is at the same time one of the most important liquids to understand but one of the least trivial [21]. It presents anomalies both in the solid state and in the liquid one [22] and it is interesting because, its simple molecular structure notwithstanding, it is difficult to model. One important feature of water is that its crystalline phase is less dense than the liquid phase at normal pressures. This feature makes water an *anomalous* liquid because this kind of behavior cannot be described in terms of HS. The dotted line starting from the triple point in Fig. 1.1 represents qualitatively the water melting line at normal pressures. The melting temperature of water decreases on increasing pressure unlike for other systems (full green line). It is well known that the *anomalous* behavior in water is connected to the presence of directional H-bonds between its molecules [7, 23] and the presence of this kind of bonds is what usually causes non-simple (non-density scaling) behavior in other liquids too.

The second liquid is a model liquid consisting of particles interacting pairwise with Gaussian-like potential:

$$v^{GC}(r) = \epsilon \ e^{-\frac{r^2}{\sigma^2}} \tag{1.3}$$

This potential has been widely studied in computer simulations because, as pointed out by Stillinger [24] in 1976, despite its simple analytical form, it embeds a rich variety of anomalies. The most surprising characteristic of this potential is the high density behavior of the melting line, which has a negative slope at high pressures [24–27]. This behavior of the melting line is not understandable in terms of HS and it will be discussed in Chapter 6. Another interesting feature of the Gaussian Core (GC) system is its negative thermal expansion [26–28], which characterizes water too.
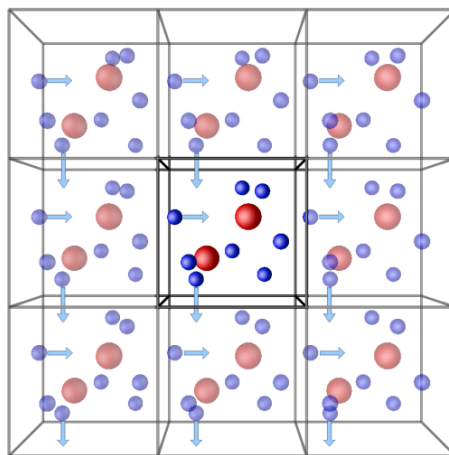
Figure 1.3: A schematic representation of the particles in a simulation box during an MD simulation. When simulating a given model system, the number of particles N is often fixed and small compared to the number of atoms and molecules of a real substance. In order to avoid problems related to the presence of surfaces (box boundaries), the simulation box is surrounded by its virtual copies (periodic boundary condition). This means that when a particle exit the simulation box from the left side, another one enters the box on the right side with the same velocity. In this way the number of particles in the box is conserved and the system can be used to calculate average bulk quantities. Figure is taken from Ref. [29].

1.2 Molecular dynamics

Molecular dynamics (MD) is an excellent tool to test model systems. A sketch of a MD simulation is given in Fig. 1.3. The unique input needed is the interaction potential between particles (pairwise or not). Once the potential is chosen, the MD program will solve the equations of motion of the system particles using a discretization scheme. The equations of motion for a system of particles in classical mechanics are differential equations of second order and, in general, it is not possible to solve them analytically. This problem can be remedied assuming the interaction force to be constant for small time intervals. Under this assumption, the equations of motion can be solved by discretization of time in small steps (timesteps) and evaluating the derivatives numerically. The definition of a "small timestep" will depend on the potential chosen and on the state point studied, i.e. on the density (or alternatively pressure) and temperature of the state point.

In the following some different versions of the discretization algorithm are described and their equivalence shown [30]. Some details on differences between CPU implementations and GPU implementations of MD programs are also given and the RUMD package, used for most of the results in this thesis, is introduced.

1.2.1   The Verlet algorithm

The Verlet algorithm [31] is a discretization of Newton's second law; it is therefore based on the assumption that for a given state point and potential, it is possible to find an adequate discrete time increment, which allows one to reproduce the correct dynamics. From a theoretical point of view it is always possible to find this time increment (timestep), but from a computational point of view this may be not accessible, if it's too small for the machine precision. As we will see in the following this problem is one of the reasons why Leap-Frog algorithm can be preferred to Verlet algorithm.

Newton second law for a system of N particles interacting via a pair potential $\phi_{i,j}$ is

$$m\ddot{\mathbf{r}}_i = - \sum_{j=1, j \neq i}^{N} \nabla \phi_{i,j} = \mathbf{f}_i. \tag{1.4}$$

in which $\mathbf{r_i}$ is the position vector of the particle i with mass m and $\mathbf{f_i}$ is the force vector acting on it. The discretized version of the Eq. 1.4 can be obtained using the central difference approximation for the second derivative (with time increment h):

$$\frac{\mathbf{r}_i(t+h) - 2\mathbf{r}_i(t) + \mathbf{r}_i(t-h)}{h^2} = \frac{\mathbf{f}_i(t)}{m}. \tag{1.5}$$

In order to obtain energy conservation in an MD algorithm, Eq. 1.5 needs to be invariant under time inversion [30, 32–35]. The position of particle i after the time increment h is:

$$\mathbf{r}_i(t+h) = 2\mathbf{r}_i(t) - \mathbf{r}_i(t-h) + h^2 \mathbf{f}_i(t). \tag{1.6}$$

The calculation of the new position of any particle requires the knowledge of where the particle is, $\mathbf{r}_i(t)$, where it was at the previous timestep $\mathbf{r}_i(t-h)$ and the force acting on it, $\mathbf{f}_i(t)$.

In Eq. 1.6 the squared timestep appears and this can be a problematic limitation on how small the timestep can be due to machine precision. The problem is more relevant in GPU codes, where, sometimes, single precision is preferred to double.

In the Verlet algorithm velocities are not taken into account as dynamical variables, but they are calculated at any timestep from the central difference of particles' positions:

$$\mathbf{v}_i(t) = \frac{\mathbf{r}_i(t+h) - \mathbf{r}_i(t-h)}{2h}. \tag{1.7}$$

The velocity Verlet algorithm

Starting from the Verlet algorithm it is possible to obtain a different way to update the system state, which explicitly takes into account velocities. This algorithm is called velocity Verlet. The equation for updating positions is obtained recognising that the difference between positions of the same particle at different times can be written as its velocity; using Eq. 1.7, Eq. 1.6 becomes:

$$
\begin{aligned}
2\mathbf{r}_i(t+h) &= \mathbf{r}_i(t+h) + 2\mathbf{r}_i(t) - \mathbf{r}_i(t-h) + h^2\mathbf{f}_i(t) \\
2\mathbf{r}_i(t+h) &= 2\mathbf{r}_i(t) + 2h\mathbf{v}_i(t) + h^2\mathbf{f}_i(t) \\
\mathbf{r}_i(t+h) &= \mathbf{r}_i(t) + h\mathbf{v}_i(t) + \frac{h^2}{2}\mathbf{f}_i(t).
\end{aligned}
\tag{1.8}
$$

It is worth pointing out that also this new equation is invariant under time inversion and it will therefore produce a constant energy MD algorithm equivalent to the previous one [30, 32–35]. In order to obtain the equation for velocities' update, first we need to write Eq. 1.6 in the two following ways:

$$
\begin{aligned}
\mathbf{r}_i(t+2h) &= 2\mathbf{r}_i(t+h) - \mathbf{r}_i(t) + h^2\mathbf{f}_i(t+h) \tag{1.9} \\
-\mathbf{r}_i(t) &= \mathbf{r}_i(t) - \mathbf{r}_i(t+h) - \mathbf{r}_i(t-h) + h^2\mathbf{f}_i(t) \tag{1.10}
\end{aligned}
$$

and inserting Eqs. 1.9 and 1.10 into Eq. 1.7 evaluated for $\mathbf{v_i(t+h)}$:

$$
\begin{aligned}
2h\mathbf{v}_i(t+h) &= \mathbf{r}_i(t+2h) - \mathbf{r}_i(t) \\
\mathbf{v}_i(t+h) &= \mathbf{v}_i(t) + \frac{h}{2}\left[\mathbf{f}_i(t+h) + \mathbf{f}_i(t)\right].
\end{aligned}
\tag{1.11}
$$

Equations 1.8 and 1.11 can be used to implement a discretization scheme of Newton's second law, which is completely equivalent, from a formal point of view, to the classical Verlet algorithm; the equations for velocity Verlet algorithm are:

$$
\begin{cases}
\mathbf{r}_i(t+h) = \mathbf{r}_i(t) + h\mathbf{v}_i(t) + \dfrac{h^2}{2}\mathbf{f}_i(t) & (1.8) \\[2mm]
\mathbf{v}_i(t+h) = \mathbf{v}_i(t) + \dfrac{h}{2}\left[\mathbf{f}_i(t+h) + \mathbf{f}_i(t)\right] & (1.11)
\end{cases}
$$

From a computational point of view, velocity Verlet has the advantage of explicitly calculating at any timestep the value of the velocities. When velocity is calculated using Eq. 1.7 there is a risk of incurring problems of precision. The calculation of the difference between nearby positions, i.e. the position of a particle at t and at $t+h$, and the calculation of the ratio between this small difference and the timestep, which is generally small too, can cause loss of precision. Another advantage is in not requiring the use of $\mathbf{r}_i(t-h)$. Velocity Verlet can also be easily coupled to a thermostat, discussed in Sec. 1.2.2, but it still requires the calculation of the squared timestep; this problem is avoided in the Leap-Frog algorithm.

The Leap-Frog algorithm

The last MD algorithm we will discuss is the Leap-Frog algorithm. The special features of this algorithm are:

1. There is no need to square the timestep for updating the system state;

2. Velocities and positions are saved at different times.

It's important to be aware of the second point, because it will become important when calculating the kinetic energy of the system and when coupling the system to a thermostat. This algorithm can be easily derived from Newton's second law in the form:

$$\begin{cases} \mathbf{f} = m\dot{\mathbf{v}} \\ \mathbf{v} = \dot{\mathbf{r}} \end{cases}$$

These equations can be discretized using a central difference approximation (with increment h as before):

$$\begin{cases} \mathbf{f}_i(t) = \dfrac{\mathbf{v}_i\left(t + \frac{h}{2}\right) - \mathbf{v}_i\left(t - \frac{h}{2}\right)}{h} \\ \mathbf{v}_i\left(t + \dfrac{h}{2}\right) = \dfrac{\mathbf{r}_i(t + h) - \mathbf{r}_i(t)}{h} \end{cases}$$

and then rewritten in the following form:

$$\begin{cases} \mathbf{v}_i\left(t + \dfrac{h}{2}\right) = \mathbf{v}_i\left(t - \dfrac{h}{2}\right) + h\mathbf{f}_i(t) & (1.15\text{a}) \\ \mathbf{r}_i\left(t + h\right) = \mathbf{r}_i(t) + h\mathbf{v}_i\left(t + \dfrac{h}{2}\right) & (1.15\text{b}) \end{cases}$$

In order to verify the equivalence between the Leap-Frog, Eqs. 1.15a and 1.15b, and the Verlet algorithm, Eq. 1.6, it is sufficient to insert Eq. 1.15a in Eq. 1.15b and use Eq. 1.7 in the form:

$$\mathbf{v}_i\left(t - \frac{h}{2}\right) = \frac{\mathbf{r}_i(t) - \mathbf{r}_i(t - h)}{h}.$$

Note that no squared timestep is needed in this discretization.

1.2.2 Nosé-Hoover thermostat: NVT MD

The solution of Newton's second law using one of the discretization schemes presented before generates the so-called NVE ensemble, i.e., constant number of particles N, volume V (or density $\rho = N/V$) and total mechanical energy E. It is often more interesting for the comparison of model systems with real systems to simulate a NVT ensemble, i.e., constant temperature T instead of constant total mechanical energy E. The temperature can be kept constant in different ways; the most commonly used are the Nosé-Hoover thermostat [36], the Langevin, rescaling velocities and others [1]. In the following we will introduce only the first method because it is the one used in the simulations for this thesis.

The Nosé-Hoover thermostat [36] introduces an additional force, a "friction", in order to keep the kinetic energy constant. This additional force couples with the total kinetic energy and it "corrects" velocities every timestep. The equations of motion for a system of particles coupled with a Nosé - Hoover thermostat are:

$$
\begin{cases}
\ddot{\mathbf{r}}_i(t) = \dfrac{\mathbf{f}_i(t)}{m} - \eta(t)\mathbf{v_i(t)} & \text{(1.16a)} \\[4mm]
\dot{\eta}(t) = \dfrac{K(t) - K_T}{d(N-1)T\tau_{Th}^2} & \text{(1.16b)}
\end{cases}
$$

where $K(t) = \frac{1}{2}\sum_N m_i v_i^2(t)$ is the kinetic energy of the system at the present time, K_T is the kinetic energy of the system in thermal equilibrium at temperature T and d the number of spatial dimensions; in the denominator of Eq. 1.16b the system degrees of freedom are $d(N-1)$ due to the conservation of centre of mass momentum. In Eq. 1.16b the quantity η is called thermostat state and its variation is related to the thermostat relaxation time τ_{Th}. The thermostat relaxation time τ_{Th} defines how strongly the thermostat is coupled with the system.

Eqs. 1.16a and 1.16b can be discretized as in the case of Newton's second law. The discretization will be different if a Leap-Frog or a Velocity Verlet algorithm is employed. In order to update the thermostat state, it's necessary to calculate the kinetic energy of the system at timestep t. In a Leap-Frog algorithm velocities are calculated at $t - \frac{h}{2}$ and $t + \frac{h}{2}$ and the velocity at time t is obtained as a mean of these two values. In velocity Verlet algorithm the velocities at the time t are known from Eq. 1.11.

The equations obtained using the Leap-Frog discretization scheme on Eqs. 1.16a and 1.16b are [37]:

$$\begin{cases} \mathbf{v}_i\left(t+\dfrac{h}{2}\right) = \dfrac{\left(1-h\frac{\eta(t)}{2}\right)\mathbf{v}_i\left(t-\frac{h}{2}\right)+h\mathbf{f}_i(t)/m}{\left(1+h\frac{\eta(t)}{2}\right)} & \text{(1.17a)} \\[4ex] \mathbf{r}_i\left(t+h\right) = \mathbf{r}_i(t)+h\mathbf{v}_i\left(t+\dfrac{h}{2}\right) & \text{(1.17b)} \\[4ex] \eta(t+h) = \eta(t)+h\dfrac{K(t)-K_T}{d(N-1)T\tau_{Th}^2} & \text{(1.17c)} \end{cases}$$

Note that the equation for positions' update has not been changed with respect to those for NVE dynamics. This equation will be changed if a barostat, i.e. a constraint on the system pressure, is introduced as will be discussed in appendix B.

If we set $\eta(t)=0$ in Eqs. 1.17a and 1.17c , Eqs. 1.15a and 1.15b are recovered and therefore NVE dynamics. In this way it is possible to use the same program for simulating both the NVE and the NVT dynamics. The calculation of the total kinetic energy $K(t)$ is usually performed assuming that the velocity of the system centre of mass is zero. If this is not the case, the kinetic energy due to the streaming of the entire system should be removed. This problem is avoided in MD programs by keeping the center of mass momentum zero, by periodically resetting it.

1.2.3 CPUs and GPUs

The acronyms CPU and GPU stand for Central Processing Unit and Graphics Processing Unit respectively. The first one is commonly called processor while the second one graphics card. The first molecular dynamics codes used a single processor. As the possibility of using many processors for a simulation became available, more advanced molecular dynamics codes started using parallel computing on CPUs. The most expensive parts, in terms of computer time, of an MD code are, depending on how the program is structured, the force calculation and the neighborlist update. At this stage it is not important to understand what these two calculations do, but details are given in appendix A; the main feature of both these calculations is that they are related to the difference in position of pairs of particles, when a pairwise potential is used. This means that these calculations scale as N^2 and this is the reason why they are the most important to take into account when optimizing an MD program. The calculation of the difference between two particles' positions is a simple operation but it is expensive when a huge number of this same operation are needed. This feature makes the possibility of using Graphics Processing Unit for performing these calculations especially appealing. A GPU has a really large number, of order 10^3 in a
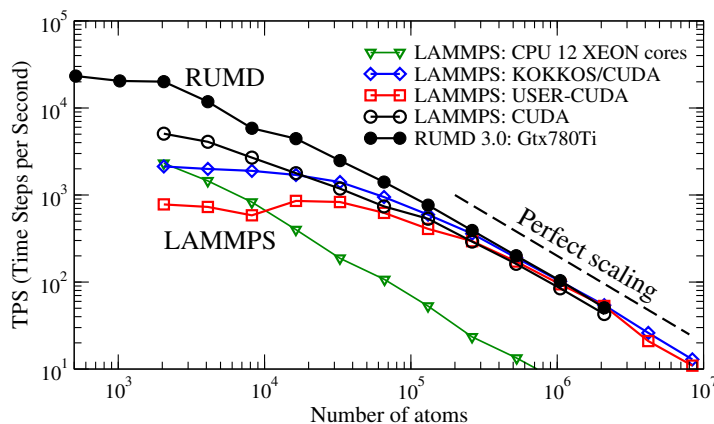
Figure 1.4: Benchmarks for different molecular dynamics code available at the moment. Both programs using parallelization on CPUs and on GPUs are included. Performances are measured in TPS, i.e., timesteps per second at a given system size N. The figure has been taken from Ref. [38] where more details on these benchmarks and on RUMD can be found.

modern GPU, of processing cores able to perform simple operations in short time. All these processing cores can work simultaneously. It it therefore possible to use a different processing core for each particle, or even more than a single core for each particle. This way of parallelizing the force calculation and/or the neighborlist calculation can significantly improve the performance of an MD program. Some benchmarks of modern MD programs working on CPUs or GPUs are shown in Fig. 1.4. Performances are measured in TPS, i.e., timesteps per second at a given system size N.

1.2.4 Rumd

RUMD is the molecular dynamics program developed at Roskilde University starting from 2008 and it has been released in 2012. The name is an acronym for Roskilde University Molecular Dynamics and, according to the newest benchmarks [38], is the fastest code available at the moment; benchmarks are shown in Fig. 1.4. The program is open source and can be downloaded at rumd.org. RUMD uses the CUDA programming library [39] for C++ developed by Nvidia starting from 2007 in order to parallelize the computation on GPUs. One of the strengths of this code, which has been relevant for our work, is the optimized used of GPUs processing cores when simulating small systems, $N < 8000$. In this range of system sizes, the number of available computation parallel processes (thread) is larger than the number of particles and it is therefore necessary to use more than one thread for each particle in order to take advantage of the hardware's full capability.

Chapter 2

Isomorph Theory

In this chapter isomorph theory is presented. The main features of the theory are derived from the general definition of Roskilde matter [40] and then specialized to the Lennard-Jones system [41] for further use in the following chapters. More details can be found in Refs. [42–44]. Some differences between isomorph theory and inverse power law (IPL) scaling or hard sphere (HS) modelling of a simple liquid are also discussed. Specifically referring to the Lennard-Jones system, the difference between the Weeks-Chandler-Andersen (WCA) [45–47] description of the liquid state and isomorph theory is also elucidated. All simulation data in this chapter have been produced by the author and details on the simulations can be found in appendix C.

2.1 Roskilde matter

Starting from 2008, the Roskilde group has pointed out the existence of strong correlations between potential energy and virial fluctuations in the NVT ensemble of some model liquids [48, 49]. An example of these strong correlations for the Lennard-Jones model liquid is given in Fig. 2.1. The consequences of these correlations on the physical properties of the system have been investigated in many works [48, 50–53] and led to the discovery of invariance curves for structure and dynamics in the phase diagram of the class of strongly correlated liquids and to a new definition of simplicity for the liquid state [2].

Nowadays systems with strong potential energy-virial correlations are named Roskilde simple systems, or just Roskilde (R) systems, and the invariance curves are called isomorphs. Invariance curves were found both in the liquid and in the crystalline phase [54] and therefore we will speak about R systems and not simply liquids. The theory describing R systems
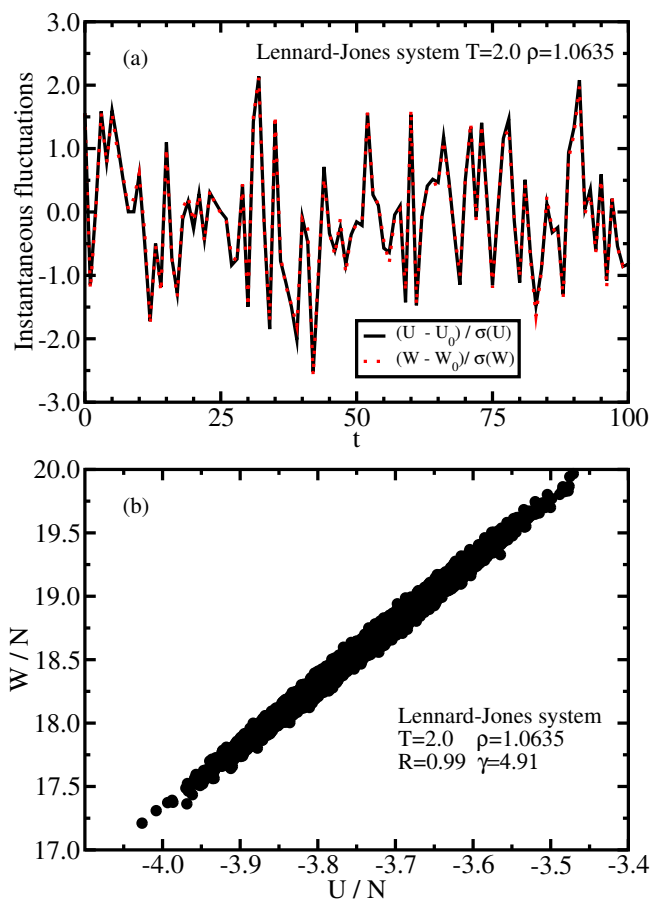
Figure 2.1: Correlations between potential energy and virial of the Lennard-Jones system at the state point $(\rho, T) = (1.0635, 2.0)$. (a) Instantaneous deviations from the mean value of the potential energy per particle and virial per particle normalized by their standard deviations. The deviations follow each other showing the presence of strong correlations between the two quantities. (b) Virial W as function of potential energy U at different configurations sampled in the NVT ensemble. The correlation coefficient R is calculated using Eq. 2.1 and the scaling exponent γ using Eq. 2.18.

is called isomorph theory, from the name of the invariance curves, and it will be described in the following because it will be necessary to understand the remaining chapters in this thesis. Isomorph theory is exact only for systems with an Euler-homogeneous potential energy function, for instance systems interacting via an inverse-power-law (IPL) pair-potential [48, 50]. This means that for these systems it is possible to derive directly from the pair potential the existence of the potential energy-virial correlations [48, 50]. For a general R system, it will be necessary to evaluate the correlation coefficient R (defined below) from a computer simulation and the property of being Roskilde simple will hold only in a certain region of the

phase diagram; it will in fact depend on the density ρ and temperature T of the chosen state point. The correlation coefficient is defined as

$$R(\rho, T) = \frac{\langle \Delta W \Delta U \rangle}{\sqrt{\langle (\Delta W)^2 \rangle \langle (\Delta U)^2 \rangle}} \tag{2.1}$$

where Δ denotes the instantaneous deviations from the equilibrium mean value and the brackets denote NVT ensemble averages, W the virial and U the potential energy of the system. A system is Roskilde simple when $R > 0.9$. Bearing in mind these limitations, the theory can be used as a good approximation for a wide class of systems. Examples of model systems that are R simple [2] in part of their thermodynamic phase diagram, in liquid and solid state [54], are the standard and generalized Lennard-Jones systems (single-component as well as multi-component) [52, 53, 55], systems interacting via the exponential potential [56, 57] and systems interacting via the Yukawa potential [58, 59]. R systems include also some molecular systems like, e.g., the asymmetric dumbbell models [60], the Lewis-Wahnström's three-site model of OTP [60], the seven-site united-atom model of toluene [48], the EMT model of liquid Cu [48] and the rigid-bond Lennard-Jones chain model [10]. Predictions of the isomorph theory have been shown to hold in experiments on glass-forming van der Waals liquids by Gundermann *et al* [61], by Roed *et al* [62], and by Xiao *et al* [63].

2.2 General definition

Recently isomorph theory has been reformulated in a slightly more general way starting from a simple condition on the energy landscape for R systems. The advantage of the new definition is that it is able to better describe the behavior of the excess specific heat C_V^{ex} [40], as will become clear in the following. The new formulation of the theory [40] is consistent with the previous findings and the original theory [52] can be obtained through a first order Taylor expansion of the general case.

A Roskilde system is a system of N particles for which taken any two configurations with potential energies $U(\mathbf{R}_i)$ and $U(\mathbf{R}_j)$ with $U(\mathbf{R}_i) < U(\mathbf{R}_j)$, a uniform scaling of the two configurations will preserve the potential energy ordering:

$$U(\mathbf{R}_i) < U(\mathbf{R}_j) \implies U(\lambda \mathbf{R}_i) < U(\lambda \mathbf{R}_j). \tag{2.2}$$

In this definition $\mathbf{R}$ represents the $d \cdot N$ dimensional vector describing the micro-configuration i or j of a system of N particles embedded in d spatial dimensions. The scaling factor λ can assume any value in $\mathbb{R}_0^+$ and Eq. 2.2 holds therefore also with an equal sign. The choice of not limiting the theory to the 3-dimensional case is related to the study of the general d-dimensional case that will be presented in Chapter 5.
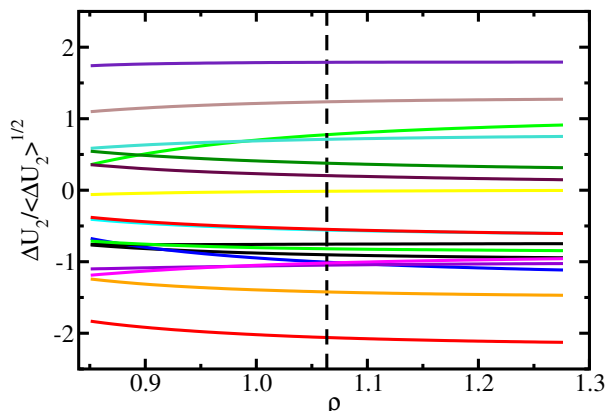
Figure 2.2: Direct check of Eq. 2.2 for the LJ system at the state point $(\rho, T) = (1.0635, 2.0)$. Different equilibrium configurations are selected from an NVT simulation at the given state point and then scaled to 200 different densities in the range $[0.85\rho, 1.28\rho]$. After the scaling is done, the potential energy is calculated and its deviation from the mean value (evaluated from all the scaled configuration at each density) is evaluated. The ordinate axes is scaled using the standard deviation, analogously of what is done in Ref. [40].

If the potential is Euler-homogeneous, i.e.,

$$v(\lambda r) = \lambda^a v(r) \tag{2.3}$$

with a in $\mathbb{N}_0$, Eq. 2.2 is trivially verified:

$$U(\lambda \mathbf{R}_i) = \lambda^a U(\mathbf{R}_i) \tag{2.4}$$

$$U(\lambda \mathbf{R}_j) = \lambda^a U(\mathbf{R}_j) \tag{2.5}$$

$$\text{and so} \quad U(\mathbf{R}_i) < U(\mathbf{R}_j) \implies U(\lambda \mathbf{R}_i) < U(\lambda \mathbf{R}_j). \tag{2.6}$$

For this reason, any system interacting via Euler-homogeneous potential is a Roskilde liquid, as stated previously. For other systems, Eq. 2.2 will only approximately hold, as in the case of the Lennard-Jones (LJ) system [41] for which the validity of Eq. 2.2 is checked in Fig. 2.2. The scaled configurations are *mostly* not crossing each other.

The entropy S of any physical system can be written as the sum of the entropy of an ideal gas at the same temperature and density and an excess term, S_{ex}, which is related to the interaction between particles. If we now consider *physically relevant* micro-configurations with the same density ρ and the same potential energy $U(\mathbf{R})$, we can formally define a microscopic excess entropy S_{ex} simply by choosing it to be the S_{ex} corresponding to the potential energy surface that the configuration $\mathbf{R}$ belongs to [40, 64]:

$$S_{\text{ex}}(\mathbf{R}) \equiv S_{\text{ex}}(\rho, U(\mathbf{R})). \tag{2.7}$$

The restriction of considering *physically relevant* micro-configurations reflects the fact that for real systems isomorph theory is only approximate.

The *non physically relevant* micro-configurations are the ones that are less likely, i.e., corresponding to a low Boltzmann factor. Under the assumption of $S_{\text{ex}}(\rho, U(\mathbf{R}))$ being bijective, Eq. 2.7 can be used to express potential energy as function of excess entropy:

$$U(\mathbf{R}) = U(\rho, S_{\text{ex}}(\mathbf{R})). \tag{2.8}$$

These equations, Eqs. 2.7 and 2.8, can be used to define relations between excess entropy and potential energy for every system. Nevertheless, they are of particular interest for Roskilde systems because they imply the existence of curves of invariant structure and dynamics. It can be proved [40] that two isotropic scaled micro-configurations satisfying Eq. 2.2 have the same excess entropy S_{ex}. The relation between the state vector $\mathbf{R}$ of the two scaled configurations $\mathbf{R}_1$ and $\mathbf{R}_2 = \lambda \mathbf{R}_1$ is:

$$\rho_1^{1/d} \mathbf{R}_1 = \rho_2^{1/d} \mathbf{R}_2 \equiv \tilde{\mathbf{R}} \tag{2.9}$$

where the last equality defines the reduced coordinate vector $\tilde{\mathbf{R}}$. In this case, the λ in Eq. 2.2 is equal to $\rho_1^{1/d} \rho_2^{-1/d}$. The invariance of S_{ex} under isotropic scaling implies that the excess entropy for a Roskilde system depends only on the reduced coordinate vector $\tilde{\mathbf{R}}$.

$$S_{\text{ex}}(\mathbf{R}) = S_{\text{ex}}(\tilde{\mathbf{R}}) \tag{2.10}$$

and therefore Eq. 2.8 can be recast as:

$$U(\mathbf{R}) = U(\rho, S_{\text{ex}}(\tilde{\mathbf{R}})). \tag{2.11}$$

When defining the reduced coordinate $\tilde{\mathbf{R}}$, we use the density of the system. The idea of using macroscopic thermodynamic quantities as reference units for the description of the system was originally introduced by Rosenfeld [65, 66] and it is used to define invariant quantities in isomorph theory. Henceforth quantities expressed using macroscopic thermodynamic quantities as reference units are named 'in reduced units' and represented with a tilde; distances are measured in units of $\rho^{-1/d}$, energies in units of $k_B T$ and time in units of $m^{1/2}(k_B T)^{-1/2}\rho^{-1/d}$, where m is the average particle mass.

Isomorphs are defined as configurational adiabats, i.e curves along which the S_{ex} is constant, in the region of the phase diagram where the system is R simple. Starting from Eq. 2.11, it is possible to show that the structure and dynamics of a Roskilde liquid along isomorphs are invariant, when expressed in reduced units.

2.3   Isomorph invariants and isomorph shape

Invariance of structure and dynamics

In order to show the invariance of structure and dynamics along an isomorph it is sufficient to show that Newton's second equation of motion, in reduced units, is invariant along an isomorph. The reduced units version of Newton's second law is:

$$\frac{d^2\tilde{\mathbf{R}}}{d\tilde{t}^2} = \tilde{\mathbf{F}}(\mathbf{R}) \equiv \frac{\mathbf{F}(\mathbf{R})\rho^{-1/d}}{k_B T} \tag{2.12}$$

The force at any given time will be function of the particles' positions in non reduced units. If the system of interest is R simple, we know from Eq. 2.11 that the potential energy U is function of the reduced coordinate vector $\tilde{\mathbf{R}}$. The reduced force vector $\tilde{\mathbf{F}}(\mathbf{R})$ in Eq. 2.12 is, for conservative forces:

$$\mathbf{F} = -\nabla U(\rho, \tilde{\mathbf{R}}) = -\left.\frac{\partial U(\rho, S_{\text{ex}})}{\partial S_{\text{ex}}}\right|_{\rho} \nabla S_{\text{ex}}(\tilde{\mathbf{R}}) \tag{2.13}$$

which, using $\nabla = \rho^{1/d}\tilde{\nabla}$ and $\partial U/\partial S_{\text{ex}}|_{\rho} = T$, becomes:

$$\mathbf{F} = -\rho^{1/d}T\tilde{\nabla}S_{\text{ex}}(\tilde{\mathbf{R}}) \quad \text{or} \quad \tilde{\mathbf{F}}(\mathbf{R}) = -\frac{1}{k_B}\tilde{\nabla}S_{\text{ex}}(\tilde{\mathbf{R}}). \tag{2.14}$$

Eq. 2.14 shows that the reduced force to be a function of the reduced coordinate vector and therefore to be invariant along an isomorph for configurations with given reduced coordinates. This implies that structure and dynamics, in reduced units, are invariant along an isomorph [40].

Scaling exponent γ

The first characterization we gave of a Roskilde system is the strong correlations between potential energy and virial fluctuations in the NVT ensemble. This feature can be derived from Eq. 2.2 in the following way. For two configurations $\mathbf{R}_1$, $\mathbf{R}_2$ at the same density and potential energy $U(\mathbf{R}_1) = U(\mathbf{R}_2)$, Eq. 2.2 states that, for a Roskilde system, $U(\lambda\mathbf{R}_1) = U(\lambda\mathbf{R}_2)$. We can now take the derivative of $U(\lambda\mathbf{R}_i)$ respect to λ and obtain:

$$\mathbf{R}_1 \cdot \nabla U(\lambda\mathbf{R}_1) = \mathbf{R}_2 \cdot \nabla U(\lambda\mathbf{R}_2) \tag{2.15}$$

and, using the definition of virial $W(\mathbf{R}) \equiv \frac{1}{d}\mathbf{R} \cdot \nabla \mathbf{U}(\mathbf{R})$, we obtain, for $\lambda = 1$:

$$W(\mathbf{R}_1) = W(\mathbf{R}_2). \tag{2.16}$$

The knowledge of how potential energy scales allows one to predict the virial of a different configuration. The two quantities W and U are therefore perfectly correlated. This perfect correlation will exist only for systems that fully satisfy Eq. 2.2 and it will hold for Roskilde systems only to a good

approximation. As consequence of that, the correlation coefficient R, defined in Eq. 2.1, between W and U is not identically equal to 1 but only close to. For some systems, the Lennard-Jones system for example, the correlation coefficient R, defined through Eq. 2.1, can be really close to unity, as shown in Fig. 2.1 (b).

When the correlations between W and U are present, it is possible to introduce a proportionality constant between the instantaneous fluctuations of the two quantities:

$$\Delta W(t) \cong \gamma \Delta U(t) \tag{2.17}$$

or, equivalently,

$$\gamma = \frac{\langle \Delta W \Delta U \rangle}{\langle (\Delta U)^2 \rangle} \tag{2.18}$$

where the least-squares approach has been used to calculate the slope γ of the linear regression of W as function of U. The Pearson correlation coefficient of this linear regression is the R defined in Eq. 2.1.

Using the fluctuation relation [48]

$$\left. \frac{\partial \langle A \rangle}{\partial \beta} \right|_\rho = -\langle \langle AU \rangle - \langle A \rangle \langle U \rangle \rangle = -\langle \Delta A \Delta U \rangle \tag{2.19}$$

where A is a generic thermodynamic quantity and $\beta = (k_B T)^{-1}$. Choosing in particular W and U we get

$$\left. \frac{\partial \langle W \rangle}{\partial \beta} \right|_\rho = -\langle \Delta W \Delta U \rangle, \quad \left. \frac{\partial \langle U \rangle}{\partial \beta} \right|_\rho = -\langle (\Delta U)^2 \rangle, \tag{2.20}$$

together with the Maxwell relation [52]

$$\rho \left. \frac{\partial \langle W \rangle}{\partial T} \right|_\rho = -\rho^2 \left. \frac{\partial S_{\text{ex}}}{\partial \rho} \right|_T \tag{2.21}$$

and the definition of thermodynamic temperature ($\langle U \rangle = U$)

$$\left. \frac{\partial U}{\partial S_{\text{ex}}} \right|_\rho = T, \tag{2.22}$$

Eq. 2.18 becomes

$$\gamma = -\frac{\rho \left. \dfrac{\partial S_{\text{ex}}}{\partial \rho} \right|_T}{T \left. \dfrac{\partial S_{\text{ex}}}{\partial T} \right|_\rho} = -\frac{\left. \dfrac{\partial S_{\text{ex}}}{\partial \ln \rho} \right|_T}{\left. \dfrac{\partial S_{\text{ex}}}{\partial \ln T} \right|_\rho}. \tag{2.23}$$

The right-hand side of Eq. 2.23 is the logarithmic derivative of temperature T as function of density ρ along a constant excess entropy S_{ex} curve ($dS_{\text{ex}}(\rho, T) = 0$) and therefore

$$\gamma = \left. \frac{\partial \ln T}{\partial \ln \rho} \right|_{S_{\text{ex}}}. \tag{2.24}$$
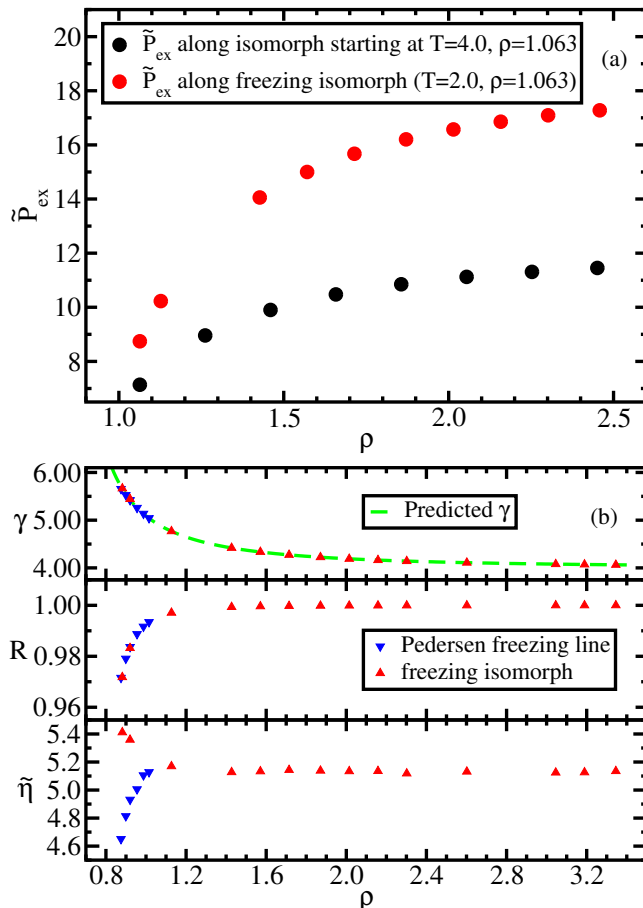
Figure 2.3: Data obtained from NVT simulations (SLLOD simulations for viscosity η) of the Lennard-Jones model system. Details in appendix C. (a) Excess pressure in reduced units, $\tilde{P}_{ex} = W/(Nk_BT)$, along two different isomorphs. For inverse power-law pair potentials this quantity is invariant, while for the LJ system it clearly is not. This shows that isomorph scaling is not simply a trivial IPL scaling. (b) In the top panel, the scaling exponent γ, Eq. (2.18), is shown as a function of density along the freezing line of the LJ system and the isomorph from $(\rho_0, T_0) = (1.0635, 2.0)$, named the freezing isomorph for reasons that will be discussed in Chapter 3. The green line is the predicted value from Eq. 2.24 [55, 67] and Eq. 2.39. The middle and bottom panels show the virial potential-energy correlation coefficient R and the reduced viscosity $\tilde{\eta}$ along the freezing line of the LJ system and the freezing isomorph. The freezing line data are taken from Pedersen [68] and the values of γ, R and $\tilde{\eta}$ at these points are marked in blue; the red symbols are the same quantities calculated at freezing isomorph state points.

The proportionality constant defined in Eq. 2.18 is the scaling exponent that produces constant excess entropy S_{ex} curves in the R simple region of the phase diagram, previously named, isomorphs. Eq. 2.24 allows one to generate isomorphs *step-by-step*, i.e., for small density changes, due to its differential form.

Connection with the first formulation of the theory

Starting from Eq. 2.8 the old formulation of the isomorph theory [48, 50–53] can be recovered as a first order Taylor expansion; let's consider a single *physically relevant* micro-configuration $\mathbf{R}_0$ at the state point (ρ_0, T_0); its microscopic excess entropy is $S_{\text{ex}}(\tilde{\mathbf{R}}_0)$ and, assuming that the value of $S_{\text{ex}}(\tilde{\mathbf{R}}_0)$ is close to the thermodynamic excess entropy $S_{\text{ex},0}$ at the state point (ρ_0, T_0), it is possible to write its potential energy $U(\rho_0, S_{\text{ex}}(\tilde{\mathbf{R}}_0))$ using a first order Taylor expansion:

$$U(\rho_0, S_{\text{ex}}(\tilde{\mathbf{R}}_0)) \approx U_0 + T_0(S_{\text{ex}}(\tilde{\mathbf{R}}_0) - S_{\text{ex},0}) \tag{2.25}$$

where we made use of Eq. 2.8, of $T = \partial U / \partial S_{\text{ex}}|_\rho$ and of Eq. 2.10. The term $U_0 = U(\rho_0, T_0)$ is the mean value of the potential energy at the state point (ρ_0, T_0). If $(\rho_1, \mathbf{R_1})$ and $(\rho_2, \mathbf{R_2})$ are two micro-configurations corresponding to the same reduced configuration $\tilde{\mathbf{R}}_1 = \tilde{\mathbf{R}}_2 = \tilde{\mathbf{R}}$ the potential energy of the two micro-configurations are:

$$\frac{U(\rho_1, S_{\text{ex}}(\tilde{\mathbf{R}}_1)) - U_1}{k_B T_1} = \frac{U(\rho_2, S_{\text{ex}}(\tilde{\mathbf{R}}_2)) - U_2}{k_B T_2} \tag{2.26}$$

due to the invariance of $S_{\text{ex}}(\tilde{\mathbf{R}}) - S_{\text{ex},0}$ and accordingly the definition of Roskilde simple systems from Ref. [48] is recovered. Eq. 2.26 has been obtained using an approximation for the S_{ex} dependency. If this approximation is dropped, a generalized version of Eq. 2.26 is:

$$U(\mathbf{R}_2) = f_{\rho_1}(\rho_2, U(\mathbf{R}_1)). \tag{2.27}$$

This last equation is equivalent to Eq. 2.2 as discussed in Ref. [40]. Therefore the temperatures corresponding to the configurations $\mathbf{R}_1$ and $\mathbf{R}_2 = \lambda \mathbf{R}_1$ along the same isomorph will be related by, always using $T = \partial U / \partial S_{\text{ex}}|_\rho$:

$$T_2 = \left. \frac{\partial f_{\rho_1}(\rho_2, U(\mathbf{R}_1))}{\partial U(\mathbf{R}_1)} \right|_{\rho_1, \rho_2} T_1 \tag{2.28}$$

remembering that due to Eq. 2.11, the potential energy U depends on the micro-configuration $\mathbf{R}_i$ through the excess entropy $S_{\text{ex}}(\tilde{\mathbf{R}}_i)$. Eq. 2.28 gives the density dependence of the temperature along an isomorph. It is therefore possible to define the shape function for isomorphs as follows:

$$h(\rho_1, \rho_2, U_1) = \left. \frac{\partial f_{\rho_1}(\rho_2, U(\mathbf{R_1}))}{\partial U(\mathbf{R_1}))} \right|_{\rho_1, \rho_2} \tag{2.29}$$

21

and Eq. 2.28 becomes

$$T_2 = h(\rho_1, \rho_2, U_1)T_1. \tag{2.30}$$

For state points along an isomorph starting from (ρ_1, T_1), it is also possible to use the function $h(\rho_1, \rho_2, U_1)$ to obtain the density dependence of the scaling exponent γ substituting Eq. 2.30 into Eq. 2.24:

$$\gamma(\rho_2, S_{\text{ex}}(\tilde{\mathbf{R}})) = \left. \frac{\partial \ln h(\rho_1, \rho_2, U_1)}{\partial \ln \rho_2} \right|_{S_{\text{ex}}}. \tag{2.31}$$

2.3.1   Estimating specific heat along an isomorph

The excess specific heat at constant volume C_V^{ex}, i.e. the difference between the system C_V and the specific heat at constant volume of an ideal gas at the same density and temperature, is defined by

$$C_V^{ex} = \left. \frac{\partial U}{\partial T} \right|_\rho. \tag{2.32}$$

If two isomorphic state points are taken into account it is possible to express the excess specific heat of the state point (ρ_2, T_2) as function of the excess specific heat of the state point (ρ_1, T_1) using Eqs. 2.27 and 2.30 [40].

$$C_{V,2}^{ex} = \left. \frac{\partial U(\mathbf{R}_2)}{\partial T_2} \right|_{\rho_2} = \left. \frac{\partial U(\mathbf{R}_2)}{\partial U(\mathbf{R}_1)} \right|_{\rho_2} \left. \frac{\partial U(\mathbf{R}_1)}{\partial T_2} \right|_{\rho_2} \tag{2.33}$$

and therefore

$$\frac{1}{C_{V,2}^{ex}} = \frac{1}{C_{V,1}^{ex}} + \frac{T_1}{h(\rho_1, \rho_2, U(\mathbf{R_1}))} \left. \frac{\partial h(\rho_1, \rho_2, U(\mathbf{R_1}))}{\partial U(\mathbf{R_1})} \right|_{\rho_1, \rho_2} \tag{2.34}$$

$$C_{V,2}^{ex} = C_{V,1}^{ex} \left[1 + \left. \frac{\partial \ln h(\rho_1, \rho_2, U(\mathbf{R_1}))}{\partial \ln T_1} \right|_{\rho_1, \rho_2} \right]^{-1}. \tag{2.35}$$

Excess specific heat data for the LJ system along three different isomorphs are shown in Fig. 2.4. The full lines are predicted excess specific heat at constant volume C_V^{ex} from Eq. 2.35.

If in Eq. 2.35 the partial derivative term is ignored, the prediction from the first formulation of isomorph theory [52] is recovered. From data in Fig. 2.4 it is clear that the approximation of considering the specific heat invariant along an isomorph provides results worse than Eq. 2.35 but still not too far from the simulation data [69].
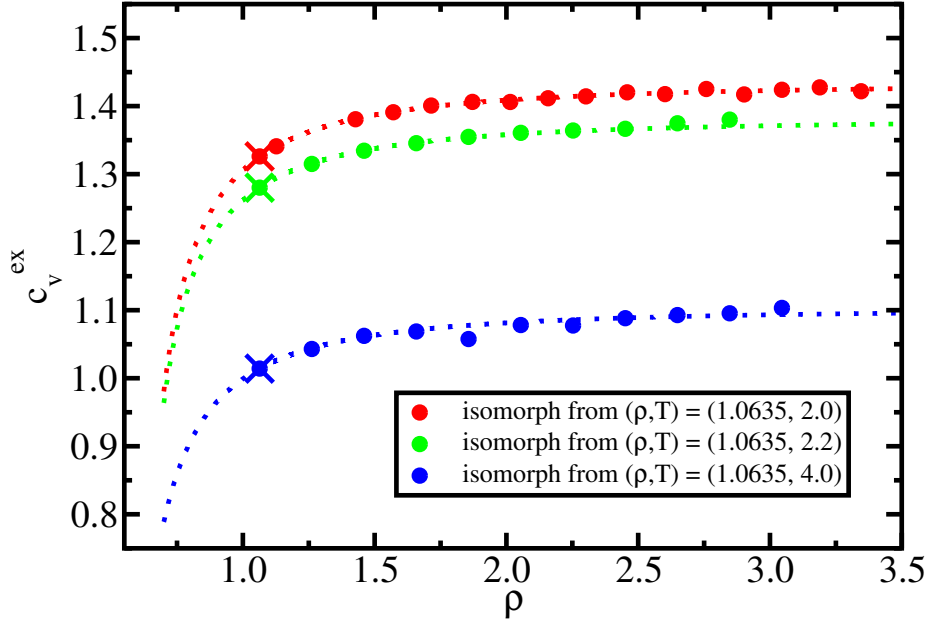
Figure 2.4: Excess specific heat at constant volume per particle c_V^{ex} along three different isomorphs. Density ρ and temperature T of the starting points for the three isomorphs are given in the legend and the value of c_V^{ex} per particle at these starting points is marked with a cross in figure. Dotted lines are the predictions from isomorph theory for c_V^{ex} from Eq. 2.35. At high densities the data exhibit a plateau which correspond to the prediction of the first formulation of isomorph theory [52], i.e. constant c_V^{ex}.

2.3.2 Isomorph shape function $h(\rho)$ from the pair potential

In previous sections the function $h(\rho_1, \rho_2, U_1)$ have been introduced but no details are given on its functional form. In Refs. [55, 67, 70] the question of relating the function $h(\rho_1, \rho_2, U_1)$, which in the following will be referred as $h(\rho)$, has been addressed. It can be shown in fact that the density dependence of the scaling exponent γ can be obtained from the pair potential through:

$$\gamma(\rho, S_{\text{ex}}) = \frac{1}{d}\left(-2 - r\frac{v^{(3)}(r)}{v^{(2)}(r)}\right)\Bigg|_{r=\Lambda(S_{\text{ex}})\rho^{-1/d}} \tag{2.36}$$

where the second and third derivative of the pair potential, respectively $v^{(2)}$ and $v^{(3)}$, are involved and d is the number of spatial dimensions. The quantity $\Lambda(S_{\text{ex}})$ takes into account the dependence on excess entropy of Eq. 2.31. The physical meaning of $\Lambda(S_{\text{ex}})$ is that along an isochore the scaling exponent slightly changes with temperature and therefore Eq. 2.36 needs to be specialized to the considered isomorph, which is identified by its (conserved) excess entropy S_{ex}. The shape function $h(\rho)$ can be obtained

by integration from Eq. 2.36, as it is clear from Eq. 2.31:

$$h(\rho, S_{\text{ex}}) = A \, \rho^{-2/d} v^{(2)}(r)\Big|_{r=\Lambda(S_{\text{ex}})\rho^{-1/d}}. \tag{2.37}$$

The parameter A takes into account that the function $h(\rho)$ is defined up to a positive multiplicative constant. In the case of the Lennard-Jones potential [41] in $d = 3$

$$v^{LJ}(r) = 4\epsilon \left[\left(\frac{\sigma}{r}\right)^{12} - \left(\frac{\sigma}{r}\right)^{6} \right], \tag{2.38}$$

Eq. 2.37 becomes:

$$h(\rho, S_{\text{ex}}) = \left(\frac{\gamma_0(S_{\text{ex}})}{2} - 1 \right) \left(\frac{\rho}{\rho_0} \right)^4 - \left(\frac{\gamma_0(S_{\text{ex}})}{2} - 2 \right) \left(\frac{\rho}{\rho_0} \right)^2 \tag{2.39}$$

where the function has been evaluated at a state point (ρ_0, T_0) with scaling exponent γ_0. As already pointed out, the dependence on S_{ex} can be dropped when considering a single isomorph since the excess entropy is constant along any given isomorph, as stated in Eq. 2.10.

It is interesting to note that the right hand side of Eq. 2.36 is proportional to the approximate IPL exponent of order $p = 2$ [48, 50]:

$$n^{(p)}(r) = \left(-p - r \frac{v^{(p+1)}(r)}{v^{(p)}(r)} \right). \tag{2.40}$$

In the case of a simple IPL potential with exponent n, $n^{(p)}(r) = n$ for every p. For the IPL potential, the scaling exponent from Eq. 2.36 will be identically n/d for any distance. In $d = 3$, the function $h(\rho)$ can be used to understand why the density-scaling discussed in Chap. 1 holds. In Fig. 2.3, the density dependence of γ along an isomorph is shown for the LJ potential and the data are compared with Eq. 2.36. The scaling coefficient γ exhibits a slow variation with density ρ (it changes from ≈ 6 to ≈ 4 while density is changed a factor 2) and this is why density-scaling with fixed scaling exponent [13–16] is obeyed [55].

2.4 Differences and analogy between liquid state theories

Now that the main features of isomorph theory have been highlighted it is possible to compare isomorph theory with the previous approaches used to describe the liquid state, i.e. the HS paradigm introduced in Chap. 1 and the well known Weeks-Chandler-Andersen [45–47] approximation for the Lennard-Jones system.

The isomorph theory and the HS paradigm

The HS system has been the reference system of the theory of simple liquid in the last century [1] and it has been found to well describe many aspects of simple liquids. Nevertheless three important aspects of the mapping from a generic system to the HS one are still debated. The first one is the need of defining an *ad hoc* HS radius: no clear answer to how to define it has been found [71–77]. The second aspect concerns the applicability of the mapping; it is well known, for example, that many systems exhibit invariances along constant excess entropy curves in the dense region of the liquid phase [65, 78] but there is no way, given a specific state point, to verify if it is in the *well behaving* dense region or not without comparing its physical properties to the ones of another state point. The third issue is relating to the predicted invariances. Once the chosen system have been mapped to the corresponding HS system (after choosing an HS radius) it should inherit all the invariances of the HS system itself but this is not the case: as shown in Fig. 2.3 the LJ system has invariant dynamics along an isomorph, i.e. a region of a configurational adiabat for which the correlation coefficient R is larger than 0.9, as predicted in a HS picture but not invariant reduced (excess) pressure.

All these problematic aspects of the HS mapping are not present in the isomorph theory which is at the same time able to described a wide class of systems without referring to the unphysical picture of liquids as collection of spherical particles interacting via rigid collisions. In the isomorph theory there is no need for mapping from the real system to an ideal one and therefore no need of defining an *ad hoc* radius. Often the isomorph theory is confused with some sort of mapping to an IPL system [1] but this is not the case. As shown in Fig. 2.5 (a), the viscosity of the LJ system and that of the IPL describing the repulsive part of the LJ potential $v^{IPL12}(r) = 4\epsilon \left(\frac{\sigma}{r}\right)^{12}$ are different. The most striking difference, in our view, is not in the numerical difference between the computed viscosity for the two systems but in the completely different trends. While the reduced viscosity $\tilde{\eta}$ is invariant for the LJ system, Fig. 2.3, this is not true for the IPL along the same curve. In the isomorph theory the well behaving region, i.e. the region of applicability of the theory, is well defined. If the correlation coefficient R, given by Eq. 2.1, at the chosen state point is larger than 0.9 the isomorph theory can
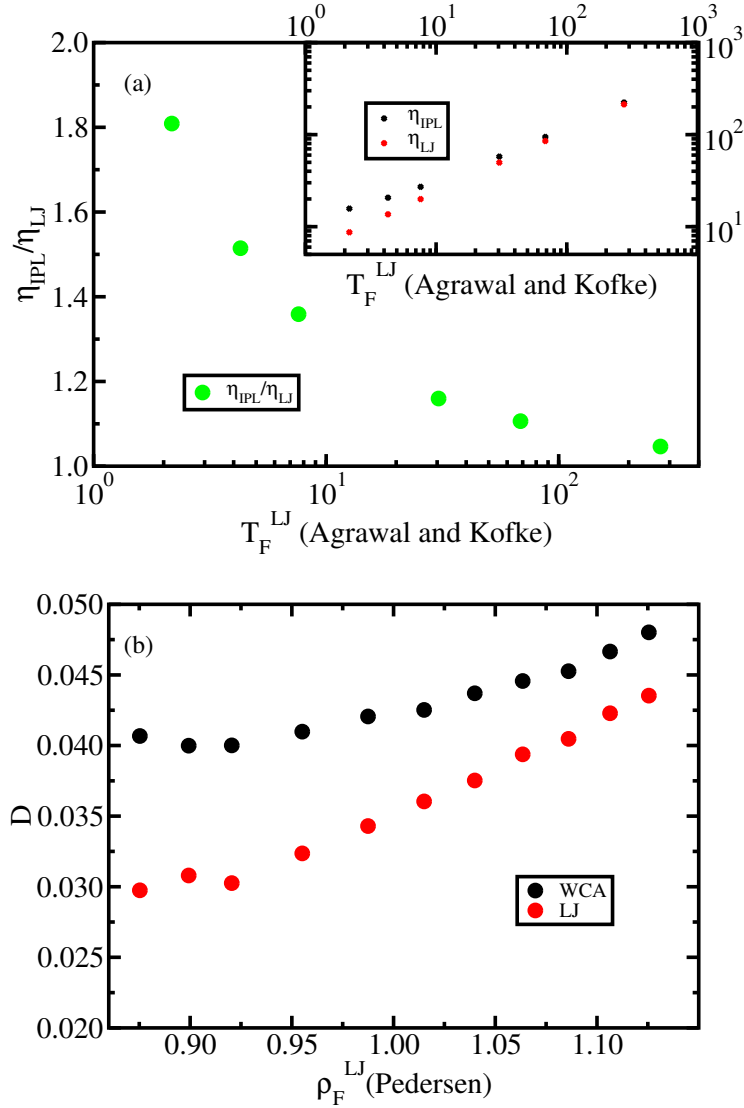
Figure 2.5: Differences between the isomorph theory and other approaches. (a) Comparison between the viscosity of the LJ system with truncation at 2.5σ and the IPL12 potential $v^{IPL12}(r) = 4\epsilon \left(\frac{\sigma}{r}\right)^{12}$ with the same truncation along the freezing line state points from Ref. [79]. The difference between the viscosity data for temperatures below $T \approx 70$ in LJ units clearly shows that the IPL12 system does not offer a reliable description of the LJ dynamics in a significant part of the phase diagram. (b) Comparison between the diffusion coefficient D of the LJ system and the WCA approximation along the Pedersen freezing line [68]. While it is well known that the structure of the LJ fluid can be described with the WCA approach, which relies on the same assumptions of the HS paradigm, this approximation completely fails in reproducing the dynamics. The same failure in describing the dynamics with WCA approximation is well known also for the LJ binary mixture [80, 81].

be used. The third issue introduced in the previous paragraph is maybe the most interesting problem of the HS mapping. Why some quantities are invariant while some others are not? In the case of isomorph theory this question is easily addressed [52]: quantities involving derivatives respect to volume of the internal energy are not invariant. This is the case for pressure for example and it explains why the excess reduced pressure $\tilde{P}_{\text{ex}}$ of the LJ system in Fig. 2.3 is not invariant.

WCA and isomorphs for the LJ system

It is well known that the structure of the LJ system in the dense liquid region can be well described using the Weeks-Chandler-Andersen (WCA) [45–47] approximation. This approximation is based on the idea that the LJ liquid can be described ignoring the effect of the attraction, in the dense liquid region. The WCA potential is obtained by cutting the LJ potential at the distance $\bar{r}$ corresponding to the minimum of the potential and shifting the potential in order to have $v^{WCA}(\bar{r}) = 0$.

The WCA approximation has been proved to well reproduce the structure of the LJ system but at the same time it has been recently proved by different authors that it gives a poor description of the dynamics [80–82]. The diffusion coefficient for two systems of particles, the first interacting via $v^{WCA}(r)$ and the latter via LJ potential with cut at 2.5σ, is shown in Fig. 2.5 for state points along the freezing line from Ref. [68]. The data differ significantly. As will be discussed in the next chapter, isomorph theory is able to describe the invariance of both dynamics and structure along the configurational adiabats without the need of ignoring the attraction between Lennard-Jones particles.

Chapter 3

The Lennard-Jones model system and its isomorphs

In this chapter we discuss how isomorph theory can be related to some well known freezing and melting criteria connecting them to the isomorph invariances of the Lennard-Jones (LJ) system [41]. A study on the relation between the correlation coefficient R and the scaling exponent γ for the generalized LJ model is also included. The work on the freezing and melting line of the LJ system has been published in Ref. [83, 84] while the results on the generalized LJ model have not been published yet. Details on the simulations can be found in appendix C.

In the last chapter we described how isomorph theory can be used to explain specific invariances of Roskilde liquids. In this chapter and in the following ones two model systems are studied: the Lennard-Jones (LJ) [41] system and the Gaussian core system. These two systems are representative of two classes of model liquids which have been widely studied in the past years: the LJ system is an example of simple liquid according to the most common definition [1] while the Gaussian core is an example of anomalous liquid [6, 24, 85]. These two systems are different in many aspects but they can both be described by isomorph theory in parts of their phase diagram.

3.1   Freezing and melting lines of the LJ system

In Chap. 1 the phase diagram of a single-component system has been introduced. When pressure and temperature are used as thermodynamical variables to define the state of a system, as in Fig. 1.1, the transition between the liquid state and the solid state is represented by a line, the melting line, in the phase diagram because the coexistence pressure between liquid and solid is unique at any temperature. Another possible choice of thermodynamical variable is to use density and temperature. In this case there exist a range of densities at which liquid and solid can coexist at equilibrium for each temperature. This coexistence region is delimited by two lines: the freezing line represents, at each temperature, the lowest density at which liquid and solid can coexist while the melting line represents the highest density.

The study of freezing and melting of a simple liquid has been broadly discussed in the past [86–88]. The aim of our study in this broad field was to understand why some liquids show invariances along their freezing and melting curves and others do not [89, 90]. Another interesting question in this context is if these invariances are peculiarities of the freezing and melting processes or if these invariances hold also elsewhere in the phase diagram. In order to answer these questions we performed an extensive study of the freezing and melting of a well known system, the Lennard-Jones model system. The reasons for studying this specific system are many, among them the most important are, in our view, the simplicity of the model liquid itself, which is also why this model system has been so widely used, and the presence of a wide literature to compare to. The results of this section have been published in [83].

3.1.1   Data and predictions for the freezing and melting lines

Already in 2009, Gnan *et al* [52] and Schrøder *et al* [53] proposed that the freezing line for the LJ system should be an isomorph. This conjecture was left without proof until 2014 when Pedersen [68] showed that an isomorph can be used to approximate well the LJ freezing line for densities of about 1.0 in LJ units. Small deviations were found close to the triple point and we will discuss them in the next section. In this section we present different estimations of the LJ freezing line that have been computed in the last twenty years and test the prediction of the LJ freezing line to be an isomorph on the full range of densities and temperatures studied in the past. The LJ model system has been used as a model system for some metals too, therefore the study of the freezing line for this system can be of interest in other fields of research as for example in the study of Earth's core [91–93].

We used the state point $(\rho, T) = (1.0635, 2.0)$ as reference point for building the freezing isomorph. This freezing state point was calculated by
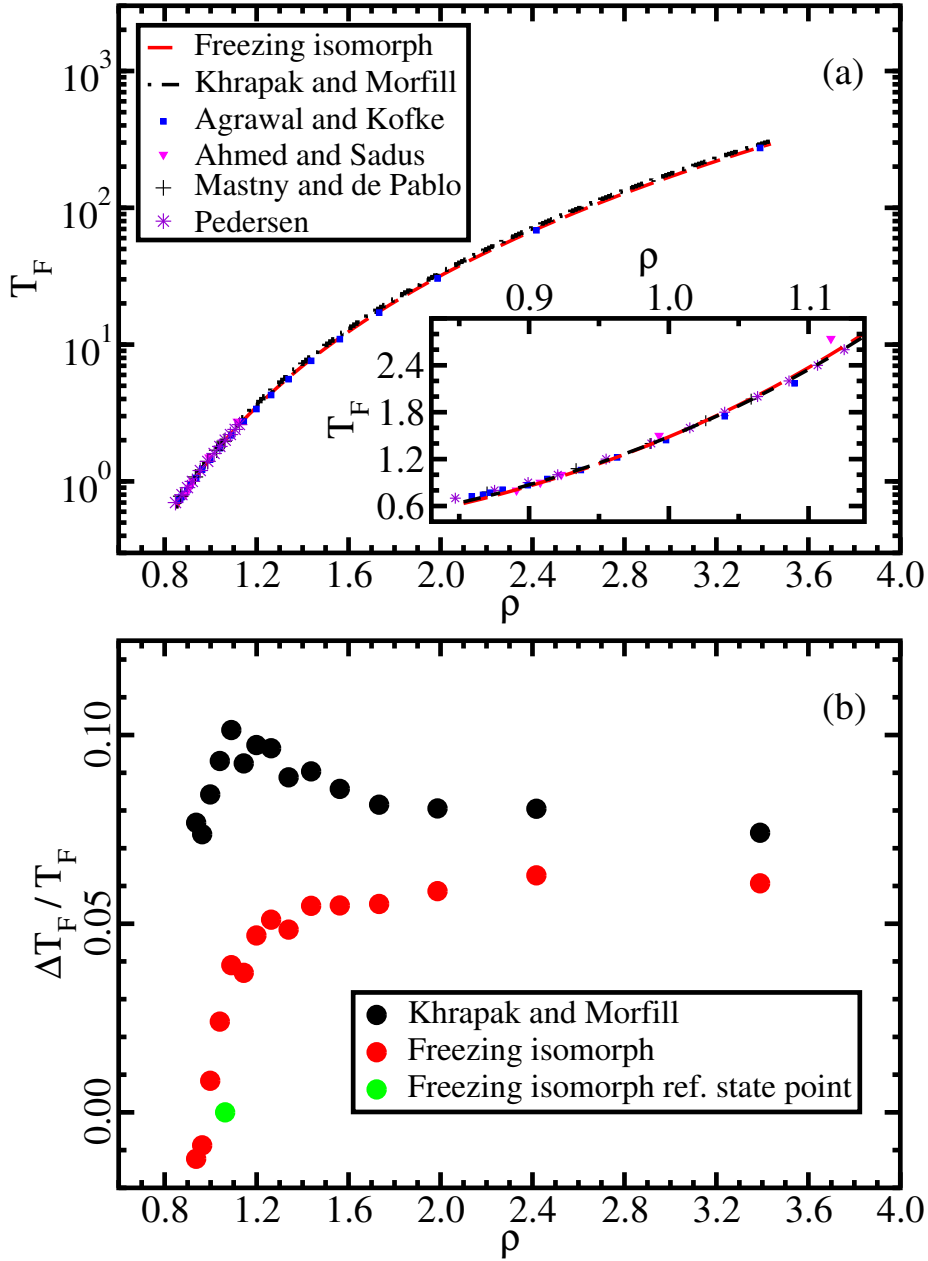
Figure 3.1: Freezing line of the LJ system. In (a) the isomorph approximation to the freezing line is marked by the red line and the Khrapak and Morfill approximation [95] by the black line ($A_{F,KM} = 2.29$ and $B_{F,KM} = 0.71$ in this case); freezing state points obtained in the recent years using various techniques are shown by symbols [68, 79, 96, 97]. Both approximations reproduce the data points well; the inset focuses on low densities. In (b) the relative difference between Agrawal and Kofke freezing-temperature data [79] and the two approximations is shown. The isomorph approximation gives smaller deviations from the simulation data. The main advantage of approximating the freezing line by an isomorph lies, however, in the possibility of predicting the full freezing line from the knowledge of a single freezing state point.

Pedersen [68] using the interface pinning method [94]. In Chap. 2 we have shown that at this state point the LJ liquid is a Roskilde liquid, Figs. 2.1 and Fig. 2.2. The correlation coefficient R and the scaling exponent γ at this state point are:

$$R_F = 0.995 \quad , \quad \gamma_F = 4.907 \quad . \tag{3.1}$$

Even though the correlation coefficient is close to 1.0, the γ value definitely differs from 4, indicating that the attractive part of the potential is not negligible. Starting from this state point it is possible to build an isomorph that we will name the approximating freezing isomorph or simply freezing isomorph. The equation of this isomorph is:

$$T_F(\rho) = A_F \rho^4 - B_F \rho^2 \tag{3.2}$$

where $A_F = 2.27$, $B_F = 0.80$ and T_F is the freezing temperature at a given density ρ. This equation have been obtained using Eq. 2.39 with the value of Eq. 3.1 for γ. It should be remembered that isomorph theory is not exact for the LJ system but it holds only approximately and the fact that the freezing line is an isomorph is an approximation itself. Because of this approximate nature of the isomorph theory, the parameters in Eq. 3.2 slightly depend on the freezing state point chosen. The same density dependence for the freezing temperature of the LJ system was suggested by Khrapak and Morfill [95] and, in fact, long ago by Rosenfeld from his "additivity of melting temperatures" (derived by reference to the hard-sphere system) [98, 99]. In Fig. 3.1, the freezing isomorph is compared with computed values for the freezing line in a wide range of densities. There is not doubt that the freezing isomorph provides a rather good approximation for the freezing line of the LJ system in the whole range of densities considered. It is also worth noting that the construction of the freezing isomorph requires only a single NVT simulation at a chosen freezing point, in our case $(\rho, T) = (1.0635, 2.0)$. Nevertheless, it is also clear, from Fig. 3.1 (b), that the freezing line is not exactly an isomorph as we will discuss in the next section.

The isomorph theory has been shown to hold for the crystalline phase too [54]. The same treatment presented here for the freezing line can therefore be repeated for the melting line. We choose to build the melting isomorph from a state point at the same temperature as the one chosen for the freezing isomorph. The state point used is $(\rho, T) = (1.132, 2.0)$ and the values of R and γ at this state point are:

$$R_M = 0.9985 \quad , \quad \gamma_M = 4.8877 \quad . \tag{3.3}$$

The melting temperature as function of density is obtained using Eq. 2.39:

$$T_M(\rho) = A_M \rho^4 - B_M \rho^2 \tag{3.4}$$

ρ_M	T_M	$T_{pinning}$	$\Delta T/T_M$
0.973	0.800	0.921	-0.132
0.989	0.900	1.006	-0.106
1.005	1.000	1.095	-0.086
1.034	1.200	1.270	-0.055
1.061	1.400	1.453	-0.036
1.087	1.600	1.636	-0.022
1.109	1.800	1.812	-0.007
1.132	2.000	2.000	$+0.000$
1.153	2.200	2.191	$+0.004$
1.172	2.400	2.371	$+0.012$
1.191	2.600	2.561	$+0.015$
3.509	258.44	275.81	$+0.067$

Table 3.1: Comparison between the melting temperature predicted using Eq. (3.4) at a given density ρ and the melting temperature calculated for the same density using the interface pinning method [94]. The freezing and melting densities at $T = 275.81$ have been calculated in Ref. [83] by the author while the other data are from Pedersen [68]. The parameters in Eq. 3.4 were calculated at the reference state point $(\rho, T) = (1.132, 2.0)$

where $A_M = 1.76$ and $B_M = 0.69$. The functional form of Eqs. 3.2 and 3.4 is exactly the same because isomorph shape depends on the chosen potential only and not on the system phase. The comparison between the temperatures estimated through Eq. 3.4 and the computed ones is shown in Table 3.1 (from Ref. [83]).

3.1.2 Invariances along the freezing and melting lines and phase transition criteria

The existence of isomorphs in the phase diagram of a Roskilde system has an important consequence in the description of phase transitions. In the region of the phase diagram where strong correlations are present, it is sufficient to know any isomorph invariant quantity on a single line, which is not an isomorph, to be able to predict the behavior of these quantities in the whole region. This is possible because from any point along the chosen line, which could be for example an isochore or an isotherm, it is possible to build an isomorph and thereafter to estimate the value of the chosen quantity along the isomorph using its invariance in reduced units. It is therefore correct to state that the phase diagram of any R system is approximately 1-dimensional when referring to isomorph invariant quantities. In this view any isomorphic invariant quantity will have a given value, in reduced units, at the phase transition and so the phase transition can be identified by a specific value of the isomorphic invariant quantity.
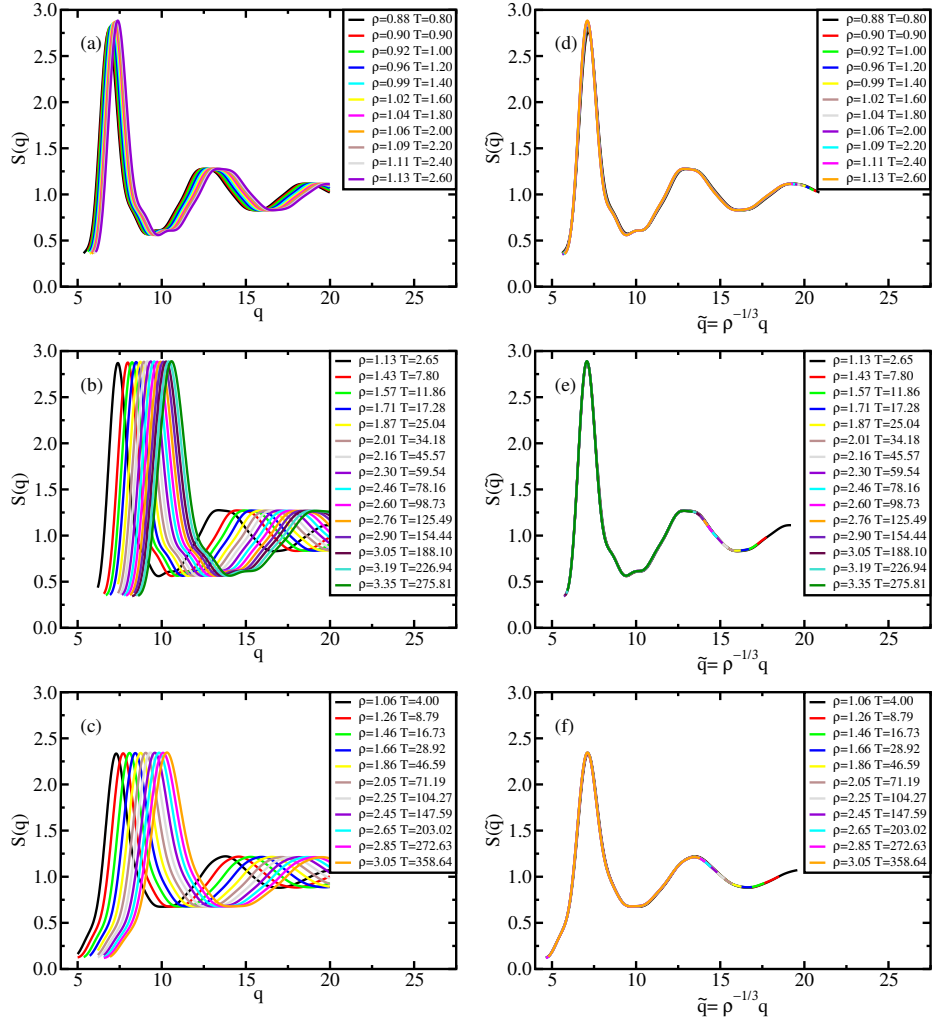
Figure 3.2: Liquid results. Structure factor $S(q)$ along the Pedersen freezing line (a,d) [68], along the freezing isomorph from Eq. 3.2 (b,e), and along an isomorph well within the liquid phase (c,f); in (a), (b) and (c), $S(q)$ is plotted as a function of wave vector q in Lennard-Jones units, in (d), (e) and (f), $S(q)$ is plotted as a function of reduced wave vector $\tilde{q} = \rho^{-1/3}q$. It is worth noting that while in (a) and (d) the density change is about 25 percent, in the other figures density is changed about a factor 3.

If for example the maximum value of the structure factor $S(q)$ at a given freezing point is $S(\tilde{q}_{max})$, where the q vector is expressed in reduced units, the maximum value at any other given freezing point will be the same due to isomorph invariance of structure, since the freezing line is approximately an isomorph. This peculiar invariance is known as Hansen-Verlet freezing criterion [100, 101] and was originally explained by reference to the HS system.

	A	B	T	ρ	γ	R
liquid isomorph	4.32	1.34	4.0	1.0635	4.7589	0.9966
freezing isomorph	2.27	0.80	2.0	1.0635	4.9079	0.9955
melting isomorph	1.76	0.69	2.0	1.132	4.8877	0.9985
crystal isomorph	0.91	0.39	1.0	1.132	4.9979	0.9986

Table 3.2: This table gives the coefficients A and B of the four isomorphs studied in this work (Eq. 3.2 and Eq. 3.4 and similar for the two other isomorphs). The first two columns contain the coefficients A and B and the latter four columns contain temperature T, density ρ, density scaling coefficient γ and correlation coefficient R of the state points the isomorphs studied in this work start from. A pure $n = 12$ IPL pair potential leads to $\gamma = 4$ as discussed in Chap. 2.

According to the same reasoning, if we consider a crystal at a state point on the melting line and study the vibrations of elements of the lattice, i.e. its dynamics, it is possible to associate with the melting of the crystal a specific value of the plateau of the reduced mean-squared-displacement (MSD) $< u^2 >_m /\rho_m^{2/3}$ [102, 103]. Due to the invariance of dynamics along an isomorph, the melting isomorph in Eq. 3.4 in this case, this MSD is approximately invariant along the melting line and this invariance is well known as the Lindemann melting criterion [104].

In order to show that these criteria are not features of the freezing or melting process *per se*, in Figs. 3.2 and 3.3 the invariance of $S(q)$ along the freezing isomorph and along another isomorph in the liquid phase and the invariance of MSD along the melting isomorph and along another isomorph in the crystal phase are shown. The details on the starting state points for the freezing isomorph, the melting isomorph and for the other two isomorphs considered are given in Table 3.2.

The behavior of $S(q)$ (MSD) along the liquid (solid) isomorph and along the freezing (melting) line is the same and therefore freezing (melting) invariances are consequence of the more general invariance [9, 43], due to the existence of isomorphs. This point is of great interest because it means that any theory of liquid or solid state should take into account the fundamental importance of isomorphs in the phase diagram of an R simple system.
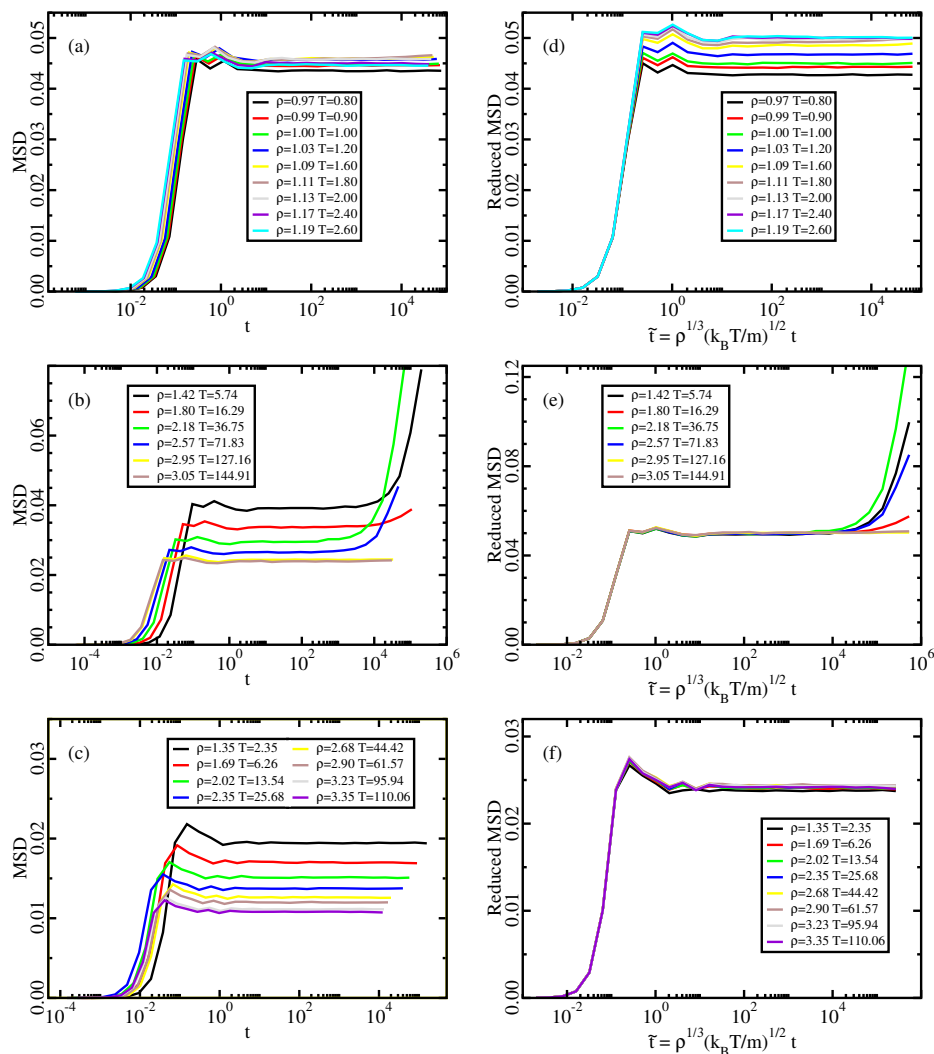
Figure 3.3: Crystal results. Mean-squared displacement (MSD) along the Pedersen melting line (a,d) [68], along the melting isomorph from Eq. 3.4 (b,e), and along an isomorph well within the crystal phase (c, f); in (a), (b) and (c), the MSDs are plotted as a function of time t in LJ units, in (d), (e) and (f), the reduced MSDs are plotted as a function of reduced time $\tilde{t}$. The invariance of the plateau of MSD along the melting line implies the Lindemann melting criterion for R liquids because the invariance of the reduced-unit vibrational mean-square displacement is equivalent to the invariance of Lindemann constant [102, 103]. Along the melting isomorph defect diffusion is observed. Defect formation is a stochastic phenomenon, as shown by the non-monotonicity of its appearance with respect to T or ρ. In order to study the isomorphic invariance of defect formation, an averaging over many simulations at every state point is necessary which could be object of future studies. The diffusion of defects, in LJ crystals, when properly averaged, has been shown to be isomorphic invariant by Albrechtsen *et al* [54].

3.1.3 Invariance of reduced viscosity and the Andrade equation for freezing viscosity

A consequence of the invariance of dynamics along an isomorph is that the reduced (bulk) viscosity

$$\tilde{\eta} = \eta \rho^{-2/3}(m k_B T)^{-1/2}, \tag{3.5}$$

as well as all the other reduced transport coefficients, is invariant. When this invariance is taken into account, together with the fact that the freezing line is an approximate isomorph, an equation for viscosity along the freezing line can be obtained:

$$\eta_F = \tilde{\eta}_0 \rho^{2/3}(m k_B T_F(\rho))^{1/2} \tag{3.6}$$

where the subscript F stands for freezing, $T_F(\rho)$ is the freezing temperature at density ρ and $\tilde{\eta}_0 = 5.2$ is the reduced value of η at the reference state point $(\rho_0, T_0) = (1.0635, 2.0)$. Using Eq. 3.2 it is possible, for the LJ system, to rewrite Eq. 3.6 as function of ρ (or alternatively T) only:

$$\eta_F(\rho_F) = \tilde{\eta}_0 \cdot \rho_F^{2/3} \sqrt{m k_B \left(A_F \rho_F^4 - B_F \rho_F^2 \right)} \tag{3.7}$$

$$\eta(T_F) = \tilde{\eta}_0 \sqrt{m k_B T_F} \left(\frac{B_F + \sqrt{B_F^2 + 4 A_F \cdot T_F}}{2 A_F} \right)^{1/3} \tag{3.8}$$

in which $A_F = 2.27$ and $B_F = 0.80$ are the freezing isomorph coefficients as in Eq. 3.2. In Fig. 3.4, viscosities estimated with Eqs. 3.7 and Eq. 3.8 are compared with the corresponding values for the LJ system, calculated using the SLLOD algorithm [105–107]. The green line in Fig. 3.4 is obtained assuming $\tilde{\eta}_0 = 5.2$ to be constant as predicted from from isomorph theory. This dependence of viscosity on freezing density and temperature as in Eq. 3.6 is known as the Andrade equation for freezing viscosity [108–110]:

$$\eta(\rho_F, T_F) = \beta \cdot \rho_F^{2/3} \sqrt{T_F}. \tag{3.9}$$

Eq. 3.9 was proposed in 1931 to describe the viscosity of liquid alkali metals along their freezing line. The coefficient β depends on the chosen material and, analogously, the reduced viscosity at freezing $\tilde{\eta}_F$ depends on the potential. Even though alkali metals can be considered much more complex than the Lennard-Jones system, the isomorph theory can be used to describe them both. It was in fact shown by Hummel $et\ al$ [111] that most metals exhibit strong correlations between virial and potential energy and therefore are Roskilde simple. The existence of strong correlations and isomorphs is the reason why Andrade equation for freezing viscosity [108–110] holds.
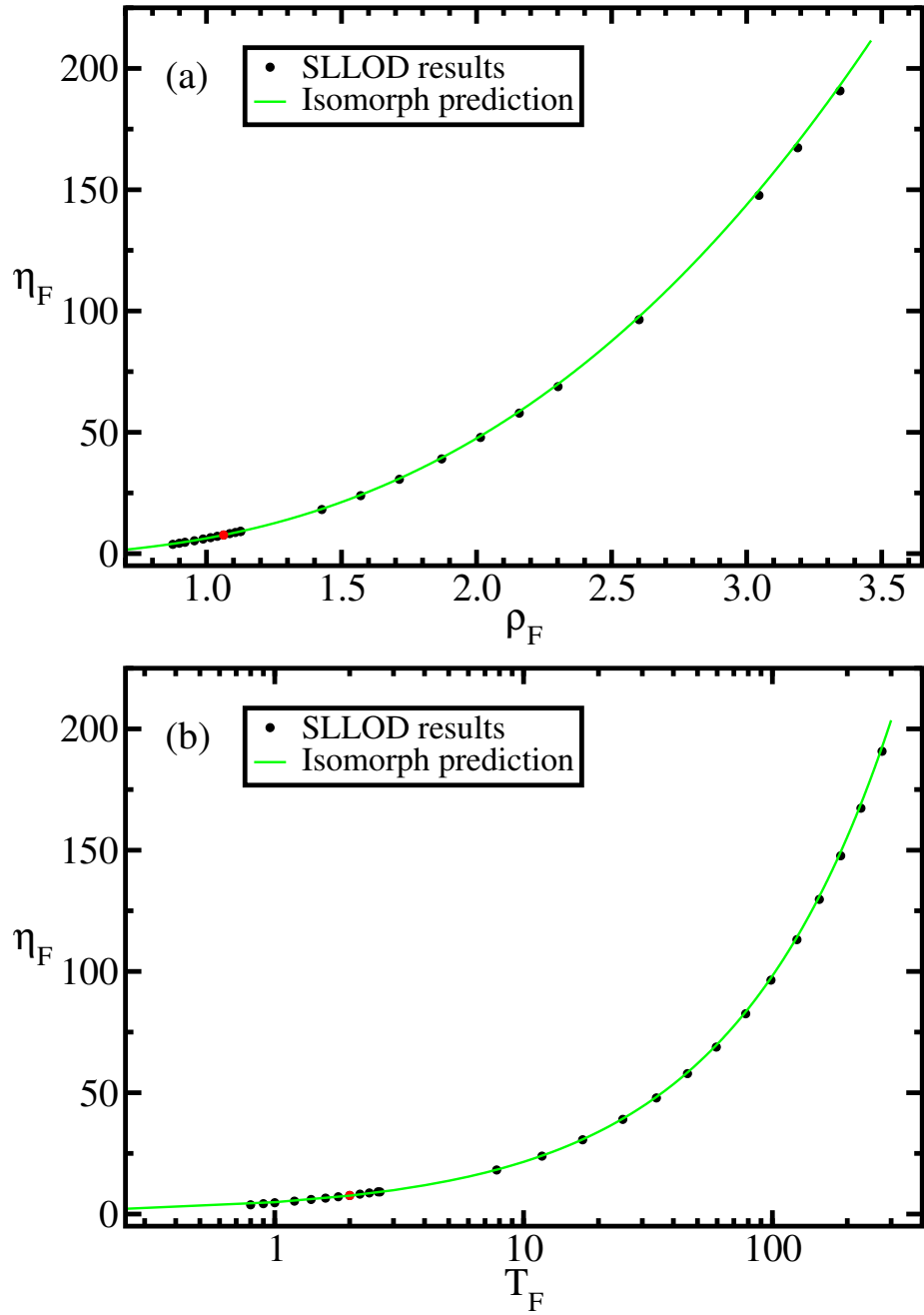
Figure 3.4: Viscosity along the freezing line and along the freezing isomorph, Eq. 3.2, as a function of density (a) and of temperature (b). The black dots represent results for the viscosity obtained from our SLLOD simulations [105–107]. The green line is the predicted viscosity assuming the invariance of reduced viscosity along an isomorph (Eqs. 3.7 and 3.8). The red dot is the viscosity of the state point from which the freezing isomorph is built and from which the constant $\tilde{\eta}_0$ in Eq. 3.6 is determined, $(\rho, T) = (1.0635, 2.0)$. The reduced viscosity at this state point is $\tilde{\eta}_0 = 5.2$.

3.2 Thermodynamics of freezing and melting at low densities

In the previous section we showed that the freezing and melting isomorphs provide good approximations of the freezing and melting line for the LJ system. It can be seen that this approximation works best when the density ρ is larger than 1.0. Looking at Fig. 3.2 (a) and (b), it could be noted that the peak height of the structure factor $S(q)$ is slightly increasing with increasing density in (a) while it is quite constant in (b), even though the range of densities in (b) is much larger. A similar small difference between isomorph predictions and results from simulations can be seen in Fig. 3.3, where the plateau value of the MSD is slightly increasing for increasing density (or increasing pressure). This density dependence of the Lindemann constant was pointed out also in Ref. [112].

In this section we study the behavior of freezing and melting lines near the triple point, showing that it is possible to correct the predictions of the last section in order to get an even better description of the freezing and melting lines and of the dynamics. In the following we will reproduce some of the results from Ref. [84].

The author's main contribution to this work was the study of viscosity presented in Fig. 3.6. The data for viscosity in this section have been obtained using the SLLOD algorithm [105–107], as those of the last section, but the cutoff radius of the potential (and consequently the system size) has been changed. In this case in fact the LJ potential is studied with a cutoff of 6σ in order to reduce the effect of using a truncated potential instead of the full one. The effect of potential truncation on the melting line of the LJ system near the triple point is studied in Ref. [68] where data for truncation at 2.5σ and 6σ are compared. More information on the simulations can be found in appendix C.

We will start by focusing on the description of melting in the pressure-temperature (p, T) phase diagram, in which there is no difference between freezing and melting line, and then in the density-temperature (ρ, T) phase diagram. In the following, starting from the knowledge of equilibrium properties at a given coexistence state point for the LJ system, $(p_0, T_0, \rho_{0l}, \rho_{0s}) = (20.857, 2.0, 1.0635, 1.132)$ from [68], the coexistence line is predicted and the prediction compared with the simulation data.

3.2.1 The melting pressure

The coexistence line between the liquid and the solid is where the two phases have the same pressure, temperature and Gibbs free energy per particle [89]. Consider now two state points at the same temperature $T \neq T_0$, the first one (p_m, T) along the melting line and the second one (p^I, T) along the isomorph starting from (p_0, T_0). These two state points have a slightly
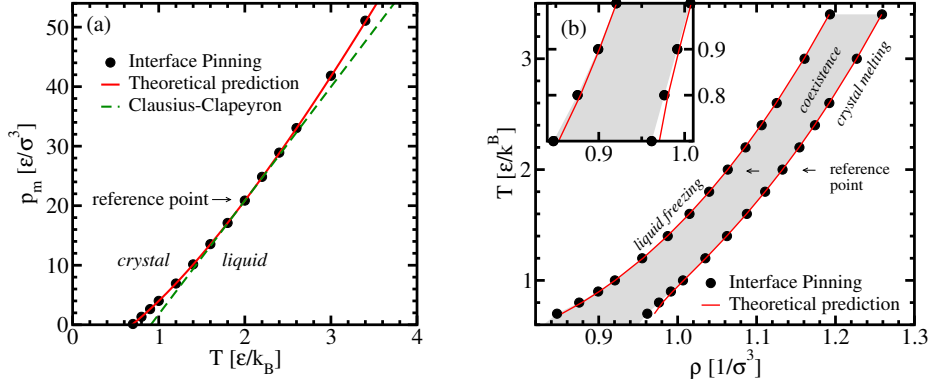
Figure 3.5: Phase boundaries. (a) melting line of the LJ system in the (p, T) phase diagram. The simulation data obtained with interface pinning method [68, 94] (black dots) are compared with the prediction of the melting line from Eq. 3.12 and from the extrapolation of the Clausius-Clapeyron equation [89] assuming constant ΔV, i.e. constant difference between the volume of the solid and of the liquid at the melting pressure, and constant excess entropy difference ΔS_{ex} between the two phases. The reference point has been indicated with an arrow. (b) freezing and melting lines of the LJ system in the (ρ, T) phase diagram. The simulation data obtained with interface pinning method [68, 94] (black dots) are compared with the prediction obtained in Sec. 3.2.2. The reference points (one on the freezing line and one on the melting line) have been indicated with arrows. Figures taken from Ref. [84].

different pressure $\left| p_m - p^I \right| < 1$ if they are not far from the reference point (p_0, T_0). The Gibbs free energy $G(T, p_m(T))$ at the melting state point (p_m, T) can be therefore obtained as a function of the Gibbs free energy along the reference isomorph using a first order Taylor expansion:

$$
\begin{aligned}
G_l(T, p_m(T)) &\cong G_l^I(T) + V_l^I(T)(p_m(T) - p_l^I(T)) \\
&= F_l^I(T) + V_l^I(T)p_m(T)
\end{aligned}
$$

$$
\begin{aligned}
G_s(T, p_m(T)) &\cong G_s^I(T) + V_s^I(T)(p_m(T) - p_s^I(T)) \\
&= F_s^I(T) + V_s^I(T)p_m(T)
\end{aligned}
$$

where $V = \left. \frac{\partial G}{\partial p} \right|_T$ has been used and l and s indicate the liquid or solid phase while I is used to label quantities along an isomorph built from the starting state point. In the last equality, the relation $G(T, p) - V(T)p(T) = F(V, T)$ connecting Gibbs free energy and Helmholtz free energy $F(V, T)$ has been used. The coexistence state point at the new temperature, can be found using the equality $G_l(T, p_m(T)) = G_s(T, p_m(T))$ which implies

$$
p_m(T)(V_l^I - V_s^I) = F_s^I(T) - F_l^I(T). \tag{3.10}
$$

When the difference in Helmholtz free energy between the two phases can be evaluated, it is possible to find the coexistence pressure $p_m(T)$ at the new

temperature. The definition of Helmholtz free energy is:

$$F_{l/s}^I(T) = U_{l/s}^I(T) - T S_{\mathrm{ex},l/s} + F_{id}(T, \rho_{l/s}^I(T)) \qquad (3.11)$$

where F_{id} is the ideal gas contribution. The ideal term is known at any state point. The difference in excess entropy S_{ex} between the liquid and solid phase, necessary for the calculation of $p_m(T)$ from Eq. 3.10, can be obtained using the condition $G_l(T_0, p_0) = G_s(T_0, p_0)$ at the starting state point. Since the excess entropy S_{ex} along an isomorph is constant, the excess entropy difference between two isomorphs is constantly equal to the difference at the starting state points [84]. The equation for the melting pressure p_m at temperature T, for an R simple system, is therefore:

$$
\begin{aligned}
p_m(V_l^I - V_s^I) &= \left(U_s^I - \frac{T}{T_0} U_{s,0} \right) - \left(U_l^I - \frac{T}{T_0} U_{l,0} \right) \\
&+ \frac{T}{T_0}(W_{l,0} - W_{s,0}) + N k_B T \ln \left(\frac{\rho_s^I}{\rho_{0s}^I} \frac{\rho_{0l}^I}{\rho_l^I} \right) \qquad (3.12)
\end{aligned}
$$

where $W_{l/s}$ is the virial at the starting state point. In the case of the LJ system, the virial $W_{l,s}^I$ and potential energy $U_{l,s}^I$ along an isomorph can be calculated analytically [53, 84] from knowing only the physical quantities at the starting state point. The predicted melting pressure from Eq. 3.12 for the LJ system is compared with the melting line evaluated by Pedersen [68] using the interface pinning method [94] in Fig. 3.5 (a). The last term in Eq. 3.12 is responsible for corrections to the isomorph theory prediction of the last section. This correction is less and less relevant as temperature increases because the ratio between the liquid and solid density at a given temperature becomes constant.

3.2.2 The freezing and melting densities

In order to bring these results on the melting line from the (p, T) phase diagram to the (ρ, T) one, it is necessary to know the densities of the liquid and solid at the coexistence pressure given by Eq. 3.12. In the case of the LJ system this can be done because, along an isomorph, the dependence of the virial on density is known [53, 84]. From the coexistence pressure $p_m(T)$ the virial is obtained as function of density and temperature:

$$\frac{W_{l/s,m}(T)}{N} = \frac{p_m(T)}{\rho_{l/s,m}(T)} - k_B T \qquad (3.13)$$

At the same time, the virial at (p_m, T) can be obtained from a first order Taylor expansion with respect to the reference isomorph:

$$W_m(T) = W^I(T) + \left. \frac{\partial W(T)}{\partial \ln(\rho/\rho_0)} \right|_T^I \ln \left(\rho_m/\rho^I \right) \qquad (3.14)$$
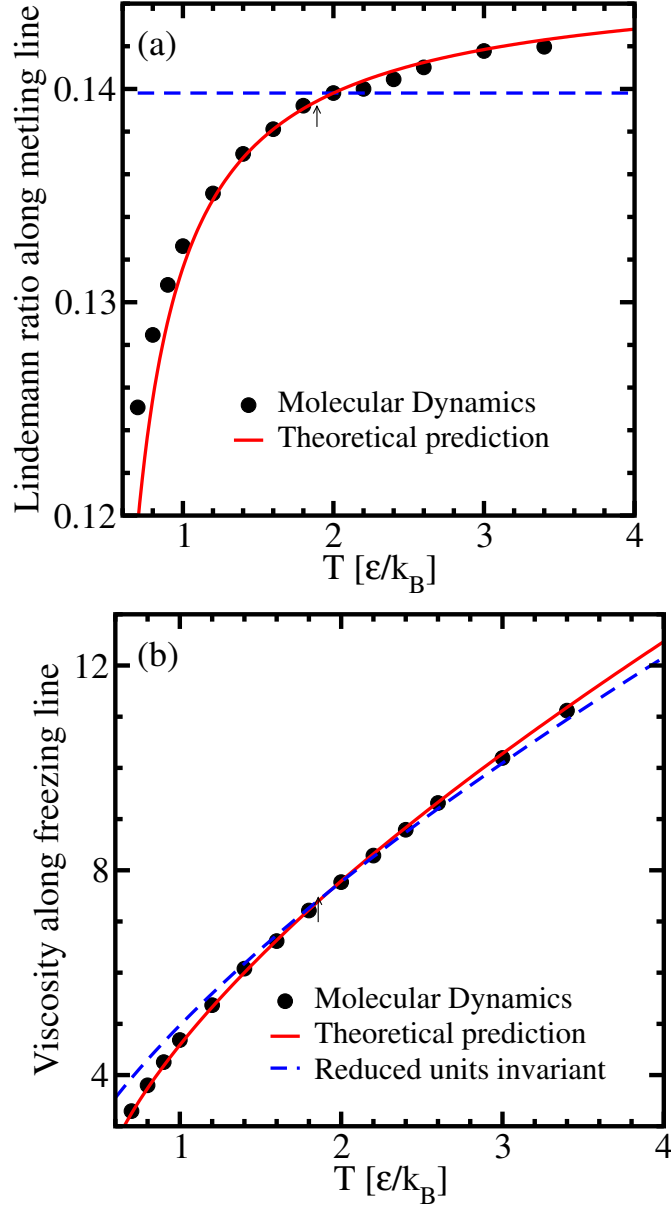
Figure 3.6: Dynamics along the melting and freezing line in the (ρ, T) phase diagram. (a) Lindemann ratio as a function of temperature T along the melting line. The black dots represent the Lindemann constant obtained from the plateau of the MSD of the crystal, the blue dashed line the prediction from last section, i.e. constant Lindemann ratio, and the red curve the prediction from Eq. 3.16. (b) freezing viscosity as a function of temperature T along the freezing line. Data from SLLOD simulations (black dots) are compared with the prediction assuming constant reduced viscosity, Eq. 3.6, and with the prediction from Eq. 3.16. The correction is fairly small when compared to the case of the Lindemann ratio, but it's still appreciable. For the difference between these SLLOD simulations and those of Sec. 3.1.3, we refer to appendix C. Figures taken from Ref. [84].

where the subscript s/l have been removed for clarity. This equation holds both for the liquid and the solid case. Eqs. 3.13 and 3.14 are a set of two equations in $W_m(T)$ and ρ_m and can be solved numerically at any T.

The freezing and melting densities predicted from Eqs. 3.13 and 3.14 are shown in Fig. 3.5 (b) and compared with the values for the freezing and melting line computed by Pedersen [68].

3.2.3 Corrections for isomorph invariant quantities along the freezing and melting lines

In the start of this section it was pointed out that some isomorph invariances do not hold perfectly along the LJ freezing and melting lines in the neighborhood of the triple point. The cause of this discrepancy resides in the assumption that in this region of the phase diagram, the freezing and melting lines are isomorphs. Even though approximating the phase boundaries with the freezing and melting isomorphs allows one to explain why freezing and melting invariances exist [83], it is possible to give a better description of the dynamical quantities in analogy with what is done for the freezing and melting lines themselves. A generic isomorphic invariant quantity in reduced units is a function of excess entropy S_{ex} only (along an isomorph):

$$\tilde{X} = \phi(S_{\text{ex}}). \tag{3.15}$$

The value of the quantity X along the freezing or melting line will be slightly different from the one along the freezing or melting isomorph. We can always find the value of the quantity X at a state point close to the reference isomorph using a first order Taylor expansion:

$$\tilde{X} = \tilde{X}_0 + \phi^{'}(S_{\text{ex}})\Delta S_{\text{ex}} \cong \tilde{X}_0 + \phi^{'}(S_{\text{ex}}) \left. \frac{\partial S_{\text{ex}}}{\partial \rho} \right|_T^I (\rho_m - \rho^I) \tag{3.16}$$

where the quantity $\phi^{'}(S_{\text{ex}})$ can be calculated at the starting state point of the isomorph [84]. Using Eq. 3.16 it is possible, for example, to calculate the value of X along the freezing line starting from the value of X along the freezing isomorph. This approach allows one to take into account the density dependence of the Lindemann ratio, shown in Fig. 3.3 (d), and of reduced viscosity, shown in Fig. 2.3 (b), for densities close to the triple point. In Fig. 3.6, the predictions of isomorph theory from the last section, i.e. constant Lindemann ratio and reduced viscosity (blue lines), and the predictions from Eq. 3.16 are compared. At low densities Eq. 3.16 provides a notable improvement, while at higher densities the results of the two approaches are comparable.
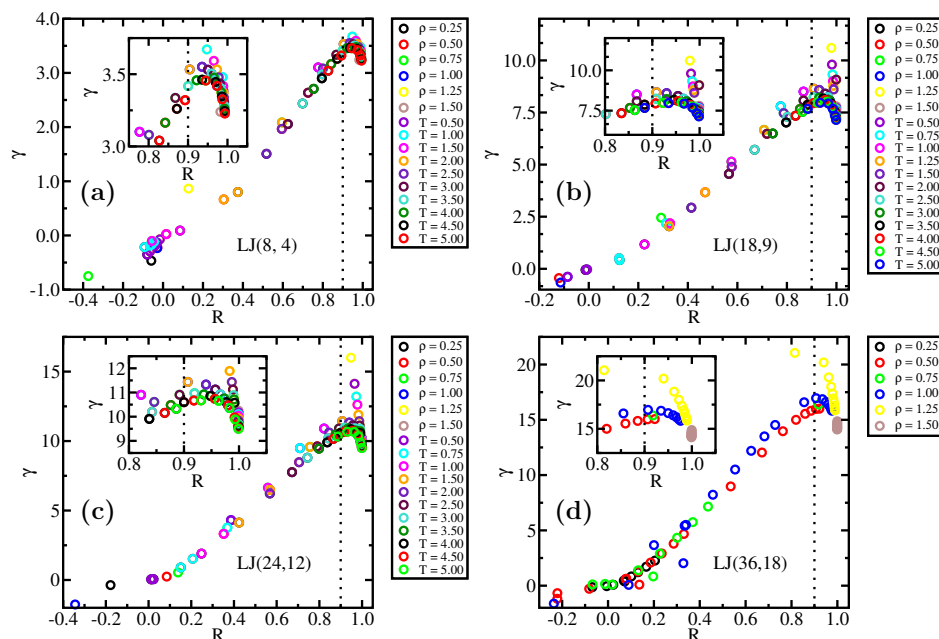
Figure 3.7: Scaling exponent γ as a function of correlation coefficient R for different generalized LJ potentials. The inset in each figure shows the crossover region and the vertical dotted black line delimits the Roskilde simple region, i.e. where $R > 0.9$. (a) LJ$(8,4)$ (b) LJ$(18,9)$ (c) LJ$(24,12)$ (d) LJ$(36,18)$.

For each system six isochores are considered $\rho = [0.25, 0.5, 0.75, 1.0, 1.25, 1.5]$. Along each isochore the temperature is changed in the range $[0.25, 5.00]$; temperatures are indicated in the legend. Along each isotherm the densities considered are $\rho = [0.25, 0.5, 0.75, 1.0, 1.25, 1.5]$.

In figure (b),(c) and (d) it is possible to distinguish between two different behaviors of the dependence of γ from R which are related to the liquid and the crystal phase, the latter being the steepest. In figure (d) all the simulations at density $\rho = 1.5$ and all the simulations at $\rho = 1.25$ except for the one at lowest temperature were in the crystal phase. State points with negative correlation coefficient R, and close to zero, are in the gas-liquid coexistence region.

3.3 Relation between the correlation coefficient R and the scaling exponent γ (Part 1)

In the last section of this chapter a study of the generalized LJ is presented. Data in this chapter have been obtained together with Ida Marie Friisberg during her master thesis at Roskilde University. The simulations on LJ$(8,4)$, LJ$(18,9)$ and LJ$(24,12)$ have been carried out by Ida Marie Friisberg, while the simulations on the LJ$(36,18)$ and the analyses presented in this section are original work of the author.

The generalized LJ potential is defined as:

$$v_{m,n}^{LJ}(r) = \frac{\epsilon}{m-n}\left[n\left(\frac{\sigma}{r}\right)^m - m\left(\frac{\sigma}{r}\right)^n\right] \tag{3.17}$$

with m and n being positive integers. The potentials studied in this section are a particular case of Eq. 3.17, i.e. when $m = 2n$:

$$v_{2n,n}^{LJ}(r) = \epsilon \left[\left(\frac{\sigma}{r} \right)^{2n} - 2 \left(\frac{\sigma}{r} \right)^{n} \right] \tag{3.18}$$

The phase diagram of the LJ$(2n, n)$ system is very sensitive to the choice of the exponent n as can be understood from the dependence of the critical point upon n, studied in Ref. [113, 114], and from the dependence of the isomorph shape function $h(\rho, S_{\text{ex}})$, Eq. 2.39, when n is changed. The critical temperature for the LJ$(2n, n)$ decreases as n is increased while the critical density slightly increases. The isomorphs become steeper with increasing n:

$$h(\rho, S_{\text{ex}}) = A(S_{\text{ex}}) \left(\frac{\rho}{\rho_0} \right)^{2n/3} - B(S_{\text{ex}}) \left(\frac{\rho}{\rho_0} \right)^{n/3} \tag{3.19}$$

and, recalling the results of the last sections, as a consequence of Eq. 3.19 the freezing and melting lines of the LJ$(2n, n)$ system get steeper with increasing n. In this scenario it is interesting to study how the correlation coefficient R, defined in Eq. 2.1, and the scaling exponent γ, defined in Eq. 2.18, change throughout the whole phase diagram.

A limitation on the region of applicability of the isomorph theory can be derived from Eq. 3.19: two competing terms are present in Eq. 3.19, a positive one ($\rho^{2n/3}$) and a negative one ($\rho^{n/3}$); while at high densities the first term is always dominant, at low densities this is not the case. The function $h(\rho, S_{\text{ex}})$ can in fact become zero and even negative upon decreasing density ρ and this will produce unphysical results when remembering that the function $h(\rho, S_{\text{ex}})$ is a ratio between two temperatures, from Chap. 2, and it must therefore be positive. The condition $h(\rho, S_{\text{ex}}) = 0$ is accomplished for $\rho = \bar{\rho}$ where:

$$\bar{\rho} = \left(\frac{B(S_{\text{ex}})}{A(S_{\text{ex}})} \right)^{3/n} \rho_0 \tag{3.20}$$

In the case of the LJ$(2n, n)$, the two coefficients A and B can be obtained from the value of $\gamma(\rho_0, T_0) = \gamma_0$ at the state point (ρ_0, T_0) the isomorph is built from:

$$A = \frac{3}{n} \gamma_0 - 1 \tag{3.21}$$

$$B = \frac{3}{n} \gamma_0 - 2 \tag{3.22}$$

Since both A and B are positive, from Eqs. 3.21 and 3.22 it follows that $A > B$. The density $\bar{\rho}$ for which $h(\bar{\rho}, S_{\text{ex}}) = 0$ is therefore lower than the starting density ρ_0. This means that when moving along an isomorph toward lower densities there should always be a density $\rho > \bar{\rho}$ at which the R simple condition, $R > 0.9$, breaks down in order to avoid unphysical

predictions from the theory. This is well known to happen for the Lennard-Jones potential ($n = 6$, LJ(12, 6)) [69] because the correlation coefficient R decreases with decreasing density and with decreasing temperature [48] and it becomes lower than the threshold value 0.9 well before approaching $\bar{\rho}$.

It would be nice if the end of the region in which strong correlations exist could be associated with a change of some observable physical quantity (or alternatively with a change of behavior of some quantity) which can be measured in experiments. With this goal in mind we studied the relation between the correlation coefficient R and the scaling exponent γ for four different values of the exponent n: $n = 4$, $n = 9$, $n = 12$, $n = 18$. The scaling exponent γ is the logarithmic derivative of the function $h(\rho, S_{\text{ex}})$ with respect to density ρ along an isomorph (Eq. 2.24). As a consequence of this, at the density $\bar{\rho}$ the scaling exponent γ is diverging. The parameter γ can be an interesting quantity to consider because it is possible to measure it in experiments [13–16, 61] and the theory has an unphysical prediction for its value at $\rho = \bar{\rho}$.

In Fig. 3.7 the scaling exponent γ is shown as a function of the correlation coefficient R along several isochores and isotherms for the four different generalized LJ potentials studied. Approximately when the correlation coefficient R crosses the threshold value 0.9, the scaling exponent γ changes behavior and it starts to decrease. While the fact that the scaling exponent γ should decrease toward zero when R approaches zero, it is not obvious that the change of behavior in γ corresponds to the system no longer being R simple. This change in the behavior of γ could, in theory, be measured in experiments, even though it will require really high accuracy due to the slow variation in γ with density and temperature [13–16, 61]. More plots as the ones in Fig. 3.7 will be shown in Chap. 5 where the LJ(12, 6) system is studied in a number of spatial dimensions different from 3 and a similar behavior is found.

Chapter 4

Viscosity of the LJ system in the supercritical region

An extensive study of viscosity of the Lennard-Jones (LJ) model system [41] in the supercritical region is presented in this chapter. A new empirical formula for viscosity based on the isomorph theory makes it possible to describe viscosity in the whole region. The behavior of viscosity is also studied in connection with the 2-body excess entropy, the specific heat and the diffusivity of the system. Results in this chapter have not been published elsewhere. Details on the simulations can be found in appendix C.

The transport coefficients for the LJ system have been broadly investigated by different authors. Particular focus has often been given to the behavior of viscosity in the liquid region next to the freezing line and at temperatures usually not too high compared to the critical temperature [115–117]. In this chapter the study of viscosity is extended to a wider range of densities and temperatures, along five different isochores starting from the freezing temperature and increasing temperature up to $200T_F$ for the lowest density. An equation for describing the viscosity data in the full range of densities and temperatures is also presented. In the derivation of this equation, previous works in the same context [65, 78, 98, 108–110, 118–120] have been used as starting points together with results from isomorph theory of Chap. 3.

The first section deals with the prediction from the isomorph theory about the density dependence of isomorphic invariant quantities and in the following sections the data are presented and analyzed.
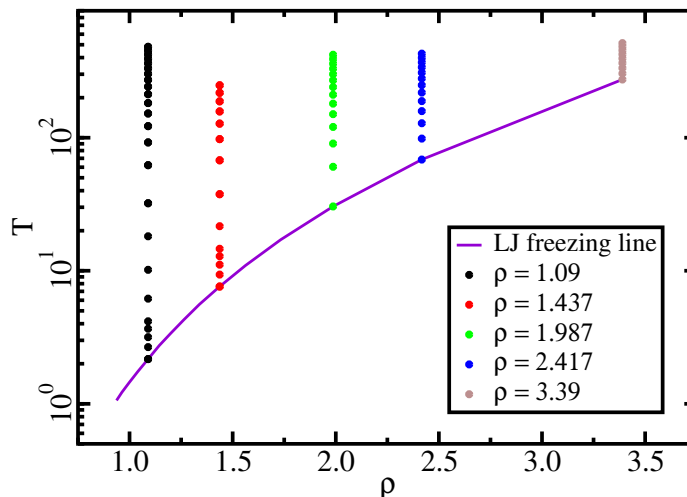
Figure 4.1: Freezing line of the LJ system from Ref. [79] and state points studied in this chapter. The densities of the five different isochores that have been studied are indicated in legend. The lowest temperature studied for each isochore is the freezing temperature, from Ref. [79].

4.1 Isomorph theory constraint on isochoric dependences

We discussed in Chap. 2 the existence of invariance curves for the Roskilde (R) systems. Along these curves structure and dynamics are invariant and it is therefore sufficient to know the dynamical properties at a single state point to predict the behavior along the entire isomorph. The isomorph theory allows one to know even more about the system, in particular it is possible to obtain a constraint on the isochoric dependence of a given isomorphic invariant quantity.

All state points in the (ρ, T) phase diagram belonging to the same isomorph satisfy the relation:

$$T(\rho) = T_0 \cdot h(\rho, \rho_0) \tag{4.1}$$

in which (ρ_0, T_0) are the density and temperature of the state point the isomorph starts from. In Eq. 4.1 the dependence of $h(\rho, \rho_0)$ on S_{ex}, from Eq. 2.39, is neglected. The choice of the state point is not relevant as long as the correlation coefficient R, defined in Eq. 2.1, is larger than 0.9. The functional form of $h(\rho)$ depends on the model system but at this stage we do not choose any specific model system because the following argument holds for any R liquid. In the case of two isomorphs starting from different state

points along the same isochore, Eq. 4.1 becomes:

$$T_{iso1}(\rho) = T_{0,1} \cdot h(\rho, \rho_0) \tag{4.2}$$

$$T_{iso2}(\rho) = T_{0,2} \cdot h(\rho, \rho_0) \tag{4.3}$$

where the subscripts $1, 2$ identify the isomorph starting at temperatures T_1 and T_2 respectively. These equations imply that:

$$\frac{T_{iso1}(\rho)}{T_{0,1}} = \frac{T_{iso2}(\rho)}{T_{0,2}} = h(\rho, \rho_0) \tag{4.4}$$

$$\frac{T_{iso1}(\rho)}{T_{iso2}(\rho)} = \frac{T_{0,1}}{T_{0,2}} \tag{4.5}$$

and therefore the ratio between temperatures of two isomorphs is the same at any density. Eq. 4.5 constrains any given isomorphic invariant quantity along an isochore to depend on the ratio between the state point temperature and a reference temperature in order to be consistent with isomorph theory. If we chose as reference temperature the freezing temperature T_F, Eq. 4.5 implies that along any isomorph the temperature of the isomorph is proportional to that of the freezing isomorph at the same density. A generic isomorph invariant quantity $\tilde{X}(S_{\text{ex}})$ is therefore a function of the ratio T/T_F along any given isochore:

$$\tilde{X}(\rho, T) = f\left(\frac{T}{T_F(\rho)}\right) \tag{4.6}$$

where the tilde indicates that reduced units are used, as usual. The function $\tilde{X}(\rho, T)$ depends on density ρ only through the freezing temperature $T(\rho)$. This result in the context of isomorph theory, as well as the following one, has been obtained by the author.

4.1.1 Prediction for stationary points along isochores

Given a generic isomorph invariant quantity X and the corresponding reduced units quantity $\tilde{X} = X\rho^{-\alpha}T^{-\beta}$, it is also possible to predict that the state points (ρ, T) at which the quantity X exhibits a stationary point define an isomorph. In particular, this holds for maximum or minimum values of X along an isochore, if there is any. As before, the proof does not require the choice of a specific model liquid.

$$X = \tilde{X}\rho^\alpha T^\beta \tag{4.7}$$

$$\left.\frac{\partial X}{\partial T}\right|_\rho = \rho^\alpha \left[\beta T^{\beta-1} f\left(\frac{T}{T_F}\right) + \frac{T^\beta}{T_F} f'\left(\frac{T}{T_F}\right)\right] \tag{4.8}$$

$$= \rho^\alpha T^\beta \left[\beta T^{-1} f\left(\frac{T}{T_F}\right) + \frac{1}{T_F} f'\left(\frac{T}{T_F}\right)\right] \tag{4.9}$$
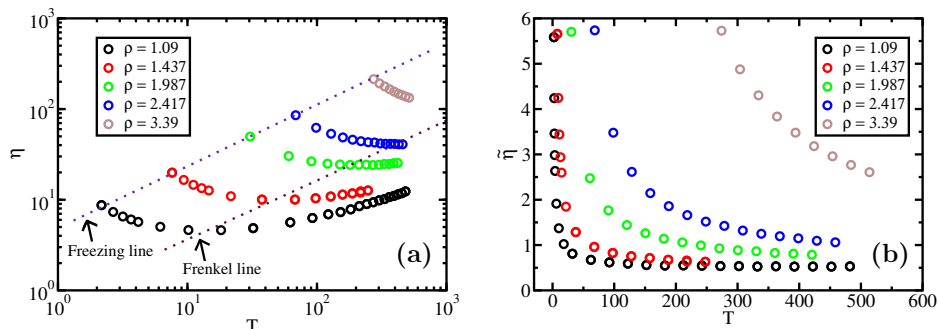
Figure 4.2: Viscosity data (a) for the LJ system obtained from SLLOD simulations [105–107] are showed for five different isochores whose density are indicated in the legend.The same data are shown in reduced units in (b). The starting temperature along each isochore is the freezing temperature reported in Ref. [79]. For the isochores with low density it is possible to clearly see how viscosity exhibits a minimum after which it increases with increasing temperature. This fact is well known in the literature, see Ref. [3] and its references. As temperature increases, reduced viscosity becomes less and less dependent on temperature reaching a plateau value for isochores $\rho = 1.09, 1.437$. The existence of this plateau is consistent with kinetic theory [121]. A consistency check on the high temperature data can be found in the appendix C.

where Eq. 4.6 has been used. This implies that, if $X(\rho, T)$ has a stationary point along an isochore, the temperature $\bar{T}$ at which it occurs must satisfy

$$f'\left(\frac{\bar{T}}{T_F(\rho)}\right) = -\beta \frac{T_F(\rho)}{\bar{T}} f\left(\frac{\bar{T}}{T_F(\rho)}\right). \qquad (4.10)$$

In both sides of Eq. 4.10 only functions of $\bar{T}/T_F$ appear and therefore the set of points defined by Eq. 4.10 is an isomorph identified by a certain value of the ratio $\bar{T}/T_F$. One of the implications of Eq. 4.10 is that the Frenkel line [3] (when defined as the line of viscosity minima along an isochore) is an isomorph in the region of the phase diagram where the system is R simple.

4.2 Viscosity data for the LJ system

In Fig. 4.2, data for the viscosity of LJ system along five different isochores are shown. It is interesting to note that while the viscosity η exhibits a minimum along isochores [3], Fig. 4.2 (a), reduced viscosity $\tilde{\eta}$ does not, Fig. 4.2 (b), and it shows a clear plateau (at least for the isochore at the lowest density). It is not needed to show the presence of a plateau at any other density than the lowest one because, due to isomorph invariance of reduced viscosity along isomorphs (Chap. 3), the presence of a plateau for a reduced quantity along an isochore implies that there will be a plateau on every other isochore in the R simple region of the phase diagram.

The existence of this plateau can be understood from kinetic theory [121]. The viscosity of a dilute gas of HS is:

$$\eta_0 = \frac{2(mk_BT)^{1/2}}{3\pi^{3/2}\sigma^2} \tag{4.11}$$

where σ is the diameter of the HS. The reduced viscosity will therefore be:

$$\tilde{\eta}_0 = \frac{\eta_0}{\rho^{2/3}(mk_BT)^{1/2}} = \frac{2}{3\pi^{3/2}}\frac{1}{\rho^{2/3}\sigma^2} \tag{4.12}$$

This implies that at any given density ρ a high temperature plateau value should exists. Hildebrand [122] noted in 1976 that Eq. 4.11 can be used to describe the viscosity of a wide class of fluids when the value of σ is determined by the density, i.e., $\sigma \propto \rho^{-1/3}$. When this assumption is done, Eq. 4.12 becomes independent of density ρ and consistent with isomorph invariance.

4.2.1 Isochoric dependence of viscosity

With the goal in mind of describing viscosity of the LJ system in the supercritical region, we now focus on the behavior of reduced viscosity along a single isochore. The isomorph theory will then allow us to extend the result to any other isochore using isomorph invariance of reduced viscosity. The starting point is the Andrade equation for freezing viscosity, Eq. 3.9, already examined in Chapter 3. This equation has been suggested by Andrade himself first [108–110] and by Kaptay [118] more recently in order to predict the behavior along an isochore. The monotonic decrease of viscosity for temperatures close to the freezing one, which can be seen in Fig. 4.2, can be described as an Arrhenius decrease:

$$\eta(\rho, T) = A \ (mk_BT)^{1/2}\rho^{2/3}\exp\left(B\frac{T_F(\rho)}{T}\right) \tag{4.13}$$

which in reduced units becomes:

$$\tilde{\eta}(\rho, T) = A\exp\left(B\frac{T_F(\rho)}{T}\right) \tag{4.14}$$

where the coefficient A can be identified as the value of the reduced viscosity at freezing $\tilde{\eta}_F$. This equation is consistent with the constraint of Sec. 4.1 but, even though it succeeds in describing the viscosity of many metals, it is not able to describe the data in Fig. 4.2 with A and B independent of density.

We found that the data in Fig. 4.2 can be instead described introducing a non-Arrhenius dependence of viscosity, which is also consistent with the constraint in Sec. 4.1. The equation we propose is:

$$\tilde{\eta}(\rho, T) = A\exp\left[B\left(\frac{T_F(\rho)}{T}\right)^{\beta}\right] \tag{4.15}$$
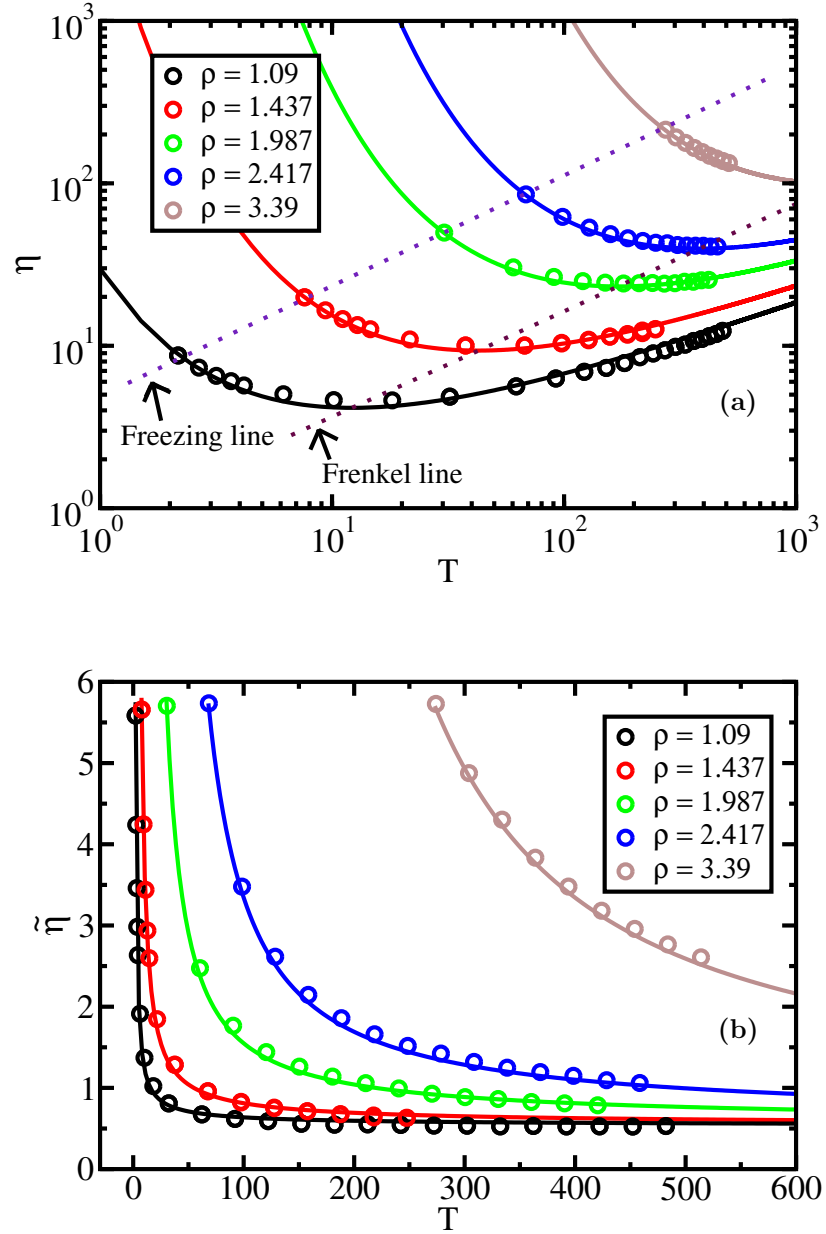
Figure 4.3: (a) Viscosity η of the LJ system along five isochores as in 4.2. The full line indicates the viscosity η estimated using Eq. 4.19. The dotted lines are the freezing line and the Frenkel line [3], here defined as the line of viscosity minima along an isochore, and predicted using Eq. 4.20. (b) Reduced viscosity $\tilde{\eta}$ of the LJ system along five isochores as in 4.2. The full line indicates the reduced viscosity $\tilde{\eta}$ estimated using Eq. 4.18.

This equation has a single free parameter, β, because A and B can be calculated from the high temperature plateau value of reduced viscosity $\tilde{\eta}_0$ and the reduced freezing viscosity $\tilde{\eta}_F$:

$$\begin{cases} \tilde{\eta}(\rho, T_F) = A \exp(B) = \tilde{\eta}_F \\ \tilde{\eta}(\rho, T \to \infty) = A \end{cases} \tag{4.16}$$

The values for A and B so obtained are $A = \tilde{\eta}_0 = 0.53$ and $B = 2.37$. Eq. 4.16 can be rewritten as:

$$\begin{cases} A = \tilde{\eta}_0 \\ B = \ln\left(\tilde{\eta}_F / \tilde{\eta}_0\right). \end{cases} \tag{4.17}$$

The β coefficient in Eq. 4.15 is found by fitting the data for viscosity along the isochore $\rho = 1.09$ and it is found that $\beta \approx 2/3$. No theoretical argument to justify this value of the coefficient β has been found.
The final equation is:

$$\tilde{\eta}(\rho, T) = \tilde{\eta}_0 \exp\left[B\left(\frac{T_F(\rho)}{T}\right)^{2/3}\right] \tag{4.18}$$

and correspondingly for full viscosity we have:

$$\eta(\rho, T) = \rho^{2/3}(m k_B T)^{1/2} \tilde{\eta}_0 \exp\left[B\left(\frac{T_F(\rho)}{T}\right)^{2/3}.\right] \tag{4.19}$$

In Fig. 4.3 the values obtained using this equation are compared with the data from SLLOD simulations already shown in Fig. 4.2. It is worth noting that the values used here for the reduced viscosity at freezing are slightly different from the one of Chap. 3. This difference is due to the fact that here we used data for the freezing line from Ref. [79] which includes the broadest studied density range nowadays available in the literature.

Eq. 4.18 allows also one to find an equation for the minima of viscosity along isochores using Eq. 4.10:

$$T_{min}(\rho) = \left(\frac{4B}{3}\right)^{3/2} T_F(\rho) \tag{4.20}$$

The freezing temperature $T_F(\rho)$ can be estimated using Eq. 3.2 and therefore Eq. 4.20 is an analytical equation for the Frenkel line [3], when defined as isochoric minima of viscosity. The prediction of viscosity minima from Eq. 4.20 is tested in Fig 4.3 where the full set of viscosity data is also shown.
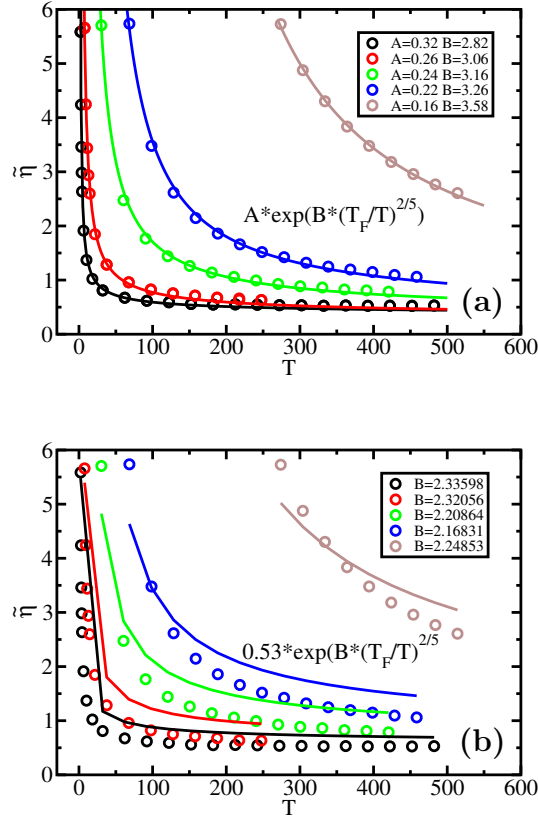
Figure 4.4: (a) Rosenfeld-Tarazona expression for reduced viscosity $\tilde{\eta}$ obtained combining Eq. 4.21 and Eq. 4.24. The coefficients A and B are calculated fitting the viscosity data for the LJ system separately for each isochore (same data as Fig. 4.2). The coefficients A and B so obtained are functions of density ρ and therefore do not provide an universal description of viscosity. (b) Rosenfeld-Tarazona expression for reduced viscosity $\tilde{\eta}$ obtained combining Eq. 4.21 and Eq. 4.24. In this case the coefficient A is fixed to the value obtained from the reduced viscosity plateau but the fit of the SLLOD data is poor.

4.2.2 Rosenfeld excess entropy scaling

Different studies have been carried out in the past to describe the behavior of transport coefficients for simple liquids. Two remarkable examples are the works of Rosenfeld [65] and Dzugutov [78]. In these two works, transport coefficients, expressed in reduced units, are shown to depend only on the excess entropy S_{ex}. The dependence of the transport coefficients on S_{ex} is exponential [65, 78]:

$$\ln \tilde{\eta} \quad \propto \quad -B_{\tilde{\eta}} S_{\text{ex}} \tag{4.21}$$

$$\ln \tilde{D} \quad \propto \quad B_{\tilde{D}} S_{\text{ex}} \tag{4.22}$$
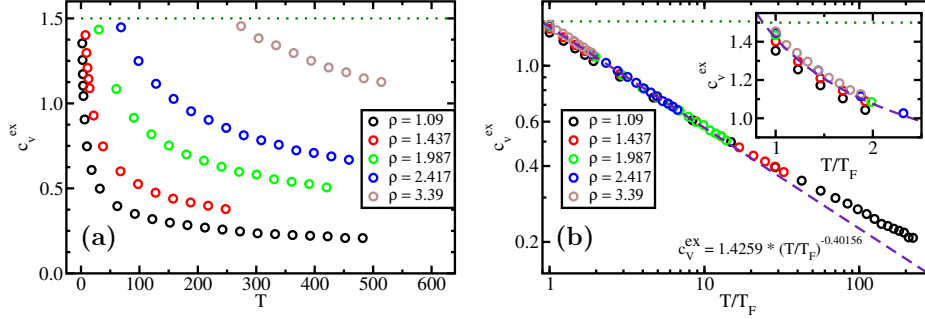
Figure 4.5: Excess specific heat at constant volume per particle c_V^{ex} for the LJ system along five isochores whose densities are indicated in legend. (a) c_V^{ex} as a function of temperature T (b) c_V^{ex} as a function of $T/T_F(\rho)$, i.e the temperature is measure as a multiple of the freezing temperature at any chosen density.

Both these works rely on the analogy between a simple liquid and the HS paradigm; Dzugutov's derivation of Eq. 4.22 uses the Chapman–Enskog theory [123]. The same conclusion can be derived from the isomorph theory, in fact both the excess entropy and the reduced transport coefficients are invariant along an isomorph. As a consequence it is possible to express one as function of the other, both excess entropy and reduced transport coefficients being monotonic functions of temperature at constant density.

In 1998, Rosenfeld and Tarazona [124] proposed an equation for the excess specific heat at constant volume C_V of simple liquids.

$$C_{V,ex}(\rho, T) = \frac{3}{5}\alpha(\rho)T^{-2/5} \qquad (4.23)$$

which implies

$$S_{\text{ex}}(\rho, T) = -\frac{3}{2}\alpha(\rho)T^{-2/5} \qquad (4.24)$$

since $C_V = \frac{\partial S}{\partial \ln T}\big|_V$.

Eqs. 4.21 and 4.24 suggest that the exponent β in Eq.4.18 for reduced viscosity $\tilde{\eta}$ should be equal to 2/5. The choice of $\beta = 2/5$ is tested in Fig. 4.4 (a). The other two parameters A and B are fitted to the viscosity data. Using Rosenfeld-Tarazona approach it is possible to describe the data but the coefficients A and B depend on the specific isochore. In Fig. 4.4 (b) the parameter A is fixed to the high temperature limit of reduced viscosity, following the same scheme used for Eq. 4.18 while the coefficient B is fitted. The results are much worse than using Eq. 4.18. This discrepancy could be related to the non-correctness of Eq. 4.23 in the whole range studied here. As we discussed in Chap. 2, the excess specific heat $C_{V,ex}$ is not exactly invariant along an isomorph and therefore the function $\alpha(\rho)$ could be slightly dependent on T implying Eq. 4.24 to be incorrect. This conjecture is tested
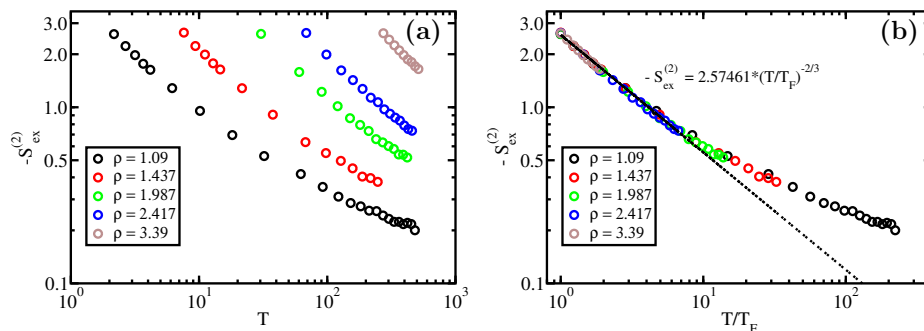
Figure 4.6: Data for 2-body excess entropy $S_{ex}^{(2)}$, obtained from Eq. 4.25, for the LJ system along five isochores whose densities are indicated in legend. (a) $S_{ex}^{(2)}$ as function of temperature T (b) $S_{ex}^{(2)}$ as a function of $T/T_F(\rho)$, i.e the temperature is measure as a multiple of the freezing temperature at any chosen density. The 2-body excess entropy data can be fitted by a power law in $T/T_F(\rho)$ for temperatures below 10 as Rosenfeld suggests, Eq. 4.24, but with the same exponent 2/3 as in Eq. 4.18 and not with the exponent 2/5 suggested by Rosenfeld.

in Fig. 4.5: for temperatures close to the freezing one the C_V data do not collapse perfectly. It is not completely surprising that Eq. 4.23 does not well describe the LJ system close to freezing because its derivation assumes that LJ particles can be modelled as HS, according to the HS paradigm discussed in Chap. 1.

In Fig. 4.6, 2-body excess entropy data are shown. The 2-body excess entropy $S_{ex}^{(2)}$ can be calculated from the radial distribution function (RDF) $g(r)$ using the following expression [125]:

$$S_{ex}^{(2)} = -\frac{1}{2}\rho \int \left[1 - g(r) + g(r)\ln\left(g(r)\right)\right] r^2 dr \qquad (4.25)$$

where the spherical symmetry of the RDF for fluids has been used. The behavior for temperatures below 10 T_F can be well described with the same functional form as Eq. 4.24 but using the exponent 2/3 as in Eq. 4.18. It should be noted that the high temperature estimates of $S_{ex}^{(2)}$ ($T > 100$) along the isochore $\rho = 1.09$ are noisy due to insufficient precision in the high temperature data for RDFs. Longer simulations would be required in that region. A justification for using the $S_{ex}^{(2)}$ instead of the full excess entropy S_{ex} can be found, for a R simple system, in the fact that this two quantities are both invariant along an isomorph, the first one because of the invariance of the RDF on isomorphs and the second one because of the isomorph definition. The practical reason is that calculating the $S_{ex}^{(2)}$ from Eq. 4.25 is straightforward, while the calculation of the full excess entropy requires a different treatment.
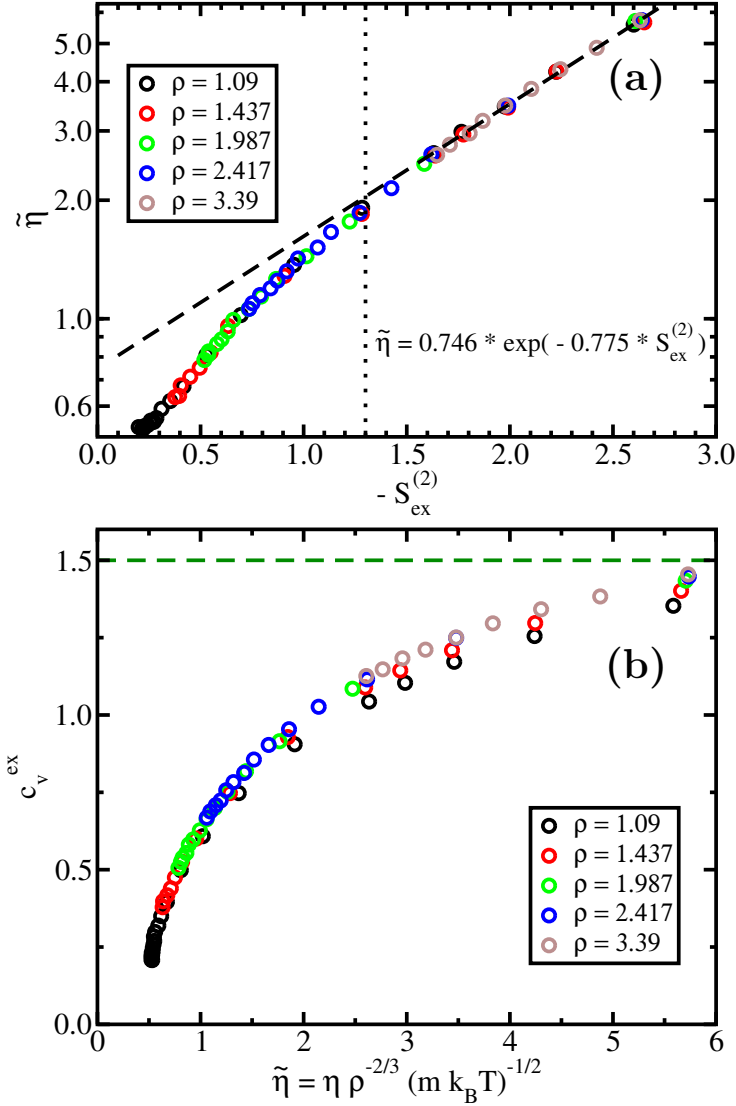
Figure 4.7: Relations between reduced viscosity $\tilde{\eta}$, 2-body excess entropy $S_{\mathrm{ex}}^{(2)}$ and specific heat at constant volume per particle c_V^{ex}. (a) Excess entropy scaling for viscosity as suggested by Eq. 4.21. The linear relation between $\ln(\tilde{\eta})$ and $S_{\mathrm{ex}}^{(2)}$ holds while reduced viscosity is above ≈ 2.0, i.e. for temperature below $2T_F$. (b) Specific heat at constant volume per particle c_V^{ex} as a function of reduce viscosity $\tilde{\eta}$. In Eq. 4.23 the quantity c_V^{ex} is supposed to obey the same scaling with temperature as excess entropy in Eq. 4.24. It makes therefore sense to investigate if c_V^{ex} is an universal function of $\tilde{\eta}$. From the data it follows that this is the case for high temperatures but not close to freezing. This is a consequence of the fact that while reduced viscosity $\tilde{\eta}$ is isomorph invariant, c_V^{ex} varies slightly on isomorphs, Chap. 2.

In Fig. 4.7 (a), Rosenfeld entropy scaling for reduced viscosity from Eq. 4.21 is compared with our viscosity data showing a rather good agreement at low temperatures (corresponding to high values of $-S_{\text{ex}}$) but a significant deviation at high temperatures. In a HS picture, which is the background for Rosenfeld entropy scaling, both the excess specific heat at constant volume C_V^{ex} and the reduced viscosity $\tilde{\eta}$ should be functions only of the excess entropy S_{ex}. Since they are both functions of the same quantity, they should also be an unique function of each other. In Fig. 4.7 (b), the excess specific heat at constant volume per particle c_V^{ex} is plotted as a function of the reduced viscosity $\tilde{\eta}$. At low temperatures, corresponding to high values of the reduced viscosity, c_V^{ex} is not a unique function of reduced viscosity $\tilde{\eta}$ showing, as already happened in the case of reduced excess pressure in Chap. 2, that the HS approach fails to describe the system in a satisfying way. As discussed in Chap. 2, the specific heat at constant volume C_V^{ex} is not exactly invariant along an isomorph, especially at low densities and temperatures, and so is not a function of the excess entropy only while the reduced viscosity is. Isomorph theory can be therefore used to justify the behavior of c_V^{ex} and $\tilde{\eta}$.

4.3   Diffusivity data for the LJ system

The isomorph theory can be used to predict both the viscosity η and the diffusion coefficient D of an R liquid. In this section we focus on comparing the results of the previous section on viscosity with the behavior of diffusivity along the same isochores. The diffusivity data shown in this section, as well as the data for C_V and S_{ex}, are obtained independently of the viscosity data: while for viscosity we used SLLOD simulations [105–107] for these other quantities NVT simulations are used. More details can be found in appendix C.

The predictions formulated in Sec. 4.1 are applicable to any isomorph invariant quantity and therefore hold for the diffusivity too. In Fig. 4.8 (a), the reduced diffusivity $\tilde{D}$ [52], calculated from the long time behavior of the mean squared displacement (MSD), is shown as function of the ratio T_F/T. The data for the five isochores perfectly collapse showing that a similar description to the one used for viscosity in Eq. 4.18 can be reproduced.

Nevertheless, there is an important difference between the high temperature behavior of diffusivity and viscosity. While the latter has been shown to have a high temperature plateau, Sec. 4.2, this is not the case for diffusivity.

For temperatures well above the freezing one, i.e. where the plateau of viscosity appears, it is reasonable to consider the LJ particles interacting through pure IPL12 potential:

$$v^{IPL12}(r) = 4\epsilon \left(\frac{\sigma}{r}\right)^{12}. \tag{4.26}$$

Support in this direction comes from the scaling exponent γ being close to 4 at high temperatures. For example, $\gamma = 4.20$ at $(\rho, T) = (1.09, 302.17)$. When the system is at equilibrium it is possible to define an effective radius of the IPL particle as:

$$v^{IPL12}(r = \sigma_{eff}) = k_B T. \tag{4.27}$$

The effective radius σ_{eff} is

$$\sigma_{eff} \propto (k_B T)^{-1/12}. \tag{4.28}$$

A consequence of Eq. 4.28 is that at high temperature particles have a small effective radius σ_{eff}. The mean free path l is defined as [121]

$$l \sigma_{eff}^2 \rho = 1 \tag{4.29}$$

and therefore, using Eqs. 4.28 and 4.29, the mean free path along an isochore, at high temperature, scales with T as:

$$l \propto (k_B T)^{1/6}. \tag{4.30}$$

The diffusion coefficient can be obtained as :

$$D = l \frac{v_{th}}{3} \tag{4.31}$$

with v_{th} the thermal velocity $v_{th} \propto (k_B T)^{1/2}$ [121]. The reduced diffusion coefficient, along an isochore, can be obtained using Eqs. 4.30 and 4.31

$$\tilde{D} \propto \frac{D}{(m k_B T)^{1/2}} \propto (k_B T)^{1/6}. \tag{4.32}$$

No plateau is therefore present for the reduced diffusivity $\tilde{D}$.

In Fig. 4.8 (b) data for reduced diffusivity $\tilde{D}$ and reduced viscosity $\tilde{\eta}$ of the LJ system along the isochore $\rho = 1.09$ are compared. We also show the product of the two quantities, which is constant under the hypothesis of a constant hydrodynamics radius for the particles. The constancy of the product of the two reduced transport coefficient is the well known Stokes-Einstein relation [126–128], as shown in the following.

$$\tilde{D}\tilde{\eta} = D \rho^{1/3} \left(\frac{m}{k_B T} \right)^{1/2} \frac{\eta}{\rho^{2/3}(m k_B T)^{1/2}} = \frac{D\eta}{\rho^{1/3}(k_B T)} \tag{4.33}$$

and so

$$D\eta = k_B T \rho^{1/3} \tilde{D}\tilde{\eta} \tag{4.34}$$

Eq. 4.34 reduces to Stokes-Einstein relation when $\tilde{D}\tilde{\eta}\rho^{1/3} = (6\pi \bar{r})^{-1}$ with $\bar{r}$ being the hydrodynamic radius of the particle. The invariance of $\tilde{D}$ and $\tilde{\eta}$ ensures the validity of Eq. 4.34 along an isomorph but its validity is not ensured
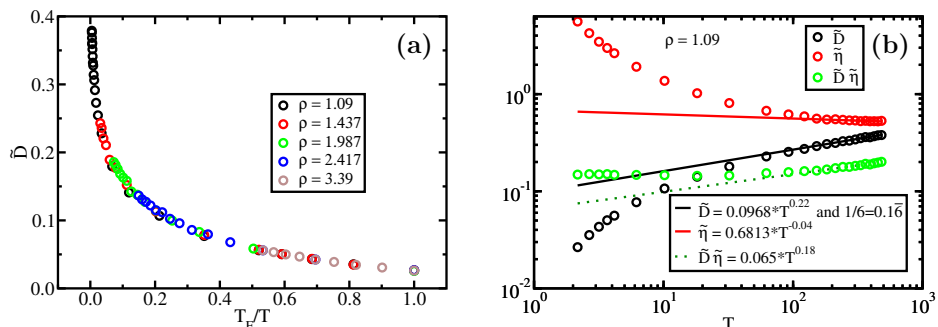
Figure 4.8: Results for diffusivity and comparison with viscosity results. (a) The reduced diffusivity is plotted as a function of $T_F(\rho)/T$. The data along the five isochores studied collapse onto a master curve in analogy with what happens in the case of reduced viscosity and as predicted by Eq. 4.6. (b) Data for reduced diffusivity (black dots), reduced viscosity (red dots) and their product $\tilde{D}\tilde{\eta}$ (green dots) along the isochore $\rho = 1.09$. The lines represent the result of a power law fitting of the data corresponding to temperatures above ≈ 100 in LJ units. While the reduced viscosity exhibits a plateau, the reduced diffusivity keep increasing with increasing temperature T with an exponent similar to the one predicted from Eq. 4.32. The discrepancy between the exponent from power law fitting and the one from Eq. 4.32 could be related to the approximation done in obtaining Eq. 4.32, i.e. assuming the LJ system being effectively an IPL12. The effect of these different behaviors is the violation of the invariance of $\tilde{D}\tilde{\eta}$ which is equivalent to the violation of Stokes-Einstein relation [126–128], see text.

along an isochore. In the high temperature limit, i.e. at temperatures of about ≈ 100 in LJ units, the assumption of a constant hydrodynamic radius break down as can be immediately understood from the different behavior of $\tilde{D}$ and $\tilde{\eta}$: the first quantity keeps decreasing on increasing temperature while the latter one tends to a constant value; their product therefore cannot be constant. In Fig. 4.8 (b) the high temperatures data for $\tilde{\eta}$, $\tilde{D}$ and $\tilde{D}\tilde{\eta}$ are fitted to power law functions of temperature. The power law exponent for $\tilde{D}$ is close to the $1/6$ predicted from Eq. 4.32, while the exponent for $\tilde{\eta}$ is about five times smaller. The result is a breakdown of Stokes-Einstein relation at high temperatures, represented in Fig. 4.8 by an increase of $\tilde{D}\tilde{\eta}$ with increasing temperature (green data).

Chapter 5

Isomorph theory in d dimensions

This chapter is dedicated to the study of the Lennard-Jones (LJ) model system [41] in 2d, 3d and 4d. The aim of this study was to investigate whether the correlation coefficient R increases when the dimensionality of the space increases and therefore to probe whether every system becomes strongly correlated in a part of its phase diagram when the dimensionality is increased. The results of this chapter, with exception of Sec. 5.3, have been published in Ref. [129]. Data presented in this chapter have been obtained by the author using the MD code described in the appendix A; details on the simulations can be found in appendix C.

An important, but often forgotten, ingredient in the modelling of physical properties of a specific system is the dimensions it lives in. Theories of critical phenomena [35] and mean field theories (as Ising model) have been shown to produce better description of systems in a number of dimensions greater than 3. Isomorph theory as recently been argued to be valid for every system, in a region of their phase diagram, in higher number of dimensions [130] due to the predominant role of the first coordination shell, i.e., the fact that a particle is mostly affected only by its closest neighbors. This conjecture was first formulated in [44] and it is tested against MD simulations in this chapter. Another way of expressing the same concept is that every system, in a region of their phase diagram, is an R liquid in high enough dimensions. In the following our focus will be on the Lennard-Jones (LJ) model system [41] for practical reasons.
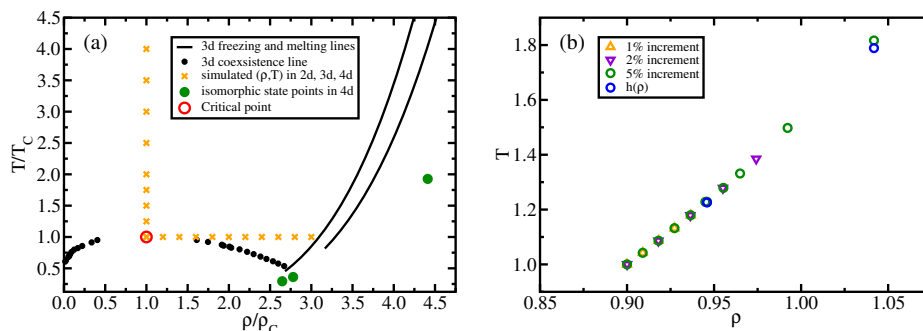
Figure 5.1: (a) Phase diagram of the LJ(12,6) system in 3d [83, 131]. Orange crosses represent the simulated state points along the critical isotherm and the critical isochore in 2d, 3d and 4d. Temperatures and densities are scaled respect to the critical ones, taken from Refs. [132–134] respectively for 2d, 3d and 4d. The green dots represent the isomorphic state points in 4d studied in the following. At these state points the LJ system in 4d is liquid (according to our simulations) giving insights on the difference between the phase diagram of the LJ system in 3d and 4d. (b) Consistency check between Eq. 5.5 and Eq. 2.24. The isomorph starting from the state point $(\rho, T) = (0.9, 1.0)$ in 4d is built incrementing density of 1, 2 and 5 per cent and finding the isomorph temperature through Eq. 2.24. This way of building an isomorph is computationally expensive because it requires many intermediate simulations but it can be used for any R system. The results are then compared with Eq. 5.5. The agreement is perfect as long as the increment in density is not too big, in fact an increment of 5 per cent in density is a rather big one. The use of Eq. 2.24 is not suggested when Eq. 5.5 can be used instead because the latter equation does not require any intermediate simulation.

5.1 Isomorphs in d dimensions for the generalized LJ system

As pointed out in Chap. 2, for the LJ system it is possible to find an analytical expression for isomorphs in 3d. This is true for any potential defined by the sum of 2 IPL potentials and therefore results in this section will be obtained for the generalized LJ(m, n) potential. The peculiarity of this family of systems that allows one to find an analytical expression for isomorphs is the way potential energy and virial scale with density [53]:

$$U(\hat{\rho}) = \hat{\rho}^{\frac{m}{3}} U_{m,0} + \hat{\rho}^{\frac{n}{3}} U_{n,0} \tag{5.1}$$

$$W(\hat{\rho}) = \frac{m}{3}\hat{\rho}^{\frac{m}{3}} W_{m,0} + \frac{n}{3}\hat{\rho}^{\frac{n}{3}} W_{n,0} \tag{5.2}$$

where $\hat{\rho} = \rho/\rho_0$, (ρ_0, T_0) is a reference state point, $U_{m,0}$ refers to the part of potential energy deriving from the IPL with exponent m evaluated at the reference state point and analogously for $U_{n,0}$ and for the virial $W_{m,0}$ and $W_{n,0}$. Eqs. 5.1 and 5.2 are obtained taking into account that the potential energy of the LJ(m, n) system is the sum of two terms, U_m and U_n. These

terms scale with density as $U_m(\rho) = (\rho/\rho_0)^{m/3} U_m(\rho_0)$ along an isomorph [53] due to the invariance of the radial distribution function (RDF) $g(r)$. In the case of d dimensions, Eqs. 5.1 and 5.2 can be written as:

$$U(\hat{\rho}) = \hat{\rho}^{\frac{m}{d}} U_{m,0} + \hat{\rho}^{\frac{n}{d}} U_{n,0} \tag{5.3}$$

$$W(\hat{\rho}) = \frac{m}{d}\hat{\rho}^{\frac{m}{d}} W_{m,0} + \frac{n}{d}\hat{\rho}^{\frac{n}{d}} W_{n,0} \tag{5.4}$$

Using the definition of temperature $T = \left.\frac{\partial U}{\partial S_{\text{ex}}}\right|_\rho$, Eqs. 5.3 and 5.4 and the equation for the scaling exponent γ along an isomorph, Eq. 2.24, it is possible to obtain that the isomorphs for a generalized LJ($m = 2n, n$) system in d dimensions are:

$$\frac{T(\rho)}{T_0} = \frac{h(\rho,\rho_0)}{h(\rho_0,\rho_0)} = \left(\frac{d}{n}\gamma_0 - 1\right)\left(\frac{\rho}{\rho_0}\right)^{2n/d} - \left(\frac{d}{n}\gamma_0 - 2\right)\left(\frac{\rho}{\rho_0}\right)^{n/d} \tag{5.5}$$

where the $h(\rho,\rho_0)$ function has been normalized to 1 at the reference point (ρ_0, T_0). This result is similar to the one of the $3d$ case, whose complete derivation can be found in the supplementary material of Ref. [84] reprinted in appendix D. The dependence of $h(\rho,\rho_0)$ on the excess entropy S_{ex}, see Eq. 2.37, has been omitted because it is irrelevant when studying a single isomorph. Eq. 5.5 is the analogue of Eq. 2.39 for a LJ($m = 2n, n$) potential in d dimensions. The scaling exponent $\gamma_0 = \gamma(\rho_0, T_0)$ in d dimensions is always defined by Eq. 2.18:

$$\gamma = \frac{\langle \Delta W \Delta U \rangle}{\langle (\Delta U)^2 \rangle} \tag{2.18}$$

but it should be noted that the definition of the virial in d dimensions is:

$$W = -\frac{1}{d}\sum_i \mathbf{r}_i \nabla_{\mathbf{r}_i} U_i. \tag{5.6}$$

Details on how to derive Eq. 2.18 can be found in the appendix of [84] for the 3d case and their generalization is straightforward, taking into account Eqs. 5.3 and 5.6. The second term in Eq. 5.5 will vanish in the limit of high densities when $\gamma = 2n/d$ and the conventional IPL scaling is recovered. Eq. 5.5 can be used to obtain the equation for the scaling exponent γ along an isomorph, using Eq. 2.24:

$$\gamma = \left.\frac{\partial \ln T}{\partial \ln \rho}\right|_{S_{\text{ex}}} \tag{2.24}$$

For a generalized LJ($m = 2n, n$) system, γ is a decreasing function of density. Therefore $\gamma > 2n/d$ for the LJ($m = 2n, n$) system in the region where the system is R simple. This can be understood from Eq. 5.5 when considering that the coefficient $\left(\frac{d}{n}\gamma_0 - 2\right)$ is defined to be positive; as consequence,
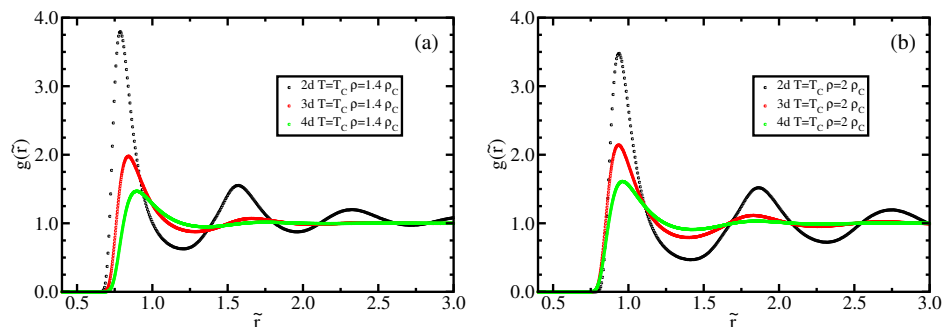
Figure 5.2: Reduced radial distribution function (RDF) $g(\tilde{r})$ for the LJ system along the critical isotherm $T = T_c$ in 2d, 3d and 4d. (a) RDFs at the state point with density $\rho = 1.4\rho_C$. (b) RDFs at the state point with density $\rho = 2.0\rho_C$. The effect of increasing the dimensionality of the space is a decrease in the peaks' height. The second peak of the RDFs in 3d and 4d is barely present, showing the increasing importance of the first coordination shell [2] with increasing dimensionality.

the freezing line, which can be approximated by an isomorph as shown in Chap. 3, is steeper and steeper when decreasing dimensions. The same effect is obtained if the number of dimensions is kept fixed and the exponent n increased because the relevant quantity is the ratio of n over d, as can be understood from Eq. 5.5. In other words, decreasing the number of dimensions has, on the freezing line of a LJ(2n, n) and on every isomorph, the same effect of increasing the exponent n keeping fixed the number of dimensions. In order to keep the same steepness of the freezing line, it is necessary to scale the exponent n with the number of dimensions d. In this view it can be understood why the HS system, i.e. the limit of a soft sphere potential for $n \to \infty$, provides a good approximation for R simple liquids. The mapping from a R system to HS system is a mapping from a given n to an infinite one and at the same time to infinite dimensions where every system is R simple (in the "hard" region of the phase diagram) as recently discussed in Ref. [130] and previously conjectured in Ref. [44].

Another interesting consequence can be derived from Eq. 5.5 which has been already pointed out in Chap. 3 for the 3d case: isomorphs described by Eq. 5.5 cannot exist at low densities because the isomorph temperatures corresponding to these densities will be negative. This is the reason why the correlation coefficient R must decrease as density is decreased, for the LJ(m,n).

In Fig 5.1 (b) an isomorph in 4d is shown. The consistency between Eq. 5.5 and the iterative construction of the isomorph through Eq. 2.24 is verified. Different density increments are used and the results are consistent with the prediction from Eq. 5.5, except in the case of the largest density change (5%). This is not surprising because the *step-by-step* construction
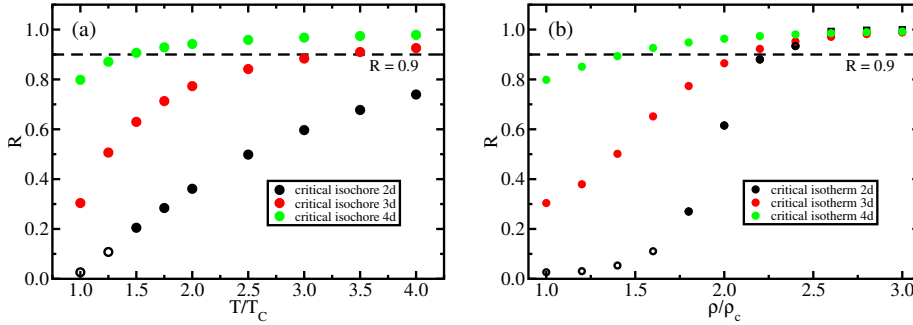
Figure 5.3: Correlation coefficient R, defined in Eq. 2.1, as a function of temperature T/T_c (density ρ/ρ_c) along the critical isochore (isotherm). (a) R monotonically increases both as a function of temperature along the critical isochore and with increasing dimension at a given ratio T/T_c. (b) As for the critical isochore, R monotonically increases as a function of density along the critical isotherm. R also increases with increasing number of dimensions as long as the same system phase is studied. For densities above $\rho = 2.5\rho_c$ the LJ in 2d crystallizes in a hexagonal close packing (HCP) lattice, for a system size of $N = 1225$ LJ particles, and the correlation coefficient R becomes approximately unity. These state points are marked with squares instead of circles.

For the 2d case some state points are marked with open circles. At these state points violent density fluctuations, resulting in strong non homogeneity ("holes"), have been observed.

relies on the discretization of Eq. 2.24 and it is expected to fail when the density increment is too large.

5.2 Correlation coefficient R of the LJ system in 2, 3 and 4 spatial dimensions

The first choice in studying the behavior of a system when changing the number of spatial dimensions is to identify reasonable state points to compare. The phase digram of the LJ system changes when studied in a different number of spatial dimensions. Our aim is to study the LJ system in 2d, 3d and 4d but, while the phase diagram of the LJ system is well known in 2d [132, 135, 136] and 3d [68, 83, 131, 133], not much information on the 4d phase diagram is available. Nevertheless, the position of the critical point is known in 2d, 3d and 4d [132–134]. The reason why the LJ system has not been studied in higher dimensions than 4 is related to the fact that in 5d the LJ system has no thermodynamic limit [134]. We start from studying the behavior of the LJ at the critical point (ρ_C, T_C) while changing the number of dimensions. In order to have a more general feeling on how the LJ system behaves in 4d, and 3d and 2d as well, simulations have been performed also along the critical isochore $\rho = \rho_C$ and the critical isotherm $T = T_C$. The choice we made for comparing the different dimensions is to
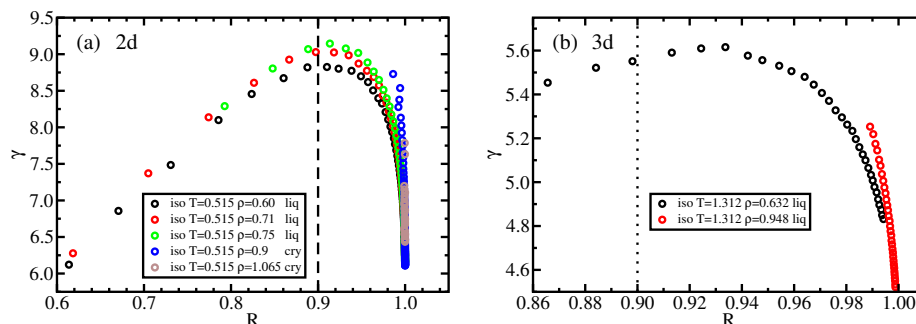
Figure 5.4: Scaling exponent γ, from Eq. 2.18, as a function of the correlation coefficient R, from Eq. 2.1, along several configurational adiabats in 2d and 3d. (a) Three curves in the liquid phase and two in the crystalline phase are generated using Eq. 2.24 for the 2d LJ system. The scaling exponent γ increases for values of R below the 0.9 threshold and then it starts to decrease. For the crystal phase the correlation coefficient R is always larger than 0.9 and γ is monotonically decreasing. (b) Two configurational adiabats for the liquid phase of the 3d LJ system in the liquid phase. The decrease in γ starts slightly after the 0.9 threshold for the black line.

scale temperatures and density by the critical values.

In Fig. 5.2 the RDFs at $\rho = 1.4\rho_C$ and $\rho = 2\rho_C$ are shown for the LJ system in 2d, 3d, 4d. In both cases the structure is less pronounced when the dimensionality is higher.

In Fig. 5.3 the correlations coefficient R, calculated using Eq. 2.1, is shown at different state points along the critical isochore and the critical isotherm. The LJ system at the critical point exhibits stronger correlations when the dimensionality d is increased. The data for state points along the critical isochore and the critical isotherm clearly confirm that increasing the dimensionality d produces better correlations between potential energy and virial.

5.3 Relation between the correlation coefficient R and the scaling exponent γ (Part 2)

In Chap. 3 the correspondence between the correlation coefficient R crossing the threshold of 0.9 and the start of the decreasing behaviour of the scaling exponent γ has been studied for the generalized LJ($m = 2n, n$) system. Here that study is extended, considering the LJ system, which corresponds to $n = 6$, in 2d and 3d. The study in 4d is less interesting due to the fact that the correlation coefficient is close to or above 0.9 in the whole region of the phase diagram studied, as shown in Fig 5.3, and the data are more computationally expensive to obtain. In Fig. 5.4, the scaling exponent γ is plotted as a function of the correlation coefficient R for three constant-S_{ex}
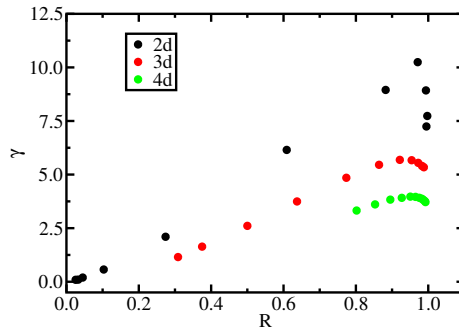
Figure 5.5: Scaling exponent γ, from Eq. 2.18, as a function of the correlation coefficient R, from Eq. 2.1, along configurational adiabats starting from the critical point of the LJ system in 2d, 3d and 4d. In all cases γ exhibits a maximum in the region where the correlation coefficient is crossing the value 0.9. The maximum value of γ is decreasing with increasing dimensions due to the *softening* of the potential discussed in Sec. 5.1.

curves (configurational adiabats) in the liquid phase and two in the crystal phase for the 2d LJ system (a), and along two curves in the liquid phase for the 3d LJ system (b). For all the considered isomorphs in the liquid phase, the correspondence between the correlation coefficient R crossing the threshold of 0.9 and the start of the decreasing behaviour of the scaling exponent γ is found, while for the crystal the correlation coefficient is always above 0.9. In Fig. 5.5 an isomorph starting from the critical point in 2d, 3d and 4d is studied and the same conclusion can be obtained. Even though the LJ system is not Roskilde simple at the critical point in any studied number of dimensions, Eq. 2.24 can still be used to generate constant S_{ex} curves, but the invariances predicted by isomorph theory will hold only when $R > 0.9$. It is important to underline the difference between an isomorph and a configurational adiabat: isomorphs are subset of configurational adiabats for which $R > 0.9$.

5.4 Invariance of structure and dynamics along an isomorph in 4d

In Sec. 5.2 we showed that the correlation coefficient R in 4d for densities higher than the critical one is above 0.9, see Fig. 5.3. This means that the invariance of structure and dynamics predicted by isomorph theory should hold in this region of the phase diagram. Eq. 5.5 can be used to generate an isomorph in 4d and, as known from the previous chapters, it is possible to choose density quite far from the reference one and still find the same structure and dynamics when the temperature is properly chosen. The starting point of the isomorph is $(\rho, T) = (0.9, 1.0)$. The state point at density
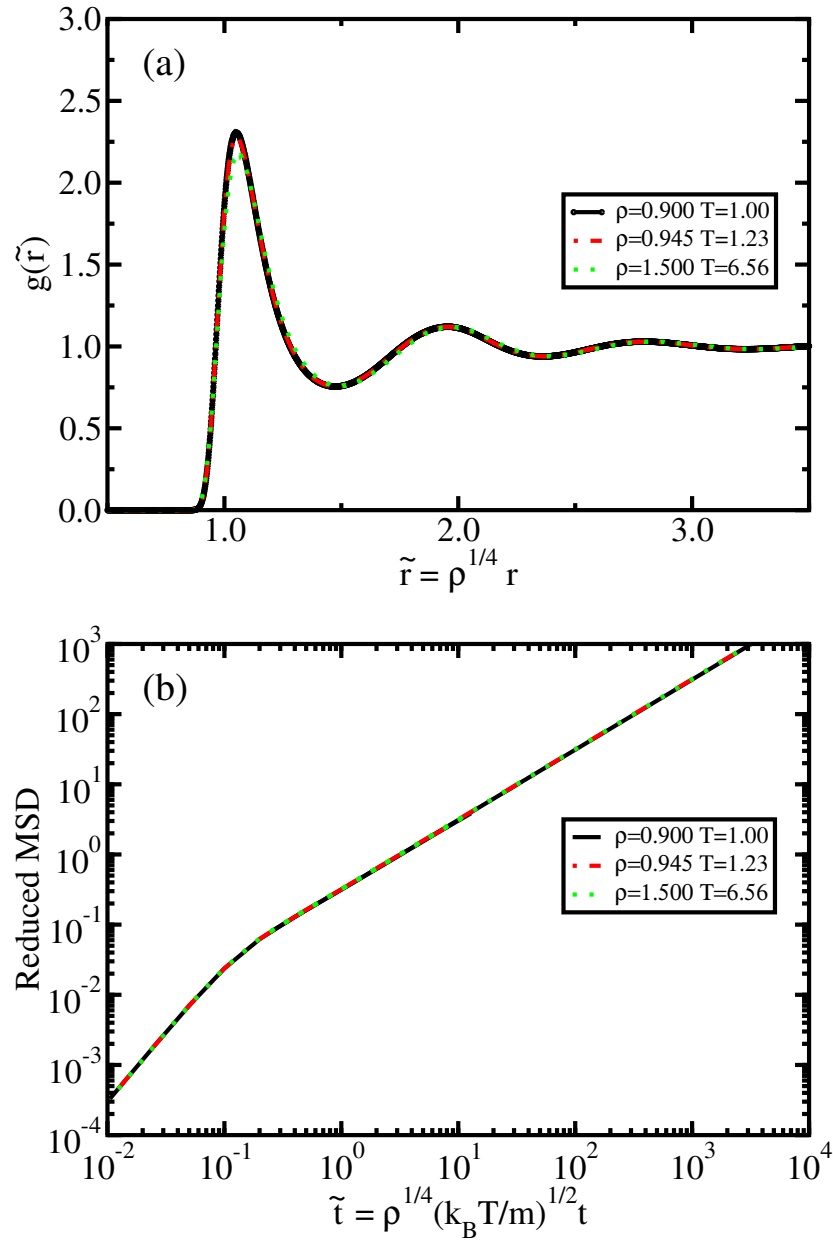
Figure 5.6: Structure and dynamics studied at three different state points along the same isomorph. The description of how these isomorphic state points are obtained is in the main text. (a) Reduced radial distribution function (RDF) $g(\tilde{r})$ at the three state points considered. (b) Reduced mean-squared displacement (MSD) at the three state points considered. The MSD is calculated using the standard tool from RUMD [38] and therefore only three components of the four-dimensional vector displacement are taken into account. Due to isotropy of the liquid phase it is correct to calculate the MSD using three components of the position vector only. Nonetheless we checked that all the possible choices of the three components out of four give the same results.

$\rho = 0.945$ is found using Eq. 2.24 recursively, i.e. with the *step-by-step* method, while the second state point, at density $\rho = 1.5$, is found using Eq. 5.5. The choice of using two different methods was made in order to further validate the result. The consistency between the two methods was verified in Fig. 5.1 (b).

In Fig. 5.6, the reduced RDF and the reduced MSD for a 4d LJ system are shown at three different state points along the same isomorph, starting from $(\rho, T) = (0.9, 1.0)$. The reduced-unit structure, probed by the RDF, and the reduced-unit dynamics, probed by the MSD, of the three isomorphic state points studied exhibit a perfect collapse clearly showing that isomorph invariances hold in 4d.

Chapter 6

Negative correlation coefficient and isomorphs: the Gaussian core model

As briefly discussed in Chap. 1, it is possible to describe the behavior of the Gaussian core (GC) [24] model liquid in the low density region using the HS paradigm. In this chapter we show that isomorph theory can be applied to the GC model liquid even in a part of the anomalous region, i.e. where the freezing line has a negative slope. Data presented in this chapter have been obtained by the author and they are part of an ongoing project that has not been published yet. Details on the simulations can be found in appendix C.

6.1 The phase diagram of the Gaussian core system

The Gaussian core (GC) [24] model system is the system of particles interacting via the pairwise potential:

$$v^{GC}(r) = \epsilon \; e^{-\frac{r^2}{\sigma^2}} \tag{1.3}$$

as already introduced in Chap. 1. In all our simulations the potential parameters (ϵ, σ) were set to unity. Many authors have focused on the features of this system due to its complex behavior [24, 25, 137–141]. The GC phase diagram has been studied in a wide range of densities [25–27, 142–144], highlighting the existence of a *well behaved* low density region and an *anomalous* region at high density. As predicted by Stillinger [24], the

GC has a low density-low temperature regime in which the fluid crystallizes when increasing density at constant temperature in a FCC crystal or in a BCC crystal, depending on the chosen isotherm. For high enough temperatures it is no longer possible to crystallize the fluid and only the fluid phase is observed. An interesting feature of GC model is the negative slope of the freezing and melting lines at high density [24, 26] which is typical for *anomalous* liquids [7]. In Fig. 6.1 the phase diagram for the GC model system with data from Ref. [142, 143] is shown and the different phases are indicated: the face-centered-cubic (FCC) crystal, the body-centered cubic (BCC) crystal and the fluid (F). The difference between the freezing and the melting temperatures at constant density for the GC system is very small [142, 143] and cannot be resolved on the scale of the figure. For this reason only data for the freezing line are shown in Fig. 6.1. The high density limit of the freezing line is well described by a power-law function of density, as different authors reported [25, 145].

6.2   Simplicity of the GC model

The low density region the GC phase diagram can be described in terms of HS [24]. In the following the term 'low density region' will be used for state points in the fluid region on the left side of the freezing line, i.e. for densities smaller than the density at which the freezing line exhibits the maximum (Fig. 6.1), while the term 'high density region' for state points in the fluid region on the right.

In general, every time that a system is well described by HS in a part of its phase diagram it is also well described in terms of isomorph theory in the same region at least. This conjecture is checked in Fig. 6.2 (a) and 6.3 (b). In the first figure, the validity of the general definition of Roskilde (R) simple systems, i.e. Eq. 2.2, is checked for a state point in the low density region and the correlation coefficient R, defined in Eq. 2.1, and the scaling exponent γ, defined in Eq. 2.18, are reported. Even though the scaled potential energies cross each other, most of them cross only neighboring lines. This is the same of what happens in the case of the LJ system, where Eq. 2.2 was not even perfectly obeyed because of the approximate nature of the isomorph theory. The GC system is R simple at the chosen state point and therefore it is possible to build an isomorph in the low-density region.

In Fig. 6.2 (b), the same check is performed at a state point in the high density region. At this state point Eq. 2.2 is also satisfied but the correlation coefficient R and the scaling exponent γ are both negative. Negative correlations between virial and potential energy were first reported in hard-core colloidal particles interacting with a short range of attractive squared-well [146] but the validity of isomorph theory in the case of strong negative correlations has not been investigated. In Chap 2, where isomorph
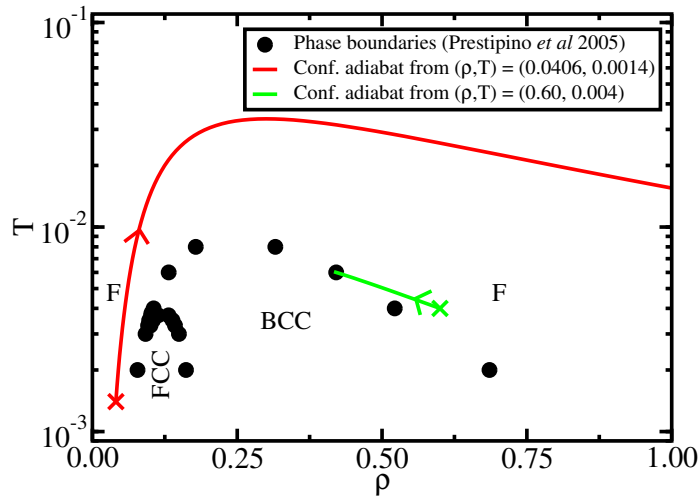
Figure 6.1: Phase diagram of the Gaussian core model system. Data for the freezing line from Ref. [142, 143] are shown together with two configurational adiabats, i.e. constant excess entropy S_{ex} curves. Both configurational adiabats have been obtained with the *step-by-step* method: the scaling exponent γ is evaluated from an NVT simulation at a given state point, the density is increased (decreased for the green line) by 1 per cent and the temperature corresponding to the new density along the same configurational adiabat is calculated using Eq. 2.24. The starting point of each configurational adiabat is marked by a cross. The arrow along each configurational adiabat indicates whether the curve has been built by increasing or decreasing density. The red line is a configurational adiabat constructed from a state point in the low density region (positive correlations) while the green line is a configurational adiabat from a state point in the high density region (negative correlations, see text). The configurational adiabat starting from high density (green line) intersects the freezing line showing that in the high density region the freezing line is not a configurational adiabat.

theory is presented, it is shown that Eq. 2.2 implies the existence of strong correlations between virial and potential energy but no requirement for these correlations to be positive is given. It is therefore interesting to investigate whether negative correlations still produce isomorphs in the phase diagram or not. A negative γ implies that the system will have a decreasing freezing temperature upon increasing density, if we assume that the freezing line and isomorphs have at least similar density dependence, and this is what can be observed in Fig. 6.1.

In Fig. 6.2 (c), it is shown the effect of scaling configurations on the potential energy in the case of a non strongly correlated state point. The state point considered here belongs to the high density freezing line from Ref. [25]. In this case Eq. 2.2 is strongly violated because many curves cross the entire figure and their behavior is not a monotonic function of density.
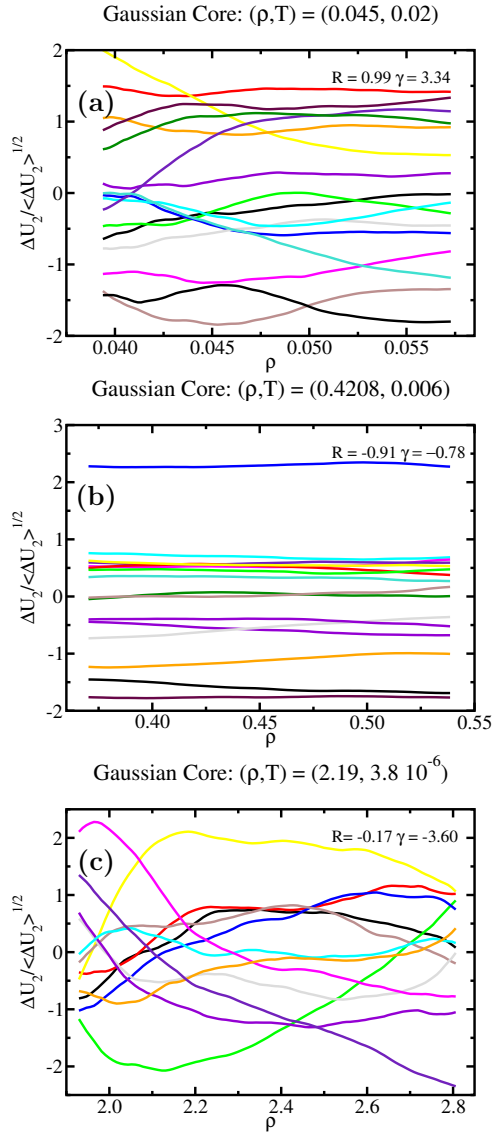
Figure 6.2: Direct check of Eq. 2.2 at three state points in the fluid phase of the GC system. The state point from which the equilibrium configurations were taken and at which R, defined in Eq. 2.1, and γ, defined in Eq. 2.18, are evaluated is indicated on top of each figure. The way these curves are produced is described in the caption of Fig. 2.2. (a) fluid state point $(\rho, T) = (0.045, 0.02)$ in the low density region. The correlation coefficient R is above 0.9 and the scaling exponent γ is positive. (b) fluid state point $(\rho, T) = (0.4208, 0.006)$ in the high density region. R is strongly negative, i.e. $R < -0.9$, and γ is negative too. (c) fluid state point $(\rho, T) = (2.19, 3.8 \cdot 10^{-6})$ at even higher densities (this state point is along the freezing line evaluated in Ref. [25]). R is negative but close to zero. In this last situation many of the curves cross the entire figure and have a non monotonic behavior as function of density.
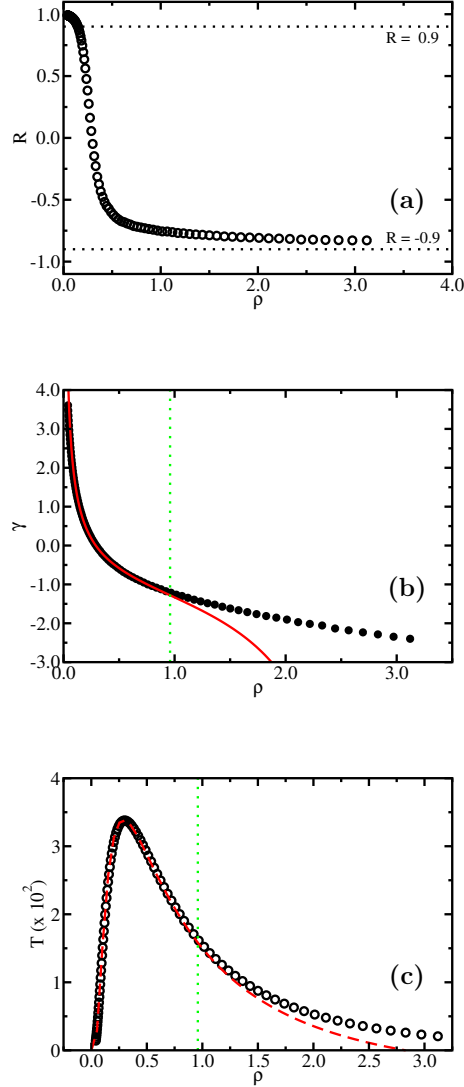
Figure 6.3: Correlation coefficient R, scaling exponent γ and configurational adiabat shape $h(\rho)$, from Eq. 6.2, along the configurational adiabat starting from the state point $(\rho, T) = (0.0406, 0.0014)$. (a) correlation coefficient R as a function of density ρ along the chosen configurational adiabat. The drop from strong positive correlation to fairly strong negative correlation is sharp and it is in the same region of densities where the freezing line exhibits the maximum. (b) scaling exponent γ along the chosen configurational adiabat. The red line represents the prediction for the scaling exponent γ from the pair potential [70], Eq. 6.1. The agreement between the data and the prediction is satisfying for densities lower that unity. (c) configurational adiabat shape prediction from Eq. 6.2, i.e., from the pair potential. The agreement is good in the same region as for γ, not surprisingly because γ is the logarithmic derivative of $h(\rho)$, from Eq. 2.31. It's important to remark that the regions in which the configurational adiabat is also an isomorph are only the ones in which Eq. 2.2 is satisfied. This statement is clarified in the text and in Sec. 6.6.

6.3 Scaling exponent γ of the GC system

As discussed in Chap. 2 and in Ref [70], the scaling exponent $\gamma(\rho, S_{\text{ex}})$ and the shape function for isomorphs $h(\rho, S_{\text{ex}})$ can be predicted starting from the pair potential. The scaling exponent γ is related to the derivatives of the pair potential $v(r)$ from the equation:

$$\gamma(\rho, S_{\text{ex}}) = \frac{1}{3}\left(-2 - r\frac{v^{(3)}(r)}{v^{(2)}(r)}\right)\Bigg|_{r=\Lambda(S_{\text{ex}})\rho^{-1/3}} \tag{2.36}$$

where the second and third derivative of $v(r)$, respectively $v^{(2)}(r)$ and $v^{(3)}(r)$, are involved. The coefficient $\Lambda(S_{\text{ex}})$ takes into account that the equation for distinct isomorphs can slightly differ [70] and it depends on the specific configurational adiabat, i.e. a constant excess entropy S_{ex} curve. In the following, we will assume the coefficient $\Lambda(S_{\text{ex}})$ to be identically unity for simplicity. Eq. 2.36 when specialized to the case of the GC model provides a prediction for γ along an isomorph:

$$\gamma(\rho) = \frac{2}{3}\frac{2\rho^{-\frac{4}{3}} - 5\rho^{-\frac{2}{3}} + 1}{2\rho^{-\frac{2}{3}} - 1}. \tag{6.1}$$

Eq. 6.1 predicts a monotonically decreasing dependence of γ on density ρ, see Fig. 6.3 (b) and a (negative) divergent value of γ for $\rho = \bar{\rho} = 2^{3/2} \approx 2.83$. A divergent value of the scaling exponent γ is not physical and therefore, in order for the theory to be consistent, the system should stop being R simple before reaching the density $\bar{\rho}$. There is no reason, according to Eq. 6.1, to set a lower limit to the density at which isomorph theory should work in the case of the GC system. It is interesting to note the difference between this system and the LJ system. In the latter case, the isomorph theory does not apply at low density while it works at high density and this keeps being true even in the high dimensionality limit considered in Chap. 5. For the GC system the converse happens: there is an upper limit to the density at which the theory can be used but not a lower one.

Following Ref. [70], it is possible to predict also the shape of configurational adiabats, i.e. the analytical form of the $T(\rho)$ dependence in the phase diagram, from the pair potential. In Ref. [70] the function $h(\rho, S_{\text{ex}})$ is supposed to describe the isomorph shape because isomorphs are configurational adiabats. The GC system is the first case where further attention on the distinction between configurational adiabats and isomorphs is required; a careful explanation of the difference is given in the following pages. The equation for $h(\rho, S_{\text{ex}})$ from Ref. [70] is:

$$h(\rho, S_{\text{ex}}) = A\,\rho^{-2/3}v^{(2)}(r)\Big|_{r=\Lambda(S_{\text{ex}})\rho^{-1/3}}. \tag{2.37}$$

The coefficient A incorporates the fact that the function $h(\rho, S_{\text{ex}})$ is defined up to a positive multiplicative constant. When Eq. 2.37 is specialized to the GC model and, as before, $\Lambda(S_{\text{ex}})$ is set to unity, the prediction for the shape of configurational adiabats $h(\rho)$ is:

$$h(\rho) = -A\rho^{-\frac{4}{3}}(\rho^{\frac{2}{3}} - 2)e^{-\rho^{-\frac{2}{3}}}. \qquad (6.2)$$

The temperature T along a given isomorph is proportional to $h(\rho)$ and it will become negative for densities higher than $\bar{\rho}$. As in the case of $\gamma(\rho)$, there is consistency requirement from the theory: the system must stop being R simple somewhere before reaching density $\bar{\rho}$.

In Fig. 6.1 a configurational adiabat starting from the state point $(\rho, T) = (0.0406, 0.0014)$ is shown (red curve). This curve has been constructed *step-by-step* (using a 1 per cent density increment) as described in Chap. 5, i.e., evaluating the scaling exponent γ from an NVT simulation at the starting state point, numerically solving Eq. 2.24 to find the temperature change corresponding the chosen density change and then iterating the procedure. In Fig. 6.3 (a) the correlation coefficient R, defined in Eq. 2.1, is plotted as a function of density ρ along this configurational adiabat. At low density the system is a Roskilde liquid and the correlation coefficient R decreases as density is increased. The GC system is therefore strongly correlating at small densities, while at densities corresponding to the maximum of the freezing curve the correlation coefficient R is close to zero and then it becomes strongly negative in the high density region.

Along the same configurational adiabat the scaling exponent γ has been evaluated and it is compared with predictions from Eq. 6.1 in Fig. 6.3 (b). The agreement between simulation data and Eq. 6.1 is good for $\rho < 1$. There is therefore a density at which the system stops behaving R simple, as discussed before. It is interesting to note that the value $\rho = 0.9594$ (green vertical line in figure) is where γ from Eq. 6.1 has an inflection point. This change of concavity *is needed* in order to have a negative divergence at higher densities but it is not reflected at all in the γ evaluated from NVT simulations. We can now notice a parallel with the LJ systems studied in the previous chapters: as in the case of the LJ system the change in the first derivative of γ was associated to the system ceasing to be R simple (Chap. 3 and 5), for the GC model the high density non-R simple region starts with a change in the sign of the second derivative of γ. At the present stage, these correlations between changes in γ behavior and the system ceasing to be R-simple are only the author's observations and the theoretical understanding of physics processes relating to this change in behavior is unclear. A more deep understanding of these correlations could be of interest for further development of the isomorph theory.

In the 3d space the change between different regimes of the scaling exponent γ is smooth but we can speculate that in the $d \to \infty$ limit this change

becomes sharp and it could be thought as of some sort of phase transition between an R simple domain in the phase diagram and a non-R simple domain, in analogy with what has been discussed in Refs. [129, 130]. The data we have at the present stage are not enough to give any proof of this conjecture. An extensive study of the GC system, and of other systems as well, could give further insight in this direction.

In Fig. 6.3 (c), the consistency between Eq. 6.2 and the *step-by-step* construction of the configurational adiabat is verified. Data are in agreement with the prediction for $\rho < 1$ as in the case of γ. It is worth noting that, even though the maximum of the configurational adiabat is well described by $h(\rho)$ in Eq. 6.2, in that region the GC system is not strongly correlating, as evident from Fig. 6.3 (a), and the isomorph theory is not supposed to hold there. The description of configurational adiabats through Eqs. 6.1 and 6.2 is derived starting from the assumption that the temperature along a configurational adiabat depends on density and excess entropy S_{ex} as $T = h(\rho)f(S_{\mathrm{ex}})$ [67]. This relation is restricted to R simple systems [67]. It is therefore surprising and not completely understood why the $h(\rho)$ function can describe the configurational adiabat even in the region where strong virial potential energy correlations are absent. In the case of the GC system, along the same configurational adiabat there are two regions where the system exhibits strong correlations: in the low density region strong positive correlations while at high densities strong negative ones. These two regions define two different isomorphs because they are connected by a region in which correlations are weak or absent.

The phase diagram of the GC system appears to be divided therefore in four different density regions:

1. low-density region: the GC system has correlation coefficient R close to unity and it is R simple. In this region the system is also simple according to the usual definition of Chap. 1 and Ref. [1];

2. the region around the maximum of the freezing curve: the GC system is not R-simple because the correlation coefficient R is close to zero, and it cannot be described with HS either;

3. moderate density region (approximately $0.4 < \rho < 1.0$): the correlation coefficient R is strongly negative, Eq. 2.2 is satisfied and isomorphs with negative scaling exponent γ exist;

4. high density region: even though the coefficient R is still strongly negative, the configurational adiabats are not isomorphs anymore because Eq. 2.2 is no longer satisfied, as shown in Fig. 6.4.

This division into regions based on the system density becomes irrelevant at high temperatures. Along an isochore, the correlation coefficient R for this system is monotonically increasing with temperature and the GC system

Gaussian Core: (ρ,T) = (1.110, 1.87·10^{-3})

Gaussian Core: (ρ,T) = (1.325, 1.23·10^{-4})
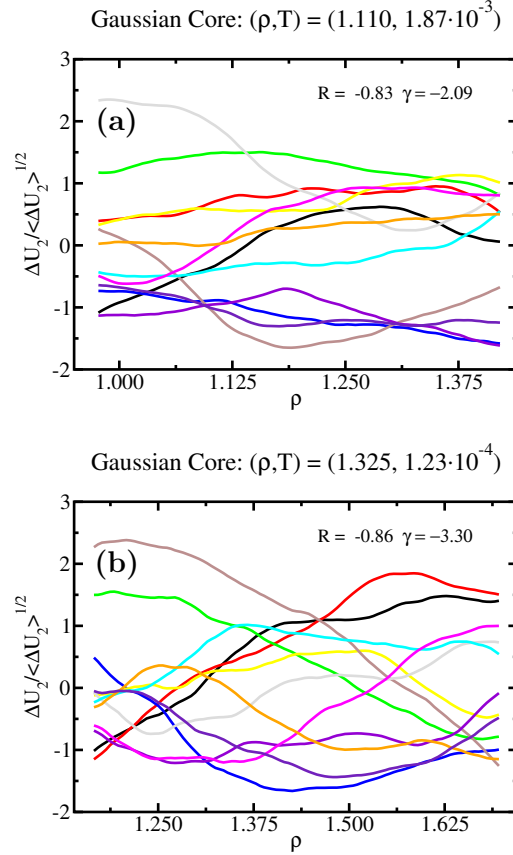
Figure 6.4: Direct check of the general definition of R simplicity (Eq. 2.2). (a) at the state point $(\rho, T) = (1.110, 1.87 \cdot 10^{-3})$ along the configurational adiabat in Fig. 6.1 (red curve). The density of this state point is higher than the density 0.9594 where γ exhibits an inflection point. (b) at the state point $(\rho, T) = (1.325, 1.23 \cdot 10^{-4})$ along the high density freezing line from Ref. [25]. Also in this case the density is higher than that of the inflection point. The difference between these figures and the ones in Fig. 6.2 is that in this case there are (more) scaled potential energy curves that cross many others, especially at $(\rho, T) = (1.325, 1.23 \cdot 10^{-4})$, showing a much stronger violation of Eq. 2.2 than in Fig. 6.2 (a) and (b).

exhibits strongly positive correlations. The study of the system has been not extended to the high temperature region both for the lack of time and because the structure and dynamics become trivial when the particles' mean kinetic energy is large compared to the interaction energy (ideal gas).

In the next sections the existence of invariance along isomorphs for the GC model both in the low density region and in the high density region is shown and the possibility of approximating the freezing line of the GC model with a freezing isomorph, in analogy with the LJ system in Chap. 3, is discussed.
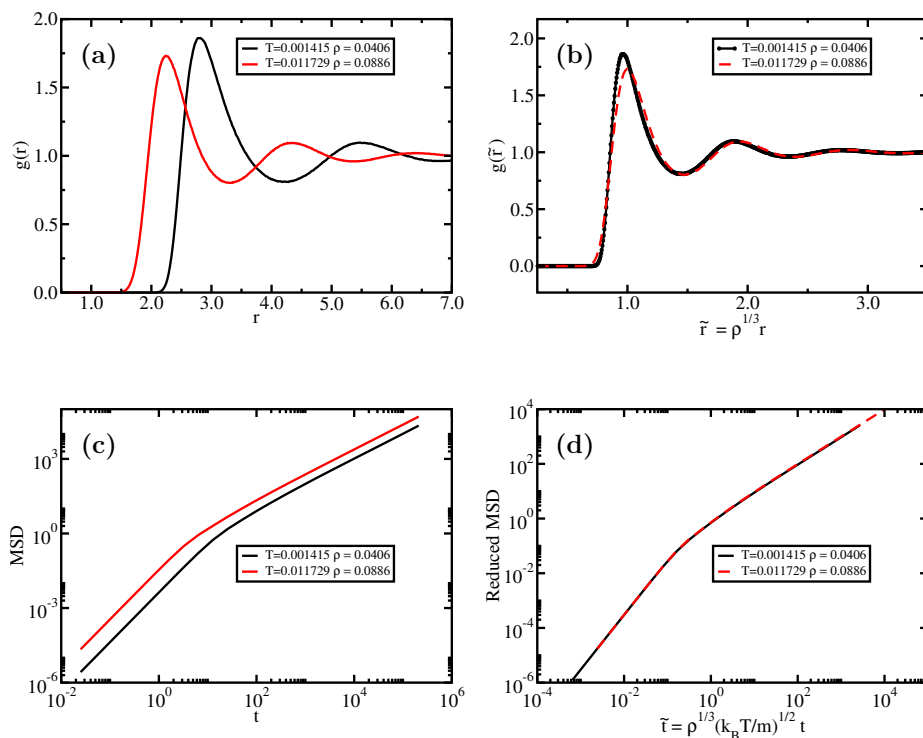
Figure 6.5: Structure and dynamics along an isomorph in the low density region of the phase diagram of the GC system. The density of the second state point is doubled respect to the density of the first one. In this region, the GC model fluid can be also described following the HS paradigm. (a) Radial distribution function (RDF) $g(r)$ at the two isomorphic state points; (b) RDF in reduced units; (c) Mean squared displacement (MSD) at the two isomorphic state points; (d) MSD in reduced units.

6.4   Low density isomorph

The existence of strong positive correlations between virial and potential energy implies the invariance of reduced structure and reduced dynamics along isomorphs. In Fig. 6.5 the structure and the dynamics for the GC model in the fluid phase is studied along the isomorph starting from the state point $(\rho, T) = (0.0406, 0.0014)$ This isomorph is the low density side of the configurational adiabat represented in Fig. 6.1 with a red curve. In this region $R > 0.9$ and therefore the configurational adiabat is an isomorph. Both structure and dynamics are plotted as a function of usual LJ units (length in units of σ and energies in units of ϵ) and as a function of reduced units, defined in Ref. [52]. Analogously to the other R systems, the invariance of structure and dynamics along the chosen isomorph is verified for the GC model too. The collapse of the radial distribution function is not
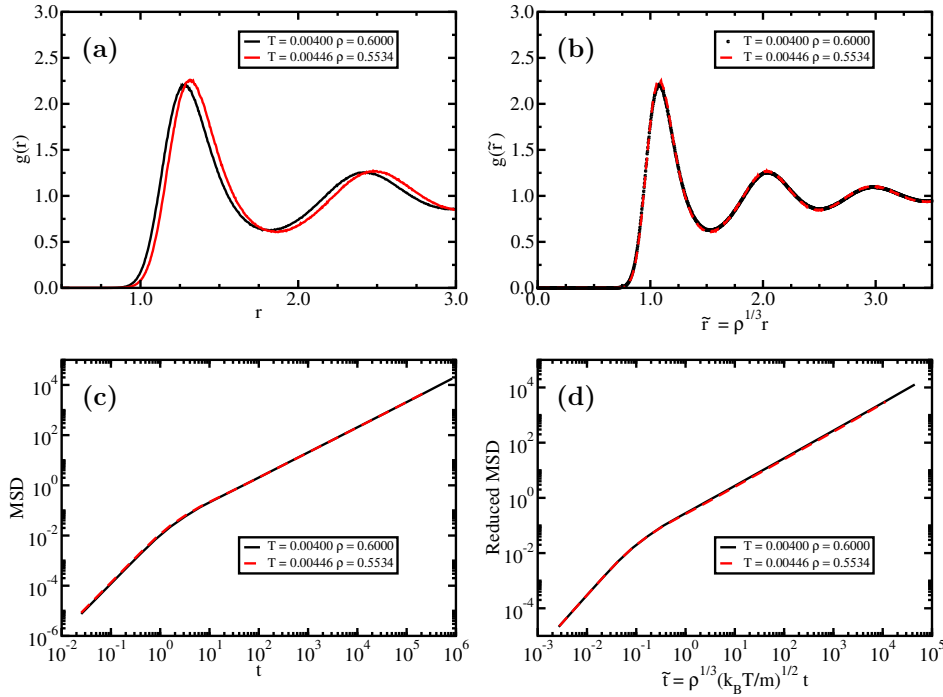
Figure 6.6: Structure and dynamics along an isomorph in the moderate density region of the phase diagram of the GC system defined in Sec. 6.3. In this region, the GC model fluid cannot be described following the HS paradigm. (a) Radial distribution function (RDF) $g(r)$ at the two isomorphic state points; (b) RDF in reduced units; (c) Mean squared displacement (MSD) at the two isomorphic state points; (d) MSD in reduced units. It is quite surprising that the two state points have the same dynamics (MSD) even in non-reduced units.

perfect, but one should notice that the density and temperature have been changed by a factor ≈ 2 and ≈ 8 respectively.

6.5   Isomorph in the moderate density region

The presence of strong negative correlations in the phase diagram should lead, as in the case of the strong positive ones, to the invariance of structure and dynamics in reduced units along configurational adiabats, which are negative R isomorphs. This conjecture is formulated in this work for the first time and is verified in Fig. 6.6. As mentioned in the start of this chapter, there is no requirement for the correlation coefficient R to be positive, but only for its absolute value to be close to unity. The two state points, whose structure and dynamics are studied in Fig. 6.6, belong to the configurational adiabat represented in Fig. 6.1 with a green line. These state points are in the moderate density region defined in Sec. 6.3, i.e. where configurational adiabats are isomorphs with negative correlation coefficient R and negative

scaling exponent γ. Invariances in this region cannot be explained referring to the HS system. In Fig. 6.6 the structure (RDF) and the dynamics (MSD) are plotted as a function of LJ units and of reduced units. The invariance in reduced units is well verified in agreement with the isomorph theory prediction. The relative change in density and temperature in this case are 8% and 11% respectively. Even though this density change seems to be small when compared to the one of the last section, one should remember that the density ranges studied in computer simulations are often of this order. In Fig. 6.6 (a) it is possible to see that this density change produces a significant variation in the RDF. The absence of any change in the MSD in non reduced units is surprising, specially when associated with an evident change in structure. A similar finding, but for a completely different system, has been reported in Ref. [147].

6.6   The freezing line of the Gaussian core system

The existence of isomorphs in the fluid phase implies, as discussed in Chap. 3 and in Refs. [83, 84], that the freezing line for the system of study can be approximated by an isomorph, the freezing isomorph. Keeping this aim in mind we constructed two different configurational adiabats with the *step-by-step* method, already explained previously, from two state points belonging to the low density side of the freezing line (positive slope) taken from Refs. [142, 143]. The two configurational adiabats, together with the entire set of freezing state point of Refs. [142, 143], are reported in Fig. 6.7. The low density region of the freezing line is well approximated by configurational adiabats, which are isomorphs since $R > 0.9$ in this region as shown in Fig. 6.7 (b). There is no difference between the configurational adiabats (isomorphs) generated from the two state points. In the region of densities where the freezing line exhibits a maximum and where the correlation coefficient drops to zero, the approximation for the freezing line stops working, as expected. The isomorph theory is, in fact, not supposed to work when $R \approx 0$.

This is strong evidence that isomorphs and configurational adiabats are not exchangeable concepts. Specifically, not all configurational adiabats are isomorphs. The role of the excess entropy S_{ex} as the relevant parameter in describing transport coefficients is, in the author's view, related to the existence of hidden scale invariance predicted by the isomorph theory and not a general feature of configurational adiabats, as suggested by Rosenfeld [65] or Dzugutov [78]. In support of this hypothesis, the breakdown of Rosenfeld entropy scaling has been observed in the anomalous region of the GC system (Ref. [148]).

For the GC system the difference between configurational adiabats and isomorphs is even more striking than for other systems; along the same
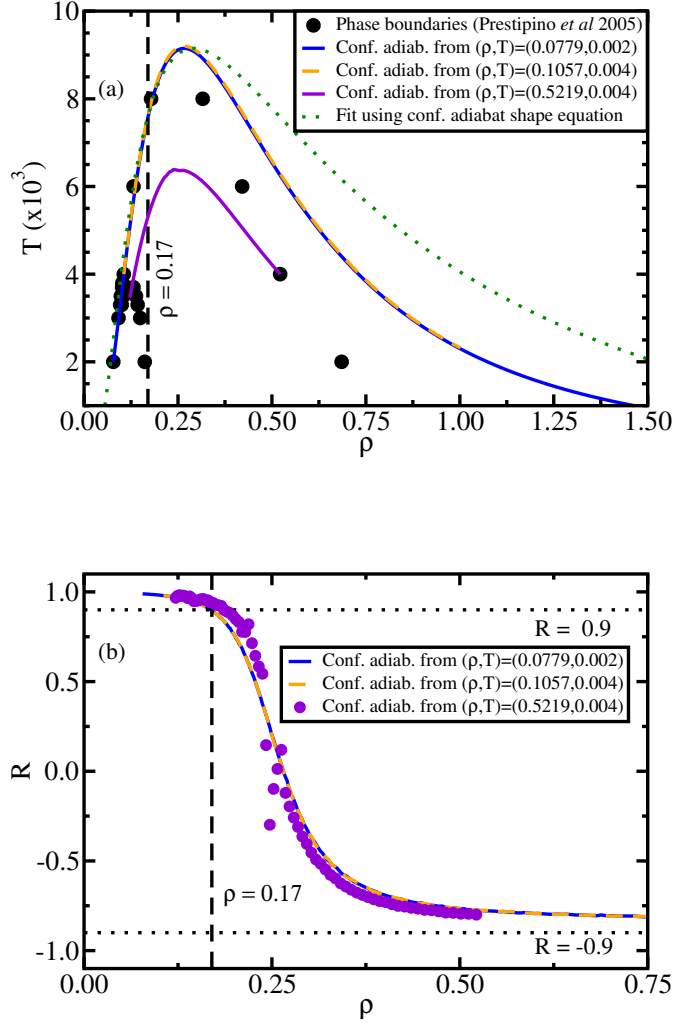
Figure 6.7: Freezing line of the GC system and isomorph approximating its low density side: (a) comparison between the freezing line from Refs. [142, 143] and the approximation provided by Eq. 6.3. Two independent configurational adiabats are built from the state points $(\rho, T) = (0.0779, 0.002)$ and $(\rho, T) = (0.1057, 0.004)$ along the GC freezing line from Refs. [142, 143] to show the uniqueness of Eq. 6.3. A third configurational adiabat starting from $(\rho, T) = (0.5219, 0.004)$ is also shown. (b) correlation coefficient R, from Eq. 2.1, along the three configurational adiabats. The black dotted line indicates the (approximate) density at which the correlation coefficient R exceeds the threshold of 0.9 and therefore it indicates the maximum density at which Eq. 6.3 well approximates the GC freezing line. For densities below $\rho \approx 0.17$ the correlation coefficient R along the configurational adiabats is above 0.9 and therefore these configurational adiabats correspond to the same isomorph.

configurational adiabat in fact the correlation coefficient R can be strongly positive (close to unity) and then strongly negative, as shown in Fig. 6.3 (a) and Fig. 6.7 (b). A consequence of this behavior of R is that along the same configurational adiabat it is possible to have two distinct isomorphs. The structure and the dynamics on the low density side of the configurational adiabats are different from those along the high density side and therefore the two strongly correlating branches of the configurational adiabat cannot be the same isomorph. This is true in particular for the isomorph starting from the two low density freezing state points considered here. While for low densities this isomorph provides a good approximation of the freezing line, the continuation of the same configurational adiabat does not describe the high density side of the freezing line, as shown in Fig. 6.7.

The function $h(\rho)$ from Eq. 6.2 gives the shape of isomorphs and therefore it can be used to obtain an analytical expression for the low density freezing line of the GC system. The coefficient A in Eq. 6.2 can be chosen by imposing to the function $h(\rho)$ to have the same maximum value as the configurational adiabat from one of the freezing state points. The choice of which freezing state point to use is irrelevant as long as the state point is in the strongly correlating region, as shown in Fig. 6.7. The value for A so obtained is $A_L = 1.10 \cdot 10^{-2}$ where the suffix L stands for low density. The low density side of the GC freezing line can be therefore approximated by:

$$T_L = -A_L \rho^{-\frac{4}{3}} (\rho^{\frac{2}{3}} - 2) e^{-\rho^{-\frac{2}{3}}} \qquad (6.3)$$

Differently from what done in Chap. 3, in this case Eq. 6.3 is a one-parameter fit and it is not a prediction of the freezing line from a single state point. For this reason this equation has not been called freezing isomorph. It should be noted that in this derivation we assumed that $\Lambda(S_{\mathrm{ex}}) = 1$, which is known to be a simplifying approximation of the general case discussed in Ref. [70] This could be an explanation of the need for a fitting parameter in obtaining Eq 6.3.

The invariance of reduced structure and reduced dynamics along the low density side of the freezing line is verified in Fig. 6.8. As in the case of the LJ system, the invariances along the low-density freezing line of the GC system can be explained in terms of isomorph theory.

We tried to approximate the freezing line of the GC system in the moderate density region, defined in Sec. 6.3, with an equation like Eq. 6.3 without success. From Fig 6.7 it is evident that after the maximum of the freezing curve, Eq. 6.3 does not even represent the correct configurational adiabat. An alternative way of proceeding could be the one adopted in Chap. 3 for the low density region of the LJ freezing line, where the bare isomorph theory does not provide an accurate approximation of the freezing line but it is still possible to obtain the right freezing line as a first order Taylor expansion. Due to lack of time, this part of the work is unfinished.
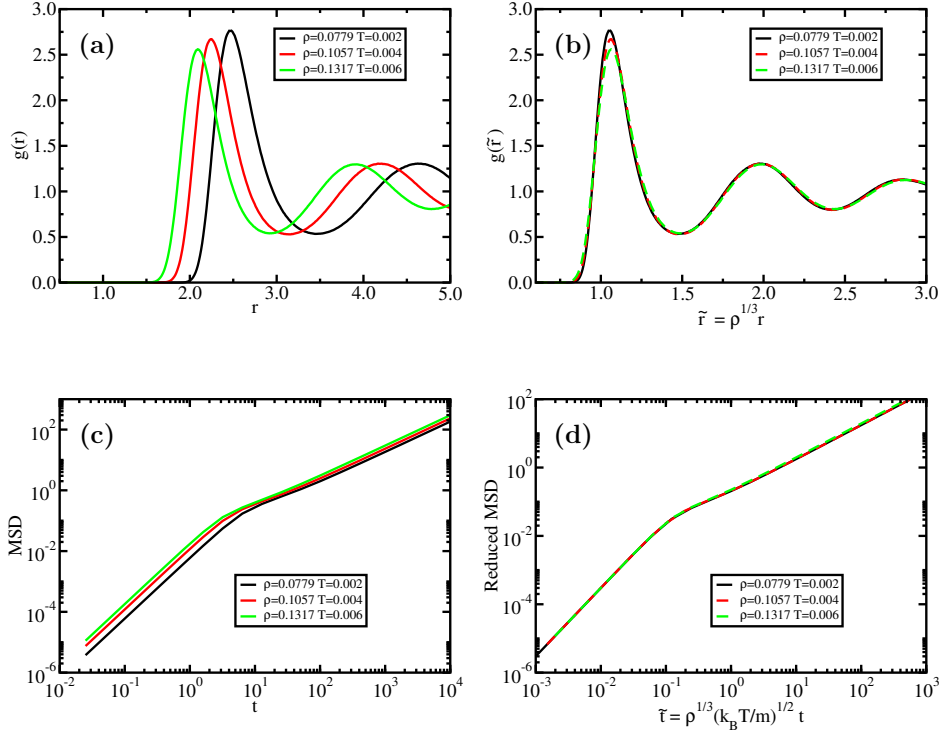
Figure 6.8: Invariances along the freezing line in the low density region. (a) Radial distribution function (RDF) $g(r)$ at three state points along the freezing line from Refs. [142, 143]; (b) RDF in reduced units; (c) Mean squared displacement (MSD) at the same state points; (d) MSD in reduced units. When using reduced units, the structure and the dynamics of the two state points collapse onto a master curve.

Summary: results, problems and outlooks

The resulting picture from our (ongoing) work on the GC system is not complete and this is one of the reasons this system deserves a more extensive study. We showed that at low density the correlation coefficient R is close to unity and isomorphs are present in this region. Both in the liquid phase and along the low density side of freezing line, isomorph invariances hold and the description of isomorphs using Eqs. 6.1 and 6.2 is confirmed. At high density a much more complex scenario appears. It is still possible to define isomorphs, and invariances still hold, but the isomorphs in this region are characterized by strongly negative correlations between virial and potential energy (instead of strongly positive as at low densities). In this region the freezing line is not a configurational adiabat and cannot be therefore approximated by an isomorph.

Conversely from the other results presented in this thesis, the data for the high density GC have only partially been double checked by the author due to the lack of time. One of the most trustworthy check of a NVT simulation is, in the author's opinion, the measurement of specific heat at constant volume. This measurement can be performed both using potential energy fluctuations and calculating the variation of potential energy when changing temperature along an isochore. A difference in the value of excess specific heat C_V^{ex} provided by the two measurements is usually related to a not sufficiently accurate choice of the thermostat relaxation time (see Chap. 1, appendix A and App. C) or problems related to loss of precision due to single precision calculation on the GPU. In the case of the data for the high temperature configurational adiabat, red line in Fig. 6.1, this test has been performed with good results: the excess specific heat at the state point $(\rho, T) = (0.4887, 0.0294)$ is $C_V^{\mathrm{ex}} = 1.035$ from potential energy fluctuations and $C_V^{\mathrm{ex}} = 1.040$ from the measurement along the isochore $\rho = 0.4887$. In the case of the configurational adiabats in Fig. 6.7 the excess specific heat C_V^{ex} from the fluctuations is wrong. The excess specific heat at the state point $\rho, T = (0.4860, 0.0067)$ is $C_V^{\mathrm{ex}} = 6.972$ from potential energy fluctuations and $C_V^{\mathrm{ex}} = 1.638$ from the measurement along the isochore $\rho = 0.4860$. The correlation coefficient R and the scaling exponent γ are usually less sensitive than C_V^{ex} to the thermostat relaxation time and the fact that the results of R are reasonable can be understood by comparing Fig. 6.3 (a) with Fig. 6.7 (b). The behavior of R as a function of density is in fact the same. A deeper understanding of why the estimation of the excess specific heat C_V^{ex} from fluctuations is so off is needed and will be matter of further study by the author. A wrong estimation of the scaling exponent γ could justify the discrepancy between the configurational adiabat (which is calculated using γ) in Fig. 6.7 and the prediction from $h(\rho)$. Despite these problems, the GC system has shown to be extremely interesting and it should be the focus of even more interest in the future studies as a playground for theories such as the isomorph theory. An interesting possible direction of extending the study of this system, on the track of what done in Chap. 5, could be in understanding how isomorphs with negative correlation coefficient behave in higher number of dimensions.

Appendix A

Description of the homemade molecular dynamics code

In this appendix the molecular dynamics program developed by the author for simulating a system of particles in d dimensions is described. This program has been used to produce the data in Chapter 5 and it is available at `http://dirac.ruc.dk/~lorenzoc/` together with some analysis tools.

As described in Chapter 1, a molecular dynamics (MD) program integrates the equations of motion of a system of N particles interacting via a chosen potential. The discretized equations of motion for the Leap-Frog NVE, i.e. constant number of particles N volume V and total mechanical energy E, and NVT, where T stands for constant temperature, dynamics [149] can be generalized to an arbitrary number of spatial dimensions due to their vectorial form. The necessity of dealing with vectorial calculations in an arbitrary number of dimensions is one of the reasons for developing our MD program in Fortran 90. Other reasons for this choice are that Fortran 90 represent a good compromise between easy coding and parallelization opportunities. Both CUDA environment [39] and OpenMP environment [150] have been developed for Fortran 90 and therefore it is possible to parallelize a Fortran code on GPUs and/or CPUs. The present code utilizes parallel computing on CPUs for the calculation of the neighborlist. A GPU implementation of the neighborlist and of the force calculation could be a future development. All calculations in this program are in double precision.

A.1 Program structure

The program is structured in different libraries; this way of structuring the code has two main advantages: the code is more readable (when appropriately commented) and the different libraries can be modified independently from each other. The interaction potentials available are exclusive libraries. The structure of the code is the following:

1. $PhD\_MDfortran.f90$: this is the main file where the Leap-Frog equations for NVE and NVT dynamics are integrated;

2. $MDneighborlist.f90$: contains the implementation of neighborlist calculation using OpenMP parallelization [150] on CPUs;

3. $MDoutputmanager\_lib.f90$: contains all the functions and subroutines related to reading the starting configuration and to writing the output;

4. $MDpotential\_lib.f90$: there are 3 versions of this file and each of them implements a different pair potential and it contains the specific force calculation

   (a) LJ(12,6) (future plan for LJ(8,4) and LJ(16,8))

   (b) Exp potential [56, 57]

   (c) mW potential (only pairwise term) [151]

5. $general\_func\_lib.f90$ and $MDfunction\_lib.f90$ contain functions for general use.

A.1.1 Input and Output

The program needs to be compiled for the chosen pair potential. Informations about how to compile the program can be found at `http://dirac.ruc.dk/~lorenzoc/`. In order to run a simulation a starting configuration at density 1.0 and a text file containing the parameters of the simulation (described in the following) are needed.

The starting configuration can be created using a stand-alone code named Nd_start_conf that produces a configuration with the specified number of particles in a simple cubic (SC) lattice structure and it takes as input the number of particles in one direction (this number, as example, is 3 if a SC of 9 particles in $2d$ is desired) and the number of dimensions. The starting configuration is saved as a compressed gzip file.

An example of the parameters' file, named $sim\_info.mydat$, is given in Fig. A.1. In this file the information on the state point to simulate, as density and temperature, the output schedule and the integrator (NVE or NVT) can be chosen.

#Starting configuration:

Mystart_N1728_T1.312_rho0.9.xyz.gz

#d, N, Nsteps

3 1728 2000000

#block_size, record_en_int, record_traj_int

10000 200 500

#density, T, timestep, cutoff, skin

0.90D0 1.3120D0 0.00250D0 2.5D0 0.3D0

#integrator , targetT, thermo_relax, SF_on

NVT 1.3120D0 80.0D0 1

Figure A.1: Example of parameters' file. A detailed explanation of each parameter is given in the text.

In the following each line of *sim_info.mydat* is described and all the meaning of all the parameters explained.

The file name of the starting configuration is read from the second line. This file can be produced using *Nd_start_conf* or can be a restart file from an old simulation.

On the fourth line there is information regarding the dimensionality of the system d, the number of particles N in the starting configuration and the number of timesteps $Nsteps$ to simulate. The program will verify if the number of particles N inserted corresponds to that in the starting configuration and it will throw an error otherwise.

On the sixth line there is the output information. Output is divided into blocks in order to make easier to check the results while the simulation is still running (using the analysis tools). At the end of each block a restart file is written; this file can be used as starting configuration to restart the simulation whether is needed. The three parameters on this line specify how long, in terms of how many timesteps, an output block should be and how often energies and trajectories are saved. The block size needs to be an integer multiple of each of the other two numbers. If this is not the case, the program will throw an error. At the present stage no logarithmic saving of trajectories is implemented, this could be part of future development.

On line eight the informations about density ρ, temperature T, *timestep*, *cutoff* and neighborlist *skin* are given. The meaning of *skin* and *cutoff* parameters will be discussed in Secs. A.1.2 and A.1.3. This MD program performs simulations in reduced units; a reason for doing that is to produce the output configurations directly in the reduced units relevant for the isomorph theory. The density and the temperature of the system are therefore set to unity before the simulation starts while the length scale and the en-
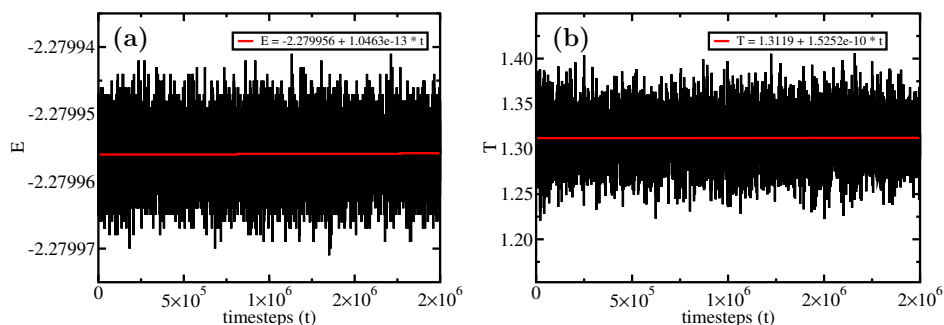
Figure A.2: Check for the NVE and NVT integrators. (a) total mechanical energy for an NVE simulation in 3d at the state point $(\rho, T) = (0.9, 1.312)$ for the LJ system using SF cutoff. (b) output temperature for an NVT simulation in 3d at the state point $(\rho, T) = (0.9, 1.312)$ for the LJ system using SF cutoff.

ergy scale of the potential are scaled in order to get the right density and temperature in usual MD units. If for example the desired temperature is $T = 0.5$ in MD units with $\sigma = \epsilon = 1$ parameters of the potential, a simulation with $T = 1$ and $(\sigma, \epsilon) = (1, 2)$ will be performed. The reason for this is that in any MD code, changing density ρ and temperature T or changing the length scale σ and the energy scale ϵ of the potential is completely equivalent. The input file is thought in a way to allow the beginner user to be able to perform simulations easily and this is why the input parameters are in terms of density and temperature and not of σ and ϵ. The energy output is also given in usual MD units.

In the last line it is possible to specify the integrator (NVE or NVT, NPT could be a further development), the target temperature and the thermostat relaxation time. The NVT program uses the Nosé-Hoover thermostat [36] already presented in Sec. 1.2.2. The thermostat relaxation time is given as a multiple of the timestep. In the example in Fig. A.1, the thermostat relaxation time will be 80 timesteps. The last parameter specifies the cutoff method: the program can use a shifted potential (SP) or shifted force (SF) cutoff. The SP cutoff is selected inserting 0, corresponding to $SF\_on = false$, while SF cutoff inserting 1. Any other number either than 0 or 1 will produce an error.
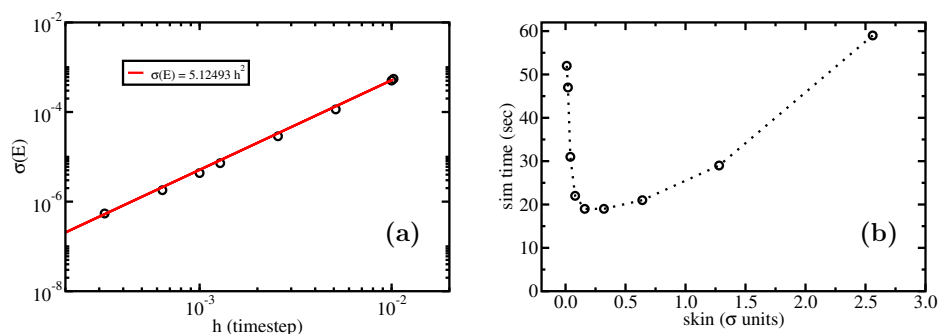
Figure A.3: (a) check of ideal scaling relation between the energy fluctuation ΔE and the timestep h:

$\log(\Delta E) \propto 2 \cdot \log(h)$ from Ref. [33]. Several NVE simulations at the state point $(\rho, T) = (0.9, 1.312)$ for the LJ system using SF cutoff have been performed with different timesteps. The values of the energy standard deviation so obtained have then been fitted to verify if the MD code is able to reproduced the ideal scaling of Ref. [33] and this is the case. (b) time required (in seconds) in order to perform a simulation in 3d at the state point $(\rho, T) = (0.9, 1.312)$ for the LJ system using SF cutoff for different values of the *skin* parameter. The choice of the optimal *skin* for a given system at a given state point can seriously improve the performances of an MD code as discussed in Refs. [153, 154].

A.1.2 Cutoff methods and energy conservation

This MD program allows one to chose between two different cutoff methods: shifted force (SF) [152] and shifted potential (SP). The shifted potential (SP) method is commonly used in molecular dynamics simulation codes and it consists in setting the potential to zero when the distance between two particles is larger than the chosen cutoff. This cutoff method introduces a discontinuity in the force. The shifted force (SF) method sets the force to zero for distances larger than the cutoff and smoothly shifts the potential in order to avoid discontinuity. In a recent work, Toxvaerd and Dyre [152] have shown that using SF cutoff it is possible to obtain a better scaling between energy fluctuation in the NVE ensemble and timestep than when using SP. The ideal scaling is given by $\log(\Delta E) \propto 2 \cdot \log(h)$ and in Fig. A.3 (a) it is verified that MD code presented here can reproduce this ideal scaling when using SF. In Fig. A.2 (a) the total mechanical energy E is shown as function of time for an NVE simulation. Only small drift in the total energy can be observed on a simulation of $2 \cdot 10^6$ timesteps.

Another advantage of SF is that it is possible to reproduce the correct structural and dynamical quantities using a smaller value for the cutoff than the one needed in the case of SP [152]. This feature can be useful when simulating dense systems, where the number of neighboring particles is high.
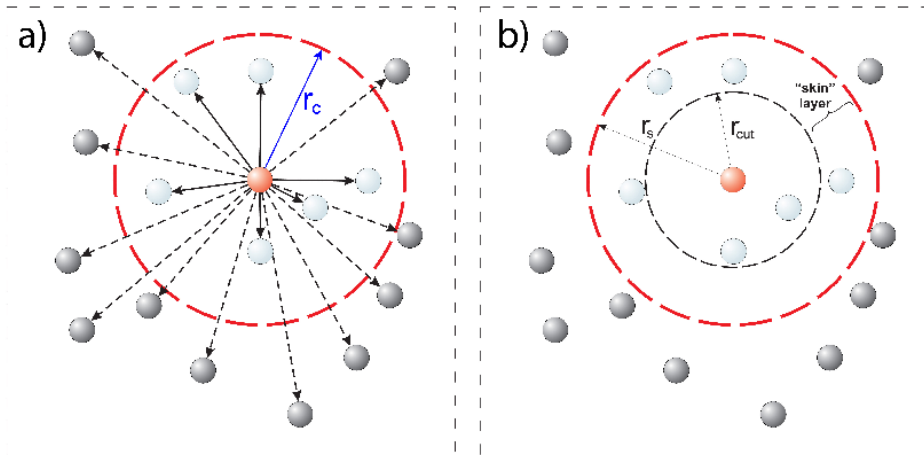
Figure A.4: (a) representation of force calculation is performed in a program using neighborlist. The force acting on the red particle is calculated summing all the forces if the neighborlist is absent even though only particles closer than the cutoff radius r_c give a contribution to the total force. The use of a neighborlist allows one to restrict the force calculation to the particles which are not much farther away that r_c. (b) representation of the *skin* parameter. When the neighborlist is built all particles inside a sphere of radius $r_c + skin$ are recorded. If the skin is chosen to be zero, the neighborlist needs to be updated at each timestep because particles that where closer than r_c could have moved away and vice-versa with particles farther away than r_c. In this case the neighborlist will not produce any improvement on the code performances. When the *skin* is not zero, all the particles in the sphere of radius $r_c + skin$ are taken into account in the force calculation. The force calculation will require $N * Nb$ calculations as maximum if we indicate with Nb the maximum number of neighbors. In order to ensure that at every timestep all the particles closer than r_c are taken into account in the force calculation, the neighborlist is updated every time than one particle travel more than $0.5skin$ from the position at which it was when the neighborlist was built the last time. This figures has been taken from Ref. [155].

A.1.3   Neighborlist

When simulating system with a large number of particles interacting via short range potentials, it is convenient to use a neighborlist [31] in order to avoid performing useless force calculation between particles which are far enough to be weakly interacting or not interacting at all if the distance between the particles is longer than the cutoff. A neighborlist is an array of integers which registers the neighbors of every particle. When using a neighborlist, the loop for force calculation only takes into account the neighbors of a given particle. If the maximum number of neighbors is Nb the force calculation will need $N \cdot Nb$ pairwise distances instead of N^2. The introduction of a neighborlist can significantly improve the performances for big system sizes. The two parameters which determine how the neighborlist is built and how it is updated are the potential *cutoff* and the *skin*. This

two parameters are represented in Fig. A.4. The *cutoff* has already been described in Sec. A.1.2. The *skin* is the parameter that determines how often the neighborlist is updated. A smaller skin it will imply a more frequent update of the neighborlist but at the same time a smaller number of neighbors. The neighborlist is built recording, for each particle, all the neighbors defined as the particles at distance not larger than $r_c + skin$ and it is updated when a particle moves more that half *skin* from the position where it was when the neighborlist was built the last time. The importance of the *skin* parameter can be understood from Fig. A.3 (b), where the time needed to simulate 10000 timesteps for a LJ system in 3d at the state point $(\rho, T) = (0.9, 1.312)$ is plotted as a function of the chosen *skin*. As pointed out in Refs. [153, 154], the choice of the optimal skin can be crucial in order to obtain reasonable simulation times when working with big system sizes.

In order to optimize the performance of the MD code, the neighborlist is calculated in parallel on CPUs using the OpenMP environment [150].

A.2 Comparison with RUMD on structure and dynamics

The MD code discussed in this appendix has been tested against RUMD [38]. In Fig. A.5 the structure, probed by the radial distribution function (RDF), and the dynamics, probed by the mean-squared displacement (MSD), of the LJ system at the state point $(\rho, T) = (0.9, 1.312)$ in 3d are shown. The black lines have been obtained from an NVT simulation with the MD code. The RDF is calculated using the $myMD\_rdf$ tool available at `http://dirac.ruc.dk/~lorenzoc/` while the MSD is calculated using $rumd\_msd$ tool, after converting the output in RUMD format. The red lines have been obtained from an NVT simulation with RUMD and using the standard RUMD tools for calculation of RDF and MSD. The results from the two codes are in perfect agreement.
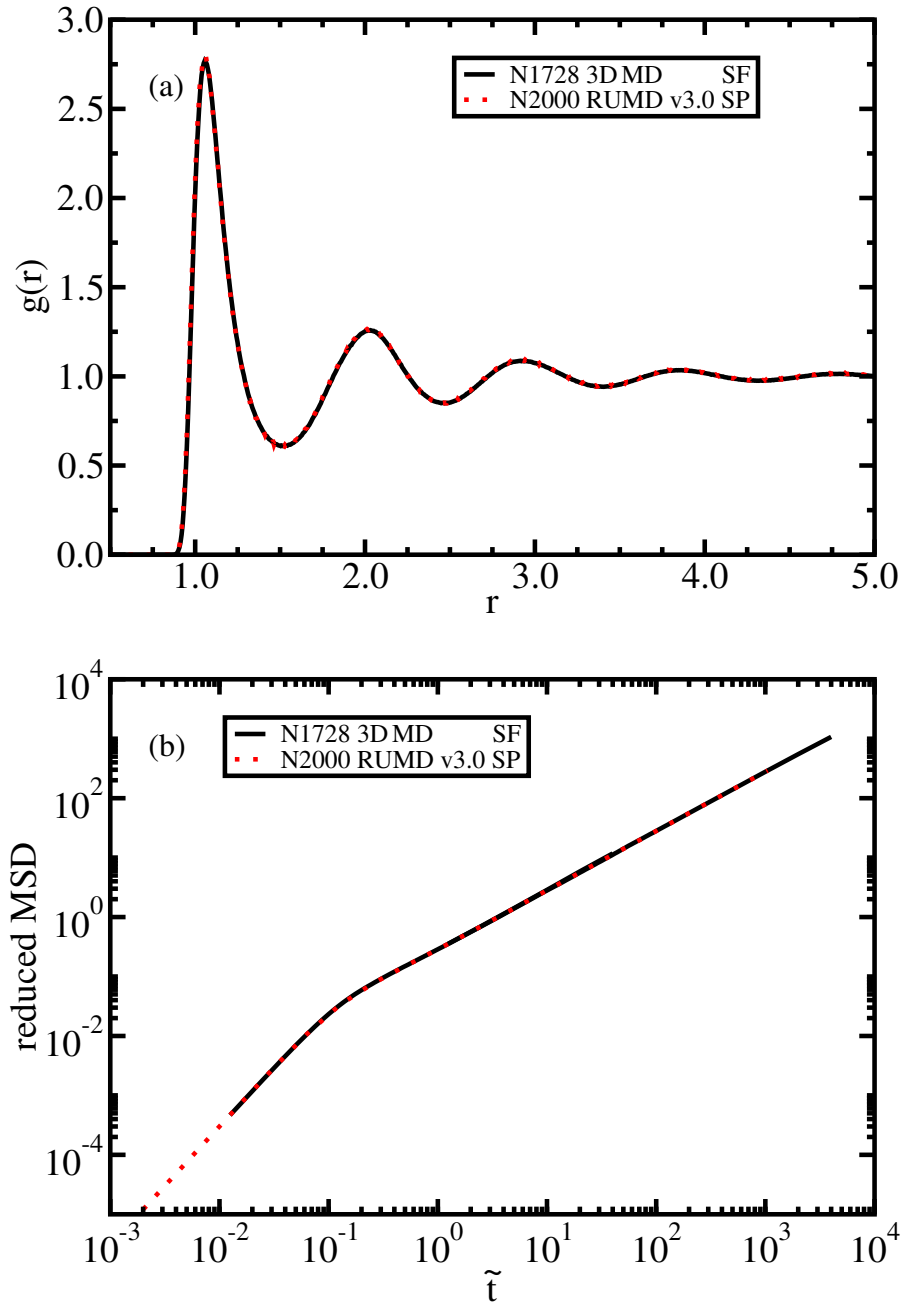
Figure A.5: Structure and dynamics of the LJ system at the state point $(\rho, T) = (0.9, 1.312)$ in 3d. Results from the MD code described in this appendix are compared with RUMD [38]; SF and SP indicate if shifted force (SF) [152] either shifted potential (SP) cutoff is used for the interaction potential. (a) Radial distribution function (RDF) $g(r)$ (b) Reduced mean-squared displacement (MSD), i.e., expressed in reduced units as defined in Ref. [52].

Appendix B

Additions to RUMD: NPT integrator

In this appendix the atomic NPT integrator implemented by the author together with Ulf R. Pedersen in the RUMD code is described. The implementation of the NPT integrator is base on Ref. [156]. The simulation data presented have been obtained by the author using RUMD [38].

One of the fundamental classes in the RUMD program structure is the integrator class. This class is responsible for the integration of the equations of motion. The NPT integrator is an implementation of the integrator class that allows the program to integrate the equations of motion coupled with a thermostat and a barostat, correspondingly necessary to keep temperature T and pressure P constantly equal to the desired values. The implementation scheme used for the NPT integrator is a variation of the scheme proposed in Ref. [156] and it was developed together with Ulf R. Pedersen. The difference between the two schemes is the way the equations of motion are discretized: Martyna *et al* [156] used a velocity Verlet algorithm, while the scheme we implemented uses a Leap-Frog algorithm consistently with the other integrators in RUMD. For the differences and analogies between the NVE implementation of velocity Verlet and Leap-Frog algorithms see Chap. 1.

At every timestep the positions and velocities of every particles are updated. Kinetic energy and virial are calculated and used to keep track of temperature and pressure. No long range corrections are used for calculating the pressure.

The integrator is written in C++ CUDA which is an environment for C++ which allows one to parallelize on Nvidia graphic cards (GPUs). All RUMD integrators are parallelized in CUDA.

B.1 NPT Leap-Frog: the equations of motion

The equation of motion proposed in Ref. [156] are:

Equations of motion

$$\dot{\mathbf{r}}_i = \frac{\dot{\mathbf{p}}_i}{m_i} + \frac{p_\epsilon}{W}\mathbf{r}_i \tag{B.1}$$

$$\dot{\mathbf{p}}_i = \mathbf{F}_i - \left(1 + \frac{d}{N_f}\right)\frac{p_\epsilon}{W}\mathbf{p}_i - \frac{p_\eta}{Q}\mathbf{p}_i \tag{B.2}$$

Barostat and thermostat state

$$\dot{p}_\epsilon = Vd(P_{\text{int}} - P_{\text{ext}}) + \frac{d}{N_f}\sum_{i=1}^{N}\frac{\mathbf{p}_i^2}{m_i} - \frac{p_\epsilon}{Q}p_\eta \tag{B.3}$$

$$\dot{p}_\eta = \frac{p_\epsilon^2}{W} - (N_f + 1)k_BT + \sum_{i=1}^{N}\frac{\mathbf{p}_i^2}{m_i} \tag{B.4}$$

It has been proved that these equations reproduce the NPT ensemble with respect to both mean values and fluctuations [156]. The volume change at every timestep is calculated from:

$$\dot{V} = Vd\frac{p_\epsilon}{W} \tag{B.5}$$

The equations for Leap-Frog NPT integrator are obtained by discretization of the equations of motion respect to time in analogy with what done in Sec. 1.2.2 for the NVT integrator. The discretized equations are:

Equations of motion

$$\mathbf{p}_i(t + h/2) = \frac{1}{1 + A}\{h\dot{\mathbf{F}}_i(t) + \mathbf{p}_i(t - h/2)[1 - A]\} \tag{B.6}$$

$$A = \frac{h}{2}\left[\left(1 + \frac{d}{N_f}\right)\frac{p_\epsilon(t)}{W} + \frac{p_\eta(t)}{Q}\right]$$

$$\mathbf{r}_i(t + h) = \frac{h}{m_i}\mathbf{p}_i(t + h/2) + \left[1 + \frac{p_\epsilon(t)}{W}\right]\mathbf{r}_i(t) \tag{B.7}$$

Barostat and thermostat states

$$p_\eta(t + h) = p_\eta(t) + h\left[2K(t) + \frac{p_\epsilon^2(t)}{W} - (N_f + 1)k_bT\right] \tag{B.8}$$

$$p_\epsilon(t + h) = hVd(P_{int} - P_{ext}) + \frac{hd}{2N_f}K(t) + p_\epsilon\left[1 - h\frac{p_\eta(t)}{Q}\right] \tag{B.9}$$

Volume change

$$V(t + h) = V(t)\left[1 + hd\frac{p_\epsilon}{W}\right] \tag{B.10}$$

τ_p	T	p	V	ΔV	c_p^{ex}
5	2.000	4.700	5304.506	23.431	3.036
20	2.000	4.700	5303.084	23.939	3.106
50	2.000	4.700	5303.141	23.694	3.069
200	1.998	4.699	5303.035	44.676	7.665
500	1.986	4.688	5302.351	129.40	56.84

Table B.1: Mean values of the temperature T, the pressure p, the volume V, the volume fluctuations and excess specific heat at constant pressure per particle c_p^{ex} for the LJ system are shown for different choices of the barostat relaxation time τ_p at the state point $(T, p) = (2.0, 4.7)$. The values indicated in the table for temperature T and pressure p are the mean values measured for input parameters $(T, p) = (2.0, 4.7)$. The data clearly shows that at this state point a good choice of the τ_p is a value in the range $[20, 50]$. The data for c_p^{ex} and ΔV strongly depend on the τ_p if the latter value is not well chosen.

These equations of motion have a similar structure of the ones for NVT dynamics derived in Chap. 1 but, while in NVT dynamics only the velocities are rescaled, in this case the positions are scaled too in order to be consistent with the volume scaling in Eq. B.5.

B.2   Tests on NPT implementation

The implementation of the NPT integrator have been checked in two ways. The first test is the stability against changes of the barostat relaxation time; this test it is needed in order to understand in which range of values of the relaxation time the integrator reproduces the expected thermodynamic ensemble. The second test is a consistency check between the value for the excess specific heat at constant pressure obtained from enthalpy fluctuations and the value obtained from the derivative of the enthalpy along an isobar.

Stability vs changes of the barostat relaxation time

The barostat relaxation time is the parameter that regulates how strongly the barostat is coupled with the equations of motion. As shown in Eqs. B.6 and B.7, the correction to the position and velocity of each particle due to the presence of the barostat are related to this parameter. If the coupling is too strong the simulation could produce unrealistic results, while if the coupling is too weak the barostat is not able to keep the pressure constant. It is therefore important to be aware of which is the range of values of the barostat relaxation time that ensures a correct NPT dynamics. This range of values is, in general, dependent on the interaction potential chosen and

therefore no default value for the relaxation time of the barostat has been chosen for the NPT integrator in RUMD. The user must choose the barostat (and the thermostat) relaxation time when the NPT integrator is associated with the simulation object in RUMD.

In Table B.1 the mean values of the temperature T, the pressure p, the volume V, the volume fluctuations and excess specific heat at constant pressure per particle c_p^{ex} are shown for different choices of the barostat relaxation time τ_p at the state point $(T, p) = (2.0, 4.7)$. The system we simulated is the Lennard-Jones system which is in the liquid phase at the chosen state point. The number of particles is $N = 4096$ and the potential cutoff is 2.5σ. The thermostat relaxation time for these simulations is fixed to $\tau_{Th} = 0.4$

Excess specific heat at constant pressure

At the same state point $(T, p) = (2.0, 4.7)$, the excess specific heat at constant pressure per particle c_p^{ex} is evaluated from the derivative of the enthalpy with respect to temperature at constant pressure. Two new simulations are performed at the state points $(T, p) = (1.9, 4.7)$ and $(T, p) = (2.1, 4.7)$ and c_p^{ex} is found using a linear regression. The value of c_p^{ex} so obtained is $c_p^{\text{ex}} = 2.965$ consistently with the values from Table B.1 when τ_p is chosen in the range $[20, 50]$.

Appendix C

Simulation details

This appendix describes how the simulation data presented in this thesis have been obtained by the author. The program used to perform the simulations is specified together with the relevant parameters to reproduce the simulations.

C.1 NVT simulations of the LJ system and the generalized LJ system

The NVT simulations presented in Chaps. 2, 3 and 4 have been performed using RUMD [38]. The system size used for these simulations is $N = 1000$. The cutoff for the LJ potential was 2.5σ (shifted potential) and the LJ parameters (σ, ϵ) were both set to unity.

The timestep t used for each simulated state point (ρ, T) was chosen keeping the reduced timestep $\tilde{t} = \rho^{1/3}(k_B T/m)^{1/2} t = 0.001$ constant. At each state point the system was equilibrated for $2 \cdot 10^6$ timesteps starting from an FCC crystal configuration and the data runs were of $5 \cdot 10^8$ timesteps. The simulations used to find the scaling exponent γ at the state point $(\rho, T) = (1.0635, 2.0)$ and $(\rho, T) = (1.132, 2.0)$ were $5 \cdot 10^9$ timesteps long in order to reduce the statistical error on γ. These state points have been used in Chap. 3 to determine the freezing and melting isomorphs.

The NVT integrator in RUMD utilizes a Nosé-Hoover thermostat. The relaxation time of the thermostat τ_{Th} was left equal to the default RUMD value ($\tau_{Th} = 0.2$) for the simulations in the liquid state. For the simulations of FCC crystals along the melting line, τ_{Th} was scaled in order to keep its reduced value constantly equal to $\tilde{\tau}_{Th} = 0.2$. This is equivalent to the use of a τ_{Th} which corresponds to a fixed number of timesteps.
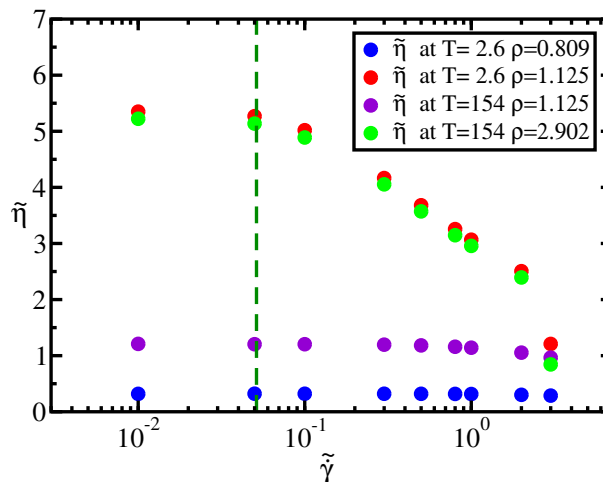
Figure C.1: Measured reduced viscosity from equation C.1 at different reduced strain rates. Two of the four state points (green and red dots) are on the same isomorph (the freezing isomorph of Chap. 3) and their behavior in reduced unit is the same. As a consequence, the reduced strain rate at which reduced viscosity start to be strain rate dependent is isomorphic invariant, consistent with results from Separdar *et al* [157]. The blue (violet) dots are results of simulations at state points along the same isochore (isotherm) of $(\rho, T) = (1.125, 2.6)$. The behavior of reduced viscosity as function of strain rate is strongly modified by changing density or temperature if the chosen state points are not isomorphic.

C.2 SLLOD simulations of the LJ system and of the IPL12 system

The SLLOD simulations [105–107] presented in Chaps. 2, 3 and 4 have been performed using RUMD [38]. As in the case of NVT simulations the system size was $N = 1000$, the potential cutoff was 2.5σ (shifted potential) and the LJ parameters were set to unity. The reduced timestep for these simulations was kept constantly equal to $\tilde{t} = 0.001$. At each state point (ρ, T) the system was equilibrated for $2 \cdot 10^6$ timesteps and the data runs were of $5 \cdot 10^8$ timesteps. Only for the simulations presented in Sec. 3.2, the cutoff of the potential was 6.0σ and the system size was $N = 4096$. The temperature in a SLLOD simulation is kept constant by rescaling the velocities and not by using a Nosé-Hoover thermostat; no thermostat relaxation time is therefore involved.

In the two following sections how to obtain the viscosity from a SLLOD simulation (which is an extended version of the appendix of Ref. [83], see appendix D) is described and the tests performed on the high temperature data in Chap. 4 are presented.

C.2.1 Determining the zero-strain rate bulk viscosity from a SLLOD simulations

A SLLOD simulation[105–107] is a molecular dynamics simulation performed by shearing the simulation box with constant speed. Between the bottom part of the box and the top part there is a relative shearing motion with strain rate $\dot{\gamma} = \frac{\partial u_x}{\partial y}$, where u_x is the streaming velocity at ordinate y when the box is sheared in the x direction. Under low strain-rate conditions, this kind of simulation reproduces an ordinary, laminar Couette flow and the linear, shear-rate-independent, bulk viscosity can be calculated from the stress tensor σ_{ij} through the equation

$$\eta = \frac{\sigma_{xy}}{\dot{\gamma}}. \tag{C.1}$$

Equation (C.1) holds only when the viscosity is independent of strain rate, i.e., at a sufficiently small shear rate. As shown by Separdar *et al* [157] the strain rate $\dot{\gamma}$ for which the measured viscosity starts to be strain-rate dependent is isomorph invariant when given in reduced units.

The behavior of the reduced viscosity $\tilde{\eta}$ as a function of the reduced strain rate $\tilde{\dot{\gamma}}$ is shown in Fig. C.1. When the two considered state points are on the same isomorph, they exhibit the same shear-thinning behavior in reduced units; this is not true if we move along an isochore or along an isotherm. The dotted green line in Fig. C.1 marks the reduced strain rate used for the simulations along the freezing line reported in Chap. 3.

If two simulations are performed at different temperatures along the same isochore, as the simulations in Chap. 4, a strain rate in the linear region for the simulation at the lowest temperature, when used for the simulation at the highest temperature, ensures that the system satisfies the shear-rate-independent condition also at the highest temperature. This can be understood from Fig. C.1 when comparing the data at $(\rho, T) = (1.125, 2.6)$ and at $(\rho, T) = (1.125, 154)$. When temperature is increased along an isochore, the shear-thinning behavior in reduced units 'moves' toward higher strain rates. For this reason the strain rate used at the lowest studied temperature along an isochore, can be used at any higher temperature along the same isochore.

C.2.2 High temperature simulations presented in Chap. 4

These tests were made to verify whether the plateau of reduced viscosity discussed in Chap. 4 is a real physical phenomenon or an artifact of the simulation due to numerical instabilities due to precision issues. We verified that the shear-thinning behavior in reduced units at the state points $(\rho, T) = (1.09, 482.17)$ and $(\rho, T) = (1.09, 1000)$ is the same using the single precision version of RUMD, the double precision version of RUMD and performing the
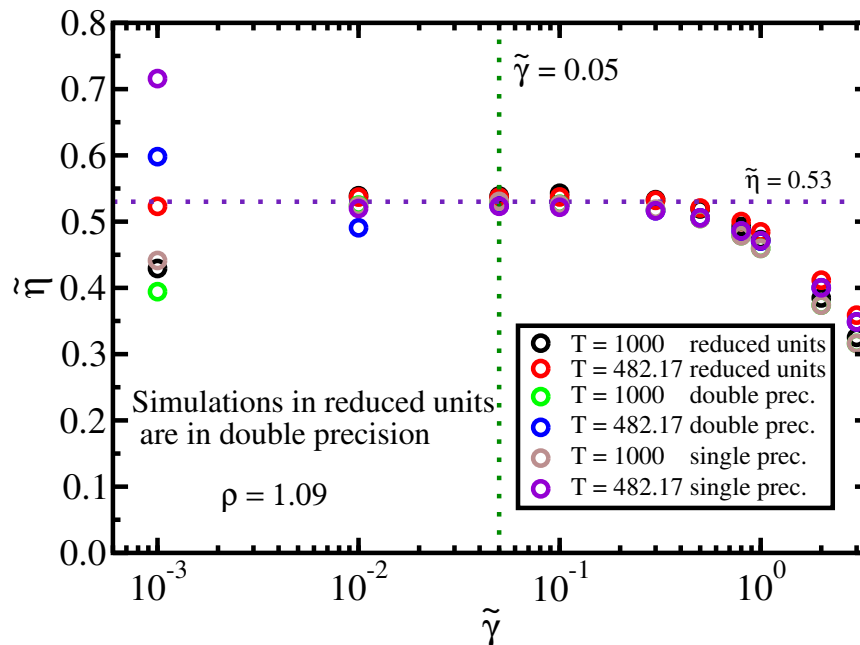
Figure C.2: Shear-thinning behavior in reduced units at the state points $(\rho, T) = (1.09, 482.17)$ and $(\rho, T) = (1.09, 1000)$. At each state point three different simulations are performed: (a) a SLLOD simulations using RUMD; (b) a SLLOD simulation using the double precision version of RUMD; (c) a SLLOD simulation in reduced units (see text) using the double precision version of RUMD. Except at the two lowest strain rates, where the results are not reliable due to precision problems, the shear-thinning curves collapse onto a single one, showing that the three different simulations give the same value of reduced viscosity $\tilde{\eta} \approx 0.53$. The fact that at the two temperatures along the same isochore the reduced viscosity is the same, is a confirmation that the viscosity exhibits a plateau at high temperatures as discussed in Chap. 4.

simulation in reduced units with the double precision code. A simulation in reduced units is accomplished by changing the potential parameters instead of changing the thermostat temperature and the simulation box size. For example, a simulation of the state point $(\rho, T) = (0.027, 0.5)$ of a system of LJ particles with potential parameters $(\sigma, \epsilon) = (1.0, 1.0)$ is equivalent to a simulation in reduced units in which $(\rho, T) = (1.0, 1.0)$ and $(\sigma, \epsilon) = (\rho^{1/3}, 1/T) = (0.3, 2.0)$. All these different tests give compatible results.

In Fig. C.2 the shear-thinning behavior in reduced unit at the two state points is compared. The results for the reduced viscosity of the two state points confirm that at high temperature the reduced viscosity does not depend on temperature. The use of the three different kinds of simulations previously described at the each state point ensures that the results for reduced viscosity are reliable. In Table C.1 the results for reduced viscosity

$\tilde{t}$	$precision$	$\tilde{\eta}(T = 482.17)$	$\tilde{\eta}(T = 1000)$
0.0050	$single$	0.5234	0.5255
0.0050	$double$	0.5232	0.5308
0.0010	$single$	0.5212	0.5335
0.0010	$double$	0.5248	0.5271
0.0005	$single$	0.5201	0.5322
0.0005	$double$	0.5298	0.5277
0.0001	$single$	0.6065	0.6317
0.0001	$double$	0.5073	0.5245

Table C.1: Reduced viscosity at the state points $(\rho, T) = (1.09, 482.17)$ and $(\rho, T) = (1.09, 1000)$. In this table the results for reduced viscosity obtained from simulations with different reduced timestep $\tilde{t}$ at the two state points are compared. For each timestep two simulations were performed, one using the single precision version of RUMD and one using the double precision version of RUMD. The values of reduced viscosity obtained are independent of the chosen timestep and the results in single and double precision are consistent. The only case in which the data significantly differs is for the choice of $\tilde{t} = 0.0001$ while using the single precision code. In this case the discrepancy is due to the choice of a too small timestep for a single precision code.

obtained from the single precision version of RUMD are compared with the ones from the double precision version. For the calculation of the reduced viscosities in Table C.1, the same stain rate $\tilde{\dot{\gamma}}$ is used. For each state point four simulations, using different reduced timesteps $\tilde{t}$, performed using both RUMD versions (single and double precision) are compared. There are no significant differences between the values of reduced viscosity. The only exception is the case in which the reduced timestep $\tilde{t} = 0.0001$ is employed in the single precision version of RUMD, but in this case the discrepancy is related to the use of single precision as it can be understood from the fact that the double precision version at the same reduced timestep gives values consistent with the other ones.

C.3 NVT simulations with the homemade MD code in 2d, 3d and 4d

In the case of the NVT simulations with the homemade MD code described in appendix A, the system size was changed when changing the number of dimensions d. In all cases the system was large enough to ensure the half box length being larger than the cutoff radius of the LJ potential which was 2.5σ in all cases. The shifted force cutoff method [152] has been used for these simulations. For simulations in 2d $N = 1225$ particles were used, for simulations in 3d $N = 1728$ and for simulations in 4d with $N = 2401$. The timestep for all simulations was $t = 0.001$ and the simulations were $2 \cdot 10^7$ timesteps long. Each simulation was first equilibrated for 10^6 timesteps. Only in the case of the 2d crystals the timestep was $t = 0.0005$ and the simulation time $4 \cdot 10^7$ timesteps. The input for the relaxation time of the thermostat was 80, i.e. the thermostat relaxation time was equal to 80 timesteps (for details see appendix A). The starting configurations were produced using the program *Nd_start_conf* as described in appendix A.

C.4 NVT simulations of the Gaussian core system

For the NVT simulations of the Gaussian core system $N = 4096$ particles were used. The cutoff used was 5σ (shifted potential) and the reduced timestep $\tilde{t} = 0.025$. These same cutoff has been used by Ikeda and Miyazaki in Ref. [25, 140]. The potential parameters (ϵ, σ) were set to unity. The starting configurations (FCC crystals) were equilibrated for $5 \cdot 10^6$ timesteps and the data run were $5 \cdot 10^7$ timesteps long. The relaxation time was kept fixed in reduced units. The relaxation time at the state point $(\rho, T) = (0.05, 0.002)$ was $\tau_{Th} = 15.0$.

Appendix D

Reprints of articles

Freezing and melting line invariants of the Lennard-Jones system

Lorenzo Costigliola,* Thomas B. Schrøder and Jeppe C. Dyre

The invariance of several structural and dynamical properties of the Lennard-Jones (LJ) system along the freezing and melting lines is interpreted in terms of isomorph theory. First the freezing/melting lines of the LJ system are shown to be approximated by isomorphs. Then we show that the invariants observed along the freezing and melting isomorphs are also observed on other isomorphs in the liquid and crystalline phases. The structure is probed by the radial distribution function and the structure factor and dynamics are probed by the mean-square displacement, the intermediate scattering function, and the shear viscosity. Studying these properties with reference to isomorph theory explains why the known single-phase melting criteria hold, *e.g.*, the Hansen–Verlet and the Lindemann criteria, and why the Andrade equation for the viscosity at freezing applies, *e.g.*, for most liquid metals. Our conclusion is that these empirical rules and invariants can all be understood from isomorph theory and that the invariants are not peculiar to the freezing and melting lines, but hold along all isomorphs.

1 Introduction

The phase transition from liquid to crystal and *vice versa* is not yet completely understood.[1–3] Reasons for searching for a better understanding of freezing/melting invariants are many. One is the possibility of using freezing/melting invariance to evaluate specific system properties under conditions not easily accessible by experiments. An example could be the estimation of liquid iron's viscosity under Earth-core pressure and temperature conditions, a quantity that is necessary for developing reliable geophysical models for the core.[4–6]

In this work several freezing line and melting line invariants, both structural and dynamical, of the Lennard-Jones (LJ) system[7] are derived from isomorph theory[8] and validated in computer simulations. The existence of invariances along isomorphs is used to explain the Hansen–Verlet and Lindemann freezing/melting criteria as well as the Andrade equation for the freezing viscosity for the LJ system.

Many theories have been proposed to explain freezing and melting[9,10] and why certain quantities are often invariant along the freezing and melting lines. Examples of such invariants are the excess entropy, the constant-volume entropy difference between liquids and solids on melting,[11–13] the height of the first peak of the static structure factor on freezing (the Hansen–Verlet freezing criterion[14,15]), and the viscosity of liquid metals on freezing when made appropriately dimensionless.[16–18] The Lindemann[19,20] melting criterion states that a crystal melts

when the mean vibrational displacement of atoms from their lattice position exceeds 0.1 of the mean inter-atomic distance, independent of the pressure. This is equivalent to the invariance of $\langle u^2 \rangle / r_m{}^2$ along the melting line,[20] where $\langle u^2 \rangle$ is the atomic root-mean-squared vibrational amplitude and r_m is the nearest neighbor distance. The most common approaches for explaining such invariants attempt to connect them to the kinetics of the freezing/melting process. For instance, going back to Born it has been suggested that a crystal becomes mechanically unstable when $\langle u^2 \rangle / r_m{}^2$ exceeds a certain number.[9] From this perspective, it is not easy to understand why these invariants do not hold for all systems. It is also difficult to understand why related invariants hold for specific curves in the liquid state. Thus, in an extension of what happens along the melting line of, *e.g.*, the Lennard-Jones system, the radial distribution function is invariant along the curves at which the excess entropy S_{ex} is equal to the two-body entropy S_2.[21] Diffusivity is also constant, in appropriate units, along constant S_{ex} curves,[22] implying (from the Stokes–Einstein relation) an invariance of the viscosity in appropriate units along these curves. This relationship between viscosity and excess entropy was recently confirmed by high-pressure measurements.[23]

A possible explanation for the invariants along the freezing and melting lines, as well as along other well-defined curves in the thermodynamic phase diagram, is given by isomorph theory.[8,24–26] According to it[27] a large class of liquids exists for which structure and dynamics are invariant to a good approximation along the constant–excess–entropy curves. These curves are termed isomorphs, and the liquids which conform to isomorph theory are now called Roskilde-simple (*R*) liquids[27–32] (the original name "strongly correlating" caused confusion due to the existence

"Glass and Time", IMFUFA, Department of Sciences, Roskilde University, Postbox 260, DK-4000 Roskilde, Denmark. E-mail: lorenzo.costigliola@gmail.com

14678 | *Phys. Chem. Chem. Phys.*, 2016, **18**, 14678–14690

This journal is © the Owner Societies 2016

of strongly correlated quantum systems). Liquids belonging to this class are easily identified in computer simulations because they exhibit strong correlations between their thermal-equilibrium fluctuations of virial and potential energy in the NVT ensemble.[24,33] Isomorph theory not only offers the possibility of explaining the freezing/melting invariants without reference to the actual mechanisms of the freezing/melting process itself, but by evaluating the virial potential-energy correlation coefficient also provides a way to predict whether these invariants hold for a given liquid.

The main features of isomorph theory are summarized in Section 2 where how to identify the isomorphs of the LJ system is also shown. This is followed by a short section describing technical details of the simulations performed. The isomorph equations are used in Section 4 to show that the freezing line can be approximated by an isomorph, termed the freezing isomorph, without the need for any fitting. Section 5 deals with freezing invariants, the Hansen–Verlet criterion,[14,15] and Andrade's freezing viscosity equation;[16–18] Section 6 focuses on melting line invariants of the FCC LJ crystal and their connection with the Lindemann criterion.[19] The last section discusses the differences between isomorph theory and other approaches used to describe liquid invariances in the past years and summarizes the main results of this work.

2 Isomorphs

An R system is characterized by strong correlations between virial and potential energy equilibrium fluctuations in the NVT ensemble,[24,33] *i.e.*, by a virial potential-energy equilibrium correlation coefficient $R(\rho,T)$ greater than 0.9:

$$R(\rho, T) = \frac{\langle \Delta W \Delta U \rangle}{\sqrt{\langle (\Delta W)^2 \rangle \langle (\Delta U)^2 \rangle}} > 0.9. \tag{1}$$

Here Δ denotes the instantaneous deviations from the equilibrium mean value, the brackets denote NVT ensemble averages, W denotes the virial, U denotes the internal energy and (ρ,T) denotes the density and temperature of the system. When such strong correlations are present, the theory predicts the existence of curves in the thermodynamic phase diagram along which several structural, dynamical, and thermodynamical properties are invariant[8,24,33–35] when expressed in reduced units; these curves are termed isomorphs.[8]

Reduced quantities (marked by a tilde) are defined as follows. Distances are measured in units of $\rho^{-1/3}$, energies in units of $k_B T$, and time in units of $m^{1/2}(k_B T)^{-1/2}\rho^{-1/3}$, where m is the average particle mass (for Brownian dynamics, a different time unit applies[8]). These reduced units should not be confused with the so-called Lennard-Jones (LJ) units. We use the latter units below for reporting quantities like temperature and density.

By definition an isomorph has the following property: for any two configurations, $\mathbf{R}_1 \equiv (\mathbf{r}_1^{(1)},\ldots,\mathbf{r}_N^{(1)})$ and $\mathbf{R}_2 \equiv (\mathbf{r}_1^{(2)},\ldots,\mathbf{r}_N^{(2)})$

$$\rho_1^{1/3}\mathbf{R}_1 = \rho_2^{1/3}\mathbf{R}_2 \Rightarrow P(\mathbf{R}_1) = P(\mathbf{R}_2) \tag{2}$$

where $\mathbf{r}_i$ is the position vector of particle i, N is the number of particles and $P(\mathbf{R}_i)$ is the Boltzmann statistical weight of configuration $\mathbf{R}_i$ at the relevant thermodynamic state point on the isomorph.[24] In other words, configurations that are identical in reduced units ($\tilde{\mathbf{R}} \equiv \rho^{1/3}\mathbf{R}$) have proportional Boltzmann factors.

The isomorph theory is exact only for systems with an Euler-homogeneous potential energy function, for instance, inverse-power-law (IPL) pair-potential systems.[24,33] However, the theory can be used as a good approximation for a wide class of systems. Examples of models that are R liquids[27] in part of their thermodynamic phase diagram, in liquid and solid states,[26] are the standard and generalized Lennard-Jones systems (single-component as well as multi-component),[8,35,36] systems interacting *via* the exponential pair potential,[37] and systems interacting *via* the Yukawa potential.[28,38] R systems also include some molecular systems like, *e.g.*, the asymmetric dumbbell models,[39] Lewis–Wahnström's three-site model of OTP,[39] the seven-site united-atom model of toluene,[24] the EMT model of liquid Cu[24] and the rigid-bond Lennard-Jones chain model.[40] Predictions of isomorph theory have been shown to hold for experiments on glass-forming van der Waals liquids by Gundermann *et al.*,[41] Roed *et al.*,[42] and Xiao *et al.*[43] Power-law density scaling,[44] which is often observed in experiments on viscous liquids, can be explained by isomorph theory.[36]

Isomorphic scaling, *i.e.*, the invariance along isomorphs of many reduced quantities derived from the identical statistical weight of scaled configurations[8] does not hold for all reduced quantities. For example, the reduced-unit free energy and pressure are not invariant, whereas the excess entropy, reduced structure, and reduced dynamics are all isomorph invariant.[8] These invariances follow from the invariance along isomorphs of Newtonian and Brownian equations of motion in reduced units for R liquids.[8]

For an R system at a given reference state point (ρ_0,T_0), it is possible to build an isomorph starting from that point.[8] For R systems, a function $h(\rho)$ exists which relates the state point (ρ_0,T_0) to any other state point (ρ,T) along the same isomorph[25,36] by the identity:

$$\frac{h(\rho)}{T} = \frac{h(\rho_0)}{T_0}. \tag{3}$$

The functional form of $h(\rho)$ depends on the interaction potential, and only for simple systems it is possible to find an analytical expression. As shown by Ingebrigtsen *et al.*[25] and Bøhling *et al.*,[36] if the pair potential is a sum of inverse-power laws involving the exponents n_i ($i = 1,\ldots,N$), $h(\rho)$ can be expressed in the following way:

$$h(\rho) = \sum_{i=1}^{N} \alpha_i \left(\frac{\rho}{\rho_0}\right)^{n_i/3}. \tag{4}$$

For a LJ system, the pair potential is the well-known

$$v(r) = 4\varepsilon\left((r/\sigma)^{-12} - (r/\sigma)^{-6}\right) \tag{5}$$

This journal is © the Owner Societies 2016

Phys. Chem. Chem. Phys., 2016, **18**, 14678–14690 | **14679**

where only two IPL exponents, 12 and 6, are involved. It is not difficult to show that[25,36] for the LJ system, $h(\rho)$ is given by

$$h(\rho) = \left(\frac{\gamma_0}{2} - 1\right)\left(\frac{\rho}{\rho_0}\right)^4 - \left(\frac{\gamma_0}{2} - 2\right)\left(\frac{\rho}{\rho_0}\right)^2 \qquad (6)$$

where γ_0 is the so-called density-scaling exponent at the reference state point defined by the canonical averages

$$\gamma_0(\rho_0, T_0) = \frac{\langle \Delta W \Delta U \rangle}{\langle (\Delta U)^2 \rangle}\bigg|_{(\rho_0, T_0)}. \qquad (7)$$

Eqn (6) is easily derived from applying $\gamma = \mathrm{d}\ln h/\mathrm{d}\ln\rho$[25] at the reference state point to eqn (4), adopting the normalization $h(\rho) = 1$. The correlation coefficient R of the LJ system increases with increasing temperature and increasing density;[24] this means that if the LJ system is an R liquid at the reference state point (ρ_0, T_0), it will be strongly correlating also at higher densities on the isomorph through (ρ_0, T_0).

Recently isomorph theory has been reformulated starting from the assumption that for any couple of configurations of R systems, the potential energies obey the relation

$$U(\mathbf{R}_1) < U(\mathbf{R}_2) \Rightarrow U(\lambda\mathbf{R}_1) < U(\lambda\mathbf{R}_2) \qquad (8)$$

when the configurations are scaled to a different density.[29] All the results described in this section can be derived from this simple scaling rule. The predictions of the new isomorph theory are close to those of the old one, which is used below.

3 Simulation details

This work presents the results of molecular dynamics simulations of a single-component LJ system performed using the GPU code RUMD.[45] For each liquid state point an *NVT* simulation was used to obtain the structure and dynamics, while a SLLOD simulation[46–48] was used to find the viscosity. The simulations were carried out using a shifted-potential cutoff at 2.5σ. In the simulations the LJ parameters were set to unity, *i.e.*, $\sigma = 1.0$ and $\varepsilon = 1.0$. The time step was adjusted with increasing temperature along an isomorph to keep the reduced time step constant, equal to 0.001 for all simulations. For instance, the time step is 0.001 in LJ units for a simulation at $\rho = 1.0$ and $T = 1.0$. At every state point the system was simulated for 5×10^8 timesteps, which takes about 20 hours (in the case of SLLOD simulations) on a modern GPU card (Nvidia GTX 780 Ti). The *NVT* simulations used to calculate γ and R at the starting state point for any isomorph ran for 10^{10} time steps in order to get good statistics for γ. In the *NVT* simulations of the FCC LJ crystal, the thermostat time constant was kept constant in reduced units. The value for the reduced thermostat constant is 0.4. The details of how to obtain viscosity from SLLOD simulations can be found in the Appendix. In the liquid phase and along the freezing line, 1000 LJ particles were simulated; for the FCC LJ crystal, 4000 LJ particles were simulated.

4 The freezing line

As mentioned in Section 2, along an isomorph scaled configurations have the same statistical weight. This implies that the freezing and melting lines of an R liquid are isomorphs: consider a state point of the fluid state in which the disordered configurations are the most likely, and another state point in which the system is in a crystalline phase. Since in the latter case the ordered configurations are most likely, these two state points cannot be on the same isomorph. It follows that the freezing and melting lines cannot be crossed by an isomorph (in the region where the system is an R system), *i.e.*, in both the liquid and crystalline regions isomorphs must be parallel to the freezing and melting lines, respectively. In particular, these lines are isomorphs themselves. This statement follows from assuming that the physically relevant states obey the isomorph scaling conditions.[8]

The LJ system is an R liquid, so its freezing line is approximately an isomorph. This was first confirmed by Schrøder *et al.*[35] using data from computer simulations by Ahmed and Sadus[49] and Mastny and de Pablo,[50] and subsequently by Pedersen[51] with data obtained by his interface-pinning method.[52] Recently, the approximate isomorph nature of the freezing line has been documented in detail by Heyes *et al.*[53,54] The quoted papers all focus on densities fairly close to unity (in LJ units). From the fact that the freezing line is an isomorph it is possible to understand the invariance along the freezing line of several properties, as recently was shown by Heyes *et al.*,[53] who studied the invariance of the reduced-unit radial distribution function, mean force, Einstein frequency, self-diffusion coefficient, and linear viscoelasticity of an LJ liquid along the freezing line, for densities around unity. All these quantities were found to be approximately invariant, as predicted by isomorph theory.

In this section the validity of an equation for the freezing line of the LJ system obtained from isomorph theory is checked over a considerably wider range of temperatures and densities than previously studied. In Section 5, the results of Heyes *et al.*[53] regarding structural and dynamic invariants are extended to a wide range of densities along the freezing line.

In Fig. 1 the agreement between the freezing isomorph and the freezing line is shown to hold for the whole range of temperatures and densities studied by Agrawal and Kofke.[56] The red line in Fig. 1 is the prediction from isomorph theory; this line is built by starting from the freezing point $T_0 = 2.0$ and $\rho_0 = 1.063$, obtained by Pedersen.[51] The correlation coefficient R and the scaling parameter γ at the state point (ρ_0, T_0) are:

$$R_0 = 0.995, \quad \gamma_0 = 4.907. \qquad (9)$$

Using eqn (3) and (6) and this value for γ_0, it is possible to build the freezing isomorph from

$$T_F(\rho) = A_F\rho^4 - B_F\rho^2 \qquad (10)$$

where T_F is the freezing temperature, $A_F = 2.27$, and $B_F = 0.80$ as found from the reference state-point information given in eqn (6) and (9). The same power-law dependence for the LJ freezing line was obtained in 2009 by Khrapak and Morfill[55]

14680 | *Phys. Chem. Chem. Phys.*, 2016, **18**, 14678–14690

This journal is © the Owner Societies 2016
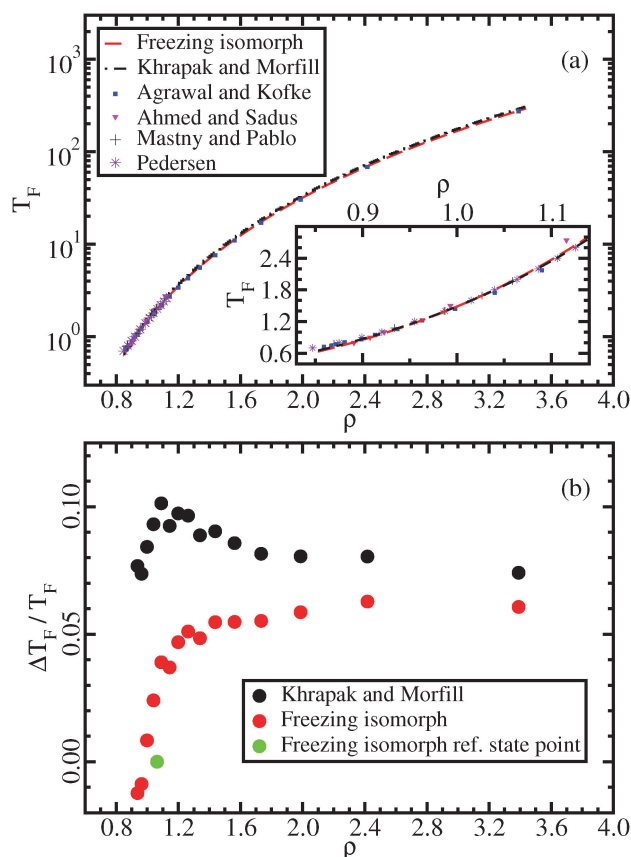
Fig. 1 Freezing line of the LJ system. In (a) the isomorph approximation to the freezing line is marked by the red line and the Khrapak and Morfill approximation[55] by the black line; freezing state points obtained in the past years using various techniques are shown by symbols.[49–51,56] Both approximations reproduce the data points well; the inset focuses on low densities. In (b) the relative difference between Agrawal and Kofke freezing-temperature data[56] and the two approximations is shown. The isomorph approximation gives smaller deviations from the simulation data. The main advantage of approximating the freezing line by an isomorph lies, however, in the possibility of predicting the full freezing line from the knowledge of a single freezing state point.

and, in fact, long ago by Rosenfeld from his "additivity of melting temperatures" (derived with reference to the hard-sphere system).[57,58] This is consistent with isomorph theory because Rosenfeld's rule can be derived from the quasi-universality of single-component R liquids.[31,32]

Fitting to the same simulations for the freezing line as referenced above,[49,50,56] Khrapak and Morfill[55] found the following values for the coefficients: $A = 2.29$ and $B = 0.71$. The line obtained inserting these values of A and B into eqn (10) is shown in Fig. 1(a) (black line). There is a significant difference in the second coefficient between the two equations. The second coefficient of Khrapak and Morfill is obtained using data for the triple point which may explain the difference; in that region isomorph theory does not provide a good approximation for the freezing line of the LJ system, as Pedersen recently showed.[51] Nevertheless, the two curves are close to each other. The freezing isomorph provides a slightly better prediction of freezing temperatures at any density when compared to the Khrapak and Morfill fit (inset of Fig. 1(a) and (b)).

The main result of this section is that isomorph theory provides a technique for approximating the freezing line of an R liquid from simulations at a single state point, *i.e.*, without any fitting, and that this approximation is valid over a wide range of densities. The relative difference between the predicted freezing temperature and the one obtained from computer simulations[56] is about 6% for density change of more than a factor of 3 and temperature change of more than a factor of 100, as shown in Fig. 1. Isomorph theory allows, therefore, estimating the freezing temperatures with small relative uncertainties, and it may be useful for estimating the freezing temperatures in the high density regimes, where it is difficult to perform direct experiments for real liquids, which are R liquids in the relevant part of the phase diagram.

5 Invariants along the freezing line

In this section we discuss different invariants along the freezing isomorph as well as another isomorph "parallel" to it in the liquid state, generated from the state point $(\rho,T) = (1.063,4.0)$. It is demonstrated that invariants originally proposed for the freezing line are also found along the liquid isomorph. Along the two isomorphs investigated, the excess pressure in reduced units is also evaluated (Fig. 2(a)). This quantity is invariant for any IPL system, but not for the LJ system. In the framework of isomorph theory, it is well understood why some quantities are invariant, *e.g.*, the reduced viscosity, while others are not, *e.g.*, the reduced pressure.[8] This shows that the scaling properties studied in this work are not simply the consequences of an effective IPL scaling. Also note that it is necessary to go to quite high densities before $\gamma \approx 4$, as shown in Fig. 2(b). In the same figure, the correlation coefficient R and the reduced viscosity are plotted as a function of density along the freezing isomorph. The reduced viscosity is predicted to be invariant.[8] For $\rho > 1.1$, the reduced viscosity is invariant to a good approximation. At lower densities, the correlation coefficient R decreases and the reduced viscosity begins to vary.

5.1 Structure and the Hansen–Verlet freezing criterion

Fig. 3 shows the radial distribution functions (RDF) $g(r)$ at different state points along the freezing line (a and d), the approximate freezing isomorph (b and e), and the liquid isomorph (c and f). In Fig. 3(a)–(c), $g(r)$ is expressed as a function of the pair distance, while in Fig. 3(e)–(g), the $g(r)$ is expressed as a function of the reduced distance, $\tilde{r} = \rho^{1/3} r$. When the RDFs are plotted in reduced units, they collapse onto master curves, as predicted by isomorph theory. The results obtained for the freezing line confirm the recent findings of Heyes *et al.*,[53] who showed the same collapse albeit for a smaller density range.

Starting from the invariance of $g(r)$ it is easy to show that the structure factor $S(q)$ is invariant when considered as a function of the reduced wave vector,

$$S(q) - 1 = \rho \int_V d\mathbf{r}\, e^{-iq\cdot\mathbf{r}} g(r)$$
$$= \int_{\tilde{V}} d\tilde{\mathbf{r}}\, e^{-i(\rho^{-1/3}\mathbf{q})\cdot\tilde{\mathbf{r}}} g(\tilde{r}) = S(\tilde{q}) - 1. \quad (11)$$

This journal is © the Owner Societies 2016

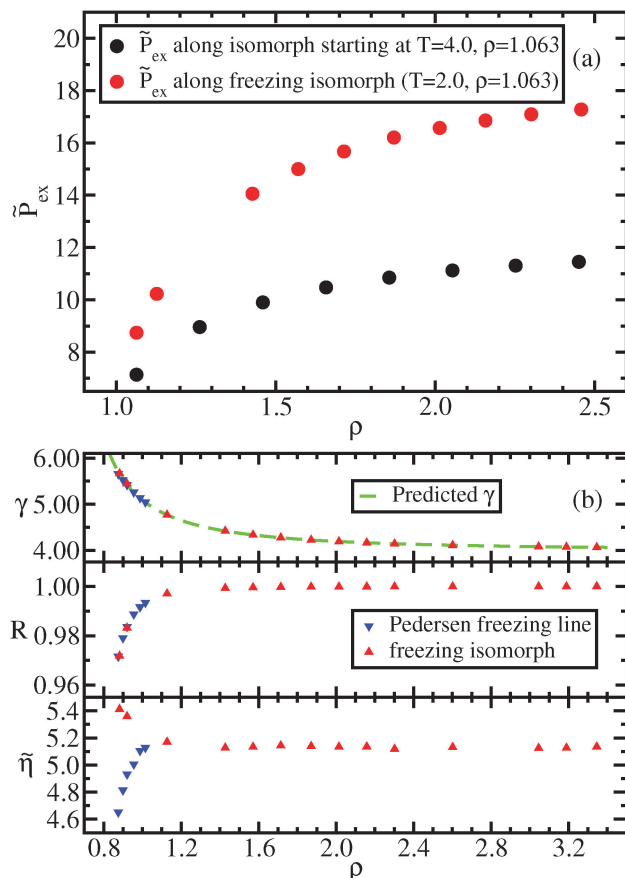*Phys. Chem. Chem. Phys.*, 2016, **18**, 14678–14690 | **14681**

Fig. 2 (a) Excess pressure in reduced units, $\tilde{P}_{ex} = W/(Nk_BT)$ along two different isomorphs, the freezing isomorph and a liquid isomorph. For inverse power-law pair potentials this quantity is invariant, while for the LJ system clearly it is not. This shows that isomorph scaling is not simply a trivial IPL scaling. (b) In the top panel, the scaling coefficient γ, eqn (7), is shown as a function of density along the freezing line and the freezing isomorph. The green line is the predicted value from $\gamma = d \ln h(\rho)/d \ln\rho$.[25,36] The middle and bottom panels show the virial potential-energy correlation coefficient R and the reduced viscosity $\tilde{\eta}$ along the freezing line and the freezing isomorph. The blue symbols mark data at freezing state points taken from Pedersen;[51] the red symbols are the same quantities calculated at freezing isomorph state points.

Structure factors $S(q)$ along the freezing line, the approximate freezing isomorph, and the liquid isomorph are shown in Fig. 4. The invariance of the structure factor implies the Hansen–Verlet freezing criterion[14,15] stating that the LJ system freezes when the height of the first peak of the structure factor reaches a definite value close to 3 (equal to 2.85 in the original work[14,15]): if $S(q)$ is invariant along an isomorph, points which are on the same isomorph have the same height of the first peak. And since the freezing line for R liquids is well approximated by an isomorph, the invariance of $S(q)$ implies the validity of the Hansen–Verlet freezing criterion. Fig. 4 confirms this.

5.2 Dynamic invariants: mean-squared displacement and intermediate scattering function

The dynamical behavior of the system is described by the mean-squared displacement (MSD) and the self-intermediate scattering function (ISF). In Fig. 5 and 6, the MSDs and ISFs are shown,

respectively, as functions of non-reduced and reduced quantities. As for the structure, the curves collapse onto master curves.

5.3 Viscosity along the freezing line and the Andrade equation

In order to evaluate the viscosity the system was simulated using the SLLOD algorithm[48] (details are given in the Appendix). Studies of the viscosity of the LJ system were done in the past, e.g., by Ashurst and Hoover,[59] and more recently by Galliero et al.[60] and Delage-Santacreu et al.,[61] in all cases for densities fairly close to unity.

Isomorph theory predicts the reduced viscosity to be constant to a good approximation along an isomorph (and therefore along the freezing line),

$$\tilde{\eta} \equiv \frac{\eta}{\rho^{2/3}\sqrt{mk_BT}} = \text{const.} \tag{12}$$

From this equation it is clear that if we know the value of η at a given state point we can calculate the expected viscosity at any state point on the same isomorph. Along the freezing line (F) this equation can be written as

$$\eta_F(\rho) = \tilde{\eta}_0 \cdot \rho^{2/3}\sqrt{mk_BT_F(\rho)} \tag{13}$$

where the subscript F stands for freezing, $T_F(\rho)$ is the freezing temperature at density ρ and $\tilde{\eta}_0 = 5.2$ is the reduced value of η at the reference state point $(\rho_0,T_0) = (1.063,2.0)$. Eqn (13) is identical to the Andrade equation for the freezing viscosity[17,18] from 1934:

$$\eta(\rho_F, T_F) = \beta \cdot \rho_F^{2/3}\sqrt{T_F} \tag{14}$$

where ρ_F is the density at freezing. This is well known to apply for most metals to a good approximation.[62] The parameter β in eqn (14) depends on the system, just as the value of $\tilde{\eta}_0$ in eqn (13) depends on the chosen potential.

In Fig. 7 viscosity results are compared to the values of the viscosity predicted from isomorph theory using eqn (13).

The green line in Fig. 7(b) is obtained by solving eqn (10) with respect to ρ^2 and using the solution to remove the ρ dependence from eqn (13). This results in

$$\eta(T_F) = \tilde{\eta}_0\sqrt{mk_BT_F}\left(\frac{B_F + \sqrt{B_F^2 + 4A_F \cdot T_F}}{2A_F}\right)^{1/3} \tag{15}$$

in which $A_F = 2.27$ and $B_F = 0.80$ are the freezing isomorph coefficients identified in Section 4 using eqn (6) and (9), i.e., based exclusively on simulations at the reference state point $(\rho,T) = (1.063,2.0)$ (the units of A_F and B_F are $\sigma^{12}\cdot\varepsilon/k_B$ and $\sigma^6\cdot\varepsilon/k_B$, with ε and σ being LJ parameters). The red dot in Fig. 7 marks the reference state point.

In Fig. 8 we show the reduced viscosity along the freezing isomorph as well as along the liquid isomorph with reference state point $(\rho_0,T_0) = (1.063,4.0)$. The figure demonstrates that invariance of the reduced viscosity along the freezing line is not a specific property of the freezing line, but a consequence of the more general isomorph invariance.

Andrade's equation for the freezing viscosity, which is explained by isomorph theory, was also discussed recently

Fig. 3 Liquid results. Radial distribution function along the Pedersen freezing line (a and d),[51] along the approximating freezing isomorph (b and e) and along an isomorph well within the liquid state (c and f); in (a–c), the RDFs are plotted as a function of distance in Lennard-Jones units, in (d–f), the RDFs are plotted as a function of the reduced distance. It is worth noting that while in (a) and (d) the density change is only a few percent, in the other figures density changed by about a factor of 3. The same holds for Fig. 4–6.
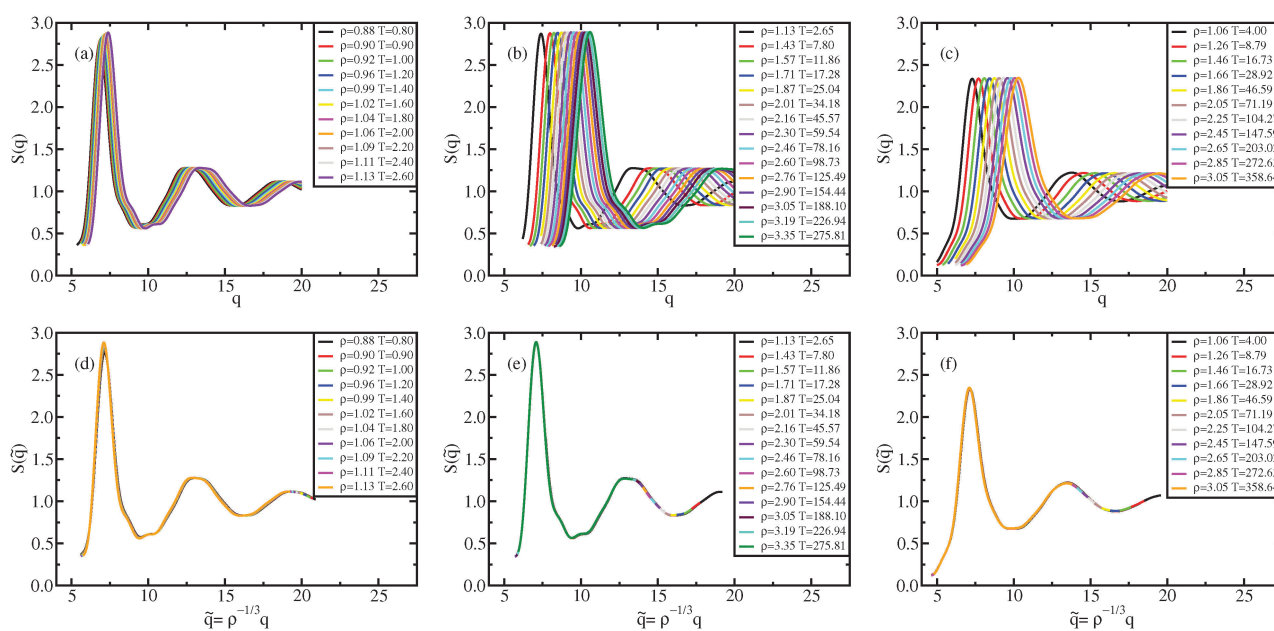
Fig. 4 Liquid results. Structure factor along the Pedersen freezing line (a and d),[51] along the approximate freezing isomorph (b and e), and along an isomorph well within the liquid state (c and f); in (a–c), $S(q)$ is plotted as a function of wave vector in Lennard-Jones units, in (d–f), $S(q)$ is plotted as a function of reduced wave vector.

by Fragiadakis and Roland.[63] It is interesting to compare the temperature range accessible to experiments with that of the present work. Fragiadakis and Roland[63] reported data on liquid argon in a range of temperatures corresponding to [0.75,4.17] in LJ units. This is impressive, but simulations allow one to cover an even wider range of freezing temperatures.

6 Invariants along the melting line

Following the same argument as for the freezing line (Section 4), the melting line is also an approximate isomorph. A study similar to that of Section 5 was performed, evaluating the structure and MSD, for an FCC LJ crystal along the melting line as well as another isomorph in the crystalline phase. The starting

This journal is © the Owner Societies 2016

Phys. Chem. Chem. Phys., 2016, **18**, 14678–14690 | **14683**
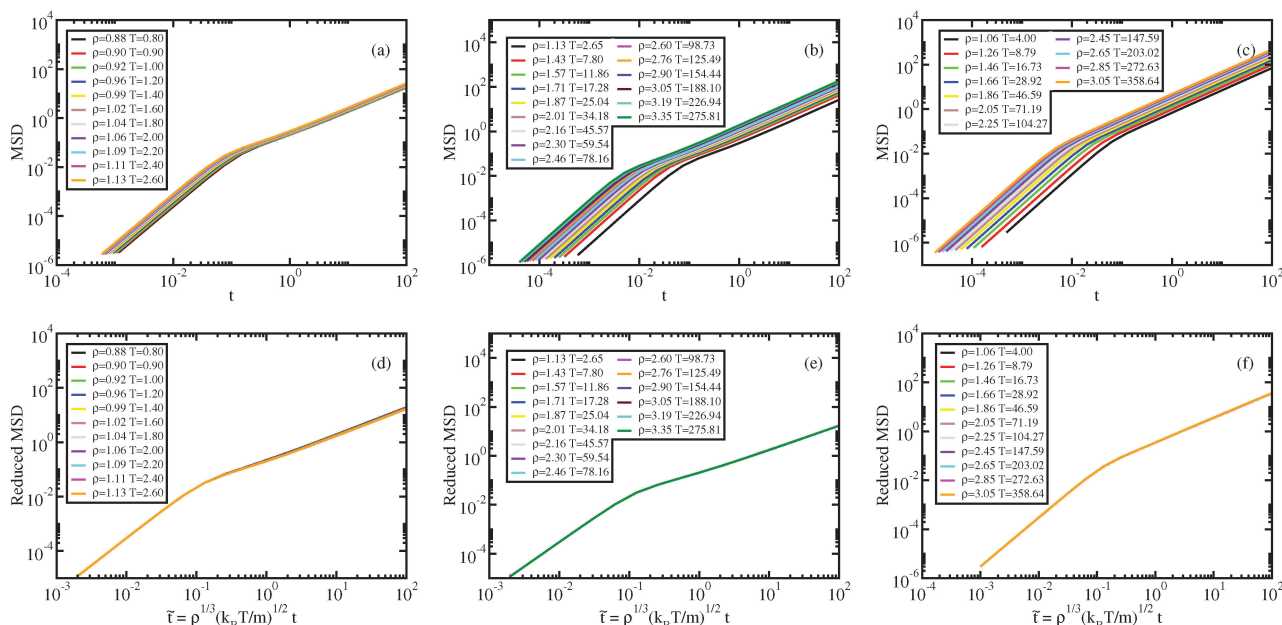
Fig. 5   Liquid results. Mean-squared displacement along the Pedersen freezing line (a and d),[51] along the approximating freezing isomorph (b and e) and along another isomorph in the liquid state (c and f); in (a–c), the MSDs are plotted as a function of time in LJ units, in (d–f), the reduced MSDs are plotted as a function of reduced time.
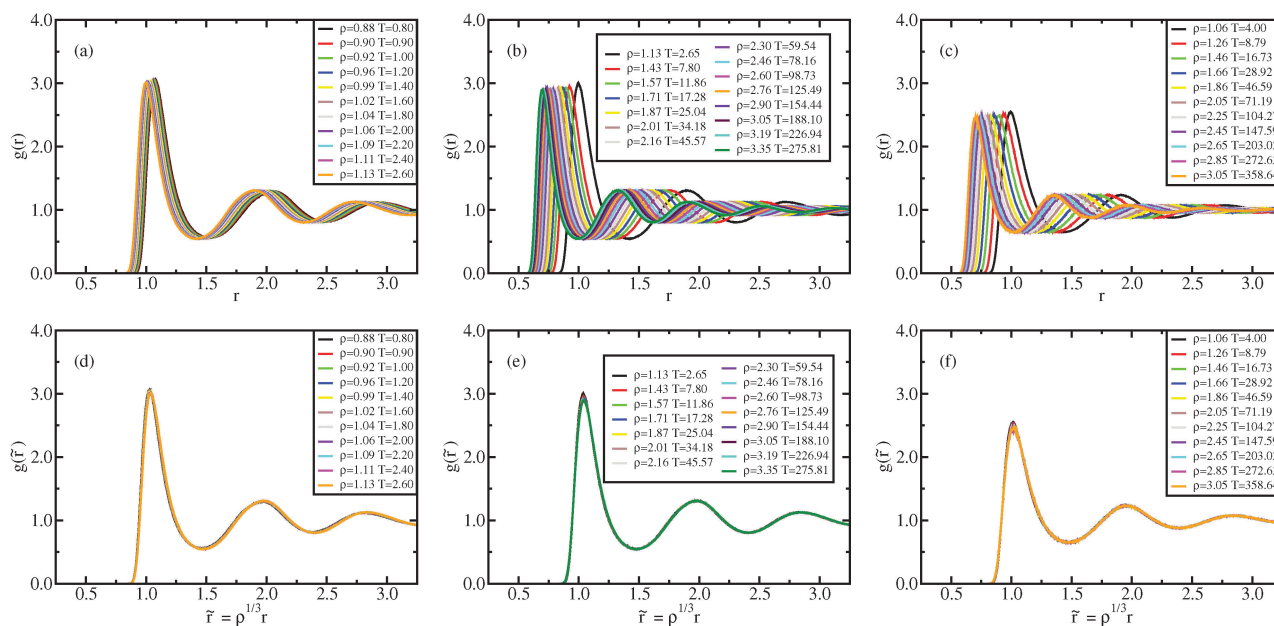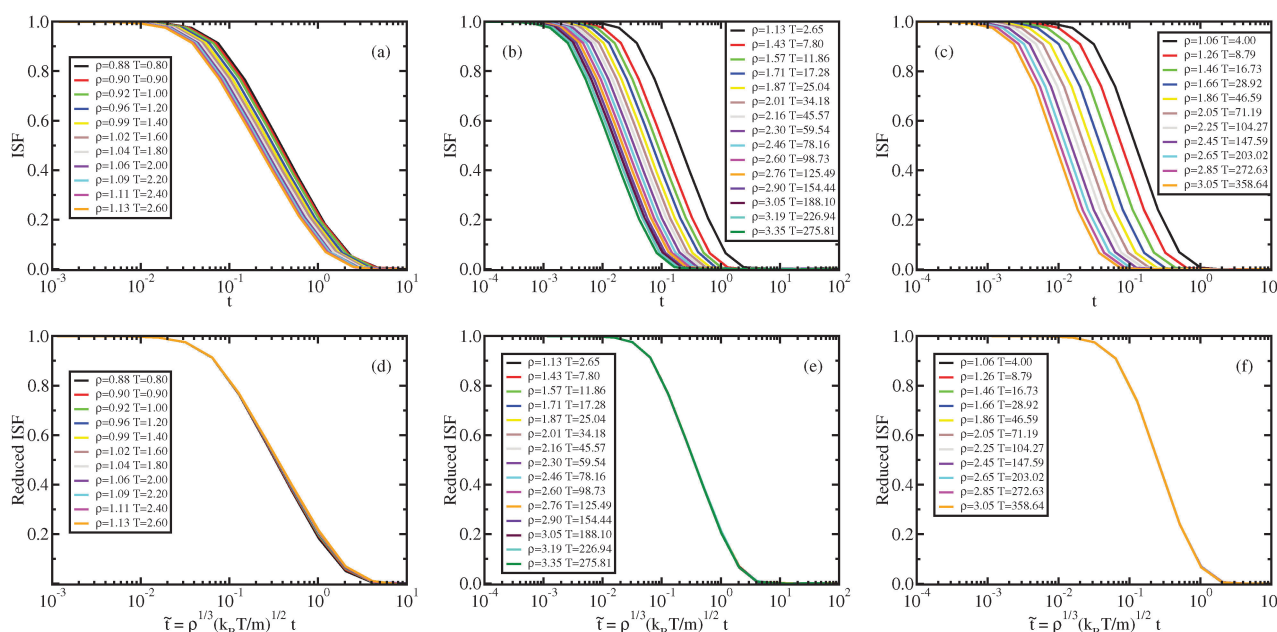

Fig. 6   Liquid results. Self-intermediate scattering function along the Pedersen freezing line (a and d),[51] along the approximating freezing isomorph (b and e), and along another isomorph in the liquid state (c and f); in (a–c), the ISFs are plotted as a function of time in Lennard-Jones units, in (d–f), the ISFs are plotted as a function of reduced time. All the ISFs correspond to the q value of the first peak of $S(q)$, q_{max}. The quantity $\tilde{q}_{max}$ is invariant along an isomorph due to the invariance of $\tilde{S}(\tilde{q})$, eqn (11).

point for the melting isomorph is taken from Pedersen;[51] this is the state point $(\rho, T) = (1.132, 2.0)$. The starting point for the crystal isomorph is $(\rho, T) = (1.132, 1.0)$, which is well within the crystalline phase. The melting isomorph equation for the LJ system is

$$T_M(\rho) = A_M \rho^4 - B_M \rho^2 \qquad (16)$$

where $A_M = 1.76$ and $B_M = 0.69$. The equation has the same mathematical form as the freezing equation, eqn (10), (but different coefficients) because the shape of isomorphs reflects the pair potential, not the phase. The existence of isomorphs in the crystalline phase was demonstrated in a recent publication by Albrechtsen et al.;[26] this paper showed that isomorph theory, in fact, is more accurate in the crystalline phase than for
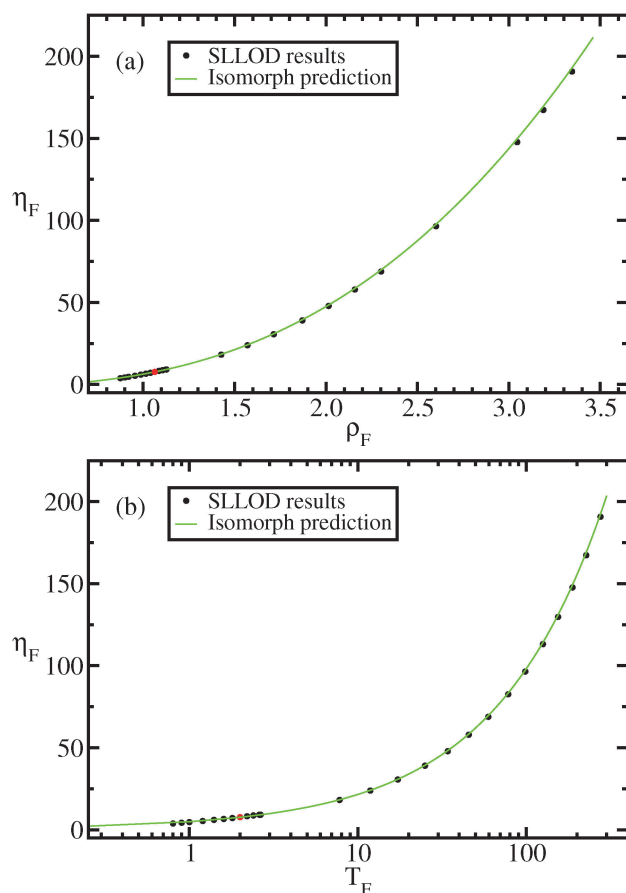
Fig. 7 Viscosity along the approximate freezing isomorph, eqn (10), as a function of density (a) and temperature (b). The black dots represent results for the viscosity obtained from our SLLOD simulations (Appendix). The green line is the predicted viscosity assuming the invariance of reduced viscosity along an isomorph (eqn (13)). The red dot is the viscosity of the state point from which the freezing isomorph is built and the constant of eqn (13) determined, $(\rho,T) = (1.063,2.0)$. The reduced viscosity at this state point is $\tilde{\eta}_0 = 5.2$.
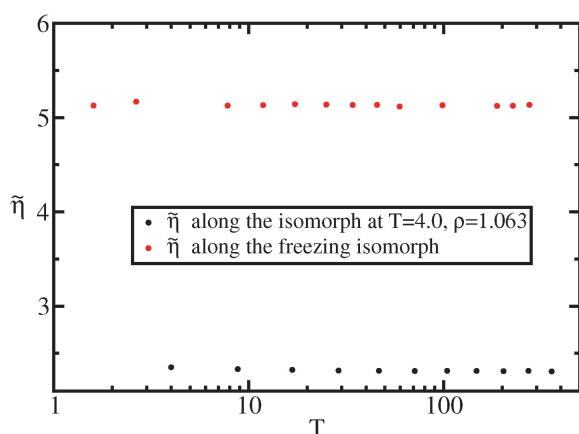
Fig. 8 Reduced viscosity along the freezing isomorph and along an isomorph well within the liquid state.

liquids. In Table 1 the predicted melting temperature at density 3.509 from eqn (16) is compared to the results for the melting line obtained in the present work using Pedersen's interface

Table 1 Comparison between the melting temperature at a given density, predicted using eqn (16), and that calculated for the same density using the interface pinning method.[52] The freezing and melting state temperatures at $\rho = 3.509$ have been calculated in this work, while the other data are from Pedersen.[51] The parameters in eqn (16) were calculated at the reference state point $(\rho,T) = (1.132, 2.0)$

ρ_M	T_M	$T_{pinning}$	$\Delta T/T_M$
0.973	0.800	0.921	-0.132
0.989	0.900	1.006	-0.106
1.005	1.000	1.095	-0.086
1.034	1.200	1.270	-0.055
1.061	1.400	1.453	-0.036
1.087	1.600	1.636	-0.022
1.109	1.800	1.812	-0.007
1.132	2.000	2.000	$+0.000$
1.153	2.200	2.191	$+0.004$
1.172	2.400	2.371	$+0.012$
1.191	2.600	2.561	$+0.015$
3.509	258.44	275.81	$+0.067$

pinning method.[51,52] As for the liquid-state isomorphs and the freezing line, the RDF is invariant both along the melting isomorph and along the crystal isomorph when expressed as a function of the reduced pair distance (Fig. 9). The MSD is shown in Fig. 10. The plateau of the MSD at melting confirms the pressure invariance of the Lindemann melting criterion.[19,20,64] The approximate invariance of reduced-unit MSD in the crystal implies that the value of the plateau for the mean atomic displacement is constant in reduced units along an isomorph (and consequently along the melting line), and is consistent with the Lindemann criterion. At low densities the invariance of the MSD plateau is violated. This is the region where the melting isomorph provides a worse approximation to the LJ melting line, Fig. 10(d), as also shown by Pedersen.[51] The Lindemann constant increases slightly with increasing density along melting, as reported by Luo *et al.*[65] For temperatures above 1.8, the Lindemann criterion is accurately satisfied, *i.e.*, the reduced vibrational mean-square displacement becomes density independent, Fig. 10(d) and (e).

7 Discussion

We have studied several properties of the LJ model along its freezing and melting lines, as well as along isomorphs well within the liquid and crystalline phases. In Table 2 the coefficients describing the four isomorphs studied in this work are given together with the relative reference state points. The primary aim was not to report that these invariances hold, which is already well known[9,14,16,66,67] albeit over smaller melting temperature/density ranges than studied here, but to relate these invariances to isomorph theory. With this goal in mind we investigated whether the invariants, thought to be peculiar to the freezing/melting process, also hold along other isomorphs in the liquid and crystalline phases. The results show that this is indeed the case. This means that these invariants are consequences of the LJ system being an R liquid in the relevant part of its phase diagram, not a specific property of freezing or melting.

This journal is © the Owner Societies 2016

Phys. Chem. Chem. Phys., 2016, **18**, 14678–14690 | **14685**

Fig. 9 Crystal results. Radial distribution function along the Pedersen melting line (a and d),[51] along the approximating melting isomorph (b and e), and along an isomorph well within the crystalline state (c and f); in (a–c), the RDFs are plotted as a function of distance in Lennard-Jones units, i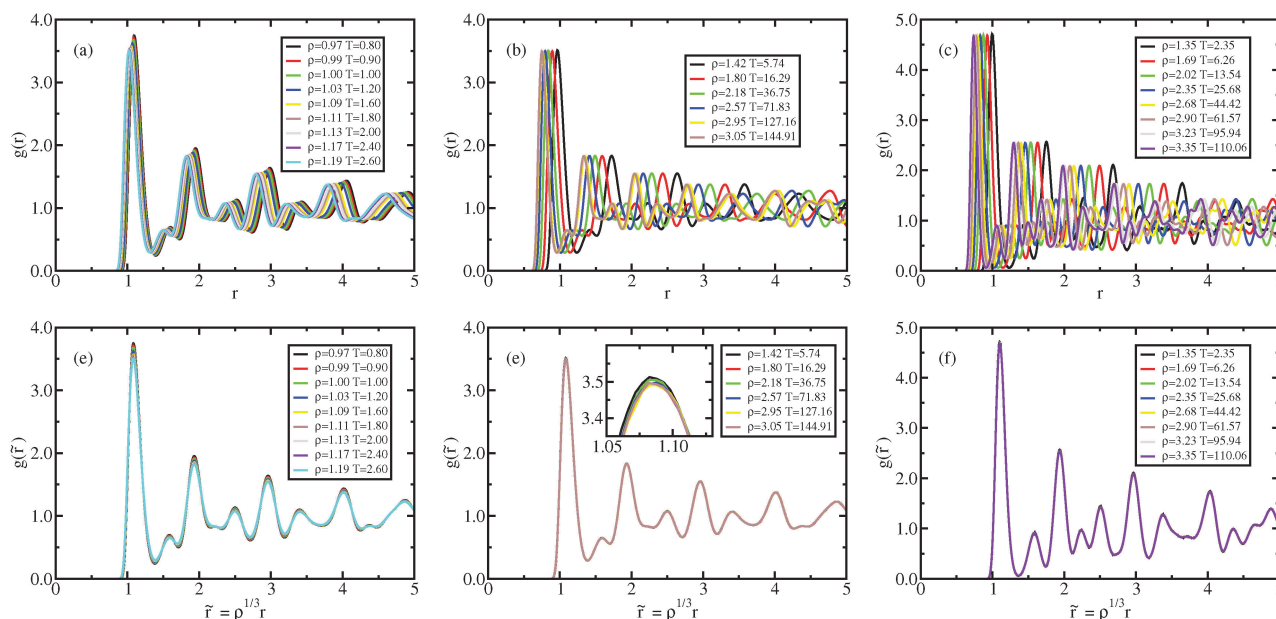n (d–f), the RDFs are plotted as a function of reduced distance. It is worth noting that while in (a) and (d) the density change is only a few percent, in the other figures density changed by about a factor of 3. The same holds for Fig. 10.
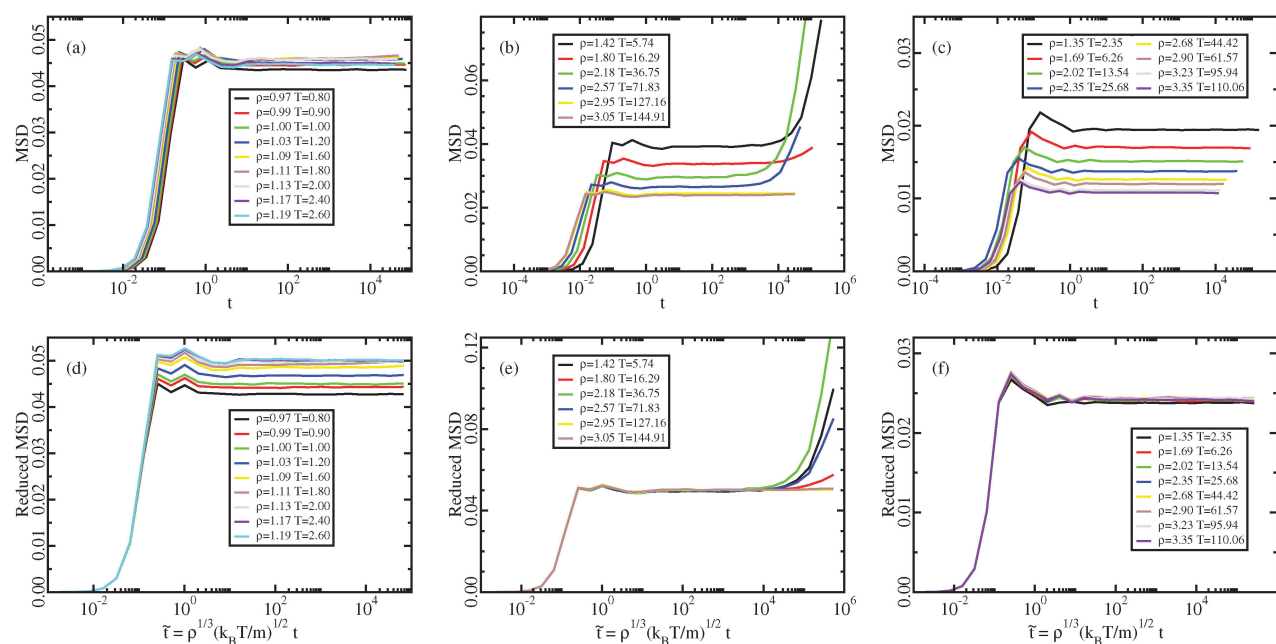
Fig. 10 Crystal results. Mean-squared displacement along the Pedersen melting line (a and d),[51] along the approximate melting isomorph (b and e), and along an isomorph well within the crystalline state (c and f); in (a–c), the MSDs are plotted as a function of time in LJ units, in (d–f), the reduced MSDs are plotted as a function of reduced time. The invariance of the plateau of MSD along the melting line implies the Lindemann melting criterion for R liquids because the invariance of the reduced-unit vibrational mean-square displacement in equivalent to the invariance of the Lindemann constant (Section 6). Along the melting isomorph diffusion of defects is observed. Defect formation is a stochastic phenomenon, as shown by the non-monotonicity of its appearance with respect to T or ρ. In order to study the isomorphic invariance of defect formation, it is necessary to average over many simulations at every state point and it could be the object of future studies. The diffusion of defects in crystal, when appropriately averaged, has been shown to be an isomorphic invariant by Albrechtsen et al.[26]

Nevertheless it should be stressed that invariances of reduced unit quantities, which would be exact if the freezing/melting lines were perfect isomorphs, are violated somewhat close to the triple point.

14686 | *Phys. Chem. Chem. Phys.*, 2016, **18**, 14678–14690

This journal is © the Owner Societies 2016

Table 2 Coefficients A and B of the isomorph in eqn (10) for the four isomorphs studied in this work. The first two columns contain the coefficients and the latter four columns contain temperatures, densities, density scaling coefficients γ, and correlation coefficients R of the state points the isomorphs studied in this work start from. A pure $n = 12$ IPL pair potential leads to $\gamma = 4$

	A	B	T	ρ	γ	R
Liquid isomorph	4.32	1.34	4.0	1.063	4.7589	0.9966
Freezing isomorph	2.27	0.80	2.0	1.063	4.9079	0.9955
Melting isomorph	1.76	0.69	2.0	1.132	4.8877	0.9985
Crystal isomorph	0.91	0.39	1.0	1.132	4.9979	0.9986

Before discussing our results in detail, we would like to point out the differences between isomorph theory and other approaches often used to describe the LJ system invariances. These other attempts to describe LJ invariances are the well-known hard sphere (HS) paradigm and the WCA (Weeks, Chandler, Andersen) approximation. The HS paradigm and isomorph theory are able to describe the nature of the same invariances, but with some important differences. A first difference is in the possibility of determining when the theory is expected to work and when it is not. In the case of isomorph theory there is a simple prescription: if the system is strongly correlating then it is possible to build isomorphs along which many reduced quantities are invariant. In the framework of hard spheres it is not possible to proceed in this way. It is not even possible to know from one single state point if some invariances will hold in the region around that state point because there is no equivalent of the correlation coefficient R defined in eqn (1). Another fundamental difference between the two approaches is the presence of an *ad hoc*-defined hard sphere radius that is in general state-point dependent. Isomorph theory works without the need of introducing any *ad hoc* parameters. A last difference, which is perhaps the most important, lies in the possibility of predicting which invariances the system will have. According to the HS paradigm, once the mapping from the studied system to the HS system is done using the *ad hoc* defined HS radius, the invariances of the HS system are inherited from the studied system. This means that the structure, dynamics and thermodynamic quantities should be invariant along constant-packing-fraction curves. In Fig. 2 we showed that the reduced pressure of the LJ system is not invariant along an isomorph (a) while the reduced viscosity is (b), as predicted from isomorph theory. Another possible comparison is between isomorph theory and the WCA approximation for the LJ system. While in isomorph theory there is no reference system, the WCA approximation is based on the idea that only the repulsive part of the LJ potential is relevant to the description of the system, providing a convenient reference system, and that LJ invariances can be derived from HS invariances.[68]

In Fig. 11(a) the viscosity is shown along the freezing line data from Agrawal and Kofke[56] for the LJ system and for the IPL potential:

$$\nu_{\text{IPL}}(r) = 4r^{-12} \qquad (17)$$
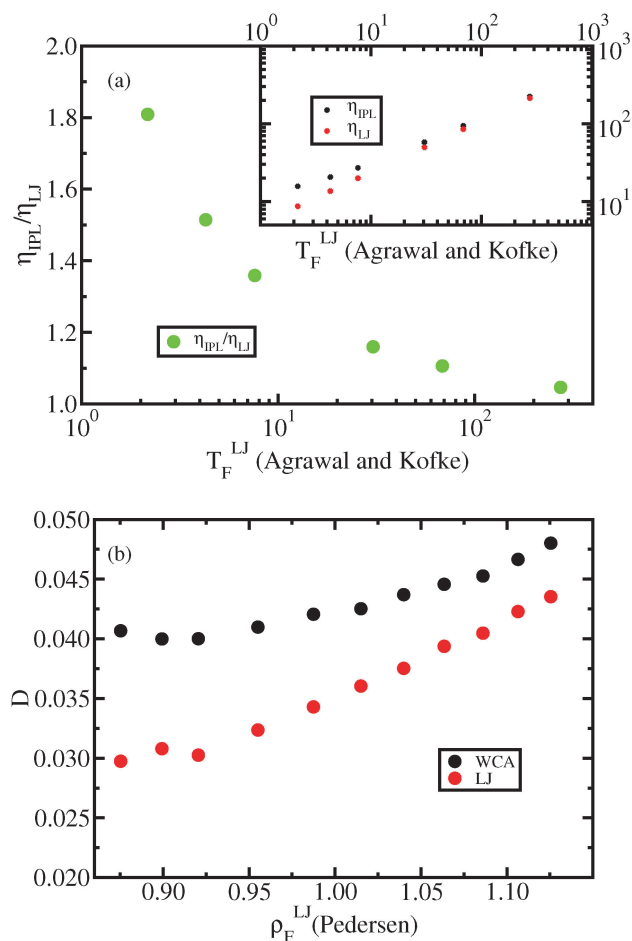
Fig. 11 (a) Viscosities (inset) of the IPL12 system and the LJ system along the freezing line (data from Agrawal and Kofke[56]) and their ratio (main figure). The viscosities are calculated using the SLLOD algorithm.[46–48] The viscosity of the IPL12 system is substantially different from that of the LJ system for temperatures lower than $T = 68.5$ in LJ units. (b) Diffusion constant for the LJ system and the WCA system along the Pedersen freezing line. It is well known that the WCA potential reproduces with good accuracy the structure of the LJ system while this is not the case for dynamics, as the figure shows.

which is the repulsive term of the LJ potential. The viscosity calculated using the two different potentials along the freezing line is very different. The difference is larger than 10% before reaching considerably high densities and temperatures $((\rho,T) = (2.417,68.5)$ in LJ units). This means that the effects of attraction are not negligible up to really high densities. As Rosenfeld wrote in 1976 "It is important here to emphasize that the r^{-6} term of the L-J potential gives appreciable contribution to the thermodynamic properties of the system up to very high temperatures"[58] regarding the difference between the freezing line of IPL12 and LJ.

In Fig. 11(b) the diffusion constant D for the LJ system with the WCA approximation and with the 2.5σ cutoff are shown. The WCA approximation is well known to reproduce with good accuracy the structure of the LJ system, but it fails in reproducing the dynamics. Berthier and Tarjus[69] already underlined that this was the case for the Kob–Andersen binary LJ system,

and Pedersen *et al.*[70] showed how isomorph theory provides a better description of the LJ system dynamics while preserving the good description of the structure.

In Sections 5 and 6 we discussed the relationship between isomorph theory and freezing/melting criteria. It was shown that the invariance along the freezing line of the maximum of the static structure factor $S(q)$ (the Hansen–Verlet criterion) results from a general invariance along isomorphs of the entire $S(q)$ function. The first peak of the structure factor along an isotherm decreases gradually with decreasing density. This means that there will be a specific value which corresponds to the freezing phase transition. The evidence that the value of this height is constant along the freezing line is not a peculiarity of the freezing process itself, but a consequence of isomorph scaling. The reason why the maximum height of $S(q)$ is 2.85[14,15] cannot be explained within isomorph theory, but is a feature of the freezing process. In order to explain the universality of the number 2.85, as well as the universality of the Lindemann melting criterion number, one must refer to quasiuniversality, a further consequence of the isomorph theory detailed, *e.g.*, by Bacher *et al.*[71] Note the compatibility of the general isomorph theory with the results of Saija *et al.*[72] on the pair-potential dependence of the maximum height of $S(q)$ at freezing.

The study of the LJ structure factor along the freezing line also allows explaining some properties of structure factors for liquid metals observed in X-ray experiments. As shown by Waseda and Sukuri in 1972,[73] for some liquid metals the ratio of the position of the first and second peaks in the structure factor is the same while there are others for which this does not hold, for example, Ga, Sn, and Bi. The first set of metallic liquids are the ones which are *R* liquids (*i.e.*, exhibit strong virial potential-energy correlations) and therefore are similar to the LJ system studied in this work, while those in the second do not, as shown very recently by Hummel *et al.*[74] from *ab initio* density functional theory calculations.

Along the melting line we studied the Lindemann criterion, which has been widely discussed[65,66,72,75] and also experimentally tested,[76] and the same conclusion holds as for the Hansen–Verlet criterion. Isomorphs' existence implies that an *R* liquid's thermodynamic phase diagram becomes effectively one-dimensional with respect to the isomorph-invariant quantities. The reduction of the 2d phase diagram to an effectively 1d phase diagram is crucial for understanding the connection between isomorph theory and the Lindemann criterion, because it removes one of the main criticisms against this criterion, *i.e.*, its being a single-phase criterion.[9] If the phase diagram is effectively one-dimensional, there is a unique melting process and the Lindemann constant is the value associated with this phase transition; the invariance of the Lindemann constant along the melting line is, in this view, a consequence of isomorph invariance. This argument also explains why one can use a single-phase criterion to predict where the melting process takes place for *R* liquids. According to the Lindemann criterion, the crystal melts when the vibrational MSD exceeds a threshold value, which in reduced units is constant along the melting line. This condition is equivalent to the invariance of the MSD along the melting line, an isomorph prediction. Note that

isomorph theory can be used to predict for which systems the Lindemann criterion (at least) must hold, namely all *R* liquids. Recent comprehensive density-functional theory (DFT) simulation data from Hummel *et al.*[74] show that most metals are *R* liquids and therefore the Lindemann criterion must apply for them in the sense that the reduced-unit MSD is approximately invariant along the melting line. On the other hand, systems that do not exhibit strong correlations between virial and potential-energy do not necessarily obey the Lindemann criterion. Thus as discussed by Stacey and Irvine already in 1977,[67] the Lindemann criterion applies for systems which "undergo no dramatic changes in coordination on melting". This is not the case for hydrogen-bonding systems, which are not *R* liquids.[24,27] The non-universal validity of the Lindemann criterion is also supported by Lawson[66] and by Fragiadakis and Roland.[63] Another interesting point is the connection between the Lindemann and Born criteria, relating melting to the vanishing of the shear modulus in the crystal. Jin *et al.*[77] showed that for a LJ system when the Lindemann criterion is satisfied, the Born criterion[78] too holds to a good approximation. In view of isomorph theory this is not surprising, because the reduced shear modulus is invariant along an isomorph and therefore constant on melting.

In Section 5 we discussed the relation between isomorph theory and Andrade's viscosity equation from 1934 for the viscosity of liquid metals at freezing. This equation is equivalent to stating invariance of the reduced viscosity along an isomorph, eqn (13) and (14). As for the Lindemann criterion, isomorph theory provides the possibility to predict whether a liquid will obey the Andrade equation. The DFT simulation data from Hummel *et al.*[74] explain why this equation holds for liquid alkali metals (as well as other invariances[79]); likewise one also expects this equation to hold for many other metals, for example, iron. The last point is of significant interest because the estimation of viscosity of liquid iron close to the freezing line in the Earth core is of crucial relevance for the development of Earth-core models,[4–6] but is still widely debated.[80–82] Isomorph scaling predicts an increase of the real (non-reduced) viscosity along the freezing line consistent with the results of Fomin *et al.*[81]

8 Conclusions

We have shown that the freezing and melting lines are approximately isomorphs and how the isomorph theory can be used to explain why some liquids have simple behavior at freezing and melting, *i.e.*, have several structural and dynamical approximate invariants along the freezing and melting lines. Thus this theory can be used for *R* liquids to determine the melting and freezing physical quantities not easily accessible by experiments, ranging from noble gases like argon to liquid metals to certain molecular liquids.

A Determining the zero-strain rate viscosity from SLLOD simulations

An SLLOD simulation[46–48] is a molecular dynamic simulation performed by shearing the simulation box with constant speed.
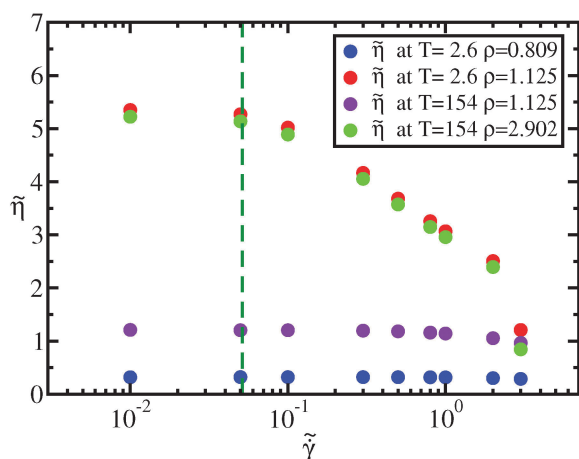
14688 | *Phys. Chem. Chem. Phys.*, 2016, **18**, 14678–14690

This journal is © the Owner Societies 2016

Fig. 12 Measured reduced viscosity from eqn (18) at different reduced strain rates. Two of the five state points (green and red dots) are on the same isomorph (the freezing isomorph of Section 4) and their behavior in reduced units is the same. As a consequence, the reduced strain rate at which reduced viscosity starts to be strain rate dependent is an isomorphic invariant, consistently with results from Separdar *et al.*[83] The blue and violet dots are results of simulations at state points isochoric or isothermic to the $(\rho,T) = (1.125, 2.6)$. The behavior of reduced viscosity as a function of the strain rate is strongly modified changing density or temperature if the chosen state points are not isomorphic.

Between the bottom part of the box and the top part there is a relative shearing motion with a strain rate $\dot{\gamma} = \dfrac{\partial u_x}{\partial y}$, where u_x is the streaming velocity at ordinate y when the box is sheared in the x direction. Under low strain-rate conditions, this kind of simulation reproduces an ordinary, linear Coulette flow and the linear, shear-rate-independent, viscosity can be calculated from the stress tensor σ_{ij} through the equation

$$\eta = \frac{\sigma_{xy}}{\dot{\gamma}} \qquad (18)$$

Eqn (18) holds only when the viscosity is independent of the strain rate, *i.e.*, at a sufficiently small shear rate. As shown by Separdar *et al.*[83] the strain rate $\dot{\gamma}$ for which the measured viscosity starts to be strain-rate dependent is isomorph invariant when given in reduced units.

The behavior of the reduced viscosity $\tilde{\eta}$ as a function of the reduced strain rate $\tilde{\dot{\gamma}}$ is shown in Fig. 12. When the two considered state points are on the same isomorph, they exhibit the same shear-thinning behavior in reduced units; this is not true if we move along an isochore or along an isotherm. The dotted green line in Fig. 12 marks the reduced strain rate used for the simulations along the freezing line reported in the paper.

Acknowledgements

References

1 R. W. Cahn, *Nature*, 1986, **323**, 668–669.
2 D. W. Oxtoby, *Nature*, 1990, **347**, 725–730.
3 R. W. Cahn, *Nature*, 2001, **413**, 582–583.
4 J.-P. Poirier, *Geophys. J.*, 1988, **92**, 99–105.
5 J.-P. Poirier, *Introduction to the Physics of the Earth's Interior*, Academic, 2nd edn, 2000.
6 F. D. Stacey, *Rep. Prog. Phys.*, 2010, **73**, 046801.
7 J. E. Lennard Jones, *Proc. R. Soc. London, Ser. A*, 1924, **106**, 441–462.
8 N. Gnan, T. B. Schrøder, U. R. Pedersen, N. P. Bailey and J. C. Dyre, *J. Chem. Phys.*, 2009, **131**, 234504.
9 A. R. Ubbelohde, *Melting and Crystal Structure*, Clarendon, London, 1965.
10 D. C. Wallace, *Statistical Physics of Crystals and Liquids*, World Scientific, Singapore, 2002.
11 J. L. Tallon, *Nature*, 1989, **342**, 658–660.
12 J. L. Tallon, *Phys. Lett. A*, 1980, **76**, 139–142.
13 S. M. Stishov, *Phys.-Usp.*, 1975, **17**, 625.
14 J.-P. Hansen and L. Verlet, *Phys. Rev.*, 1969, **184**, 151–161.
15 J.-P. Hansen, *Phys. Rev. A: At., Mol., Opt. Phys.*, 1970, **2**, 221–230.
16 E. d. C. Andrade, *Nature*, 1931, **128**, 835.
17 E. d. C. Andrade, *London, Edinburgh Dublin Philos. Mag. J. Sci.*, 1934, **17**, 497–511.
18 E. d. C. Andrade, *London, Edinburgh Dublin Philos. Mag. J. Sci.*, 1934, **17**, 698–732.
19 F. A. Lindemann, *Phys. Z.*, 1910, **11**, 609.
20 J. J. Gilvarry, *Phys. Rev.*, 1956, **102**, 308–316.
21 F. Saija, S. Prestipino and P. V. Giaquinta, *J. Chem. Phys.*, 2001, **115**, 7586–7591.
22 M. Dzugutov, *Nature*, 1996, **381**, 137–139.
23 E. H. Abramson, *J. Phys. Chem. B*, 2014, **118**, 11792–11796.
24 N. P. Bailey, U. R. Pedersen, N. Gnan, T. B. Schrøder and J. C. Dyre, *J. Chem. Phys.*, 2008, **129**, 184507.
25 T. S. Ingebrigtsen, L. Bøhling, T. B. Schrøder and J. C. Dyre, *J. Chem. Phys.*, 2012, **136**, 061102.
26 D. E. Albrechtsen, A. E. Olsen, U. R. Pedersen, T. B. Schrøder and J. C. Dyre, *Phys. Rev. B: Condens. Matter Mater. Phys.*, 2014, **90**, 094106.
27 T. S. Ingebrigtsen, T. B. Schrøder and J. C. Dyre, *Phys. Rev. X*, 2012, **2**, 011011.
28 A. A. Veldhorst, T. B. Schrøder and J. C. Dyre, *Phys. Plasmas*, 2015, **22**, 073705.
29 T. B. Schrøder and J. C. Dyre, *J. Chem. Phys.*, 2014, **141**, 204502.
30 N. P. Bailey, T. B. Schrøder and J. C. Dyre, *Phys. Rev. E: Stat., Nonlinear, Soft Matter Phys.*, 2014, **90**, 042310.
31 J. C. Dyre, *Phys. Rev. E: Stat., Nonlinear, Soft Matter Phys.*, 2013, **87**, 022106.
32 J. C. Dyre, *Phys. Rev. E: Stat., Nonlinear, Soft Matter Phys.*, 2013, **88**, 042139.
33 N. P. Bailey, U. R. Pedersen, N. Gnan, T. B. Schrøder and J. C. Dyre, *J. Chem. Phys.*, 2008, **129**, 184508.
34 T. B. Schrøder, N. P. Bailey, U. R. Pedersen, N. Gnan and J. C. Dyre, *J. Chem. Phys.*, 2009, **131**, 234503.

35 T. B. Schrøder, N. Gnan, U. R. Pedersen, N. Bailey and J. C. Dyre, *J. Chem. Phys.*, 2011, **134**, 164505.

36 L. Bøhling, T. S. Ingebrigtsen, A. Grzybowski, M. Paluch, J. C. Dyre and T. B. Schrøder, *New J. Phys.*, 2012, **14**, 113035.

37 A. Bacher and J. Dyre, *Colloid Polym. Sci.*, 2014, **292**, 1971–1975.

38 A. A. Veldhorst, PhD thesis, Roskilde Universitet, 2014.

39 T. S. Ingebrigtsen, T. B. Schrøder and J. C. Dyre, *J. Phys. Chem. B*, 2012, **116**, 1018–1034.

40 A. A. Veldhorst, J. C. Dyre and T. B. Schrøder, *J. Chem. Phys.*, 2014, **141**, 054904.

41 D. Gundermann, U. R. Pedersen, T. Hecksher, N. P. Bailey, B. Jakobsen, T. Christensen, N. B. Olsen, T. B. Schroder, D. Fragiadakis, R. Casalini, C. M. Roland, J. C. Dyre and K. Niss, *Nat. Phys.*, 2011, **7**, 816–821.

42 L. A. Roed, D. Gundermann, J. C. Dyre and K. Niss, *J. Chem. Phys.*, 2013, **139**, 101101.

43 W. Xiao, J. Tofteskov, T. V. Christensen, J. C. Dyre and K. Niss, *J. Non-Cryst. Solids*, 2015, **407**, 190–195.

44 C. M. Roland, S. Hensel-Bielowka, M. Paluch and R. Casalini, *Rep. Prog. Phys.*, 2005, **68**, 1405.

45 N. P. Bailey, T. S. Ingebrigtsen, J. S. Hansen, A. A. Veldhorst, L. Bøhling, C. A. Lemarchand, A. E. Olsen, A. K. Bacher, H. Larsen, J. C. Dyre and T. B. Schrøder, 2015, arXiv:1506.05094.

46 D. J. Evans and G. Morriss, *Statistical mechanics of non-equilibrium liquids*, Cambridge University Press, 2008.

47 P. J. Daivis and B. D. Todd, *J. Chem. Phys.*, 2006, **124**, 194103.

48 M. Evans and D. Heyes, *Mol. Phys.*, 1990, **69**, 241–263.

49 A. Ahmed and R. J. Sadus, *J. Chem. Phys.*, 2009, **131**, 174504.

50 E. A. Mastny and J. J. de Pablo, *J. Chem. Phys.*, 2007, **127**, 104504.

51 U. R. Pedersen, *J. Chem. Phys.*, 2013, **139**, 104102.

52 U. R. Pedersen, F. Hummel, G. Kresse, G. Kahl and C. Dellago, *Phys. Rev. B: Condens. Matter Mater. Phys.*, 2013, **88**, 094101.

53 D. M. Heyes, D. Dini and A. C. Brańka, *Phys. Status Solidi B*, 2015, 1–12.

54 D. M. Heyes and A. C. Brańka, *J. Chem. Phys.*, 2015, **143**, year.

55 S. A. Khrapak and G. E. Morfill, *J. Chem. Phys.*, 2011, **134**, 094108.

56 R. Agrawal and D. A. Kofke, *Mol. Phys.*, 1995, **85**, 43–59.

57 Y. Rosenfeld, *Chem. Phys. Lett.*, 1976, **38**, 591–593.

58 Y. Rosenfeld, *Mol. Phys.*, 1976, **32**, 963–977.

59 W. Ashurst and W. Hoover, *Phys. Rev. A: At., Mol., Opt. Phys.*, 1975, **11**, 658–678.

60 G. Galliero, C. Boned and J. Fernández, *J. Chem. Phys.*, 2011, **134**, 064505.

61 S. Delage-Santacreu, G. Galliero, H. Hoang, J.-P. Bazile, C. Boned and J. Fernandez, *J. Chem. Phys.*, 2015, **142**, 174501.

62 G. Kaptay, *Z. Metallkd.*, 2005, **96**, 24–31.

63 D. Fragiadakis and C. M. Roland, *Phys. Rev. E: Stat., Nonlinear, Soft Matter Phys.*, 2011, **83**, 031504.

64 M. Ross, *Phys. Rev.*, 1969, **184**, 233–242.

65 S.-N. Luo, A. Strachan and D. C. Swift, *J. Chem. Phys.*, 2005, **122**, 194709.

66 A. Lawson, *Philos. Mag.*, 2009, **89**, 1757–1770.

67 F. D. Stacey and R. D. Irvine, *Aust. J. Phys.*, 1977, **30**, 631–640.

68 H. C. Andersen, J. D. Weeks and D. Chandler, *Phys. Rev. A: At., Mol., Opt. Phys.*, 1971, **4**, 1597–1607.

69 L. Berthier and G. Tarjus, *Phys. Rev. Lett.*, 2009, **103**, 170601.

70 U. R. Pedersen, T. B. Schrøder and J. C. Dyre, *Phys. Rev. Lett.*, 2010, **105**, 157801.

71 A. K. Bacher, T. B. Schrøder and J. C. Dyre, *Nat. Commun.*, 2014, **5**, 5424.

72 F. Saija, S. Prestipino and P. V. Giaquinta, *J. Chem. Phys.*, 2006, **124**, 244504.

73 Y. Waseda and K. Suzuki, *Phys. Status Solidi B*, 1972, **49**, 339–347.

74 F. Hummel, G. Kresse, J. Dyre and U. R. Pedersen, 2015, arXiv:1504.03627.

75 H. Löwen, T. Palberg and R. Simon, *Phys. Rev. Lett.*, 1993, **70**, 1557–1560.

76 K. Sokolowski-Tinten, C. Blome, J. Blums, A. Cavalleri, C. Dietrich, A. Tarasevitch, I. Uschmann, E. Forster, M. Kammler, M. Horn-von Hoegen and D. von der Linde, *Nature*, 2003, **422**, 287–289.

77 Z. H. Jin, P. Gumbsch, K. Lu and E. Ma, *Phys. Rev. Lett.*, 2001, **87**, 055703.

78 M. Born, *J. Chem. Phys.*, 1939, **7**, 591–603.

79 U. Balucani, A. Torcini and R. Vallauri, *Phys. Rev. B: Condens. Matter Mater. Phys.*, 1993, **47**, 3011–3020.

80 M. D. Rutter, R. A. Secco, H. Liu, T. Uchida, M. L. Rivers, S. R. Sutton and Y. Wang, *Phys. Rev. B: Condens. Matter Mater. Phys.*, 2002, **66**, 060102.

81 Y. D. Fomin, V. N. Ryzhov and V. V. Brazhkin, *J. Phys.: Condens. Matter*, 2013, **25**, 285104.

82 G. Shen, V. B. Prakapenka, M. L. Rivers and S. R. Sutton, *Phys. Rev. Lett.*, 2004, **92**, 185701.

83 L. Separdar, N. P. Bailey, T. B. Schrøder, S. Davatolhagh and J. C. Dyre, *J. Chem. Phys.*, 2013, **138**, 154505.

Thermodynamics of freezing and melting

Ulf R. Pedersen,[*] Lorenzo Costigliola, Nicholas P.

Bailey, Thomas B. Schrøder, and Jeppe C. Dyre

Glass and Time, IMFUFA, Department of Science and Environment,

Roskilde University, P. O. Box 260, DK-4000 Roskilde, Denmark

(Dated: May 26, 2016)

Abstract

Although the freezing of liquids and melting of crystals are fundamental for many areas of the sciences, even simple properties like the temperature-pressure relation along the melting line cannot be predicted today. We present a theory in which properties of the coexisting crystal and liquid phases at a single thermodynamic state point provide the basis for calculating the pressure, density, and entropy of fusion as functions of temperature along the melting line, as well as the variation along this line of the reduced crystalline vibrational mean-square displacement (the Lindemann ratio) and the liquid's diffusion constant and viscosity. The framework developed, which applies for systems characterized by so-called hidden scale invariance, is validated by computer simulations of the standard 12-6 Lennard-Jones system.

[*] ulf@urp.dk

I. INTRODUCTION

Melting is the prototypical first-order phase transition [1–3]. Its qualitative description has been textbook knowledge for a century, but it has proven difficult to give quantitatively accurate predictions. This is the case not only for the *kinetics* of melting and freezing, exciting and highly active areas of research [4–8]; there is not even a theory for calculating, e.g., the entropy of fusion as a function of temperature. The below study provides a step in this direction by showing how the thermodynamics of melting and freezing for a large class of systems may be predicted from computer simulations carried out at a single coexistence state point. In particular, the theory developed quantifies the deviations from melting-line invariants discussed for a long time [9–13].

The everyday observation that matter sticks together but is at the same time almost impossible to compress [14] is modeled, e.g., in the system proposed by Lennard-Jones (LJ) in 1924 [15]. Here particles interact via a pair potential that as a function of distance r is a difference of two inverse power-law terms: $v_{\mathrm{LJ}}(r) = 4\varepsilon((r/\sigma)^{-12} - (r/\sigma)^{-6})$. The first term reflects the fact that the repulsive "Pauli" forces are harsh and short-ranged, the negative term models the softer, longer ranged attractive van der Waals forces. The 1970s led to the development of highly successful thermodynamic perturbation and integral-equation theories for simple liquids [10, 16–20]. Their main ingredient is the assumption that the structure of a dense, monatomic fluid closely resembles that of a collection of hard spheres [10, 19, 21, 22]. Confirming this, the structure of melts of, e.g., metallic elements near freezing is generally close to that of the hard-sphere system [10, 20, 22, 23]. The term "structure" generally refers to the entire collection of spatial equal-time density correlation functions, but our focus below is on the pair correlation function function as the most important structural characteristic (in the form of its Fourier transform, the structure factor).

Since the hard-sphere system has only a single nontrivial thermodynamic state parameter (the packing fraction), the phase diagram is basically one-dimensional, which implies that the system has a unique freezing/melting transition. Based on this one expects invariance along the freezing and melting lines, respectively, of structure and dynamics in proper units, as well as of thermodynamic variables like the relative density change upon melting and the melting entropy [24]. Empirical freezing and melting rules, which follow from the hard-sphere melting picture and are fairly well obeyed for most simple systems, include:

2

1. In crystals the ratio between the root-mean-square atomic displacement and the nearest-neighbor distance is known as the Lindemann ratio. The Lindemann melting rule from 1910 [9, 24–28] states that melting occurs when this ratio is about 0.1. In the hard-sphere model the Lindemann ratio is universal at melting because there is basically just a single melting point. In particular, for systems well described by the HS model the Lindemann ratio is predicted to be invariant along the melting line.

2. In properly reduced units the liquid's self diffusion constant and viscosity are invariant along the freezing line [29, 30].

3. The Hansen-Verlet rule [21, 31] that the amplitude of the first peak of the liquid static structure factor is about 2.85 at freezing reflects the invariance of structure along the freezing line.

4. The entropy of fusion ΔS_{fus} is about $1.1 k_B$ (Richard's rule) [3] – a more accurate empirical finding is that the constant-volume entropy difference across the density-temperature coexistence region is close to $0.8 k_B$ [26, 32].

This paper shows that for a large class of systems, including the LJ system, it is possible to predict the thermodynamics along the melting line – as well as deviations from HS predicted invariances along this line – from computer simulations carried out at a single coexistence state point.

II. RESULTS

A. General theory

It is well-known that adding a mean-field attractive term to the hard sphere model broadens the coexistence region which, on the other hand, narrows if the repulsive part is softened [10, 18, 33–36]. Such terms are therefore expected to modify the hard-sphere predicted invariances along the freezing and melting line. As an example Fig. 1(a) shows that in reduced units there is approximate identity of structure along the LJ freezing line, but the structure is not entirely invariant as seen in the inset where the dashed line marks the predicted maximum based on simulations at $T = 2.0\varepsilon/k_B$ if the structure were invariant.

3
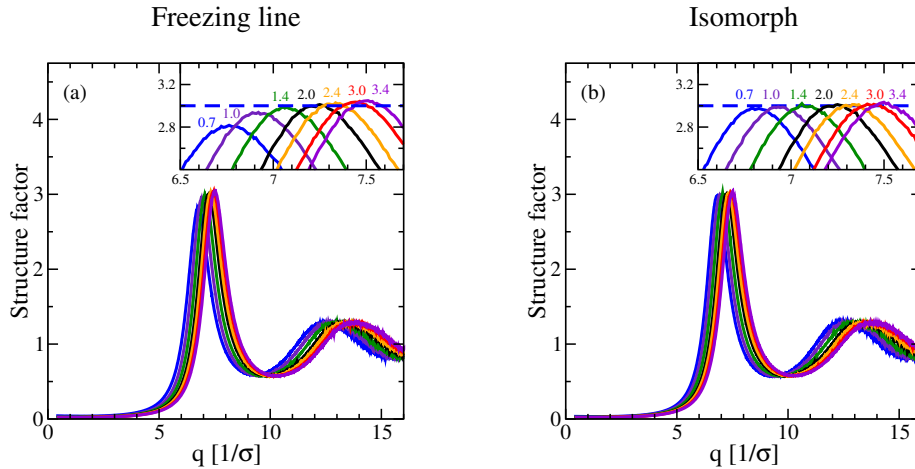
FIG. 1. Structure of the liquid Lennard-Jones system as reflected in the structure factor. (a) Liquid structure factor along the freezing line [37] showing results ranging from $T = 0.7\varepsilon/k_B$, which is close to the triple point, to $T = 3.4\varepsilon/k_B$. The hard-sphere model predicts that the height of the first peak is invariant along the freezing line as indicated by the blue dashed line in the inset. Small, but systematic deviations are observed. (b) Liquid structure factor along the isomorph crossing the melting line at temperature $T = 2.0\varepsilon/k_B$ (henceforth used as the liquid reference isomorph), demonstrating structural invariance to a much higher degree.

In order to develop a quantitative theory of freezing and melting we take as starting point the "hidden scale-invariance" property recently demonstrated for systems [38] characterized by a potential-energy function $U(\mathbf{R})$ where $\mathbf{R} = (\mathbf{r}_1, \mathbf{r}_2, \ldots, \mathbf{r}_N)$ is the collective coordinate of the system's N particles, which to a good approximation obeys the following scaling condition [39]

$$U(\mathbf{R}_a) < U(\mathbf{R}_b) \Rightarrow U(\lambda\mathbf{R}_a) < U(\lambda\mathbf{R}_b).\tag{1}$$

Here λ is a scaling factor; it is understood that the sample container undergoes the same scaling, and thus $\lambda > 1$ corresponds to a density decrease and $\lambda < 1$ to a density increase. This form of scale invariance is exact only for systems with inverse power-law type interactions [18]. It is a good approximation, however, for the condensed phase of many systems in which this property is not obvious from inspection of the analytical expression for $U(\mathbf{R})$, thus it is referred to as "hidden scale invariance" [39–42]. Equation (1), which is formally

4

equivalent to the conformal-invariance condition $U(\mathbf{R}_a) = U(\mathbf{R}_b) \Leftrightarrow U(\lambda\mathbf{R}_a) = U(\lambda\mathbf{R}_b)$, implies invariance of structure and dynamics along the configurational adiabats in the phase diagram [39]. These lines are referred to as isomorphs [42]. It was very recently shown by Maimbourg and Kurchan that in high dimensions all pair-potential systems obey hidden scale invariance [43]. Experimentally, hidden scale invariance has been demonstrated directly and indirectly for molecular van der Waals bonded liquids and polymers [44–46]. Further evidence for the existence of isomorphs come from computer simulations of single-component systems [40, 42] as well as, e.g., glass-forming mixtures [47], nanoflows [48], molecular models [38], and density-functional *ab initio* simulated metallic elements [49]. Isomorphs have also been demonstrated in simulations of out-of-equilibrium situations like zero-temperature shear flows of glasses or nonlinear steady-state liquid flows (see Ref. 38 and its references). It is important to emphasize, however, that not all condensed matter exhibits hidden scale invariance; for instance, water is a notable exception [41]. The general picture is that most metals and organic van der Waals bonded systems obey Eq. (1) to a good approximation in the condensed-phase part of their thermodynamic phase diagram, whereas systems with strong directional bonding generally do not [38]. The former systems are simpler than the latter because their phase diagram is effectively one-dimensional in regard to structure and dynamics. Systems with hidden scale invariance are sometimes referred to as Roskilde (R) simple [35, 50–62] to distinguish them from simple systems traditionally defined as pair-potential systems [10]. The theory presented below makes use of the simplicity provided by R simple systems' almost one-dimensional phase diagram [38] and gives a correction to the hard-sphere picture of melting and freezing based on first-order Taylor expansions. As will be demonstrated below, this provides excellent agreement with state-of-the-art computer simulation results.

Along an isomorph the structure is invariant in the reduced unit system defined [42] by the length unit $\rho^{-1/3}$ ($\rho \equiv N/V$ is the number density and V is the system volume), the energy unit $k_B T$ (T is the temperature), and the time unit $\sqrt{m\rho^{-2/3}/k_B T}$ (m is the particle mass). Figure 1(b) shows the LJ liquid's static structure factor $S(q)$ along an isomorph close to the freezing line (the one used below as the liquid-state reference isomorph) plotted for a range of temperatures. A comparison with Fig. 1(a) confirms the recent finding of Heyes and Branka [13] that the freezing line is not an isomorph, but it is close to one.

The melting pressure as a function of temperature, $p_m(T)$, can be predicted from infor-

mation obtained at a single coexistence reference state point. The details about how this works are given in the Supplementary Information. The argument may be summarized as follows. Recalling that the entropy as a function of density and temperature is a sum of an ideal-gas term and an "excess" term S_{ex} [10], isomorphs are the phase-diagram lines of constant excess entropy for any system obeying Eq. (1) [39, 42]. A computer simulation at the liquid/solid reference state point with density ρ_0 and temperature T_0 generates a series of configurations $\mathbf{R}_1^0, ..., \mathbf{R}_n^0$. Scaling each of these uniformly to density ρ one obtains configurations representative for the state point with density ρ and temperature T on the isomorph through the reference state point [39], in which T is identified from the configurational temperature expression $k_B T = \langle (\nabla U)^2 \rangle / \langle \nabla^2 U \rangle$ [63]. The average potential energy U and virial W at the state point (ρ, T) are likewise found by averaging over the scaled configurations. The key assumption here is that the canonical probabilities of the scaled configurations are identical to those of the original configurations, which follows from Eq. (1) [39] (note that no new molecular dynamics simulations are required). As shown in the Supplementary Information, in conjunction with the isochoric specific heat C_V calculated from the potential-energy fluctuations ($C_V = \langle (\Delta U)^2 \rangle / k_B T^2$), and the so-called density-scaling exponent $\gamma \equiv (\partial \ln T / \partial \ln \rho)_{S_{ex}}$ also calculated from the fluctuations ($\gamma = \langle \Delta U \Delta W \rangle / \langle (\Delta U)^2 \rangle$), one has enough information to determine the thermodynamics of freezing and melting as well as the variation along the melting line of isomorph-invariant properties like the reduced-unit viscosity and the Lindemann ratio.

B. Theory for the Lennard-Jones system

For the Lennard-Jones system a fairly simple analytic theory may be developed. It makes use of the fact that because the structure is isomorph invariant, it is possible to calculate the variation of the average potential energy analytically along an isomorph. This is done as follows. In reduced coordinates the pair correlation function $g(\tilde{r})$ is isomorph invariant ($\tilde{r} = \rho^{1/3} r$). Consequently, for pairs of LJ particles at distance r the thermal average $\langle r^{-n} \rangle$ scales with density as $\rho^{n/3}$ along an isomorph. Thus $\langle r^{-n} \rangle \propto \rho^{n/3}$ with a proportionality constant that only depends on S_{ex}, implying that the average potential energy U is of the form $U = A_{12}(S_{ex})\rho^4 + A_6(S_{ex})\rho^2$ (where $A_6(S_{ex}) < 0$) [64]. Since $T = (\partial U / \partial S_{ex})_\rho$, one has $T = A'_{12}(S_{ex})\rho^4 + A'_6(S_{ex})\rho^2$. It follows that if the five quantities S_{ex}, $A_{12}(S_{ex})$, $A_6(S_{ex})$,

6

$A'_{12}(S_{\mathrm{ex}})$, and $A'_6(S_{\mathrm{ex}})$ are known, the excess Helmholtz free energy, $U - TS_{\mathrm{ex}}$, is known along the reference isomorph. The required numbers are easily determined from reference state point simulations (see the Methods section and the Supplementary Information) – for instance the potential energy and virial give rise to two linear equations for determining $A_{12}(S_{\mathrm{ex}})$ and $A_6(S_{\mathrm{ex}})$. Once the excess Helmholtz free energy is known along the reference isomorph, the Gibbs free energy is found by adding the ideal-gas Helmholtz free energy and the pV term ($pV = Nk_BT + W$ in which the virial is given by $W = (\partial U/\partial \ln \rho)_{S_{\mathrm{ex}}} = 4A_{12}(S_{\mathrm{ex}})\rho^4 + 2A_6(S_{\mathrm{ex}})\rho^2$ [42]).

C.   Comparing theory to simulation results for the Lennard-Jones system

Following the above procedure we generated two reference isomorphs of the LJ system starting from the coexistence state point with temperature $T = 2\varepsilon/k_B$, a liquid-phase isomorph and a crystal-phase isomorph. Gibbs free energy of the liquid phase at coexistence, $G_l(T)$, is found by utilizing the fact that the freezing line is close to an isomorph. Since $(\partial G/\partial p)_T = V$, a good approximation to G_l at coexistence is

$$G_l(p_m(T), T) \cong G_l^I(T) + V_l^I(T)(p_m(T) - p_l^I(T)). \tag{2}$$

Here $p_m(T)$ is the coexistence pressure to be determined; $G_l^I(T)$ is the Gibbs free energy, $V_l^I(T)$ the volume, and $p_l^I(T)$ the pressure along the liquid-state reference isomorph. These are all known functions of the density on the isomorph henceforth denoted by ρ^I, which for a given temperature T is found by solving $T = A'_{12}(S_{\mathrm{ex}})(\rho^I)^4 + A'_6(S_{\mathrm{ex}})(\rho^I)^2$.

An analogous expression applies for the crystal's Gibbs free energy, of course, again involving only parameters determined from reference state-point simulations. The coexistence pressure is calculated by equating the liquid and solid phases' Gibbs free energies. As shown in the Supplementary Information this results in $p_m(T)(V_l^I(T) - V_s^I(T)) = C_1(T) + C_2(T) - C_3(T)$ in which $C_1(T)$ is the difference between $U_s^I(T) - (T/T_0)U_s^I(T_0)$ and the analogous term for the liquid reference isomorph ($U_s^I(T)$ is the crystal's potential energy along the reference isomorph), $C_2(T)$ is the difference between $Nk_BT \ln(\rho_s^I(T)/\rho_s^I(T_0))$ and the analogous liquid term, and $C_3(T)$ is the difference between $(T/T_0)W_s^I(T_0)$ and the analogous liquid term.

Figures 2(a) and (b) compare the theoretically predicted $p_m(T)$ to the coexistence pres-

7
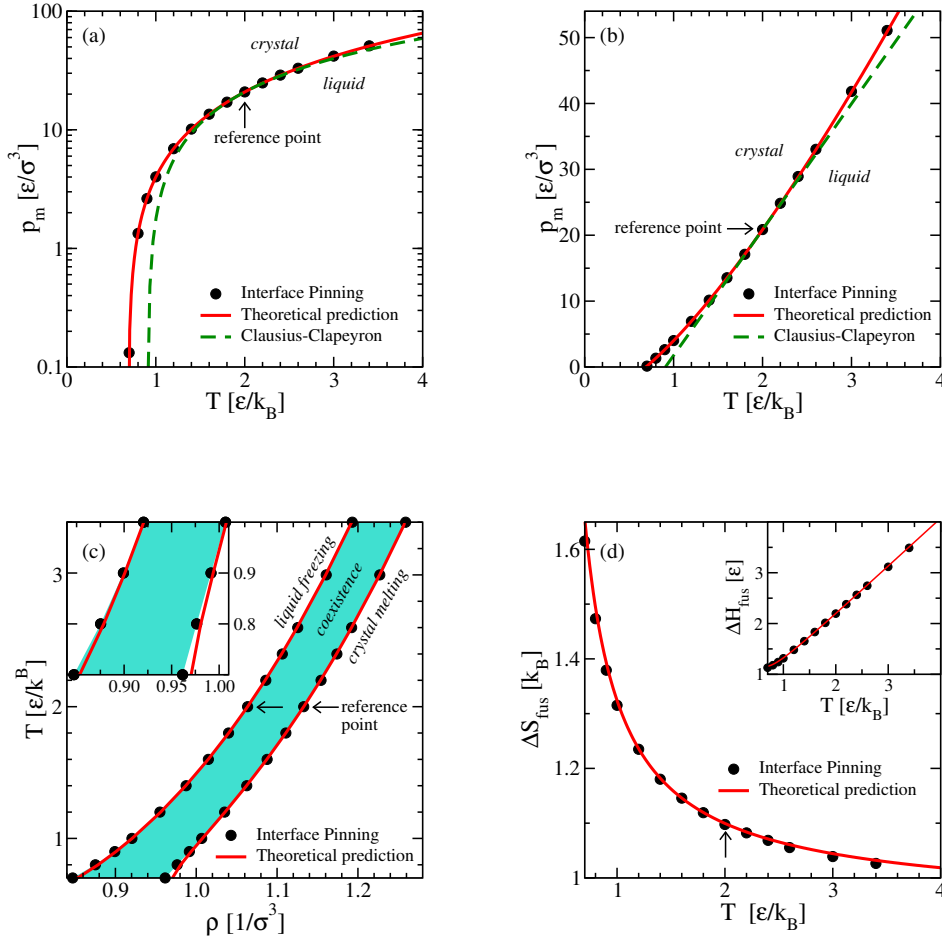
FIG. 2. Comparing theoretical predictions (full red curves) to the results of molecular dynamics simulations using the interface pinning method [37] (black dots) for the Lennard-Jones system. The theoretical predictions are based on simulations at the co-existence state point indicated by an arrow in each figure ($T_0 = 2\varepsilon/k_B$). Note that no fitting was done in these figures; the only input to the theory is properties of the co-existing liquid and crystal at the reference state point. (a) Temperature-pressure phase diagram. The green dashed line marks the expectation based on a linear extrapolation of the Clausius-Clapeyron relation $dp_m/dT = \Delta S_{\text{fus}}/\Delta V$ from the reference state point, i.e., assuming that the entropy of fusion and volume change are both constant. (b) The same data plotted with a linear pressure axis. (c) The freezing and melting lines in the density-temperature phase diagram. (d) Fusion entropy (main panel) and enthalpy (inset).

8

sure computed numerically by means of the interface pinning method [37]. The density of the crystalline and liquid phases along coexistence may likewise be computed by means of a first-order Taylor expansion (see the Supplementary Information). Figure 2(c) compares the predicted (ρ, T) phase diagram to that obtained by the interface-pinning molecular dynamics simulations. Finally, Fig. 2(d) shows the fusion entropy ΔS_{fus} and enthalpy ΔH_{fus}, the latter quantity being of course measured in experiments as the latent heat. In all cases there is good agreement between theory and simulations.

Having in mind the fact that the pressure at the triple point is very low for the LJ system, we estimate the triple point temperature to $T_{\text{tp}} = 0.688(2)\varepsilon/k_B$ from the theory by assuming zero pressure. This is within the statistical uncertainty of the triple point temperature computed with the interface pinning method. For comparison, a linear extrapolation of the Clausius-Clapeyron relation from the reference point (the green dashed lines on Figs. 2(a) and (b)) predicts a triple point temperature of $0.909(2)\varepsilon/k_B$.

Since the melting line is not an isomorph, the Lindemann ratio is not invariant along it as expected from the hard-sphere picture. The theory estimates the deviation from a constant Lindemann ratio by a first-order Taylor expansion from the reference isomorph (see the Supplementary Information). Figure 3(a) demonstrates good, though not perfect agreement between theory and numerical computations of the Lindemann ratio. The liquids' self-diffusion constant plays an important role for the crystal growth rate as expressed, e.g., in the Wilson-Frenkel law [65, 66]. This motivated us to use the theory to calculating the diffusion constant's variation along the freezing line (Fig. 3(b)). Another important component for crystal growth is the thermodynamic driving force on the crystal-liquid interface, which is determined by the Gibbs-free energy difference between the two phases, $\Delta G \cong (T_m - T)\Delta S_{\text{fus}}$ (ΔS_{fus} is shown on Fig. 2(d)). Finally, Fig. 3(c) shows the viscosity along the melting line. In all figures the blue dashed lines mark the prediction if the dynamics were invariant in reduced units, i.e., if the freezing/melting lines were isomorphs.

III. DISCUSSION

We have presented a theory for the thermodynamics of freezing and melting of systems characterized by hidden scale invariance. The theory enables one, in particular, to calculate the deviations from invariance of several quantities along the melting line predicted in the
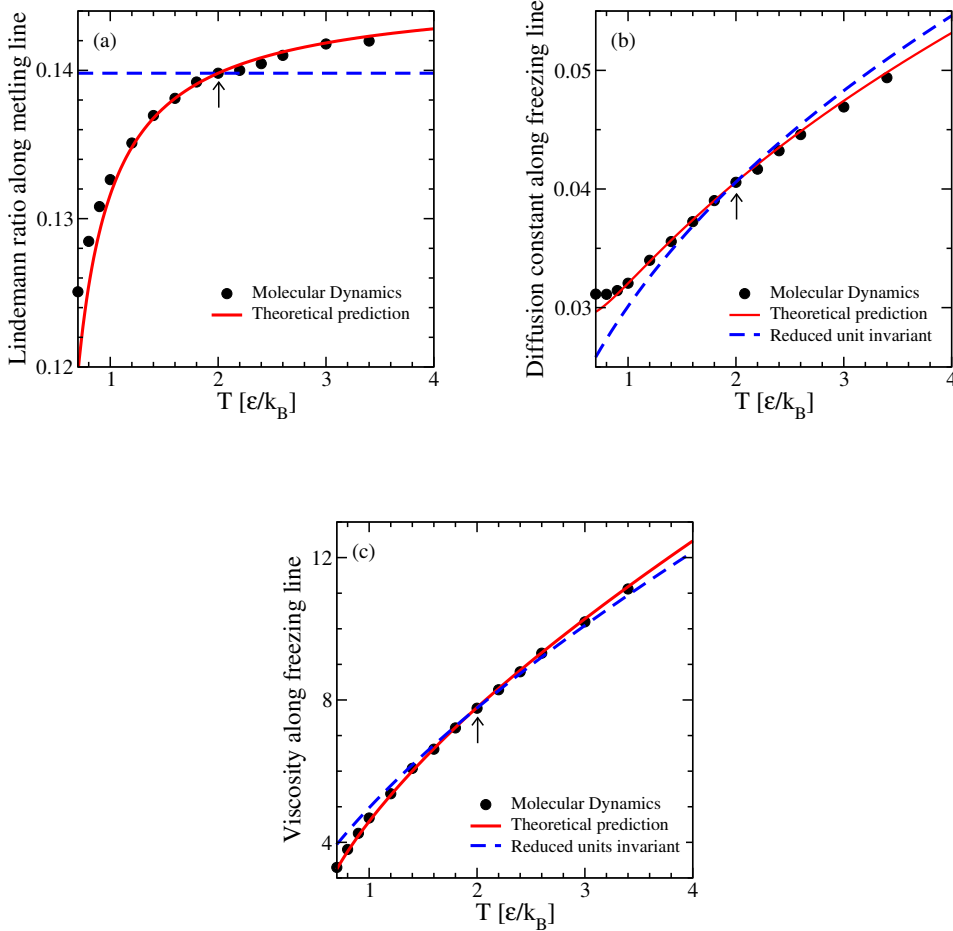
FIG. 3. (a) Lindemann ratio along the melting line. (b) Self-diffusion constant along the freezing line. (c) Viscosity along the freezing line. In all figures blue dashed lines show the predictions if perfect invariance of structure and dynamics in reduced units applied along the melting and freezing lines.

hard-sphere melting picture [9–13]. The theory is analytic for Lennard-Jones type system, i.e., systems involving a pair potential that is a difference of two inverse power laws, but the framework developed applies to any system with hidden scale invariance, including molecular systems. The theory generally works well, with the largest deviations found close to the triple point where the structure is not quite invariant along the reference isomorph (Fig. 1(b)).

Having established a firm foundation for the thermodynamics of freezing and melting for

R simple systems, it is our hope that it will soon be possible to address the challenging and exciting questions how nucleation and growth proceed, processes that are not well understood even for simple systems beyond the hard sphere system [67]. In particular, changes of the nucleation and growth mechanisms along the melting line may be analyzed in same way as above, i.e., by utilizing the fact that the freezing and melting lines are close to isomorphs along which the dynamics is invariant.

It is not clear to which degree the approach to melting may be generalized to quantum systems for which an outstanding question is the possible existence of a zero-temperature quantum fluid of metallic hydrogen. The quantum nature of the proton modifies classical melting, for example by increasing the value of the Lindemann ratio [68]. It would be interesting to investigate whether melting of quantum crystals may be understood in the above framework, but at the moment this awaits the development of an isomorph theory for quantum systems. In ongoing work we are addressing another open question, namely whether the above can be generalized to deal with more realistic systems, in particular metals for which density functional theory (DFT) computer simulations nowadays give realistic representations of the physics and have demonstrated hidden scale invariance for most metals [49].

IV. METHODS

We studied a Lennard-Jones system of $N = 5000$ particles with pair interactions truncated and shifted at 6σ. Coexistence pressures, p_m's, are computed with the interface pinning method [37] in which coexistence points are determined by computing the thermodynamic driving force on a solid-liquid interface. Table I lists the energy U_0 and virial W_0 at the reference temperature $T_0 = 2\varepsilon/k_B$ for both the liquid and crystal states at coexistence. The A_{12} and A_6 coefficients for the liquid and the crystal are computed from reference state point data using Eq. (6) in the Supplementary Material (all equation numbers in this section refer to the Supplementary Material). The derivative of the A coefficients with respect to excess entropy, A'_{12} and A'_6, are computed from reference state point data using Eq. (9) with the γ's listed in Table I. Melting pressures (Figs. 2(a) and 2(b)) are from reference state point data using Eq. (19) in which the potential energies along the isomorphs are expressed in Eq. (4). The densities along the liquid and crystal reference isomorphs are

TABLE I. Quantities at the two reference state points in coexistence. These numbers were used for calculating the theoretical predictions in Figs. 2 and 3 as detailed in the Supplementary Information.

$T_0 = 2.0\ \varepsilon/k_B$	Liquid	Crystal
$V_0/N\ [\sigma^3]$	$0.9403(2)^a$	$0.8827(2)$
$U_0/N\ [\varepsilon]$	$-4.7792(2)$	$-5.7774(2)$
$W_0/N\ [\varepsilon]$	$17.5418(7)$	$16.3628(6)$
γ_0	$4.9164(8)$	$4.8704(8)$
$C_V^{\mathrm{ex}}/N\ [k_B]$	$1.323(5)$	$1.301(7)$
$B_0 N\ [\varepsilon/k_B^2]$	$6.9(5)$	$7.2(5)$
L_0	-	$0.1398(2)$
$(\partial L/\partial T)_\rho\ [k_B/\varepsilon]$	-	$0.041(2)$
$\tilde{D}_0$	$0.02921(9)$	-
$(\partial \tilde{D}/\partial T)_\rho\ [k_B/\varepsilon]$	$0.0201(4)$	-
$\tilde{\eta}_0$	$5.2487(6)$	-
$(\partial \tilde{\eta}/\partial T)_\rho\ [k_B/\varepsilon]$	$-2.60(14)$	-

[a]Numbers in parenthesis give the estimated statistical uncertainty on the last digit using a 95% confidence interval.

found as functions of temperature by inversion of Eq. (7). The second derivative of the A coefficients, A_{12}'' and A_6'', are given by Eq. (13) where the excess heat capacity C_V^{ex} and $B \equiv \left(\partial (T/C_V^{\mathrm{ex}})/\partial \ln(\rho) \right)_{S_{\mathrm{ex}}}$ are listed in Table I. Densities of freezing and melting (Fig. 2(b)) are computed by combining Eqs. (20) and (23). The entropy of fusion ΔS_{fus} (Fig. 2d) is computed by combining Eqs. (25) to (28). The value of the Lindemann ratio L at the reference crystal, L_0, and its temperature derivative along an isochore, $(\partial L/\partial T)_\rho$, are listed in Table I. By letting $X = L$ in Eqs. (30) and (36) we arrive at the prediction shown in Fig. 3(a). Similarly, the predictions of the self-diffusion constant D (Fig. 3(b)) and viscosity η (Fig. 3(c)) are found by letting $X = \tilde{D} = D\rho^{1/3}\sqrt{m/k_B T}$ and $X = \tilde{\eta} = \eta/\rho^{2/3}\sqrt{mk_B T}$, respectively. D is determined from the long-time limit of the mean-square displacement; η was computed for a system of 4096 particles using the SLLOD algorithm as detailed in Ref. [30] except that we here have with more particles and a larger cutoff.

12

[1] D. Chandler, *Introduction to Modern Statistical Mechanics*. Oxford University Press, 1987.

[2] P. W. Atkins, *Physical Chemistry*. Oxford Univ. Press (Fourth edition), 1990.

[3] M. E. Glicksman, *Principles of Solidification: An Introduction to Modern Casting and Crystal Growth Concepts*. Springer, 2011.

[4] J. H. Eggert, D. G. Hicks, P. M. Celliers, D. K. Bradley, R. S. McWilliams, R. Jeanloz, J. E. Miller, T. R. Boehly, and G. W. Collins, "Melting temperature of diamond at ultrahigh pressure," *Nat. Phys.*, vol. 6, pp. 40–43, 2010.

[5] C. L. Guillaume, E. Gregoryanz, O. Degtyareva, M. I. McMahon, M. Hanfland, S. Evans, M. Guthrie, S. V. Sinogeikin, and H.-K. Mao, "Cold melting and solid structures of dense lithium," *Nat. Phys.*, vol. 7, pp. 211–214, 2011.

[6] N. X. Peng Tan and L. Xu, "Visualizing kinetic pathways of homogeneous nucleation in colloidal crystallization," *Nat. Phys.*, vol. 10, pp. 73–79, 2014.

[7] S. Deutschländer, A. M. Puertas, G. Maret, and P. Keim, "Specific heat in two-dimensional melting," *Phys. Rev. Lett.*, vol. 113, p. 127801, 2014.

[8] A. Statt, P. Virnau, and K. Binder, "Finite-size effects on liquid-solid phase coexistence and the estimation of crystal nucleation barriers," *Phys. Rev. Lett.*, vol. 114, p. 026101, 2015.

[9] A. C. Lawson, "An improved Lindemann melting rule," *Philos. Mag. B*, vol. 81, no. 3, pp. 255–266, 2001.

[10] J.-P. Hansen and I. R. McDonald, *Theory of Simple Liquids: With Applications to Soft Matter*. Academic, New York, fourth ed., 2013.

[11] U. R. Pedersen, F. Hummel, and C. Dellago, "Computing the crystal growth rate by the interface pinning method," *J. Chem Phys.*, vol. 142, p. 044104, 2015.

[12] R. Benjamin and J. Horbach, "Crystal growth kinetics in Lennard-Jones and Weeks-Chandler-Andersen systems along the solid-liquid coexistence line," *J. Chem. Phys.*, vol. 143, p. 014702, 2015.

[13] D. M. Heyes and A. C. Branka, "The Lennard-Jones melting line and isomorphism," *J. Chem Phys.*, vol. 143, p. 234504, 2015.

[14] J. D. van der Waals, *On the Continuity of the Gaseous and Liquid States*. PhD thesis, Universiteit Leiden, 1873.

[15] J. E. Lennard-Jones, "On the Determination of Molecular Fields. I. From the Variation of the Viscosity of a Gas with Temperature," *Proc. R. Soc. London A*, vol. 106, pp. 441–462, 1924.

[16] J. A. Barker and D. Henderson, "What is "liquid"? Understanding the states of matter," *Rev. Mod. Phys.*, vol. 48, pp. 587–671, 1976.

[17] K. Gubbins, W. Smitha, M. Tham, and E. Tiepel, "Perturbation theory for the radial distribution function," *Mol. Phys.*, vol. 22, p. 1089, 1971.

[18] W. G. Hoover, S. G. Gray, and K. W. Johnson, "Thermodynamic properties of the fluid and solid phases for inverse power potentials," *J. Chem. Phys.*, vol. 55, pp. 1128–1136, 1971.

[19] J. D. Weeks, D. Chandler, and H. C. Andersen, "Role of repulsive forces in determining the equilibrium structure of simple liquids," *J. Chem. Phys.*, vol. 54, pp. 5237–5247, 1971.

[20] C. Hausleitner, G. Kahl, and J. Hafner, "Liquid structure of transition metals: investigations using molecular dynamics and perturbation- and integral-equation techniques," *J. Phys.: Condens. Mat.*, vol. 3, no. 11, p. 1589, 1991.

[21] J.-P. Hansen and L. Verlet, "Phase transitions of the Lennard-Jones system," *Phys. Rev.*, vol. 184, pp. 151–161, 1969.

[22] Y. Rosenfeld, "Theory of simple classical fluids: Universality in the short-range structure," *Phys. Rev. A*, vol. 20, pp. 1208–1235, 1979.

[23] Y. Waseda, K. Yokoyama, and K. Suzuki, "Structure of molten Mg, Ca, Sr, and Ba by X-ray diffraction," *Z. Naturforsch. A*, vol. 30, pp. 801–805, 1975.

[24] M. Ross, "Generalized Lindemann melting law," *Phys. Rev.*, vol. 184, pp. 233–242, 1969.

[25] F. A. Lindemann, "Über die Berechning molekularer Eigenfrequenzen," *Phys. Z.*, vol. 11, p. 609, 1910.

[26] S. M. Stishov, "The thermodynamics of melting of simple substances," *Sov. Phys. Usp.*, vol. 17, no. 5, pp. 625–643, 1975.

[27] S.-N. Luo, A. Strachan, and D. C. Swift, "Vibrational density of states and Lindemann melting law," *J. Chem. Phys.*, vol. 122, p. 194709, 2005.

[28] C. Chakravarty, P. G. Debenedetti, and F. H. Stillinger, "Lindemann measures for the solid-liquid phase transition," *J. Chem. Phys.*, vol. 126, p. 204508, 2007.

[29] E. N. C. Andrade, "A theory of the viscosity of liquids - Part I," *Phil. Mag.*, vol. 17, pp. 497–511, 1934.

[30] L. Costigliola, T. B. Schrøder, and J. C. Dyre, "Freezing and melting line invariants of the Lennard-Jones system," *Phys. Chem. Chem. Phys.*, vol. 18, pp. 14678 – 14690, 2016.

[31] J.-P. Hansen, "Phase transition of the Lennard-Jones system. II. High-temperature limit," *Phys. Rev. A*, vol. 2, pp. 221–230, 1970.

[32] J. L. Tallon, "The entropy change on melting of simple substances," *Phys. Lett. A*, vol. 76, pp. 139–142, 1980.

[33] R. Agrawal and D. A. Kofke, "Solid-fluid coexistence for inverse-power potentials," *Phys. Rev. Lett.*, vol. 74, p. 122, 1995.

[34] D. Ben-Amotz and G. Stell, "Hard sphere perturbation theory for fluids with soft-repulsive-core potentials," *J. Chem Phys.*, vol. 120, p. 4844, 2004.

[35] D. M. Heyes, D. Dini, and A. C. Branka, "Scaling of Lennard-Jones liquid elastic moduli, viscoelasticity and other properties along fluid-solid coexistence," *Phys. Status Solidi (b)*, vol. 252, pp. 1514–1525, 2015.

[36] Y. Ding and J. Mittal, "Equilibrium and nonequilibrium dynamics of soft sphere fluids," *Soft Matter*, vol. 11, pp. 5274–5281, 2015.

[37] U. R. Pedersen, "Direct calculation of the solid-liquid Gibbs free energy difference in a single equilibrium simulation," *J. Chem. Phys.*, vol. 139, p. 104102, 2013.

[38] J. C. Dyre, "Hidden scale invariance in condensed matter," *J. Phys. Chem. B*, vol. 118, pp. 10007–10024, 2014.

[39] T. B. Schrøder and J. C. Dyre, "Simplicity of condensed matter at its core: Generic definition of a Roskilde-simple system," *J. Chem Phys.*, vol. 141, p. 204502, 2014.

[40] U. R. Pedersen, N. P. Bailey, T. B. Schrøder, and J. C. Dyre, "Strong Pressure-Energy Correlations in van der Waals Liquids," *Phys. Rev. Lett.*, vol. 100, p. 015701, 2008.

[41] N. P. Bailey, U. R. Pedersen, N. Gnan, T. B. Schrøder, and J. C. Dyre, "Pressure-Energy Correlations in Liquids. I. Results from Computer Simulations," *J. Chem. Phys.*, vol. 129, p. 184507, 2008.

[42] N. Gnan, T. B. Schrøder, U. R. Pedersen, N. P. Bailey, and J. C. Dyre, "Pressure-Energy Correlations in Liquids. IV. Isomorphs in Liquid Phase Diagrams," *J. Chem. Phys.*, vol. 131, p. 234504, 2009.

[43] T. Maimbourg and T. Kurchan, "Approximate scale invariance in particle systems: a large-dimensional justification," *arXiv:*, p. 1603.05023, 2016.

[44] C. M. Roland, S. Hensel-Bielowka, M. Paluch, and R. Casalini, "Supercooled dynamics of glass-forming liquids and polymers under hydrostatic pressure," *Rep. Prog. Phys.*, vol. 68, pp. 1405–1478, 2005.

[45] D. Gundermann, U. R. Pedersen, T. Hecksher, N. P. Bailey, B. Jakobsen, T. Christensen, N. B. Olsen, T. B. Schrøder, D. Fragiadakis, R. Casalini, C. M. Roland, J. C. Dyre, and K. Niss, "Predicting the density-scaling exponent of a glass–forming liquid from prigogine-defay ratio measurements," *Nat. Phys.*, vol. 7, pp. 816–821, 2011.

[46] W. Xiao, J. Tofteskov, T. V. Christensen, J. C. Dyre, and K. Niss, "Isomorph theory prediction for the dielectric loss variation along an isochrone," *J. Non-Cryst. Solids*, vol. 407, pp. 190–195, 2015.

[47] U. R. Pedersen, T. B. Schrøder, and J. C. Dyre, "Repulsive reference potential reproducing the dynamics of a liquid with attractions," *Phys. Rev. Lett.*, vol. 105, p. 157801, 2010.

[48] T. S. Ingebrigtsen, J. R. Errington, T. M. Truskett, and J. C. Dyre, "Predicting How Nanoconfinement Changes the Relaxation Time of a Supercooled Liquid," *Phys. Rev. Lett.*, vol. 111, p. 235901, 2013.

[49] F. Hummel, G. Kresse, J. C. Dyre, and U. R. Pedersen, "Hidden scale invariance of metals," *Phys. Rev. B*, vol. 92, p. 174116, Nov 2015.

[50] A. Malins, J. Eggers, and C. P. Royall, "Investigating Isomorphs with the Topological Cluster Classification," *J. Chem. Phys.*, vol. 139, p. 234505, 2013.

[51] E. H. Abramson, "Viscosity of fluid nitrogen to pressures of 10 GPa," *J. Phys. Chem. B*, vol. 118, p. (In press), 2014.

[52] J. Fernandez and E. R. Lopez, in *Experimental Thermodynamics: Advances in Transport Properties of Fluids*, ch. 9.3, pp. 307–317. Royal Society of Chemistry, 2014.

[53] E. Flenner, H. Staley, and G. Szamel, "Universal Features of Dynamic Heterogeneity in Supercooled Liquids," *Phys. Rev. Lett.*, vol. 112, p. 097801, 2014.

[54] S. Prasad and C. Chakravarty, "Onset of Simple Liquid Behaviour in Modified Water Models," *J. Chem. Phys.*, vol. 140, no. 16, p. 164501, 2014.

[55] U. Buchenau, "Thermodynamics and dynamics of the inherent states at the glass transition," *J. Non-Cryst. Solids*, vol. 407, pp. 179–183, 2015.

[56] K. Grzybowska, A. Grzybowski, S. Pawlus, J. Pionteck, and M. Paluch, "Role of entropy in the thermodynamic evolution of the time scale of molecular dynamics near the glass transition,"

Phys. Rev. E, vol. 91, p. 062305, 2015.

[57] K. R. Harris and M. Kanakubo, "Self-diffusion, velocity cross-correlation, distinct diffusion and resistance coefficients of the ionic liquid [BMIM][Tf2N] at high pressure," *Phys. Chem. Chem. Phys.*, vol. 17, pp. 23977–23993, 2015.

[58] T. S. Ingebrigtsen and H. Tanaka, "Effect of size polydispersity on the nature of Lennard-Jones liquids," *J. Phys. Chem. B*, vol. 119, no. 34, pp. 11052–11062, 2015.

[59] W. K. Kipnusu, M. Elsayed, W. Kossack, S. Pawlus, K. Adrjanowicz, M. Tress, E. U. Mapesa, R. Krause-Rehberg, K. Kaminski, and F. Kremer, "Confinement for more space: A larger free volume and enhanced glassy dynamics of 2-ethyl-1-hexanol in nanopores," *J. Phys. Chem. Lett.*, vol. 6, no. 18, pp. 3708–3712, 2015.

[60] J. W. P. Schmelzer and T. V. Tropin, "Kinetic criteria of glass-formation, pressure dependence of the glass-transition temperature, and the PrigogineDefay ratio," *J. Non-Cryst. Solids*, vol. 407, pp. 170–178, 2015.

[61] S. A. Khrapak, B. Klumov, L. Couedel, and H. M. Thomas, "On the long-waves dispersion in Yukawa systems," *Phys. Plasmas*, vol. 23, no. 2, 023702, 2016.

[62] K. Adrjanowicz, M. Paluch, and J. Pionteck, "Isochronal superposition and density scaling of the intermolecular dynamics in glass-forming liquids with varying hydrogen bonding propensity," *RSC Adv., in press*, 2016.

[63] J. G. Powles, G. Rickayzen, and D. M. Heyes, "Temperatures: old, new and middle aged," *Mol. Phys.*, vol. 103, no. 10, pp. 1361–1373, 2005.

[64] Y. Rosenfeld, "New method for equation-of-state calculations: Linear combinationsws of basis potentials," *Phys. Rev. A*, vol. 26, pp. 3633–3645, 1982.

[65] H. A. Wilson, "On the velocity of solidification and viscosity of supercooled liquids," *Philos. Mag.*, vol. 50, pp. 238–250, 1900.

[66] J. Frenkel, *Kinetic Theory of Liquids*. Clarendon, Oxford, 1946.

[67] S. Auer and D. Frenkel, "Prediction of absolute crystal-nucleation rate in hard-sphere colloids," *Nature*, vol. 409, pp. 1021–1023, 2001.

[68] S. T. Chui, "Solidification instability of quantum fluids," *Phys. Rev. B*, vol. 41, pp. 796–798, 1990.

ACKNOWLEDGMENTS

AUTHOR CONTRIBUTIONS

The project was conceived by URP and NPB. Computations were carried out by URP and LC. The theory was made by JCD based on initial work by NPB and TBS. The paper was written by URP and JCD.

CONFLICT OF INTEREST STATEMENT

The authors declare no conflicts of interest or competing financial interests.

Thermodynamics of freezing and melting - Supplementary Information

Ulf R. Pedersen, Lorenzo Costigliola, Nicholas P.
Bailey, Thomas B. Schrøder, and Jeppe C. Dyre

Glass and Time, IMFUFA, Department of Science and Environment,

Roskilde University, P. O. Box 260, DK-4000 Roskilde, Denmark

(Dated: May 26, 2016)

I. INTRODUCTION

A thermodynamic state point usually has a unique density $\rho \equiv N/V$ and temperature T. The reference state point is selected at the coexistence line, however, i.e., with known temperature T_0 and pressure p_0. There are here *two* different reference densities, a solid and a liquid one, below denoted respectively by $\rho_{s,0}$ and by $\rho_{l,0}$. In the density-temperature phase diagram there are likewise two reference isomorphs. The arguments developed in the next two sections refer to either one of these.

II. ISOMORPH CHARACTERISTICS: THE GENERAL CASE OF AN R SIMPLE SYSTEMS

As mentioned, the temperature-pressure reference state point defines two reference density-temperature state points, a liquid and a solid one. Let us focus on one of these with density ρ_0 and temperature T_0 (dropping subscripts s and l). From an NVT molecular dynamics equilibrium simulation (with a Nose-Hoover thermostat) several configurations $\mathbf{R}_1^0, ... \mathbf{R}_n^0$ are picked out. In order to map out the reference isomorph parametrized by density, one first identifies the temperature T such that (ρ, T) is on the isomorph through the reference state point. This is done as follows. If the scaled configurations are denoted by $\mathbf{R}_1, ... \mathbf{R}_n$ in which $\mathbf{R}_i = (\rho_0/\rho)^{1/3}\mathbf{R}_i^0$, T is determined from the standard configurational temperature expression:

$$k_B T = \frac{\langle (\nabla U(\mathbf{R}_i))^2 \rangle}{\langle \nabla^2 U(\mathbf{R}_i) \rangle} . \tag{1}$$

This determines the function $T(\tilde{\rho}^I)$ where we define the relative density along the isomorph by $\tilde{\rho}^I \equiv \rho^I/\rho_0$ with superscript I indicating "isomorph" (thus $T(1) = T_0$). By averaging the potential energy $U(\mathbf{R})$ and virial $W(\mathbf{R}) \equiv (-1/3)\mathbf{R} \cdot \nabla U(\mathbf{R})$ over the scaled configurations one finds $U(\tilde{\rho}^I)$ and $W(\tilde{\rho}^I)$. $C_V^{\text{ex}}(\tilde{\rho}^I)$ is found from the scaled configurations' potential energy via $C_V^{\text{ex}} = \langle (\Delta U)^2 \rangle / k_B T^2$ and $\gamma(\tilde{\rho}^I) \equiv (\partial \ln T/\partial \ln \rho)_{S_{\text{ex}}}$ via $\gamma = \langle \Delta U \Delta W \rangle / \langle (\Delta U)^2 \rangle$ [1, 2] (recall that isomorphs are curves of constant S_{ex}).

As shown in Sec. IV below one now has enough information to calculate the pressure along the melting line, $p_m(T)$. To calculate the liquid and solid densities along the melting line (Sec. V) one needs to know the below three partial derivatives. Denoting the derivative

along the isomorph with respect to $\tilde{\rho}^I$ of the virial by $W'(\tilde{\rho}^I)$ (which is basically the so-called hypervirial) and recalling that $W = (\partial U/\partial \ln \tilde{\rho})_{S_{\mathrm{ex}}}$ and $T = (\partial U/\partial S_{\mathrm{ex}})_{\tilde{\rho}}$ [1, 2], the three required quantities are given by

$$
\begin{aligned}
\left(\frac{\partial W}{\partial \ln \tilde{\rho}}\right)^I_{S_{\mathrm{ex}}} &= \tilde{\rho}^I \, W'(\tilde{\rho}^I) \\
\left(\frac{\partial W}{\partial S_{\mathrm{ex}}}\right)^I_{\tilde{\rho}} &= \frac{\partial^2 U}{\partial S_{\mathrm{ex}} \partial \ln \tilde{\rho}} = \left(\frac{\partial T}{\partial \ln \tilde{\rho}}\right)_{S_{\mathrm{ex}}} = T(\tilde{\rho}^I) \, \gamma(\tilde{\rho}^I) \\
\left(\frac{\partial S_{\mathrm{ex}}}{\partial \ln \tilde{\rho}}\right)^I_T &= -\frac{\left(\frac{\partial T}{\partial \ln \tilde{\rho}}\right)_{S_{\mathrm{ex}}}}{\left(\frac{\partial T}{\partial S_{\mathrm{ex}}}\right)_{\tilde{\rho}}} = -\frac{T(\tilde{\rho}^I)\gamma(\tilde{\rho}^I)}{T(\tilde{\rho}^I)/C_V{}^{\mathrm{ex}}(\tilde{\rho}^I)} = -C_V{}^{\mathrm{ex}}(\tilde{\rho}^I)\,\gamma(\tilde{\rho}^I)\,.
\end{aligned}
\tag{2}
$$

The entropy of fusion ΔS_{fus} is calculated by reference to Eq. (28) below. The three quantities needed here are given by

$$
\begin{aligned}
\left(\frac{\partial U}{\partial \ln \tilde{\rho}}\right)^I_{S_{\mathrm{ex}}} &= W(\tilde{\rho}^I) \\
\left(\frac{\partial U}{\partial S_{\mathrm{ex}}}\right)^I_{\tilde{\rho}} &= T(\tilde{\rho}^I) \\
\left(\frac{\partial S_{\mathrm{ex}}}{\partial \ln \tilde{\rho}}\right)^I_T &= -C_V{}^{\mathrm{ex}}(\tilde{\rho}^I)\,\gamma(\tilde{\rho}^I)\,.
\end{aligned}
\tag{3}
$$

III. ISOMORPH CHARACTERISTICS FOR GENERALIZED LENNARD-JONES PAIR POTENTIALS

The above quantities may be calculated analytically for generalized LJ pair potentials, i.e., for systems of particles interacting via pair potential(s) given as a sum or difference of two inverse power laws (IPLs), r^{-m} and r^{-n}. The below derivation applies for any $m > n > 0$ and for general multi-component systems; its subsequent application to freezing and melting deals with single-component systems only. In the main paper we study the standard single component LJ system with $m = 12$ and $n = 6$.

Invariance of the structure along an isomorph implies that the thermodynamic average potential energy at a given state point, U, may be written $U = A_m \tilde{\rho}^{m/3} + A_n \tilde{\rho}^{n/3}$ in which the two A coefficients are functions only of the excess entropy S_{ex}. For simplicity of notation

3

we do not indicate the S_{ex} dependence. The first and second order derivatives of A_m with respect to S_{ex} are marked by A'_m and A''_m and likewise for A_n.

The identity for the virial $W = (\partial U/\partial \ln \tilde{\rho})_{S_{\text{ex}}}$ implies

$$
\begin{aligned}
U &= A_m \tilde{\rho}^{m/3} \quad + A_n \tilde{\rho}^{n/3} \\
W &= \frac{m}{3} A_m \tilde{\rho}^{m/3} + \frac{n}{3} A_n \tilde{\rho}^{n/3} \, .
\end{aligned}
\tag{4}
$$

At the reference state point $\tilde{\rho} = 1$, so for determining A_m and A_n from reference state-point data we have the following two equations:

$$
\begin{aligned}
U_0 &= A_m \quad + A_n \\
W_0 &= \frac{m}{3} A_m + \frac{n}{3} A_n \, .
\end{aligned}
\tag{5}
$$

This implies

$$
\begin{aligned}
A_m &= \frac{3W_0 - nU_0}{m - n} \\
A_n &= \frac{mU_0 - 3W_0}{m - n} \, .
\end{aligned}
\tag{6}
$$

From the identity $T = (\partial U/\partial S_{\text{ex}})_{\tilde{\rho}}$ and the definition of the density-scaling exponent, $\gamma \equiv (\partial \ln T/\partial \ln \tilde{\rho})_{S_{\text{ex}}}$, we get

$$
\begin{aligned}
T &= A'_m \tilde{\rho}^{m/3} \quad + A'_n \tilde{\rho}^{n/3} \\
\gamma T &= \frac{m}{3} A'_m \tilde{\rho}^{m/3} + \frac{n}{3} A'_n \tilde{\rho}^{n/3} \, .
\end{aligned}
\tag{7}
$$

For determining A'_m and A'_n from reference state-point data one has

$$
\begin{aligned}
T_0 &= A'_m \quad + A'_n \\
\gamma_0 T_0 &= \frac{m}{3} A'_m + \frac{n}{3} A'_n \, .
\end{aligned}
\tag{8}
$$

This implies

$$
\begin{aligned}
A'_m &= \frac{3\gamma_0 - n}{m - n} T_0 \\
A'_n &= \frac{m - 3\gamma_0}{m - n} T_0 \, .
\end{aligned}
\tag{9}
$$

4

In order to arrive at the equations for A_m'' and A_n'', we first note that $C_V{}^{\text{ex}} = (\partial S_{\text{ex}}/\partial \ln T)_{\tilde{\rho}} = T(\partial S_{\text{ex}}/\partial T)_{\tilde{\rho}}$, i.e., $(\partial T/\partial S_{\text{ex}})_{\tilde{\rho}} = T/C_V{}^{\text{ex}}$. This implies that $T/C_V{}^{\text{ex}} = A_m'' \tilde{\rho}^{m/3} + A_n'' \tilde{\rho}^{n/3}$. If we define a thermodynamic quantity B by

$$B \equiv \left(\frac{\partial (T/C_V{}^{\text{ex}})}{\partial \ln \tilde{\rho}} \right)_{S_{\text{ex}}} , \tag{10}$$

one has

$$\frac{T}{C_V{}^{\text{ex}}} = A_m'' \tilde{\rho}^{m/3} \quad + A_n'' \tilde{\rho}^{n/3}$$
$$B = \frac{m}{3} A_m'' \tilde{\rho}^{m/3} + \frac{n}{3} A_n'' \tilde{\rho}^{n/3} . \tag{11}$$

The two equations for determining A_m'' and A_n'' from reference state point data are thus

$$\frac{T_0}{C_{V0}{}^{\text{ex}}} = A_m'' \quad + A_n''$$
$$B_0 = \frac{m}{3} A_m'' + \frac{n}{3} A_n'' . \tag{12}$$

This implies

$$A_m'' = \frac{3B_0 - nT_0/C_{V0}{}^{\text{ex}}}{m - n}$$
$$A_n'' = \frac{mT_0/C_{V0}{}^{\text{ex}} - 3B_0}{m - n} . \tag{13}$$

In summary, we have shown that (for each of the two reference isomorphs) the six numbers A_m, A_n, A_m', A_n', A_m'', and A_n'' may be found from reference state-point simulations determining: 1) the potential energy U_0, 2) the virial W_0, 3) the temperature T_0, 4) the excess isochoric specific heat $C_{V0}{}^{\text{ex}}$, 5) the density-scaling exponent γ_0, and 6) the derivative of $C_V{}^{\text{ex}}$ along the isomorph via the quantity B_0 defined in Eq. (10). The three first quantities are determined directly. The next two quantities are determined from fluctuations at the reference state point: $C_{V0}{}^{\text{ex}} = \langle (\Delta U)^2 \rangle / k_B T_0^2$ and $\gamma_0 = \langle \Delta W \Delta U \rangle / \langle (\Delta U)^2 \rangle$. The quantity B_0 is most accurately found from simulations along the reference isomorph carried out close to the reference state point, but in principle B_0 can be calculated from fluctuations at the reference state point (those needed are of third order and consequently of considerable numerical uncertainty). In the analysis presented in the main paper we calculated

B_0 numerically by directly applying Eq. 10; alternatively, following the methods used in Ref. 3 one may rewrite B as $B = (\rho T / C_V^{\mathrm{ex}}) \left[1 + (\partial \ln \gamma / \partial \ln T)_\rho \right]$ and evaluate B_0 from the constant density-variation of γ at the reference state point.

IV.   THE MELTING-LINE PRESSURE

This section shows how to calculate the pressure on the melting line as a function of temperature, $p_m(T)$. This quantity is determined by equating the liquid and solid phase's Gibbs free energies. Recalling that $V = (\partial G / \partial p)_T$ we estimate these from the Gibbs free energies along the isomorphs, $G_l^I(T)$ and $G_s^I(T)$, as follows (below $F_l^I(T)$ is the Helmholtz free energy along the liquid reference isomorph, etc)

$$
\begin{aligned}
G_l(T, p_m(T)) &\cong G_l^I(T) + V_l^I(T)(p_m(T) - p_l^I(T)) = F_l^I(T) + V_l^I(T) p_m(T) \\
G_s(T, p_m(T)) &\cong G_s^I(T) + V_s^I(T)(p_m(T) - p_s^I(T)) = F_s^I(T) + V_s^I(T) p_m(T) \, .
\end{aligned}
\tag{14}
$$

The coexistence condition $G_l(T, p_m) = G_s(T, p_m)$ leads to

$$
p_m(T)(V_l^I(T) - V_s^I(T)) = F_s^I(T) - F_l^I(T) \, .
\tag{15}
$$

If F_{id} is the Helmholtz free energy of an ideal gas, the Helmholtz free energy along the liquid isomorph is given by

$$
F_l^I(T) = U_l^I(T) - T S_{\mathrm{ex},l}^I + F_{\mathrm{id}}(T, \rho_l^I(T)) \, .
\tag{16}
$$

An analogous expression applies for the solid isomorph's Helmholtz free energy, $F_s^I(T)$. The two constants $S_{\mathrm{ex},l}^I$ and $S_{\mathrm{ex},s}^I$ are not known, but one only needs their difference. This is determined from the equilibrium condition at the reference state point, $G_l(T_0, p_0) = G_s(T_0, p_0)$ as expressed in Eq. (15), leading since $pV = N k_B T + W$ and $F_{\mathrm{id}}(T, \rho_l) - F_{\mathrm{id}}(T, \rho_s) = N k_B T \ln(\rho_l / \rho_s)$ to

$$
T_0 \left(S_{\mathrm{ex},l}^I - S_{\mathrm{ex},s}^I \right) = (U_{l,0} - U_{s,0}) + N k_B T_0 \ln(\rho_{l,0} / \rho_{s,0}) + (W_{l,0} - W_{s,0}) \, .
\tag{17}
$$

The coexistence condition Eq. (15) thus becomes (dropping the explicit temperature dependencies)

6

$$p_m(V_l^I - V_s^I) = (U_s^I - U_l^I) - \frac{T}{T_0}\left((U_{s,0} - U_{l,0}) + Nk_BT_0\ln(\rho_{s,0}/\rho_{l,0}) + (W_{s,0} - W_{l,0})\right) + Nk_BT\ln(\rho_s^I/\rho_l^I)$$

$$(18)$$

or, in terms of the relative density along the respective isomorphs $\tilde{\rho}^I$,

$$p_m(V_l^I - V_s^I) = \left(U_s^I - \frac{T}{T_0}U_{s,0}\right) - \left(U_l^I - \frac{T}{T_0}U_{l,0}\right) + Nk_BT\ln(\tilde{\rho}_s^I/\tilde{\rho}_l^I) + \frac{T}{T_0}\left(W_{l,0} - W_{s,0}\right). \quad (19)$$

In the case of an arbitrary potential there is no analytical expression for the potential energy as a function of density, the density (of each phase) is the control parameter and T is identified from Eq. (1), resulting by numerical inversion in two functions $\tilde{\rho}_s^I(T)$ and $\tilde{\rho}_l^I(T)$. In the case of generalized LJ pair potentials, for a given temperature T the functions $\tilde{\rho}_l^I(T)$ and $\tilde{\rho}_s^I(T)$ are found by solving Eq. (7) (in general numerically, but analytically for the 12-6 LJ system), using the A' coefficients of Eq. (9).

V. THE MELTING LINE-DENSITIES

To calculate the liquid and solid densities at coexistence as functions of temperature we work from the respective reference isomorphs knowing the coexistence pressure as a function of temperature, as well as the pressure along the reference isomorph. From this information one calculates the solid and liquid densities by moving on an isotherm from the reference isomorph to the freezing/melting line. In both cases we define the isothermal difference $\Delta W \equiv W(T) - W^I(T)$.

At any given temperature T the density $\tilde{\rho}$ of the liquid/solid at coexistence is calculated from

$$\Delta W \cong \left(\frac{\partial W}{\partial \ln \tilde{\rho}}\right)_T^I \Delta \ln \tilde{\rho} = \left(\frac{\partial W}{\partial \ln \tilde{\rho}}\right)_T^I \ln(\tilde{\rho}/\tilde{\rho}^I). \quad (20)$$

If $(\partial W/\partial \ln \tilde{\rho})_T^I$ is known, we can from this determine $\tilde{\rho}$. The following standard identity is used

$$\left(\frac{\partial W}{\partial \ln \tilde{\rho}}\right)_T = \left(\frac{\partial W}{\partial \ln \tilde{\rho}}\right)_{S_{\text{ex}}} + \left(\frac{\partial W}{\partial S_{\text{ex}}}\right)_{\tilde{\rho}}\left(\frac{\partial S_{\text{ex}}}{\partial \ln \tilde{\rho}}\right)_T. \quad (21)$$

In the case of an arbitrary potential, the three terms on the right hand side are calculated from Eq. (2). For the generalized LJ case, these terms are expressed in terms of the A coefficients on the reference isomorph using Eqs. (4) and (7) as follows

$$
\begin{aligned}
\left(\frac{\partial W}{\partial \ln \tilde{\rho}}\right)^I_{S_{\text{ex}}} &= \left(\frac{m}{3}\right)^2 A_m(\tilde{\rho}^I)^{m/3} + \left(\frac{n}{3}\right)^2 A_n(\tilde{\rho}^I)^{n/3} \\
\left(\frac{\partial W}{\partial S_{\text{ex}}}\right)^I_{\tilde{\rho}} &= \frac{m}{3}A'_m(\tilde{\rho}^I)^{m/3} + \frac{n}{3}A'_n(\tilde{\rho}^I)^{n/3} \\
\left(\frac{\partial S_{\text{ex}}}{\partial \ln \tilde{\rho}}\right)^I_T &= -\frac{\left(\frac{\partial T}{\partial \ln \tilde{\rho}}\right)^I_{S_{\text{ex}}}}{\left(\frac{\partial T}{\partial S_{\text{ex}}}\right)^I_{\tilde{\rho}}} = -\frac{\frac{m}{3}A'_m(\tilde{\rho}^I)^{m/3} + \frac{n}{3}A'_n(\tilde{\rho}^I)^{n/3}}{A''_m(\tilde{\rho}^I)^{m/3} + A''_n(\tilde{\rho}^I)^{n/3}} .
\end{aligned} \tag{22}
$$

We thus have in the generalized LJ case

$$
\left(\frac{\partial W}{\partial \ln \tilde{\rho}}\right)^I_T = \left(\frac{m}{3}\right)^2 A_m(\tilde{\rho}^I)^{m/3} + \left(\frac{n}{3}\right)^2 A_n(\tilde{\rho}^I)^{n/3} - \frac{\left(\frac{m}{3}A'_m(\tilde{\rho}^I)^{m/3} + \frac{n}{3}A'_n(\tilde{\rho}^I)^{n/3}\right)^2}{A''_m(\tilde{\rho}^I)^{m/3} + A''_n(\tilde{\rho}^I)^{n/3}} . \tag{23}
$$

In both cases, the equation for the density $\rho(T) = N/V(T)$ is found from Eq. (20) solved numerically in the form

$$
p_m(T)V(T) - Nk_BT - W^I(T) = \left(\frac{\partial W}{\partial \ln \tilde{\rho}}\right)^I_T \ln(\tilde{\rho}/\tilde{\rho}^I) . \tag{24}
$$

VI. THE ENTROPY OF FUSION

This section calculates the constant-pressure entropy of fusion ΔS_{fus}. One way to do this is to use the Clausius-Clapeyron equation $dp_m/dT = \Delta S_{\text{fus}}/\Delta V$ in which we now know all quantities appearing except ΔS_{fus}. An alternative method similar to the above proceeds as follows. Across the melting line one has $\Delta G = \Delta H_{\text{fus}} - T\Delta S_{\text{fus}} = 0$, i.e., $\Delta E - T\Delta S_{\text{fus}} + p_m(T)\Delta V = 0$. Since the kinetic energy is the same for liquid and solid at the given temperature T, this implies $\Delta E = \Delta U$ and thus

$$
\Delta S_{\text{fus}} = \frac{\Delta U + p_m\Delta V}{T} . \tag{25}
$$

This equation is used for evaluating ΔS_{fus} from simulations. It is also used for predicting $\Delta S_{\text{fus}}(T)$ by proceeding as follows. We have predictions for $p_m = p_m(T)$ and for $\Delta V =$

$V_l(T) - V_s(T)$. The missing term is $\Delta U = \Delta U(T)$, which by analogy to Eq. (20) is estimated via

$$\Delta U = U_l^I(T) + \left(\frac{\partial U}{\partial \ln \tilde{\rho}} \right)_T^{I,l} \ln(\tilde{\rho}_l(T)/\tilde{\rho}_l^I(T)) - U_s^I(T) - \left(\frac{\partial U}{\partial \ln \tilde{\rho}} \right)_T^{I,s} \ln(\tilde{\rho}_s(T)/\tilde{\rho}_s^I(T)) \,. \quad (26)$$

The partial derivatives refer to the respective reference isomorph as in the last section, and these are evaluated like those of W. Thus

$$\left(\frac{\partial U}{\partial \ln \tilde{\rho}} \right)_T^I = \left(\frac{\partial U}{\partial \ln \tilde{\rho}} \right)_{S_{\text{ex}}}^I + \left(\frac{\partial U}{\partial S_{\text{ex}}} \right)_{\tilde{\rho}}^I \left(\frac{\partial S_{\text{ex}}}{\partial \ln \tilde{\rho}} \right)_T^I \,. \quad (27)$$

In the case of an arbitrary potential, the three terms on the right hand side are calculated from Eq. (3). For the generalized LJ case, these terms may be expressed in terms of the A coefficients on the reference isomorph as follows

$$
\begin{aligned}
\left(\frac{\partial U}{\partial \ln \tilde{\rho}} \right)_{S_{\text{ex}}}^I &= W^I = \frac{m}{3} A_m (\tilde{\rho}^I)^{m/3} + \frac{n}{3} A_n (\tilde{\rho}^I)^{n/3} \\
\left(\frac{\partial U}{\partial S_{\text{ex}}} \right)_{\tilde{\rho}}^I &= T = A'_m (\tilde{\rho}^I)^{m/3} + A'_n (\tilde{\rho}^I)^{n/3} \\
\left(\frac{\partial S_{\text{ex}}}{\partial \ln \tilde{\rho}} \right)_T^I &= -\frac{\left(\frac{\partial T}{\partial \ln \tilde{\rho}} \right)_{S_{\text{ex}}}^I}{\left(\frac{\partial T}{\partial S_{\text{ex}}} \right)_{\tilde{\rho}}^I} = -\frac{\frac{m}{3} A'_m (\tilde{\rho}^I)^{m/3} + \frac{n}{3} A'_n (\tilde{\rho}^I)^{n/3}}{A''_m (\tilde{\rho}^I)^{m/3} + A''_n (\tilde{\rho}^I)^{n/3}} \,.
\end{aligned}
\quad (28)
$$

We now have the information required for calculating the entropy of fusion.

VII. MELTING-LINE VARIATION OF ISOMORPH INVARIANTS

We finally turn to the problem of evaluating how much an isomorph invariant X, e.g., the reduced vibrational crystalline mean-square displacement or the reduced liquid-state diffusion constant, varies along the freeaing/melting line. The starting point is that

$$X = \phi(S_{\text{ex}}) \,. \quad (29)$$

On the one hand

$$\left(\frac{\partial X}{\partial T} \right)_\rho = \phi'(S_{\text{ex}}) \left(\frac{\partial S_{\text{ex}}}{\partial T} \right)_\rho = \phi'(S_{\text{ex}}) \frac{C_V^{\text{ex}}}{T} \,. \quad (30)$$

9

On the other hand we have the general fluctuation formula:

$$\left(\frac{\partial X}{\partial T}\right)_\rho = \frac{\langle \Delta X \Delta U \rangle}{k_B T^2}. \tag{31}$$

Combining these equations at the reference state point leads to (where subscript 0 denotes an equilibrium average at the reference state point)

$$\phi'(S_{\text{ex}}) = \frac{\langle \Delta X \Delta U \rangle_0}{k_B T_0 C_{V0}^{\text{ex}}}. \tag{32}$$

Consider next an arbitrary temperature T on the melting line. We estimate X via (where ΔS_{ex} is the difference between crystal, respectively liquid, excess entropy at melting and that of the corresponding reference isomorph at the same temperature and $\Delta\rho$ likewise is the difference between crystal, respectively liquid, density at melting and that of the corresponding reference isomorph)

$$X \cong X_0 + \phi'(S_{\text{ex}})\Delta S_{\text{ex}} \cong X_0 + \phi'(S_{\text{ex}})\left(\frac{\partial S_{\text{ex}}}{\partial \rho}\right)_T \Delta\rho. \tag{33}$$

Equation (2) implies

$$\left(\frac{\partial S_{\text{ex}}}{\partial \rho}\right)_T^I = -\frac{\gamma C_V^{\text{ex}}}{\rho}. \tag{34}$$

In summary we have

$$X \cong X_0 - \phi'(S_{\text{ex}})\gamma C_V^{\text{ex}}\frac{\Delta\rho}{\rho}. \tag{35}$$

This implies

$$X \cong X_0 - \left(\frac{\partial X}{\partial T}\right)_\rho \gamma T_0 \frac{C_V^{\text{ex}}}{C_{V0}^{\text{ex}}}\frac{\Delta\rho}{\rho} \tag{36}$$

in which the derivative is evaluated at the reference state point. If X is a thermodynamic quantity, one may use this fluctuation expression

$$X \cong X_0 - \frac{\langle \Delta X \Delta U \rangle_0}{k_B T_0}\gamma\frac{C_V^{\text{ex}}}{C_{V0}^{\text{ex}}}\frac{\Delta\rho}{\rho}. \tag{37}$$

One now has expressions that may be used in the case of an arbitrary potential, as well as for the generalized LJ systems in which case analytical expressions are available.

---

[1] N. P. Bailey, U. R. Pedersen, N. Gnan, T. B. Schrøder, and J. C. Dyre, "Pressure-Energy Correlations in Liquids. II. Analysis and Consequences," *J. Chem. Phys.*, vol. 129, p. 184508, 2008.

[2] N. Gnan, T. B. Schrøder, U. R. Pedersen, N. P. Bailey, and J. C. Dyre, "Pressure-Energy Correlations in Liquids. IV. Isomorphs in Liquid Phase Diagrams," *J. Chem. Phys.*, vol. 131, p. 234504, 2009.

[3] N. P. Bailey, L. Bøhling, A. A. Veldhorst, T. B. Schrøder, and J. C. Dyre, "Statistical Mechanics of Roskilde Liquids: Configurational Adiabats, Specific Heat Contours, and Density Dependence of the Scaling Exponent," *J. Chem. Phys.*, vol. 139, p. 184506, 2013.

Communication: Studies of the Lennard-Jones fluid in 2, 3, and 4 dimensions highlight the need for a liquid-state 1/*d* expansion

Lorenzo Costigliola, Thomas B. Schrøder, and Jeppe C. Dyre
*Department of Science and Environment, "Glass and Time," IMFUFA, Roskilde University, P.O. Box 260,
DK-4000 Roskilde, Denmark*

The recent theoretical prediction by Maimbourg and Kurchan [e-print arXiv:1603.05023 (2016)] that for regular pair-potential systems the virial potential-energy correlation coefficient increases towards unity as the dimension *d* goes to infinity is investigated for the standard 12-6 Lennard-Jones fluid. This is done by computer simulations for $d = 2, 3, 4$ going from the critical point along the critical isotherm/isochore to higher density/temperature. In both cases the virial potential-energy correlation coefficient increases significantly. For a given density and temperature relative to the critical point, with increasing number of dimension the Lennard-Jones system conforms better to the hidden-scale-invariance property characterized by high virial potential-energy correlations (a property that leads to the existence of isomorphs in the thermodynamic phase diagram, implying that it becomes effectively one-dimensional in regard to structure and dynamics). The present paper also gives the first numerical demonstration of isomorph invariance of structure and dynamics in four dimensions. Our findings emphasize the need for a universally applicable 1/*d* expansion in liquid-state theory; we conjecture that the systems known to obey hidden scale invariance in three dimensions are those for which the yet-to-be-developed 1/*d* expansion converges rapidly. *Published by AIP Publishing.* [http://dx.doi.org/10.1063/1.4954239]

Recent years have brought notable progress in the understanding of the liquid state coming from studies of the high-dimensional limit. With roots back in time[1–5] and in a continuation of recent progress,[6–10] Charbonneau and collaborators in 2014 in a *tour de force* replica symmetry breaking calculation solved the glass problem in high dimensions for the prototypical hard-sphere (HS) model.[11] This was followed by a proof by Maimbourg, Kurchan, and Zamponi that the dynamics satisfies a universal equation in high dimensions for the general case of a system of particles interacting via pairwise additive forces.[12] This is how a "simple" liquid is traditionally defined,[13–17] although during the last 20 years it has gradually become clear that some systems—like the Gaussian core model, the Lennard-Jones Gaussian model, and the Jagla model—exhibit quite complex behavior (see, e.g., Ref. 18 and its references).

Very recently, Maimbourg and Kurchan showed that in the condensed phase, i.e., for states dominated by hard repulsions, any well-behaved pair-potential system has strong virial potential-energy correlations in sufficiently high dimensions.[19,20] Specifically, it was shown that the Pearson correlation coefficient R of the constant-volume canonical-ensemble equilibrium fluctuations of virial W and potential energy U,

$$R = \frac{\langle \Delta W \Delta U \rangle}{\sqrt{\langle (\Delta W)^2 \rangle \langle (\Delta U)^2 \rangle}}, \tag{1}$$

converges to unity as the number of dimensions d goes to infinity. The analysis presented in Ref. 19 also showed that the EXP pair potential (a simple exponential decay in space) plays the role as a building block of all pair potentials.[21,22] Note that,

in contrast to the inverse-power-law pair potentials $\propto r^{-n}$ (r being the pair distance), due to its rapid spatial decay the EXP pair potential has a thermodynamic limit in all dimensions.

Systems with R close to unity are characterized by "hidden scale invariance," an approximate symmetry that has been studied in several publications since its introduction in 2008; there are now also experimental verifications of the concept for van der Waals liquids.[23–26] Systems with hidden scale invariance are simple because they have so-called isomorphs in the thermodynamic phase diagram, which are lines along which structure and dynamics in suitably reduced units are invariant to a good approximation. The isomorph theory has been applied to atomic and molecular liquid and crystalline models in thermal equilibrium, as well as to non-equilibrium phenomena like shear flows of liquids and glasses (see, e.g., Ref. 27 and its references). Recently, it was shown from state-of-the-art DFT *ab initio* simulations of 58 liquid elements at their triple points that most metals possess hidden scale invariance.[28] An overview of the isomorph theory was given in Ref. 27 from 2014. After that paper was written, it became clear that Roskilde (R) simple systems[29–42]—those with $R > 0.9$—are characterized by approximately obeying the following condition:[43] $U(\mathbf{R}_a) = U(\mathbf{R}_b) \Leftrightarrow U(\lambda \mathbf{R}_a) = U(\lambda \mathbf{R}_b)$ in which $\mathbf{R}$ specifies all particle positions and $U(\mathbf{R})$ is the potential-energy function. Thus hidden scale invariance is equivalent to an approximate conformal invariance property.

The non-trivial finding of the above-mentioned works is that many realistic model systems—as well as many real-world liquids and solids—obey hidden scale invariance. It appears that most metals and van der Waals bonded liquids and solids

exhibit hidden scale invariance, whereas systems with strong directional bonds like covalently or hydrogen-bonded systems do not and are generally more complex.[27]

This paper presents computer simulations of the standard 12-6 Lennard-Jones (LJ) system in two, three, and four dimensions consisting of particles interacting via the pair potential

$$v_{LJ}(r) = 4\varepsilon \left[\left(\frac{r}{\sigma} \right)^{-12} - \left(\frac{r}{\sigma} \right)^{-6} \right]. \qquad (2)$$

Here ε and σ define the characteristic energy and length scales of the pair potential. The LJ system does not have a proper thermodynamic limit in more than five dimensions, and one may argue what is the correct generalization of this system to arbitrary dimension d (for instance, $v(r) \propto (r/\sigma)^{-(d+9)} - (r/\sigma)^{-(d+3)}$ or $v(r) \propto (r/\sigma)^{-4d} - (r/\sigma)^{-2d}$ or a third option). We avoided this problem by staying at low dimensions.

It is not obvious how to compare results for different thermodynamic state points in different dimensions. In high dimensions one may compare different state points by scaling the density such that the HS packing fraction remains invariant.[44] In our case of relatively low dimensions this is too crude; in any case, we also need a scaling of the temperature in order to be able to compare results obtained in different dimensions. The critical point of the LJ system is known for $d = 2, 3, 4,$[45–47] and we used this as reference state point. This choice has the further advantage that in three dimensions the virial potential-energy correlations are weak in the vicinity of the critical point, which allows one to monitor how R increases when the condensed "strongly correlating" liquid phase is approached upon increasing density or temperature.

Molecular dynamics simulations have been performed before in four spatial dimensions.[48–50] The simulations reported below used a homemade code applicable in arbitrary dimensions.[51] The code implements NVT dynamics with periodic boundary conditions[52] based on the leap-frog algorithm coupled with a Nose-Hoover thermostat. A shifted-forces cutoff at 2.5σ was used in all simulations.[53] The time step t_s varied with state point such that the reduced time step, $\tilde{t}_s \equiv t_s \rho^{1/d} \sqrt{k_B T/m}$, was 0.001 (here $\rho \equiv N/V$ is

the particle density and m the particle mass). After melting and equilibrating from a simple cubic configuration, the LJ system was simulated at every liquid state point for $2 \cdot 10^7$ time steps. In two dimensions the system crystallized at the three highest-density state points; simulations at these state points were performed with a reduced time step of $\tilde{t}_s = 0.0005$ and the number of time steps was doubled. In all cases the thermostat relaxation time was 80 time steps. The system size was $N = 1225$ in two, $N = 1728$ in three, and $N = 2401$ in four dimensions.

Our focus is on what happens in the fluid region of phase space in which the correlation coefficient R of Eq. (1) is far from unity in 3d. This number *is* close to unity in the "ordinary" 3d condensed liquid phase not too far from the melting line, as well as in the entire crystalline phase,[54–56] but approaching the gas phase and, in particular, the critical point in 3d, R drops quickly and the system is no more R simple.[55]

Figure 1 reports the reduced-unit radial distribution function $g(r)$ at the critical temperature T_c at 1.4 and 2 times the critical density; the black symbols mark $g(r)$ in two dimensions, the red curves in three dimensions, and the green curves in four dimensions. Figure 1 nicely confirms the argument of Maimbourg and Kurchan that in higher dimensions the nearest-neighbor distance increasingly dominates the physics.[19] Thus, beyond the first coordination shell $g(r)$ converges quickly to unity in high dimensions. In the words of Ref. 19, what happens in high dimensions is that a single pair distance dominates the physics because "particles that are too close are exponentially few in numbers, while those that are too far interact exponentially weakly." This argument presupposes, of course, that the pair potential in question has been generalized to any number of dimensions in a way ensuring a proper thermodynamic limit, i.e., such that it decays more rapidly than r^{-d} at long distances.

A system for which a single pair distance dominates the physics even in three dimensions is the hard-sphere (HS) system for which the radial distribution function at contact determines the equation of state.[57,58] The above suggests that one may regard the 3d HS system as *a poor man's version of the $d \to \infty$ limit*; indeed, it has been known for some time that the pair correlations of the HS system become
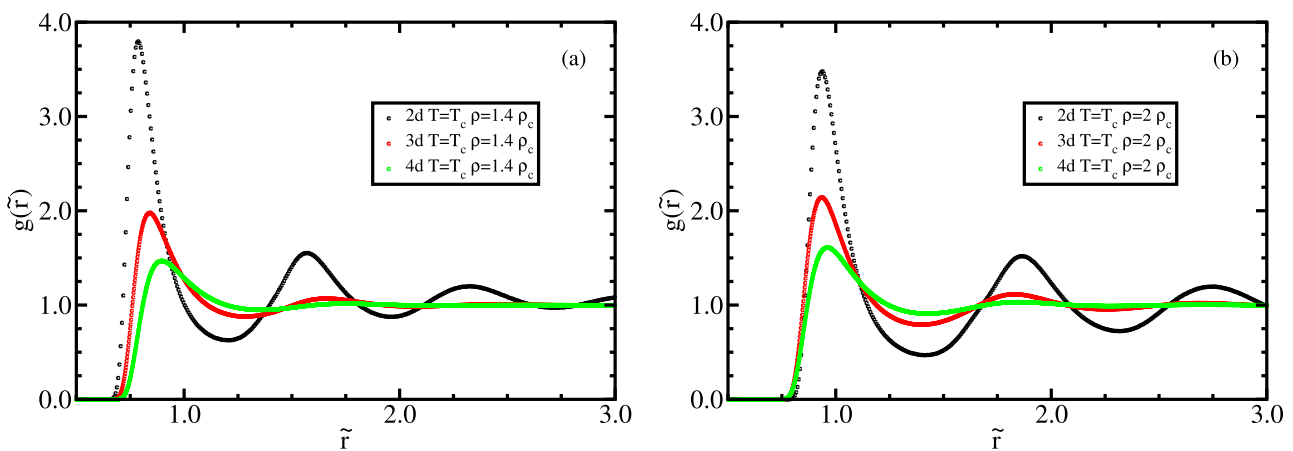

FIG. 1. Radial distribution function of the Lennard-Jones (LJ) fluid along the critical isotherm in two, three, and four dimensions (black, red, and green colors, respectively; $\tilde{r} \equiv \rho^{1/d} r$ where ρ is the particle density and r the interparticle distance). (a) shows results at 1.4 times the critical density ρ_c, (b) shows results at twice the critical density. In both cases the fluid's long-range structure becomes markedly less pronounced as the number of dimensions increases.
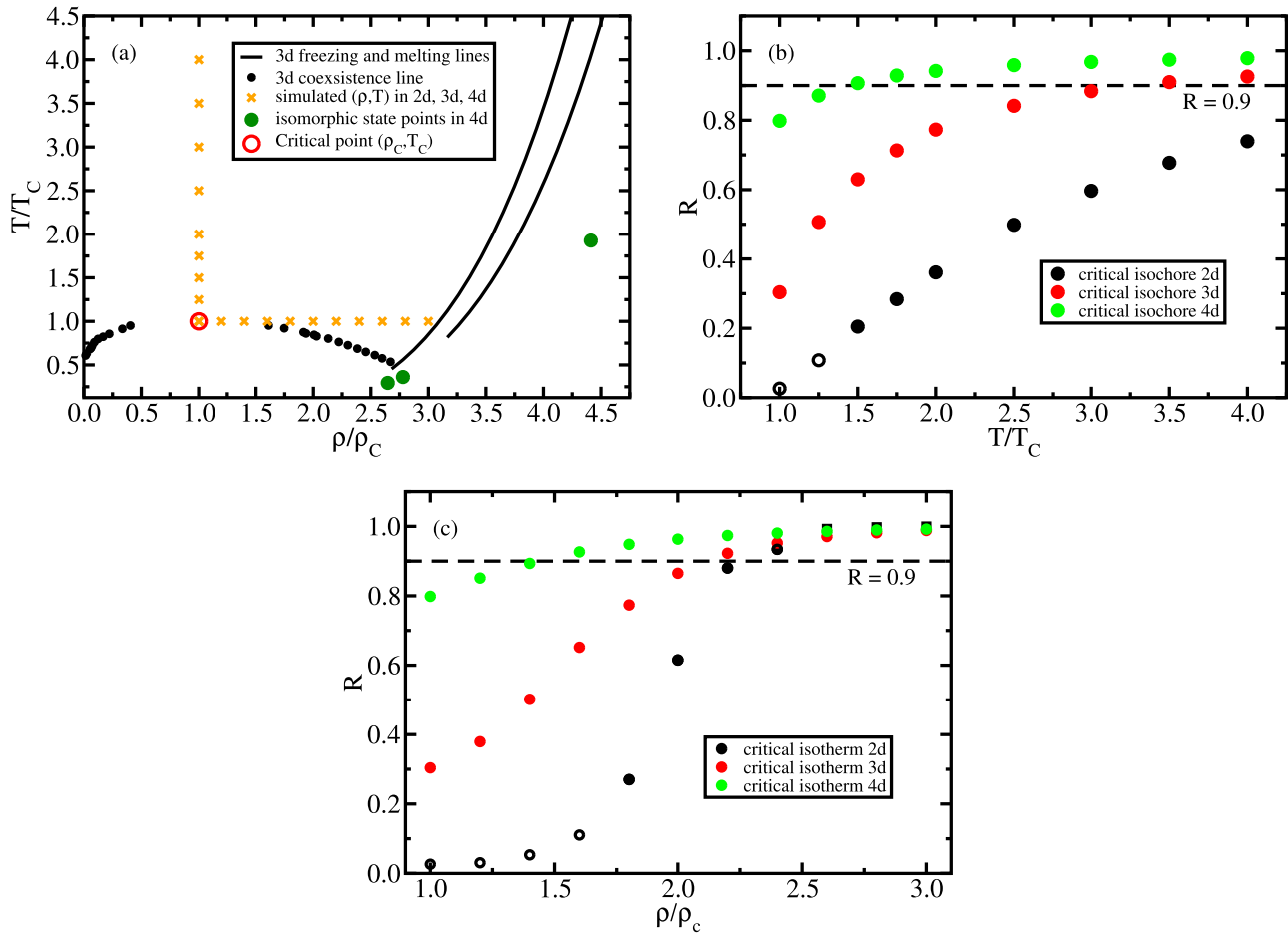
FIG. 2. The LJ fluid's virial potential-energy correlation coefficient in 2, 3, and 4 dimensions. (a) shows a sketch of the temperature-density phase diagram in which both variables are normalized to their values at the critical point, T_c and ρ_c.[45,47,63] The black symbols and full curves represent the phase limits of the LJ system in 3d (see, e.g., Refs. 64 and 65 and their references). The orange crosses mark the state points simulated in 2d, 3d, and 4d, whose virial potential-energy correlation coefficients are reported in (b) and (c), the green symbols indicate the three isomorphic state points simulated in 4d (Fig. 3). (b) The virial potential-energy correlation coefficient R (Eq. (1)) along the critical isochore. There is generally a convergence to the hidden-scale-invariance property characterizing R simple systems defined by $R > 0.9$ (dashed horizontal line), a situation that is reached much earlier in four than in three dimensions, where it is reached much earlier than in two dimensions. In two dimensions the system developed "holes" close to the critical point (see the main text), which is indicated by the two open symbols. (c) The virial potential-energy correlation coefficient at the critical isotherm. There is convergence to the hidden-scale-invariance scenario characterizing R simple systems, a situation that is reached much earlier in four than in three dimensions, where it is reached much earlier than in two dimensions. The two-dimensional system crystallized at the highest densities ($\rho/\rho_c > 2.5$), which as in (b) is indicated by black square symbols; the four open symbols at lower densities indicate that the sample developed "holes" close to the critical point.

increasingly trivial as d increases.[44,59,60] We note, however, that the HS system is not the only possibility of a 3d poor man's $d \to \infty$ limit; alternatives are the Gaussian core model[61] or the Mari-Kurchan model.[62]

In order to systematically compare what happens in different dimensions we studied the variation of the virial potential-energy correlation coefficient R of Eq. (1) as one moves away from the critical point along the critical isochore and isotherm. In units of ε/k_B for temperature and $1/\sigma^d$ for density, the critical point is given by $(\rho, T) = (0.355, 0.515)$ in two dimensions,[45] by $(\rho, T) = (0.316, 1.312)$ in three dimensions,[63] and by $(\rho, T) = (0.34, 3.404)$ in four dimensions[47] (the 2d and 3d critical point data were calculated by Monte Carlo (MC) simulations with the LJ potential truncated at the half-box length, the 4d critical point was determined by MC simulations with the potential truncated at 2.5σ).

Figure 2(a) gives an overview of the density-temperature thermodynamic phase diagram in which both variables in the standard van der Waals way were normalized to unity at the critical point. The full black curves indicate the freezing and melting lines for the 3d case, and the orange crosses mark the state points simulated. The results for R are shown in Fig. 2(b) for the critical isochore and in Fig. 2(c) for the critical isotherm (in both figures the horizontal dashed lines mark the (a bit arbitrary) threshold $R = 0.9$ defining R simple systems[54]). In two dimensions the system developed visible "holes" close to the critical point deriving from large density fluctuations;[66] the corresponding simulations are marked by open (black) symbols. In all cases, along both the isochore and the isotherm the correlations increase significantly as one moves away from the critical point. Note that in four dimensions R is fairly large already at the critical point.

When contemplating these findings one should keep in mind that R is close to unity for the LJ system in three dimensions in the "ordinary" condensed liquid phase not too far from the melting line. Our conclusions based on Fig. 2 are
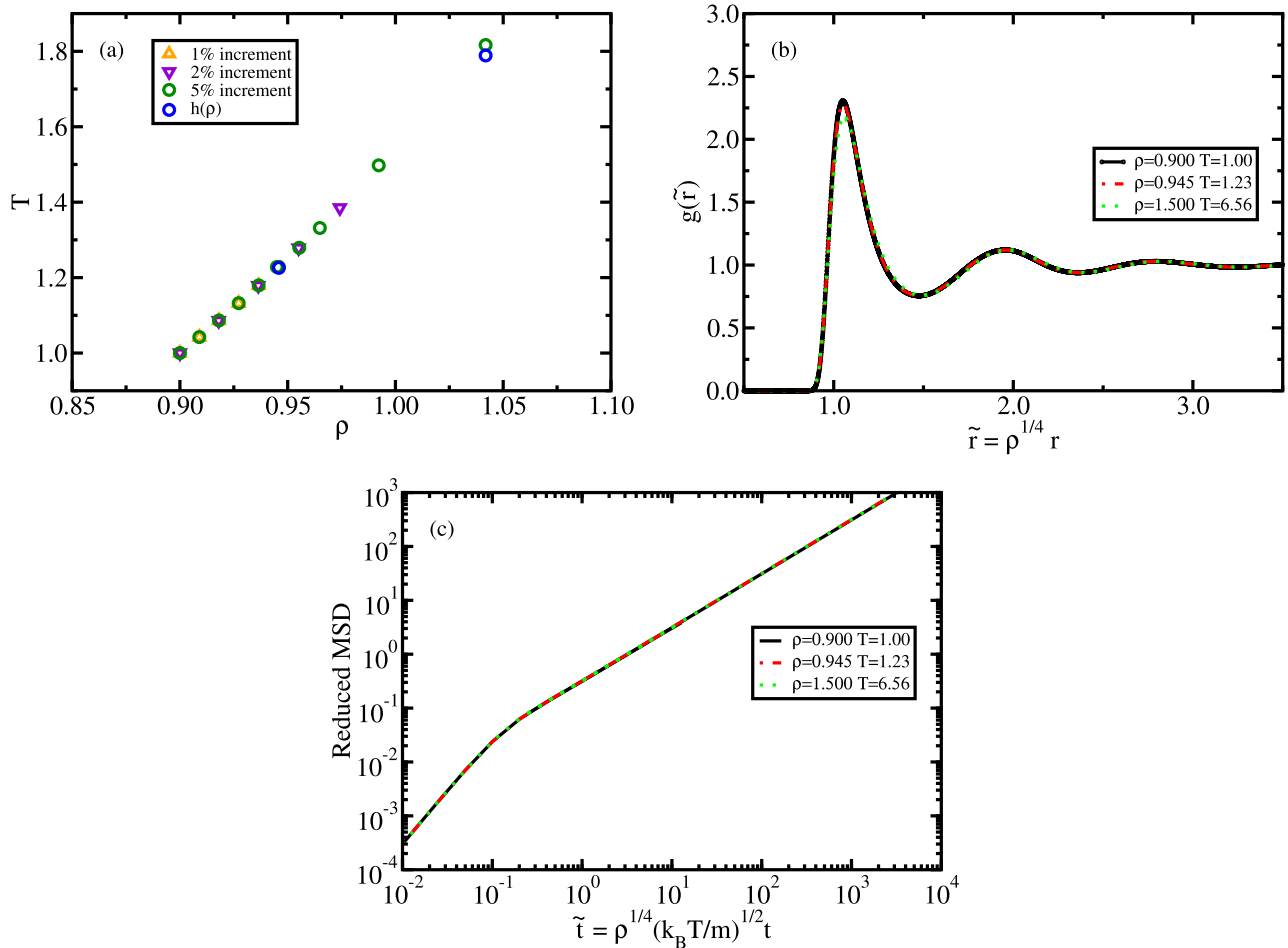
FIG. 3. Validation of isomorph invariance in four dimensions based on simulations at three state points on the same isomorph. Starting from the reference state point $(\rho\sigma^4, k_B T/\varepsilon) = (0.9, 1.0)$ two isomorphic state points were generated as described in the text. (a) Consistency check of the two different ways of generating isomorphs detailed in the text. The yellow, purple, and green symbols give the results of using Eq. (3) repeatedly for, respectively, a 1%, 2%, and 5% density increase starting from the reference state point; the blue point was calculated by the $h(\rho)$ method described in the text. (b) The pair distribution function at the three isomorphic state points plotted as a function of the reduced pair distance. The collapse demonstrates structural invariance along the isomorph. (c) Reduced mean-square displacement as a function of reduced time for the same three isomorphic state points, demonstrating isomorph invariance of the dynamics (reduced units are defined in Ref. 67).

(1) the simulations confirm the prediction of Maimbourg and Kurchan that all systems in their condensed-matter ("hard") regime have strong correlations in high dimensions. (2) There is a striking difference between two, three, and four dimensions, and already in four dimensions the correlations are strong whenever density and temperature are above their critical values.

Before proceeding to discuss the implications of these findings for liquid-state theory, we take the opportunity to demonstrate the existence of isomorphs in four dimensions. The most general method for mapping out an isomorph in the thermodynamic phase diagram makes use of the fact that isomorphs are configurational adiabats[43,67] in conjunction with the following standard fluctuation identity[67] (in which S_{ex} is the entropy minus that of an ideal gas at the same density and temperature):

$$\left(\frac{\partial \ln T}{\partial \ln \rho}\right)_{S_{ex}} = \frac{\langle \Delta W \Delta U \rangle}{\langle (\Delta U)^2 \rangle}. \quad (3)$$

We changed density in steps of 1%, 2%, and 5%, respectively, in each step calculating from Eq. (3) the temperature change

needed to keep S_{ex} constant. An alternative way of generating isomorphic state points, which is limited to LJ-type systems, utilizes the fact that due to invariance of the structure in reduced units, the quantity $h(\rho)/T$ is isomorph invariant where $h(\rho) = A\rho^{12/d} - B\rho^{6/d}$ (the two constants A and B, which are (slightly) isomorph dependent, are determined from simulations at a reference state point specifying the isomorph in question; see Refs. 65 and 68 for justification and more details of this procedure). Figure 3(a) demonstrates consistency between the two different ways of generating an isomorph in 4d, although for the largest density step (5%) there is a small disagreement.

The isomorph invariance of $h(\rho)/T$ signals a breakdown of the theory at low density at which the above expression for $h(\rho)$ becomes negative. This means that along any isomorph the virial potential-energy correlations must eventually weaken at low densities, which is also observed.[54,69] Since $R \to 1$ in high dimensions for the state points not too far away from the melting line,[19] one may speculate that in the $d \to \infty$ limit there is a phase transition between a phase of increasingly perfect hidden scale invariance and one of poor virial potential-energy correlations.[19,51]

Starting from the 4d state point $(\rho\sigma^4, k_B T/\varepsilon) = (0.9, 1.0)$ two isomorphic state points were found. The first one $(\rho\sigma^4, k_B T/\varepsilon) = (0.945, 1.23)$ was identified using Eq. (3) as described above, the second one $(\rho\sigma^4, k_B T/\varepsilon) = (1.5, 6.56)$ was determined using the isomorph invariance of $h(\rho)/T$. Figure 3(b) shows the pair distribution function as a function of reduced radius for the three state points. The collapse validates structural invariance along the 4d isomorph. Figure 3(c) shows the mean-square displacement as a function of time in reduced units for the same three state points, demonstrating isomorph invariance also of the dynamics.

Turning back to the dimensionality dependence of the virial potential-energy correlations, our findings may be summarized as follows. Above the critical point as the number of dimensions increases the LJ system converges rapidly to the state of perfect hidden scale invariance shown by Maimbourg and Kurchan to characterize the high-dimensional limit. Assuming that the challenge of generalizing arbitrary systems to arbitrary dimensions has been addressed, we conjecture the following: (1) All systems (also molecular ones) obey hidden scale invariance in sufficiently high dimensions in their condensed phases; (2) the rate with which this property translates into lower dimensions depends on the system in question. In other words, if one defines the van der Waals scaled density $\tilde{\rho} \equiv \rho/\rho_c$ and temperature $\tilde{T} \equiv T/T_c$, we conjecture that $R(\tilde{\rho}, \tilde{T}) \to 1$ as $d \to \infty$ for all systems, at least whenever $\tilde{\rho} > 1$ and $\tilde{T} > 1$. The rate of convergence determines whether or not the system is R simple in three dimensions.

If the above conjecture is correct, any system at any given condensed-matter state point has a "transition region" of dimensionalities above which it becomes R simple. This range of dimensions is located below three dimensions for systems that are R simple in three dimensions (at the state point in question) and above three for those that are not.

An important task for the future will be to construct a systematic $1/d$ expansion taking one from the case of guaranteed R simple behavior as $d \to \infty$ to three dimensions. Hints of how this may be done were given in Ref. 11 for the HS case, but a more general approach is needed. We find it conceivable that future textbooks in liquid-state theory start by deriving a simple and general theory in the limit of high dimensions and subsequently translate this into three dimensions via a $1/d$ expansion, but clearly much remains to be done before this becomes reality.

[1]F. H. Ree and W. G. Hoover, J. Chem. Phys. **40**, 2048 (1964).
[2]H. L. Frisch and J. K. Percus, Phys. Rev. A **35**, 4696 (1987).
[3]M. Luban and J. P. J. Michels, Phys. Rev. A **41**, 6796 (1990).
[4]H. L. Frisch, in *Condensed Matter Theories*, edited by L. Blum and F. B. Malik (Plenum Press, New York, 1993), Vol. 8, pp. 443–448.
[5]H. L. Frisch and J. K. Percus, Phys. Rev. E **60**, 2942 (1999).
[6]G. Parisi and F. Slanina, Eur. Phys. J. B **8**, 603 (1999).
[7]G. Parisi and F. Slanina, Phys. Rev. E **62**, 6554 (2000).
[8]G. Parisi, J. Stat. Phys. **132**, 207 (2008).
[9]P. Charbonneau, A. Ikeda, G. Parisi, and F. Zamponi, Phys. Rev. Lett. **107**, 185702 (2011).
[10]J. Kurchan, G. Parisi, and F. Zamponi, J. Stat. Mech. **2012**, P10012.
[11]P. Charbonneau, J. Kurchan, G. Parisi, P. Urbani, and F. Zamponi, Nat. Commun. **5**, 3725 (2014).
[12]T. Maimbourg, J. Kurchan, and F. Zamponi, Phys. Rev. Lett. **116**, 015902 (2016).
[13]S. A. Rice and P. Gray, *The Statistical Mechanics of Simple Liquids* (Interscience, New York, 1965).
[14]H. N. V. Temperley, J. S. Rowlinson, and G. S. Rushbrooke, *Physics of Simple Liquids* (Wiley, New York, 1968).
[15]J.-L. Barrat and J.-P. Hansen, *Basic Concepts for Simple and Complex Liquids* (Cambridge University Press, 2003).
[16]B. Kirchner, Phys. Rep. **440**, 1 (2007).
[17]J.-P. Hansen and I. R. McDonald, *Theory of Simple Liquids: With Applications to Soft Matter*, 4th ed. (Academic, New York, 2013).
[18]T. S. Ingebrigtsen, T. B. Schrøder, and J. C. Dyre, Phys. Rev. X **2**, 011011 (2012).
[19]T. Maimbourg and J. Kurchan, e-print arXiv:1603.05023 (2016).
[20]J. Kurchan, T. Maimbourg, and F. Zamponi, J. Stat. Mech. **2016**, 033210.
[21]A. K. Bacher and J. C. Dyre, Colloid Polym. Sci. **292**, 1971 (2014).
[22]A. K. Bacher, T. B. Schrøder, and J. C. Dyre, Nat. Commun. **5**, 5424 (2014).
[23]D. Gundermann, U. R. Pedersen, T. Hecksher, N. P. Bailey, B. Jakobsen, T. Christensen, N. B. Olsen, T. B. Schrøder, D. Fragiadakis, R. Casalini, C. M. Roland, J. C. Dyre, and K. Niss, Nat. Phys. **7**, 816 (2011).
[24]L. Bøhling, T. S. Ingebrigtsen, A. Grzybowski, M. Paluch, J. C. Dyre, and T. B. Schrøder, New J. Phys. **14**, 113035 (2012).
[25]L. A. Roed, D. Gundermann, J. C. Dyre, and K. Niss, J. Chem. Phys. **139**, 101101 (2013).
[26]W. Xiao, J. Tofteskov, T. V. Christensen, J. C. Dyre, and K. Niss, J. Non-Cryst. Solids **407**, 190 (2015).
[27]J. C. Dyre, J. Phys. Chem. B **118**, 10007 (2014).
[28]F. Hummel, G. Kresse, J. C. Dyre, and U. R. Pedersen, Phys. Rev. B **92**, 174116 (2015).
[29]A. Malins, J. Eggers, and C. P. Royall, J. Chem. Phys. **139**, 234505 (2013).
[30]E. H. Abramson, J. Phys. Chem. B **118**, 11792 (2014).
[31]J. Fernandez and E. R. Lopez, in *Experimental Thermodynamics: Advances in Transport Properties of Fluids* (Royal Society of Chemistry, 2014), Chap. 9.3, pp. 307–317.
[32]E. Flenner, H. Staley, and G. Szamel, Phys. Rev. Lett. **112**, 097801 (2014).
[33]S. Prasad and C. Chakravarty, J. Chem. Phys. **140**, 164501 (2014).
[34]U. Buchenau, J. Non-Cryst. Solids **407**, 179 (2015).
[35]K. Grzybowska, A. Grzybowski, S. Pawlus, J. Pionteck, and M. Paluch, Phys. Rev. E **91**, 062305 (2015).
[36]K. R. Harris and M. Kanakubo, Phys. Chem. Chem. Phys. **17**, 23977 (2015).
[37]D. M. Heyes, D. Dini, and A. C. Branka, Phys. Status Solidi (b) **252**, 1514 (2015).
[38]T. S. Ingebrigtsen and H. Tanaka, J. Phys. Chem. B **119**, 11052 (2015).
[39]W. K. Kipnusu, M. Elsayed, W. Kossack, S. Pawlus, K. Adrjanowicz, M. Tress, E. U. Mapesa, R. Krause-Rehberg, K. Kaminski, and F. Kremer, J. Phys. Chem. Lett. **6**, 3708 (2015).
[40]J. W. P. Schmelzer and T. V. Tropin, J. Non-Cryst. Solids **407**, 170 (2015).
[41]S. A. Khrapak, B. Klumov, L. Couedel, and H. M. Thomas, Phys. Plasmas **23**, 023702 (2016).
[42]K. Adrjanowicz, M. Paluch, and J. Pionteck, RSC Adv. (in press).
[43]T. B. Schrøder and J. C. Dyre, J. Chem. Phys. **141**, 204502 (2014).
[44]M. Bishop and P. A. Whitlock, J. Stat. Phys. **126**, 299 (2007).
[45]B. Smit and D. Frenkel, J. Chem. Phys. **94**, 5663 (1991).
[46]H. Okumura and F. Yonezawa, J. Chem. Phys. **113**, 9162 (2000).
[47]M. Hloucha and S. I. Sandler, J. Chem. Phys. **111**, 8043 (1999).
[48]R. C. van Schaik, H. J. C. Berendsen, A. E. Torda, and W. F. van Gunsteren, J. Mol. Biol. **234**, 751 (1993).
[49]M. Bishop, A. Masters, and J. H. R. Clarke, J. Chem. Phys. **110**, 11449 (1999).
[50]W. R. P. Scott, P. H. Hünenberger, I. G. Tironi, A. E. Mark, S. R. Billeter, J. Fennen, A. E. Torda, T. Huber, P. Krüger, and W. F. van Gunsteren, J. Phys. Chem. A **103**, 3596 (1999).
[51]L. Costigliola, "Isomorph theory and extensions," Ph.D. thesis, Roskilde University, 2016; Computer code for simulating in arbitrary dimensions available at http://dirac.ruc.dk/~lorenzoc.
[52]M. P. Allen and D. J. Tildesley, *Computer Simulation of Liquids* (Oxford Science Publications, 1987).
[53]S. Toxvaerd and J. C. Dyre, J. Chem. Phys. **134**, 081102 (2011).
[54]N. P. Bailey, U. R. Pedersen, N. Gnan, T. B. Schrøder, and J. C. Dyre, J. Chem. Phys. **129**, 184507 (2008).

55N. P. Bailey, T. B. Schrøder, and J. C. Dyre, Phys. Rev. E **90**, 042310 (2014).

56D. E. Albrechtsen, A. E. Olsen, U. R. Pedersen, T. B. Schrøder, and J. C. Dyre, Phys. Rev. B **90**, 094106 (2014).

57Y. Song, R. M. Stratt, and E. A. Mason, J. Chem. Phys. **88**, 1126 (1988).

58Y. Song, E. A. Mason, and R. M. Stratt, J. Phys. Chem. **93**, 6916 (1989).

59M. Bishop, P. A. Whitlock, and D. Klein, J. Chem. Phys. **122**, 074508 (2005).

60P. A. Whitlock, M. Bishop, and J. L. Tiglias, J. Chem. Phys. **126**, 224505 (2007).

61D. Coslovich, A. Ikeda, and K. Miyazaki, Phys. Rev. E **93**, 042602 (2016).

62R. Mari and J. Kurchan, J. Chem. Phys. **135**, 124504 (2011).

63J. J. Potoff and A. Z. Panagiotopoulos, J. Chem. Phys. **109**, 10914 (1998).

64D. M. Heyes, CMST **21**, 169 (2015).

65L. Costigliola, T. B. Schrøder, and J. C. Dyre, Phys. Chem. Chem. Phys. **18**, 14678 (2016).

66M. Rovere, D. W. Heermann, and K. Binder, J. Phys.: Condens. Matter **2**, 7009 (1990).

67N. Gnan, T. B. Schrøder, U. R. Pedersen, N. P. Bailey, and J. C. Dyre, J. Chem. Phys. **131**, 234504 (2009).

68L. Bøhling, N. P. Bailey, T. B. Schrøder, and J. C. Dyre, J. Chem. Phys. **140**, 124510 (2014).

69N. P. Bailey, L. Bøhling, A. A. Veldhorst, T. B. Schrøder, and J. C. Dyre, J. Chem. Phys. **139**, 184506 (2013).

RUMD: A general purpose molecular dynamics package optimized to utilize GPU hardware down to a few thousand particles

Nicholas P. Bailey,[1, *] Trond S. Ingebrigtsen,[1] Jesper Schmidt Hansen,[1] Arno A. Veldhorst,[1] Lasse Bøhling,[1] Claire A. Lemarchand,[1] Andreas E. Olsen,[1] Andreas K. Bacher,[1] Lorenzo Costigliola,[1] Ulf R. Pedersen,[1] Heine Larsen,[1] Jeppe C. Dyre,[1] and Thomas B. Schrøder[1, †]

[1]DNRF Center "Glass and Time", IMFUFA,

Dept. of Sciences, Roskilde University,

P.O. Box 260, DK-4000 Roskilde, Denmark

(Dated: June 10, 2016)

Abstract

RUMD is a general purpose, high-performance molecular dynamics (MD) simulation package running on graphical processing units (GPU's). RUMD addresses the challenge of utilizing the many-core nature of modern GPU hardware when simulating small to medium system sizes (roughly from a few thousand up to hundred thousand particles). It has a performance that is comparable to other GPU-MD codes at large system sizes and substantially better at smaller sizes. RUMD is open-source and consists of a library written in C++ and the CUDA extension to C, an easy-to-use Python interface, and a set of tools for set-up and post-simulation data analysis. The paper describes RUMD's main features, optimizations and performance benchmarks.

I. INTRODUCTION

This paper describes Roskilde University Molecular Dynamics (RUMD), a Graphical Processing Unit (GPU)-based molecular dynamics (MD) code developed to achieve good performance at small and medium system sizes, while remaining competitive with other GPU-MD codes at large sizes. The attention paid to small sizes distinguishes RUMD from many other GPU-MD codes. It has been in development since 2009, and available as open-source software[1], since 2011. The newest version 3.1, was released May 2016.

The rise of GPU-based computation has been discussed by various authors[2–8]. Several groups have developed molecular dynamics codes based on GPUs from scratch or incorporated GPU-acceleration into existing projects. Examples of the former include HOOMD-Blue[9–12], ACEMD[13], OpenMM[14,15] and HAL's MD[16] while the latter include NAMD[17], LAMMPS[18], AMBER[19] and Gromacs[20]. Other works involving GPU-based MD codes, going back to 2007, can be found in Refs. 21–32. We omit a detailed exposition of GPU programming basics here. For a good overview of massive multi-threading using CUDA see the relevant section in the article by Anderson *et al.*[9]. For further information the reader can consult the book by Kirk and Hwu[33] as well as the CUDA programming guide[34]. A technical overview of the Tesla architecture, which marks the first major development of GPUs for scientific computing by NVIDIA, can be found in Ref. 35. The more advanced Fermi architecture is documented in Ref. 36. The most recent architectures Kepler (2012) and Maxwell (2014) are described in Ref. 37 and 38 respectively.

The large computational power of modern GPUs comes primarily from the large number of hardware cores, each executing a number of software threads. As an example, the GeForce Gtx780Ti card has 2880 cores and a theoretical single-precision peak-performance of 5.0 TFlops (5×10^{12} floating point operations per second). A key element to achieve good performance from a GPU is that the number of active software threads should be much larger than the number of hardware cores in order to hide latency of memory access. This makes it a challenge to utilize the GPU hardware when the number of particles N is relatively small ($N \sim 10^3 - 10^4$). The obvious choice for parallelization, namely having one thread compute the forces for one particle, is clearly not efficient when the optimal number of threads exceeds the number of particles. There are three reasons to focus on utilizing the GPU hardware even at small system sizes; i) If one is interested in investigating long time scales rather than large systems. This is the case, for example, in the field of viscous liquid dynamics, where a system size of 10^4 particles is considered large, but the

interest is in studying as long time scales as possible. Note that finite size effects are relatively limited in these systems; for example Karmakar, Dasgupta, and Sastry[39] found convergence of diffusivity and relaxation time for a standard glass-forming model liquid already at N=1000. ii) As a building block for multi-GPU simulations (RUMD currently uses one GPU per simulation). If one wants to simulate, say, 10^5 particles using 10 GPU's, the single-GPU performance obviously needs to be good for 10^4 particles. iii) For the foreseeable future much of the development in GPU and other many-core hardware will probably be in increasing the number of physical cores, much more than increasing the computational power of the individual core. Thus, what might today be considered a large system, might in the future be considered a small/medium sized system where special care needs to be taken to utilize the GPU hardware. To optimize the use of the hardware RUMD allows multiple threads per particle; this approach has also been considered in two recent publications[40,41].

The paper is organized as follows. Section II contains a brief overview of RUMD's features. The main part of the paper focuses on the methods used for calculating the non-bonding pair interactions and the generation of the neighbor-list. These are the most computationally demanding parts of an MD simulation and where our code distinguishes itself from most other GPU-MD codes. Section III discusses the challenges of utilizing the GPU hardware at small system sizes, and section IV gives an overview of the optimization strategies employed in RUMD. Section V describes the calculation of non-bonding pair-forces, while sections VI and VII describes two different methods for generating the neighbor-list. Section VIII provides benchmarks of RUMD in comparison to three different GPU extensions of LAMMPS[18], as well as an analysis of the effect of the different optimizations employed in RUMD. Section IX describes RUMD's performance for electrostatic (Coulomb) interactions. Section X provides a short summary.

II. RUMD: FEATURES

RUMD is a general purpose molecular dynamics code. Below we list its main features; for more information please see the tutorial and user manual included with the software and available from the project's website `rumd.org`.

Python interface: Users control the software via a Python interface which allows simulations of considerable complexity to be implemented straightforwardly. An example of a simple user Python-script is given in Fig. 1.

```
# Import RUMD
from rumd import *
from rumd.Simulation import Simulation


# Create a simulation object, and import an initial configuration.
sim = Simulation("start.xyz.gz")


# Create a pair potential and associate it with the simulation object
pot = Pot_LJ_12_6(cutoff_method=ShiftedForce)
pot.SetParams(0, 0, Sigma=1.0, Epsilon=1.0, Rcut=2.5)
sim.SetPotential(pot)


# Create an integrator and associate it with the simulation object
itg = IntegratorNVT(timeStep=0.004, targetTemperature=1.0)
sim.SetIntegator(itg)


# Run a simulation. Data are saved on disk and can be analyzed by a number of tools
sim.Run(1000000)
```

FIG. 1: Script showing the python code needed to run a very simple simulation, in this case a single-component Lennard-Jones fluid simulated at constant temperature 1.0 for one million time steps of size 0.004 in Lennard-Jones units. The number of particles and the density is determined by the initial configuration contained in the file start.xyz.gz

Pair potentials: 12-6 Lennard-Jones, generalized Lennard-Jones, inverse power law, Gaussian core, Buckingham, Dzugotov, Girifalco, Yukawa, and more. New pair potentials are easily added, as described in the tutorial. Three different "cutoff methods" for truncating the pair potential are provided: simple truncation with no shift; truncation plus shift of the potential energy to ensure continuity; and truncation plus shift of the pair force[42] to ensure its continuity (this corresponds to adding a linear term in the potential).

Other interactions: Intramolecular interactions including constraints, bond-stretching forces, angular forces and dihedral forces.

Integrators: NVE (Verlet/Leap-frog), NVT (Nosé-Hoover), NPT[43], NVU (geodesics on the constant potential energy surface)[44,45]. Couette shear flow using the SLLOD equations of motion and Lees-Edwards boundary conditions.

File formats: configurations are stored in xyz format with extensions, compressed using gzip;

data can be saved logarithmically in time for efficient use of disk space while allowing the study of a large range of time scales in a single simulation; molecular structure (bonds, angles and dihedrals) is specified in separate topology files. Tools for creating initial configurations and topology files are provided.

Analysis tools: Basic statistics of energy, pressure, etc. for thermodynamics. Measures of structure; radial distribution function, static structure factor, radius of gyration, mean-square end-to-end distance. Measures of dynamics; mean-square displacement, incoherent intermediate scattering function, non-Gaussian parameter, end-to-end vector autocorrelation function, Rouse-mode autocorrelation function. New analysis tools are continuously being added. Analysis tools work on data stored during simulations and can thus be applied at the end of (or during) a simulation run. In addition the user can define customized on-the-fly analysis tools written in Python.

Auto-tuner: A script for optimizing internal parameters—specifically, the choice of algorithm for generating the neighbor list, the neighbor-list skin size, and the way the generation of the neighbor list and the calculation of non-bonding forces are distributed among the GPU threads.

RUMD is mostly implemented in single precision. This leads to a drift in the total energy when running long constant-energy (NVE) simulations, but is not an issue for NVT and NPT simulations where a thermostat is applied. RUMD can be made fully double precision by a search and replace in the source code - we are planning to implement a more elegant way for the user to choose between single and double precision. RUMD uses a single GPU per simulation; support for multiple GPU simulations is planned for future development.

III.   THE PROBLEM OF UTILIZING THE DEVICE AT SMALL SYSTEM SIZES

Consider NVIDIA's Kepler GK110 architecture that appeared in 2013. One of the Kepler design goals was power efficiency, which was partly achieved by increasing the number of cores while decreasing the clock speed compared to the previous Fermi architecture. Thus each streaming multiprocessor (of type SMX) has 192 cores, and the GPU has up to 15 SMX units. The GTX 780Ti card contains the maximum 15 SMX units, giving 2880 cores. Furthermore, the CUDA model requires a much greater number of threads to be active, in order to hide memory access
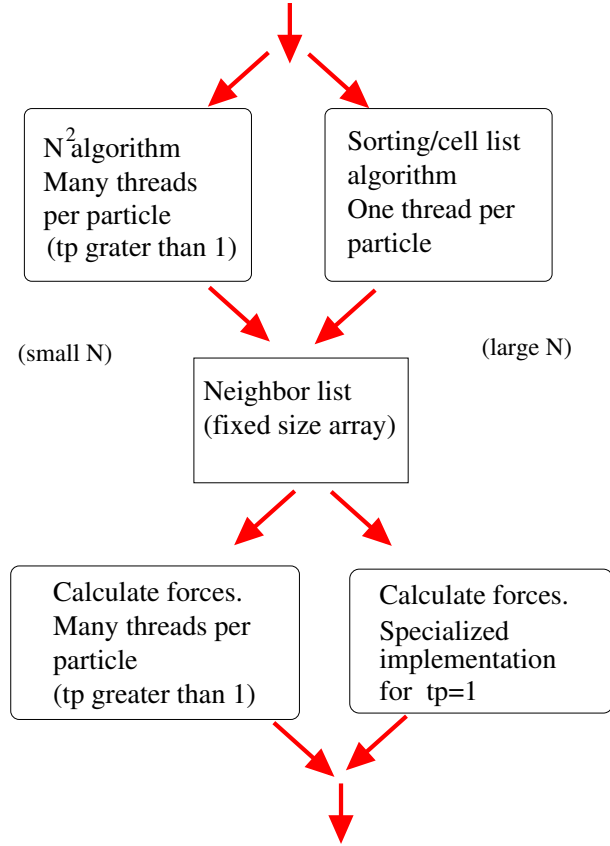
FIG. 2: Schematic diagram representation of the two algorithms for neighbor-list generation, and the force calculation algorithm. The latter uses multiple threads per particle (tp), but an implementation also exists for the special case tp=1.

latency. This poses a challenge when small systems of the order of thousands of particles are concerned. Logically, in order to use as many threads as possible, one must therefore have multiple threads computing the force on one particle.

Having multiple threads per particles entails some overhead, in particular the summing of the force contributions over the threads allocated to a given particle. This means that as the system size increases, it becomes less useful to have more than one thread per particle. We control this by the parameter t_p (threads per particle, denoted `TPerPart` in the code), and let the auto-tuner pick the optimal value for a given simulation. The optimal value of t_p depends primarily on the number of particles, but also on density and the range of the potential. We use a separate kernel involving a single thread per particle for larger sizes (see Fig. 2); this is faster than setting $t_p = 1$ in the general kernel.

Rovigatti *et al.* have recently discussed the possible advantages of "vertex-based" (atom-

decomposition[46], one thread per particle) versus "edge-based" (force-decomposition[46], one thread per interaction) parallelism[47]. Our approach includes the former, and a range of intermediate cases, while not taking it to the extreme of one thread per interaction.

IV.   OVERVIEW OF OPTIMIZATION STRATEGIES USED IN RUMD

As in any general purpose MD software some kind of data structure to keep track of neighbors for the non-bonding pair interactions is necessary to reduce the complexity of the force calculation from $O(N^2)$ to $O(N)$. We use a classical Verlet-type neighbor list, stored as 2-dimensional fixed-size array of size $Nn_{\max}$ where $n_{\max}$ is the assumed maximum number of neighbors per particle. If this happens to be exceeded the neighbor-list is automatically re-allocated with doubled capacity. For smaller systems we set $n_{\max} = N$ from the start to avoid the overhead of checking for overflow. Neighbors within $r_c + s$ are listed, where r_c is the maximum cut-off associated with the potential, and s is the extra skin included so that the neighbor-list does not need to be rebuilt every step. The optimal value of the skin is determined by the auto-tuner.

We now describe the methods employed in the calculation of short-range non-bonding forces and the generation of the neighbor-list. The main four optimizations are as follows:

1. Multiple threads per particle ($t_p \geq 1$) in force calculation and neighbor-list generation. The auto-tuner chooses the best value for t_p.

2. Two methods for rebuilding the neighbor-list: $O(N^2)$ method ($t_p \geq 1$) for small system sizes, and an $O(N)$ method ($t_p = 1$) for larger sizes. The auto-tuner picks the best method.

3. Use of the so-called "read only data-cache" for reading positions (for devices of compute capability at least 3.5 this can be done straightforwardly via the function __ldg()).

4. Use of pre-fetching when reading from the neighbor-list to compensate for memory access latency.

V.   FORCE CALCULATION

The force calculation kernel (routine executed on the GPU) is shown in Fig. 3. Short-hand notation for common quantities used in this and the following CUDA-kernels are given in Table

```
__global__ void Calcf_NBL_tp( ... )
  [ Declare shared memory ]
  float4 my_f = {0.0f, 0.0f, 0.0f, 0.0f};        // Initialize the force of this thread
  float4 my_r = LOAD(r[MyGP]);                    // Read position of this particle
  int type_i = __float_as_int(my_r.w);           // Type of this particle
  [ Read information on the simulation box from device memory ]
  [ Copy potential parameters to shared memory ]
  __syncthreads();                // Parameters loaded to shared memory before proceeding

  int nb, my_num_nbrs = num_nbrs[MyGP];          // Read number of neighbors
  nb_prefetch = nbl[nvp*MyT + MyGP];             // Read index of first neighbor
  for (int i=MyT; i<my_num_nbrs; i+=TPerPart) {  // Loop over neighbors
    nb = nb_prefetch;
    if(i+TPerPart < my_num_nbrs)
      nb_prefetch = nbl[nvp*(i+TPerPart) + MyGP];
    float4 r_i = LOAD(r[nb]);                     // Read position of neighbor
    int type_i = __float_as_int(r_i.w);          // Type of neighbor
    // Add contribution from this pair to my_f:
    fij( potential, my_r, r_i, &my_f, [parameters, simulation box] );
  }
  __syncthreads();

  // Now use the shared memory for summing force contributions:
  s_r[MyP+MyT*PPerBlock] = my_f;
  __syncthreads();
  // Sum over threads associated with the same particle:
  if( MyT == 0 ) {
    for( int i=1; i < TPerPart; i++ ) my_f += s_r[MyP + i*PPerBlock];
    my_f.w *= 0.5f;   // Compensate for double counting of potential energy
    // Write result to device memory
    if(initialize)    // Flag (templated) for whether to initialize forces
      f[MyGP] = my_f; // (can be false when multiple potentials present)
    else {
      atomicAdd(&(f[MyGP].x), my_f.x);
      [also y, z, w]
    }
  }
}
```

FIG. 3: Kernel calculating forces on particles given the neighbor-list (nbl) shown in the simplest version where only forces and potential energy of each particle are computed. For a given particle each of t_p threads ($MyT = 0, 1, ..., t_p - 1$) computes part of the total force, which is summed up at the end. The function fij (not shown) adds an individual pair contribution to the current thread's force (my_f). Note the use of __syncthreads to synchronize threads within a thread-block. This is to ensure that all data are available in shared memory before any thread reads from it (first and third occurrences) or that all threads are done with the data in shared memory before it is used for other data (second occurrence). LOAD() is a macro that reads from device memory via the read only data-cache using __ldg() on cards where this is available.

TABLE I: Short-hand notation for common quantities used in CUDA-kernels.

quantity	name in kernel	CUDA variable
Number of thread-blocks	`NumBlocks`	`gridDim.x`
Number of particles per (thread-)block (p_b)	`PPerBlock`	`blockDim.x`
Number of threads per particle (t_p)	`TPerPart`	`blockDim.y`
Particle index within block for current thread	`MyP`	`threadIdx.x`
Thread index w.r.t. given particle	`MyT`	`threadIdx.y`
Index of current thread-block	`MyB`	`blockIdx.x`
Global index of current thread's particle	`MyGP`	`MyP+MyB*PPerBlock`

I. The force kernel uses in general $t_p \geq 1$, although a separate implementation for $t_p = 1$ (not shown) was made because at large sizes it is no longer beneficial to have more than one thread per particle (there are many threads anyway), and the overhead associated with summing over threads is noticeable. The neighbor-list is arranged in column-major order, i.e., the first neighbors of all particles are consecutive in memory, then the second neighbors, etc. This allows for efficient (coalesced) memory access.

Note the use of pre-fetching when reading from the neighbor-list; while the force contribution of neighbor i is computed, the index of neighbor $i + 1$ is being read from the neighbor list.

Within the kernel a call is made to a function `fij` (not shown), which calculates the contribution to the pair force on the current particle from a neighbor particle. `fij` itself calls a function `ComputeInteraction` which is unique to each type of pair potential, and selected via templating. Templating is used so that it is known when compiling `fij` which potential, and thus which `ComputeInteraction`, is to be called. Templating is also used for some of the other user-chosen variables, including the type of boundary conditions (represented by a `SimulationBox` class) and the cutoff-method. This means that the force calculation kernel is compiled for all possible combinations of these parameters, and the user can choose the appropriate one at run time. The code for the conditional statements which allows this is tedious, but can be generated automatically by a Python script. The main disadvantage of using templating is that it increases the compile time considerably.

9

```
__global__ void calculateNBL_N2( ... ) {
  const unsigned int tid = MyP + MyT*PPerBlock;  // Thread-index within block
  [ Declare shared memory: s_r, s_Count, s_cut_skin2 ]


  if (updateRequired[0]) {
    if (MyT==0) s_Count[MyP]=0;                   // Count of neighbors for this particle
    [ Copy cut-offs plus skin squared to shared memory]
    float4 my_r = r[MyGP];                        // Position of this particle

    // Loop over blocks of particles
    for (FirstGP=0; FirstGP<numParticles; FirstGP+=TPerPart*PPerBlock) {

      // Read particle positions in block into shared memory
      if (FirstGP + tid<numParticles) s_r[tid] = r[FirstGP + tid];
      __syncthreads();                            // Shared data in s_r ready

      // Loop over particles in block
      for (int i=0; i<PPerBlock*TPerPart; i+=TPerPart) {
        OtherP = i + MyT; OtherGP = FirstGP + OtherP;
        if (MyGP<numParticles && MyGP!=OtherGP && OtherGP < numParticles) {
          float4 r_i = s_r[OtherP];              // Position of other particles
          [ Read squared cutoff distance from shared memory based on types ]
          [ Calculate squared distance dist2 ]
          if (dist2 < RcutSk2) {
            // Atomically increment counter for this particle:
            unsigned int nextNbrIdx = atomicInc(&s_Count[MyP], numParticles);
            [ If space insert index into NB-list at position nextNbrIdx ]
          } // if(dist2 ... )
        } // if (MyGP ... )
      } // for(int i ... )
      __syncthreads();

    } // for (int firstGP ... )
    __syncthreads();

    if (MyT == 0) {
      [ Store this particles number of neighbors ]
      [ Store its position so can check when rebuild needed ]
      [ Detect whether ran out of space and set flag to inform host ]
      if (MyP == 0) atomicDec(&(updateRequired[0]), NumBlocks);
    } // if (MyT == 0 ... )
  } // if(update_required[0])
}
```

FIG. 4: Kernel for order-N^2 neighbor-list generation. Note that because the number of particles is not in general a multiple of p_b, there are some threads in the last block which should not do anything, hence statements such as if(MyGP<numParticles).

10

VI.   NEIGHBOR-LIST GENERATION: ORDER-N^2

This neighbor-list generating algorithm has $O(N^2)$ complexity and is thus suitable only for small system sizes. In a serial code there would be a double loop; in a parallel code one loop (over particles whose neighbors are to be found) are handled completely by parallelization. Part of the loop over "other" particles is handled by looping over t_p-sized groups, while parallelization (the t_p threads for that particle) accounts for looping within these groups (we do not make use of Newton's third law). Shared memory is used to reduce the amount of reads from device memory; in a straight-forward implementation without shared memory, a total of N^2 reads of particle positions is necessary. By using a block-wise reading into the shared memory, this is reduced to N^2/p_b, where p_b is the number of particles in a block (denoted `PPerBlock` in the code). From this consideration p_b should be as large as possible, but on the other hand a too large p_b value would mean that the number of blocks ($\approx N/p_b$) becomes too small to occupy the number of SMX multiprocessors. RUMD uses the auto-tuner to pick the best value for p_b.

The kernel uses t_p threads for a given particle to search for neighbors. This means that we have to deal with the situation that several or all of them find a neighbor at the same time, and the writing to the neighbor list should be performed without race-conditions. This is achieved by a so-called *atomic* operation. When several threads perform an atomic operation on the same variable, all the operations are guaranteed to be performed in (an unspecified) sequential order. Here we use the atomic increment function, `atomicInc()`, which ensures that the number of neighbors is counted correctly. When a thread is calling `atomicInc()`, the function returns the value that the variable had *before* the increment of the given thread is performed. This is here used to specify an unique position in the neighbor list (`nextNbrIdx`).

The information about whether the neighbor-list needs to be rebuilt is on the device, generated by a different kernel. The kernel in Fig. 4 is called at every timestep, and then checks via `if(updateRequired)` whether there is anything to be done. This is faster than copying the value of a flag to the host and having the host decide whether to launch the rebuild-kernel. `updateRequired` is initially equal to the number of thread-blocks. One thread from each block decrements it with an atomic operation (`atomicDec()`) when it (its thread-block) is done, so that when all blocks are finished it is zero. At the next time step, assuming no particles have moved more than half the skin distance, `updateRequired` will still be zero and therefore the kernels will immediately exit. Using an atomic operation to decrement `updateRequired` is necessary

11

because the thread-blocks execute asynchronously, so none of them knows when/whether the others are finished, or even started–any unfinished blocks need to be able to see a non-zero value of the counter.

The above means that for small systems the simulations are performed entirely on the GPU without any communication with the CPU (except when output is required). Avoiding the overhead associated with communication between the GPU and CPU is important for the performance at small system sizes.

VII. NEIGHBOR-LIST GENERATION: ORDER-N

The order-N algorithm is based on a cell-index method[48] and involves (1) dividing the simulation box into rectangular spatial cells whose size is related to the potential cutoff; (2) associating particles with the appropriate cell based on the coordinates; (3) sorting the particles according to cell-index and rearranging all particle data to the sorted order (this can be done quickly with the Thrust library[49]). The advantage of rearranging the particle data to the sorted order is two fold; i) the information about which particles are in a given cell can be stored simply as two integers indicating the first (`cellStart`) and the last particle (`cellEnd`); ii) better performance of the data-cache when reading the particle information both in the neighbor list creation in the force calculation.

The kernel in Fig. 5 is called after steps (1) to (3) have been carried out via a series of small kernels and Thrust operations. It involves, for a given particle, identifying its cell coordinates and looping over neighboring cells in three dimensions to find neighbors. We have chosen cell lengths in each direction to be of order (not less than) $(r_c + s)/2$, where s is the neighbor-list skin. This means that the loop extends to plus/minus two cells in each direction, or 125 cells altogether. Such a choice of cell length means one searches a volume 58% [(125/8)/27] of that searched when using cells of length $r_c + s$. This kernel is called with one thread per particle, since that is generally most efficient at larger sizes, which is also when the linear method of neighbor-list generation becomes relevant. It is conceivable that some gain at intermediate sizes could be achieved by implementing a $t_p > 1$ version of the kernel, but this has not been tried yet.

In this case the information about whether to rebuild the neighbor-list must be communicated to the host because several kernels and Thrust functions must be called (the use of Dynamic Parallelism, available since CUDA 5.0, could change this, but has not been tried). Thus the

12

```
__global__ void calculateNBL_CellsSorted( ... ) {
  gtid = blockIdx.x*blockDim.x + threadIdx.x; Count = 0;
  [ Declare shared memory: s_r, s_cut_skin2 ]
  [ Copy cut-offs plus skin squared to shared memory ]
  __syncthreads();
  if (gtid<numParticles) {
    float4 my_r = r[gtid];
    int3 my_CellCoordinates = calculateCellCoordinates(my_r, ...);
    int3 OtherCellCoordinates;

    // Loop over neighboring cells, applying periodic boundary conditions
    for (int dZ=-2; dZ<=2; dZ++) {
      OtherCellCoordinates.z = (my_CellCoordinates.z + dZ + num_cells_vec.z)%num_cells_vec.z;
      for (int dY=-2; dY<=2; dY++) {
        OtherCellCoordinates.y = (my_CellCoordinates.y + dY + num_cells_vec.y)%num_cells_vec.y;
        for (int dX=-2; dX<=2; dX++) {
          OtherCellCoordinates.x = (my_CellCoordinates.x + dX + num_cells_vec.x)%num_cells_vec.x;

          // Loop over particles in cell
          int otherCellIndex = calculateCellIndex(OtherCellCoordinates, num_cells_vec);
          int Start = cellStart[otherCellIndex];
          int End =   cellEnd[otherCellIndex];
          for (int OtherP=Start; OtherP<=End; OtherP++) {
            if (gtid != OtherP) {
              float4 r_i = LOAD(r[OtherP]);
              [ Read squared cutoff distance from shared memory based on types ]
              [ Calculate squared distance dist2 ]
              if (dist2 < RcutSk2)
                [ If space insert index into NB-list and increment Count, else break]
            }
          } // end for (int OtherP....)
        }
      }
    } // end for (int dZ ... )
    [ Store this particles number of neighbors]
    [ Store its position so can check when rebuild needed ]
    [ Detect whether ran out of space and set flag to inform host]
    if ( gtid==0 ) updateRequired[0] = 0;
  } // if(gtid < numParticles)
}
```

FIG. 5: Kernel for order-N neighbor-list generation. `calculateCellCoordinates(...)` calculates the coordinates of the cell that a particle belongs to. `calculateCellIndex(..)` calculates the index of a cell given its coordinates. The arrays `cellStart` and `cellEnd` contain the indices of the first and last particles, respectively, associated with a given cell.
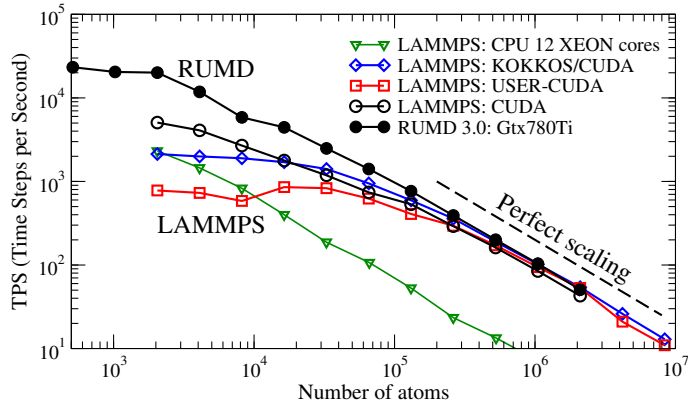
13

FIG. 6: The LAMMPS benchmark: a melting FCC crystal is simulated at constant energy. The vertical axis shows the number of simulated time steps per second of wall-clock time. At large system sizes all codes follows the ideal $1/N$ scaling, and the GPU's are 10-20 faster than LAMMPS running on 12 xeon cores. For RUMD good scaling is maintained down to quite small systems $N \sim 2000$, and at small system sizes RUMD is thus considerably faster than the three GPU versions of LAMMPS.

`updateRequired` flag is not used in the kernel because the kernel only runs at all if a rebuild is required; the flag is simply set to zero at the end by the thread handling particle 0.

VIII.   BENCHMARKS AND PERFORMANCE ANALYSIS

To benchmark RUMD we use the Lennard-Jones benchmark described on the LAMMPS home-page, involving an FCC crystal of Lennard-Jones material which is given a kinetic energy sufficient to melt it and then run for 10^4 time steps at constant total energy (NVE). Figure 6 shows as black filled symbols the number of timesteps per second (TPS) RUMD can perform on a Gtx780Ti GPU card as a function of system size. For comparison we show also the results published on the LAMMPS homepage for different versions of LAMMPS: A pure CPU version of LAMMPS running on 12 Intel Xeon cores (dual hex-core 3.47 GHz Intel Xeons X5690), and three different GPU-extensions, KOKKOS/CUDA, USER-CUDA, and GPU, all running on a K20x card with 2688 cores (these results are for 100 timesteps). All the GPU-accelerated versions of LAMMPS, together with RUMD, give similar performance for large N (above $\sim 3 \times 10^5$). In this regime near perfect scaling with N is observed, and the GPU versions are 10-20 times faster than LAMMPS running on 12 Intel Xeon cores. Differences show up at small sizes: the number of simulated time steps per second plateaus already at a few tens of thousands of particles for two of the GPU

14

TABLE II: Performance parameters chosen by the auto-tuner and the resulting TPS (Timesteps Per Second) on a Gtx780Ti card.

N	NB	pb	tp	skin	TPS
512	N^2	16	14	0.452	23281
1024	N^2	16	10	0.452	20446
2048	N^2	48	8	0.5	20068
4096	N^2	96	4	0.675	11794
8192	N	64	2	0.746	5847
16384	N	192	1	0.611	4440
32768	N	128	1	0.452	2484
65536	N	96	1	0.409	1409
131072	N	96	1	0.370	764
262144	N	128	1	0.370	390
524288	N	128	1	0.370	200
1048576	N	128	1	0.335	104
2097152	N	96	1	0.335	51

versions of LAMMPS. This plateau means running a simulation with 2000 particles takes as much time as one with 20000 particles; clearly the GPU hardware is under-utilized in this size regime. In fact, for these two implementations (the red and blue curves), it is faster to use the pure CPU version of LAMMPS at the smallest sizes. RUMD, on the other hand, maintains reasonable (though not perfect) scaling down to around $N = 2000$. We have included even smaller system sizes in the benchmarking of RUMD, to illustrate that it eventually also begins to plateau - but this only happens when the system size is less than 2000.

Table II gives the parameters chosen by the auto-tuner, as a function of system size. Note that, except for the two smallest system sizes, the auto-tuner chooses the number of threads ($N \times t_p$) to be at least 16000. This illustrates the point made in the introduction, that the number of threads should be much larger than the number of physical cores (here 2880) to get good performance. The reason that fewer threads are used for the two smallest system sizes is probably that the required large t_p values inflict too large a penalty due to the sequential summation of the t_p different contributions to the force (see Fig. 3). The switch between the two methods for neighbor-list
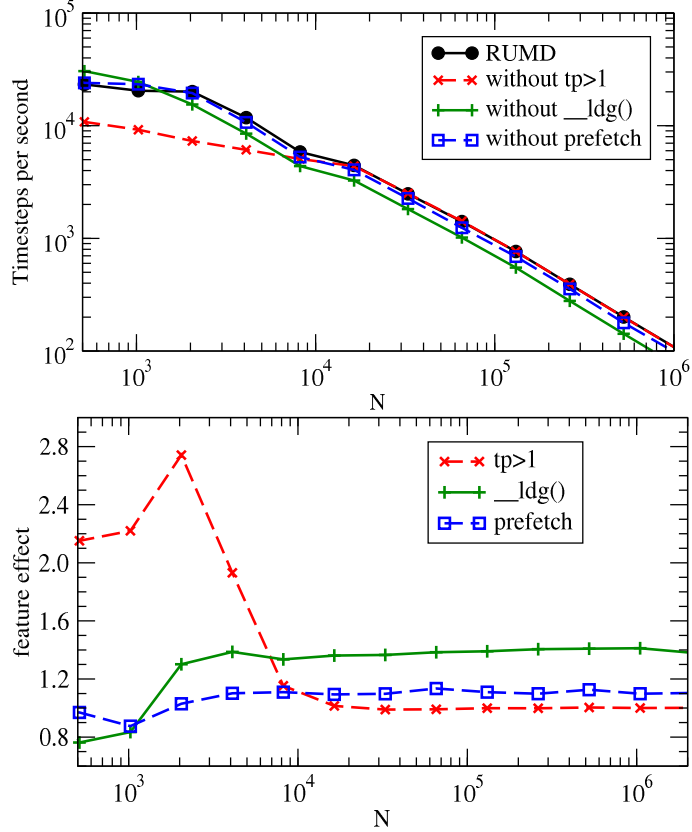
15

FIG. 7: Analyzing the effect on performance of features of RUMD. The upper panel shows, plotted as in Fig. 6, the performance of the full-RUMD and three other versions in which one feature has been disabled: multiple threads per particle ($t_p > 1$), use of read only data-cache to read positions (__ldg()), and pre-fetching. The lower panel shows the same data in terms of the relative boost in performance each feature gives, as a function of system size.

generation happens at around 8000 particles. In this range of system sizes both methods are sub-optimal and the auto-tuner compensates by increasing the skin size to make neighbor-list updates less frequent.

Figure 7 shows the effect of disabling different optimization features. The upper panel shows the same quantity as in Fig. 6, but with different curves representing different disabled features (the black curve is with all features enabled). The most dramatic difference is when $t_p = 1$ is enforced, for small and medium systems ($N < 10^4$). No difference is observed at larger N because there $t_p = 1$ is the optimal choice, see table II. Disabling the use of the read only data-cache gives the green curve, a significant drop in performance across all sizes except the very smallest $N < 2000$, while disabling pre-fetching gives a slight drop, more at larger sizes. The lower panel of Fig. 7

16

N	$2 \cdot 10^3$	$2 \cdot 10^4$	10^5
LAMMPS SP	3.26	5.66	6.06
LAMMPS WOLF	2.21	3.57	3.40
LAMMPS PPPM	0.54	0.40	0.35
RUMD SF	9.41	11.3	16.1

TABLE III: Benchmarks for a system of charged Lennard-Jone particles (see text for details) for LAMMPS (CPU) and RUMD (GPU). The metric shown is MATS (millions of atom time steps per second). LAMMPS benchmarks were performed on a Dell 630 server with dual Intel Xeon E5-2699 v3 2.3 GHz CPU's for a total of 36 cores. Coulomb interactions were evaluated using a simple shifted-potential cutoff at distance 6.0 ("SP"), using the Wolf method with the switching parameter α set to zero ("WOLF", equivalent to the shifted force method), and the Particle-Particle Particle-Mesh method ("PPPM"). RUMD benchmarks were performed on an nVidia GTX 780 Ti, using a shifted force cut-off (SF) at distance 6.0.

shows the same data, but plotted as the ratio of the speed of the full RUMD to the speed of RUMD with the given feature disabled. Plotting this ratio, on a linear scale, shows the relative effects more clearly. In particular, reading via the read only data-cache gives an effect of order 40%, while pre-fetching has an effect of order 10% at the largest sizes.

IX. ELECTROSTATICS

A general purpose MD code should include electrostatic (Coulomb) interactions and these should be sufficiently accurate and computationally efficient. While an Ewald-based method which can efficiently handle the long range part of the electrostatic interactions is planned, for our needs so far we have found it sufficient to use Coulomb forces with a long range shifted-force cut-off as documented in Ref. 50. In that paper it was shown that a shifted-force cutoff of order five inter-particle spacings gives, similar to the Wolf[51] method, results in good agreement with Ewald-based methods in bulk systems.

To benchmark the performance of Coulomb interactions, we performed simulations of a model molten salt in RUMD and the CPU version of LAMMPS. Details of the system simulated are as follows: All particles have identical Lennard-Jones parameters ϵ and σ. The charges are $\pm\sqrt{4\pi\epsilon_0\epsilon\sigma}$ (50% each). The density was 0.3677 σ^{-3} and the temperature 2 ϵ/k_B. The density is the same as was used by Hansen and McDonald in their study of a similar model salt[52]. In

17

Ref.[50] it was shown that a cutoff of 6.0σ, corresponding to ~ 330 neighbors per particle at this density, was sufficient to get satisfactory accuracy. The time step is 0.004 $\sqrt{m/\epsilon}\sigma$.

The data in Table III compare RUMD and the CPU-version of LAMMPS with different methods of evaluating Coulomb interactions and different numbers of CPU-threads. The benchmarks are expressed as MATS (million atom timesteps per second) for ease of comparing different system sizes. The smallest speed-up of RUMD over LAMMPS is here a factor of two. This smaller speed-up compared to the previous section is mostly due to the LAMMPS benchmarks being run on a faster CPU system, a Dell 630 server with 36 XEON cores. For comparison, at the time of writing the cost of the Dell 630 server is roughly 10.000$, whereas the cost of the GTX 780 Ti card is less than 1000$ (to this should be added the cost of a fairly standard PC, which can hold three GPU cards).

X. SUMMARY

We have described the RUMD software package for molecular dynamics simulation on GPUs, concentrating on the optimization strategies that distinguish it from most other GPU MD codes. We have documented its strong performance at small and medium system sizes and performance comparable to other GPU-based MD codes at larger sizes. Work will continue on RUMD both with regard to features (for example, many-body interactions and efficient long-range Coulomb interactions) and optimization opportunities (for example, dynamic parallelism). The ability to split a simulation over multiple GPUs will also be considered, which will not just allow larger systems (more than the approx. 3 million particles a single card can handle), but also allow even faster simulations of medium systems, given that RUMD already make good use of the hardware for such sizes.

XI. APPENDIX: THE AUTOTUNER

Here we describe the algorithm used by the autotuner. The basic strategy is to run a series of short simulations (a few hundred to a few thousand time steps) varying the different parameters, to find a set of of parameters giving (close to) optimal performance. Not all possible combinations of parameters are attempted in order to reduce the time taken for tuning (for Lennard-Jones-type systems without molecules or Coulomb interactions this is under a minute for small systems,

18

several minutes for larger systems). The initial state of the system is stored so that all comparisons made by the autotuner involve runs of the same length starting from the same configuration.

If the autotuner is not used, RUMD uses default values which depend on the system size: "n2" neighbor-list method for $N < 8000$, otherwise "sort"; $p_b = 32, t_p = 4$ for $N \leq 10000$, $p_b = 64, t_p = 1$ otherwise. The default skin value is 0.5, which assumes units of length such that the interparticle spacing is of order unity. In principle the default skin should be based on the interparticle spacing (e.g. $\rho^{-1/3}/2$), but in practise length units in MD are generally of order the interparticle spacing and the autotuner can quickly deal with a discrepancy. For some very small systems $N < 200$ with not too small cutoff it can be faster not to use a neighbor-list at all. The autotuner checks this possibility for systems with $N < 5000$.

The dependence of performance on the parameters p_b, t_p and neighbor-list skin is simple: the time taken shows a single minimum as a function of the parameter. This allows a relatively straightforward optimization strategy to be used. The number of steps run for the different stages depends on the system size (larger for smaller systems sizes to get better timing) and can be altered by the user but should not need to be. The overall strategy is as follows:

1. Run some steps before tuning (default: 10000) to avoid the influence of transient effects (associated for example with having changed the temperature)

2. Run with default parameters to get a baseline performance.

3. Phase 1 optimization: With the default p_b and t_p run with the different neighbor-list methods, "none", "n2", "sort". For each one the skin is optimized separately.

4. For the fastest neighbor-list method, and any others within 20% of the fastest, carry out phase 2 optimization: Optimize the parameters p_b and t_p using a double loop: first p_b considering the values 16, 32, 48, 64, 96, 128 and 192. For each p_b, values of t_p are tested starting from 1 and increasing until 64. For each combination of p_b and t_p the skin length is re-optimized starting at the last identified optimal value.

5. If the neighbor-list method "n2" is included in phase 2, it can still help to sort the particles once every few hundred times, typically for system sizes near the crossover from "n2" being optimal to "sort" being optimal. This is checked and the optimal sorting interval found.

6. If more than one neighbor-list method was optimized in phase 2, make a final comparison between the phase 2-optimized sorting methods to choose the overall optimized set of parameters (generally, except close to the cross-over from one method to another, the phase 2 optimization does not change which method is chosen, and in that case the difference is small anyway).

7. Run, using the optimized parameters, the same number of steps as for the baseline run to determine the overall improvement due to autotuning.

8. Write the tuned parameters to a file so that repeating the simulation in the same directory with the same "user parameters" does not require re-tuning. For this purpose, "same user parameters" means: same number of particles of each type, same density and temperature and potential parameters (within a tolerance), same integrator type and timestep (within tolerance), and same GPU-type. The actual configuration does not have to be the same. If there is any doubt about re-using the previously found parameters the file can just be deleted.

Some further details are noted here:

- The skin optimization starts from the default value (phase 1) or previously identified phase 1-optimal value (phase 2). Its value is increased and decreased in steps of 20% (phase 1) or 10% (phase 2) until a minimum is identified in the time taken. Attempting to optimize the skin to a precision of better than 10% is not worth the effort.

- The loop over t_p breaks out when one of the following three conditions is met: (i) the time taken exceeds the minimum time so far three times (ii) the time taken exceeds the minimum time so far by 5% (iii) some GPU resource-limit is exceeded, either the number of threads per block ($p_b t_p$) or the total register count per block.

- The loop over p_b breaks out when the time taken (having optimized t_p and skin) exceeds the previous best by 10% or more.

- For very large systems it doesn't make sense to use anything other than the "sort" method for the neighbor-list. The autotuner omits "none" for $N > 5000$ and "n2" for $N > 50000$. Moreover, large systems generally require larger p_b and so the autotuner omits $p_b = 16$ for $N > 4000$ and $p_b = 32$ for $N > 10^5$. Also for the largest systems only $t_p = 1$ is relevant; the autotuner omits checking other values for $N > 10^5$. These various cutoff-parameters

20

can be changed by the user if (s)he knows their names, but it should not be necessary and this is not included in the documentation.

Acknowledgments

---

[*] Electronic address: nbailey@ruc.dk

[†] Electronic address: tbs@ruc.dk

[1] (2014), RUMD software is freely available at http://rumd.org.

[2] J. D. Owens, D. Luebke, N. Govindaraju, M. Harris, J. Krueger, A. E. Lefohn, and T. J. Purcell, Comput. Graph Forum **26**, 80 (2007).

[3] J. D. Owens, M. Houston, D. Luebke, S. Green, J. E. Stone, and J. C. Phillips, Proc. IEEE **96**, 879 (2008).

[4] J. E. Stone, D. J. Hardy, I. S. Ufimtsev, and K. Schulten, J. Mol. Graphics Modell. **29**, 116 (2010).

[5] J. Nickolls and W. J. Dally, IEEE MICRO **30**, 56 (2010).

[6] R. M. Farber, J. Mol. Graph. Model. **30**, 82 (2011).

[7] A. Harju, T. Siro, F. F. Canova, S. Hakala, and T. Ratalaiho (2012), arXiv:1210.7930.

[8] M. J. Harvey and G. De Fabritiis, Wiley Interdiscip. Rev.-Comput. Mol. Sci. **2**, 734 (2012).

[9] J. A. Anderson, C. D. Lorenz, and A. Travesset, J. Comput. Phys. **227**, 5342 (2008).

[10] J. A. Anderson and A. Travesset, Comput. Sci. Eng. **10**, 8+ (2008).

[11] P. K. Jha, R. Sknepnek, G. I. Guerrero-Garcia, and M. O. de la Cruz, J. Chem. Theory Comput. **6**, 3058 (2010).

[12] T. D. Nguyen, C. L. Phillips, J. A. Anderson, and S. C. Glotzer, Comput. Phys. Commun. **182**, 2307 (2011).

[13] M. J. Harvey, G. Giupponi, and G. De Fabritiis, J. Chem. Theory Comput. **5**, 1632 (2009).

[14] P. Eastman and V. S. Pande, J. Comput. Chem. **31**, 1268 (2010).

[15] P. Eastman, M. S. Friedrichs, J. D. Chodera, R. J. Radmer, C. M. Bruns, J. P. Ku, K. A. Beauchamp, T. J. Lane, L.-P. Wang, D. Shukla, et al., J. Chem. Theory Comput. **9**, 461 (2013).

21

[16] P. H. Colberg and F. Höfling, Comput. Phys. Commun. **182**, 1120 (2011).

[17] J. Phillips, R. Braun, W. Wang, J. Gumbart, E. Tajkhorshid, E. Villa, C. Chipot, R. Skeel, L. Kale, and K. Schulten, J. Comput. Chem. **26**, 1781 (2005).

[18] W. M. Brown, P. Wang, S. J. Plimpton, and A. N. Tharrington, Comput. Phys. Commun. **182**, 898 (2011).

[19] R. Salomon-Ferrer, D. A. Case, and R. C. Walker, WIREs Comput. Mol. Sci. **00** (2012).

[20] S. Páll, M. J. Abraham, C. Kutzner, B. Hess, and E. Lindahl, LNCS **8759**, 3 (2015), proceedings of EASC 2014.

[21] J. E. Stone, J. C. Phillips, P. L. Freddolino, D. J. Hardy, L. G. Trabuco, and K. Schulten, J. Comput. Chem. **28**, 2618 (2007).

[22] S. Guo-Liang, W. Jing-Wei, L. Zhen-Hua, W. Wen-Ning, and F. Kang-Nian, Chem. J. Chinese U. **29**, 2425 (2008).

[23] W. Liu, B. Schmidt, G. Voss, and W. Müeller-Wittig, Comput. Phys. Commun. **179**, 634 (2008).

[24] J. A. van Meel, A. Arnold, D. Frenkel, S. F. P. Zwart, and R. G. Belleman, Mol. Simul. **34**, 259 (2008).

[25] M. S. Friedrichs, P. Eastman, V. Vaidyanathan, M. Houston, S. Legrand, A. L. Beberg, D. L. Ensign, C. M. Bruns, and V. S. Pande, J. Comput. Chem. **30**, 864 (2009).

[26] J. Xu, Y. Ren, W. Ge, X. Yu, X. Yang, and J. Li, Mol. Simul. **36**, 1131 (2010).

[27] H. J. Myung, R. Sakamaki, K. J. Oh, T. Narumi, K. Yasuoka, and S. Lee, Bull. Korean Chem. Soc. **31**, 3639 (2010).

[28] J. A. Baker and J. D. Hirst, Mol. Inf. **30**, 498 (2011).

[29] D. C. Rapaport, Comput. Phys. Commun. **182**, 926 (2011).

[30] A. P. Ruymgaart, A. E. Cardenas, and R. Elber, J. Chem. Theory Comput. **7**, 3072 (2011).

[31] K. Oguchi, Y. Shibuta, and T. Suzuki, J. Jpn. I. Met **76**, 462 (2012).

[32] S. Páll and B. Hess, Comput. Phys. Commun. **184**, 2641 (2013).

[33] D. B. Kirk and W.-m. W. Hwu, *Programming Massively Parallel Processors: A Hands-on Approach* (Morgan Kaufmann, 2010).

[34] NVIDIA, *NVIDIA CUDA Compute Unified Device Architecture Programming Guide* (NVIDIA, Santa Clara, CA, USA, 2014), version 6.5.

[35] E. Lindholm, J. Nickolls, S. Oberman, and J. Montrym, IEEE Micro **28**, 39 (2008).

[36] NVIDIA, *NVIDIAs next generation CUDA compute architecture: Fermi* (2009), white paper. Available online, Version 1.1, 22 pp.

[37] NVIDIA, *NVIDIAs next generation CUDA compute architecture: Kepler GK110* (2012), white paper.

Available online, Version 1.0, 24 pp.

[38] NVIDIA, *NVIDIA GeForce GTX 980, Featuring Maxwell* (2014), white paper. Available online, Version 1.1, 32 pp.

[39] S. Karmakar, C. Dasgupta, and S. Sastry, PNAS **106**, 3675 (2009).

[40] F. Z. an Siro T and H. A, Comput. Phys. Commun. **184(5)**, 1414 (2013).

[41] J. Glaser, T. D. Nguyen, J. A. Anderson, P. Lui, F. Spiga, J. A. Millan, D. C. Morse, and S. C. Glotzer, Comput. Phys. Commun. **192**, 97 (2015).

[42] S. Toxvaerd and J. C. Dyre, J. Comp. Phys. **134**, 081102 (2011).

[43] G. J. Martyna, D. J. Tobias, and M. L. Klein, J. Chem. Phys. **101**, 4177 (1994).

[44] T. S. Ingebrigtsen, S. Toxvaerd, O. J. Heilmann, T. B. Schrøder, and J. C. Dyre, jcp **135**, 104101 (2011).

[45] T. S. Ingebrigtsen, S. Toxvaerd, T. B. Schrøder, and J. C. Dyre, jcp **135**, 104102 (2011).

[46] S. Plimpton, J. Comp. Phys. **117**, 1 (1995).

[47] L. Rovigatti, P. Šulc, I. Z. Reguly, and F. Romano, J. Comp. Chem. **36**, 1 (2015).

[48] M. P. Allen and D. J. Tildesley, *Computer Simulation of Liquids* (Oxford University Press, 1987).

[49] (2015), thrust Parallel Algorithms Library, URL `http://thrust.github.io/`.

[50] J. S. Hansen, T. B. Schrøder, and J. C. Dyre, J. Phys. Chem. B **116**, 5738 (2012), ISSN 1520-6106.

[51] D. Wolf, P. Keblinski, S. R. Phillpot, and J. Eggebrecht, J. Chem. Phys. **110**, 8254 (1999), ISSN 0021-9606.

[52] J. P. Hansen and I. R. McDonald, Phys. Rev. A **11**, 2111 (1975).

Appendix E

Reprints of posters

Isomorph invariance of viscosity along the melting line of a Lennard-Jones system

Lorenzo Costigliola (lorenzoc@ruc.dk), Thomas Schrøder and Jeppe Dyre

DNRF Centre "Glass and Time", IMFUFA, Department of Sciences, Roskilde University, Denmark

I: Isomorph theory

According to isomorph theory there are some liquids, called Roskilde liquids, for which some structural and dynamical quantities are constant along determinate curves in the (ρ, T) phase diagram. These curves are named isomorphs[1].

One of the simplest Roskilde liquid to study is the Lennard–Jones (LJ) systems, i.e. a system of particles interacting via a LJ potential:

$$u(r) = 4\epsilon \left[\left(\frac{\sigma}{r}\right)^{12} - \left(\frac{\sigma}{r}\right)^{6} \right]$$

For this system it is possible to write a simple expression for the isomorph curves:

$$T \propto h(\rho) = \left(\frac{\gamma_0}{2} - 1\right)\left(\frac{\rho}{\rho_0}\right) - \left(\frac{\gamma_0}{2} - 2\right)\left(\frac{\rho}{\rho_0}\right)^2$$

$$\gamma_0 = \frac{\langle \Delta W \Delta U \rangle}{\langle (\Delta U)^2 \rangle}$$

II: Is Lennard–Jones melting line an isomorph?

One of the interesting results of isomorph theory is that the melting/freezing line for a Roskilde liquid is an isomorph. It is therefore possible to derive an equation for the melting point of the LJ system:

$$T(\rho) = 2.27 \cdot \rho^4 - 0.80 \cdot \rho^2$$

This equation is in good agreement with melting point data from computes simulations[2] and previous hypothesis on melting line equation[3].
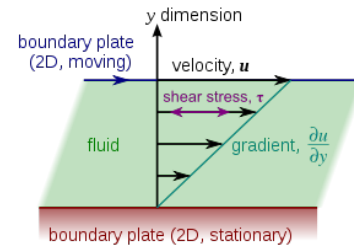Density and temperature are in reduced LJ units.
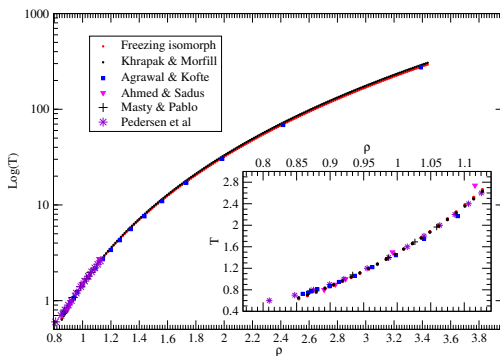
III Measuring viscosity in computer simulations

In this work we measured LJ viscosity using the SLLOD algorithm. The viscosity is measured from the response of the system to the shearing of simulation box's walls:

$$\eta = \frac{\tau}{u_{,y}}$$

IV Reduced viscosity along the melting line

Isomorph theory states that dynamical quantities are invariant along an isomorph if expressed in reduced units.

This means that reduced viscosity $\tilde{\eta}$ is invariant along the freezing/melting isomorph similarly to what Andrade supposed for liquid methals[4].

$$\tilde{\eta} = \frac{\eta}{\rho^{2/3}\sqrt{T}}$$

Knowing $\tilde{\eta}$ at one point allows to predict the behavior of η along the isomorph.
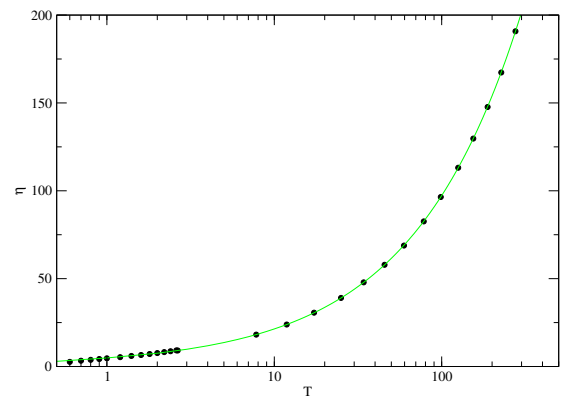
Conclusions

- We show that the freezing/melting line is an isomorph and we gave an analytical equation for it valid in a wide range of T and ρ;
- The isomorph invariance of viscosity along the freezing/melting line can be successfully used to describe viscosity behavior.

References

[1] N. Gnan, T. B. Schrøder, U. R. Pedersen, N. P. Bailey and J. C. Dyre, *J. Chem. Phys.* **131**, 234504 (2009).

[2] R. Agrawal and D. Kofte, *Mol. Phys* **85**, 43 (1995); E. A. Mastny and J. de Pablo, *J. Chem. Phys.* **127**, 104504, (2007); A. Ahmed and R. J. Sadus, *J. Chem. Phys.* **131**, 174504, (2009); U. R. Pedersen, *J. Chem. Phys.* **139**, 104102 (2013).

[3] S. A. Khrapak and G. E. Morfill *J. Chem. Phys.* **134**, 094108 (2011)

[4] E.N. da C. Andrade, *Phil. Mag* **17**, 497, 698 (1934).

All simulations are performed with **RUMD**. See rumd.org for details.

Studies of the Lennard-Jones fluid in 2, 3 and 4 dimensions

Lorenzo Costigliola (lorenzoc@ruc.dk), Thomas Schrøder and Jeppe Dyre

DNRF Centre "Glass and Time", Department of Science and Environment, Roskilde University, Denmark

I: Theory

According to isomorph theory there are some systems, called Roskilde (R) systems, for which several structural and dynamical quantities are constant along specific curves in the (ρ, T) phase diagram. These curves are named isomorphs[1]. R systems are identified by strong correlations between virial and potential energy fluctuations.

$$R = \frac{\langle \Delta W \Delta U \rangle}{\sqrt{\langle (\Delta W)^2 \rangle \langle (\Delta U)^2 \rangle}} > 0.9 \qquad (1)$$

It has been recently suggested that all pairwise model systems become R simple in a part of their (ρ, T) phase diagram in an high enough number of dimensions[2]. We verified[3] this conjecture for the Lennard–Jones (LJ) model system, i.e. a system of particles interacting via a LJ potential:

$$u(r) = 4\epsilon \left[\left(\frac{\sigma}{r}\right)^{12} - \left(\frac{\sigma}{r}\right)^{6} \right] \qquad (2)$$

Isomorphs for the LJ system in 2d, 3d and 4d have the functional shape:

$$\frac{T(\rho)}{T_0} = \left(\frac{d}{6}\gamma_0 - 1\right)\left(\frac{\rho}{\rho_0}\right)^{12/d} - \left(\frac{d}{6}\gamma_0 - 2\right)\left(\frac{\rho}{\rho_0}\right)^{6/d} \qquad (3)$$

II: LJ phase diagram in 2d, 3d, 4d

The first problem in this kind of study is the choice of how to compare state points in different dimensions. Our choice was to use the critical point as reference point for investigating the behavior of correlation coefficient R in the phase diagram. A reason for this choice is that the density and temperature for the critical point of the LJ system are known in 2d, 3d and 4d.
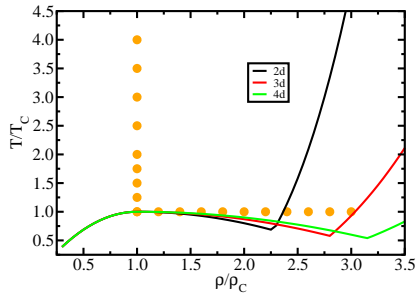
NVT simulations have been carried out at several densities ρ along the critical isotherm and temperatures T along the critical isochore for the 2d, 3d and 4d LJ system (orange points). Densities and temperatures are measured in units of the critical ones.

III: Results for the correlation coefficient R
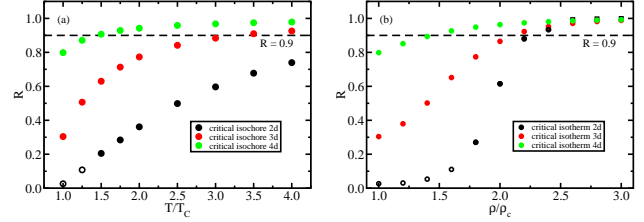
At any studied state point, the correlation coefficient increases when increasing dimensionality.

IV: Isomorphs in 4d

The 4d LJ system is an R system in a wide region of its phase diagram and therefore isomorphs should exist for this system. In the figures below, the radial distribution function (RDF) and the mean squared displacement (MSD) are plotted in reduced units, i.e. made dimensionless using the macroscopic quantities ρ, T and m (particle average mass). Reduced RDF and MSD are invariant along an isomorph.
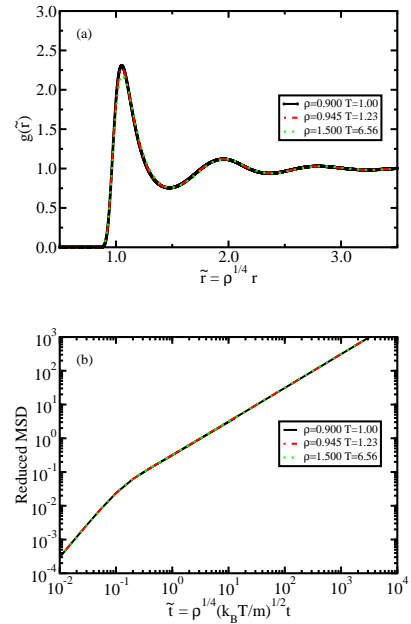
Conclusions

- We proved that the conjecture of Ref. [2] is correct for the LJ system;
- These findings[3] together with the general argument of Ref. [2] highlight the need for an $1/d$ expansion in liquid-state theory.

References

[1] N. Gnan, T. B. Schrøder, U. R. Pedersen, N. P. Bailey and J. C. Dyre, *J. Chem. Phys.* **131**, 234504 (2009).

[2] T. Maimbourg and J. Kurchan, arXiv:1603.05023 (2016).

[3] L. Costigliola, T. B. Schrøder and J. C. Dyre, arXiv:1605.06007 (2016).

All simulations are performed with an homemade code applicable in arbitrary number of dimensions available at `dirac.ruc.dk/~lorenzoc/nD_MD_code/`.

Bibliography

[1] Hansen, J.-P. and McDonald, I.R. *Theory of Simple Liquids*. Accademic, New York, 3rd edition, 2006.

[2] Trond S. Ingebrigtsen and Thomas B. Schrøder and Jeppe C. Dyre. What is a simple liquid? *Physical Review X*, 2:011011, 2012.

[3] Brazhkin, V. V. and Fomin, Yu. D. and Lyapin, A. G. and Ryzhov, V. N. and Trachenko, K. Two liquid states of matter: A dynamic line on a phase diagram. *Phys. Rev. E*, 85:031203, Mar 2012. doi: 10.1103/PhysRevE.85.031203. URL Link.

[4] Brazhkin, V. V. and Fomin, Yu. D. and Lyapin, A. G. and Ryzhov, V. N. and Trachenko, K. Universal crossover of liquid dynamics in supercritical region. *JETP Letters*, 95(3):164, 2012. doi: 10.1134/S0021364012030034. URL Link.

[5] Brazhkin, V. V. and Fomin, Yu. D. and Lyapin, A. G. and Ryzhov, V. N. and Tsiok, E. N. and Trachenko, Kostya. "Liquid-Gas" Transition in the Supercritical Region: Fundamental Changes in the Particle Dynamics. *Phys. Rev. Lett.*, 111:145901, Oct 2013. doi: 10.1103/PhysRevLett.111.145901. URL Link.

[6] Sergei M Stishov. Melting at high pressures. *Soviet Physics Uspekhi*, 11(6):816, 1969. URL Link.

[7] Pablo G. Debenedetti. Supercooled and glassy water. *Journal of Physics: Condensed Matter*, 15(45):R1669, 2003. URL Link.

[8] Matthieumarechal. Phase diagram (Wikipedia), June 2016. URL Link.

[9] Jeppe C. Dyre. Simple liquids' quasiuniversality and the hard-sphere paradigm. *J. Phys.: Condens. Matter*, 2016.

[10] Veldhorst, Arno A. and Dyre, Jeppe C. and Schrøder, Thomas B. Scaling of the dynamics of flexible Lennard-Jones chains. *Journal of Chemical Physics*, 141(5):054904, 2014. doi: 10.1063/1.4888564. URL Link.

[11] Allen, M.P. and Tildesley, D.J. *Computer Simulation of Liquids.* Oxford University Press, 1986.

[12] Widom, B. Intermolecular Forces and the Nature of the Liquid State. *Science*, 157(3787):375, 1967. doi: 10.1126/science.157.3787.375. URL Link.

[13] C. M. Roland and S. Hensel-Bielowka and M. Paluch and R. Casalini. Supercooled dynamics of glass-forming liquids and polymers under hydrostatic pressure. *Rep. Prog. Phys.*, 68(6):1405, 2005. doi: 10.1088/0034-4885/68/6/R03.

[14] Tölle, A. and Schober, H. and Wuttke, J. and Randl, O. G. and Fujara, F. Fast Relaxation in a Fragile Liquid under Pressure. *Phys. Rev. Lett.*, 80:2374, Mar 1998. doi: 10.1103/PhysRevLett.80.2374. URL Link.

[15] Albert Tölle. Neutron scattering studies of the model glass former ortho -terphenyl. *Reports on Progress in Physics*, 64(11):1473, 2001. URL Link.

[16] Casalini, R. and Roland, C. M. Thermodynamical scaling of the glass transition dynamics. *Phys. Rev. E*, 69:062501, 2004. doi: 10.1103/PhysRevE.69.062501.

[17] Fragiadakis, D. and Roland, C. M. Connection between dynamics and thermodynamics of liquids on the melting line. *Phys. Rev. E*, 83:031504, Mar 2011. doi: 10.1103/PhysRevE.83.031504. URL Link.

[18] Fragiadakis, D. and Roland, C. M. On the density scaling of liquid dynamics. *The Journal of Chemical Physics*, 134(4):044504, 2011. doi: 10.1063/1.3532545. URL Link.

[19] D. Coslovich and C. M. Roland. Pressure-energy correlations and thermodynamic scaling in viscous Lennard-Jones liquids. *J. Chem. Phys.*, 130:014508, 2009. doi: 10.1063/1.3054635.

[20] L. Bøhling and T. S. Ingebrigtsen and A. Grzybowski and M. Paluch and J. C. Dyre and T. B. Schrøder. Scaling of viscous dynamics in simple liquids: theory, simulation and experiment. *New J. Phys.*, 14:113035, 2012. doi: 10.1088/1367-2630/14/11/113035.

[21] Ball, Philip. Water - an enduring mystery. *Nature*, 452(7185):291, 03 2008. doi: 10.1038/452291a. URL Link.

[22] Brovchenko, Ivan and Oleinikova, Alla. Multiple Phases of Liquid Water. *ChemPhysChem*, 9(18):2660, 2008. doi: 10.1002/cphc.200800639. URL Link.

[23] Stokely, Kevin and Mazza, Marco G. and Stanley, H. Eugene and Franzese, Giancarlo. Effect of hydrogen bond cooperativity on the behavior of water. *Proceedings of the National Academy of Sciences*, 107(4):1301, 2010. doi: 10.1073/pnas.0912756107. URL Link.

[24] Stillinger, Frank H. Phase transitions in the Gaussian core system. *The Journal of Chemical Physics*, 65(10):3968, 1976. doi: 10.1063/1.432891. URL Link.

[25] Ikeda, Atsushi and Miyazaki, Kunimasa. Glass Transition of the Monodisperse Gaussian Core Model. *Phys. Rev. Lett.*, 106:015701, Jan 2011. doi: 10.1103/PhysRevLett.106.015701. URL Link.

[26] Giaquinta, Paolo V. and Saija, Franz. Re-entrant Melting in the Gaussian-Core Model: The Entropy Imprint. *ChemPhysChem*, 6(9): 1768, 2005. doi: 10.1002/cphc.200400565. URL Link.

[27] P. Mausbach and H.-O. May. Static and dynamic anomalies in the Gaussian core model liquid. *Fluid Phase Equilibria*, 249:17, 2006. doi: 10.1016/j.fluid.2006.07.021. URL Link.

[28] Frank H. Stillinger and Dorothea K. Stillinger. Negative thermal expansion in the Gaussian core model. *Physica A: Statistical Mechanics and its Applications*, 244:358, 1997. doi: 10.1016/S0378-4371(97)00246-X. URL Link.

[29] ISAACS program by Central Michigan University, June 2016. URL Link.

[30] Toxvaerd, Søren and Heilmann, Ole J. and Dyre, Jeppe C. Energy conservation in molecular dynamics simulations of classical systems. *The Journal of Chemical Physics*, 136(22):224106, 2012. doi: 10.1063/1.4726728. URL Link.

[31] Verlet, Loup. Computer "Experiments" on Classical Fluids. I. Thermodynamical Properties of Lennard-Jones Molecules. *Phys. Rev.*, 159: 98, Jul 1967. doi: 10.1103/PhysRev.159.98. URL Link.

[32] Levesque, D. and Verlet, L. Molecular dynamics and time reversibility. *Journal of Statistical Physics*, 72(3):519, 1993. doi: 10.1007/BF01048022. URL Link.

[33] Toxvaerd, Søren. Stability of molecular dynamics simulations of classical systems. *The Journal of Chemical Physics*, 137(21):214102, 2012. doi: 10.1063/1.4768891. URL Link.

[34] Hoover, W.G. and Hoover, C.G. *Time Reversibility, Computer Simulation, Algorithm, Chaos*, volume 13 of *Advanced Series in NonLinear Dynamics*. World Scientific, Singapore, 2nd edition edition, 2012.

[35] Goldenfeld, N. *Lectures on Phase Transitions and the Renormalization Group.* Frontiers in physics. Addison-Wesley, Advanced Book Program, 1992. URL Link.

[36] Shūichi Nosé. A molecular dynamics method for simulations in the canonical ensemble. *Molecular Physics*, 52(2):255, 1984. doi: 10.1080/00268978400101201. URL Link.

[37] Toxvaerd, Søren. Ensemble simulations with discrete classical dynamics. *The Journal of Chemical Physics*, 139(22):224106, 2013. doi: 10.1063/1.4836615. URL Link.

[38] Nicholas P. Bailey, Trond S. Ingebrigtsen, Jesper Schmidt Hansen, Arno A. Veldhorst, Lasse Bøhling, Claire A. Lemarchand, Andreas E. Olsen, Andreas K. Bacher, Lorenzo Costigliola, Heine Larsen, Jeppe C. Dyre and Thomas B. Schrøder. RUMD: A general purpose molecular dynamics package optimized to utilize GPU hardware down to a few thousand particles. *ArXiv:1506.05094*, 2015. URL Link.

[39] CUDA website http://www.nvidia.com/object/cuda_home_new.html. URL Link.

[40] Schrøder, Thomas B. and Dyre, Jeppe C. Simplicity of condensed matter at its core: Generic definition of a Roskilde-simple system. *Journal of Chemical Physics*, 141(20):204502, 2014. doi: 10.1063/1.4901215. URL Link.

[41] Lennard Jones, J. E. On the Determination of Molecular Fields. I. From Variation of the Viscosity of a Gas with Temperature. *Proceedings of the Royal Society of London A: Mathematical, Physical and Engineering Sciences*, 106(738):441, 1924.

[42] Jeppe C. Dyre. Hidden Scale Invariance in Condensed Matter. *The Journal of Physical Chemistry B*, 118(34):10007, 2014. doi: 10.1021/jp501852b. URL Link. PMID: 25011702.

[43] Jeppe C. Dyre. Isomorphs, hidden scale invariance, and quasiuniversality. *Physical Review E*, 88:042139, 2013.

[44] Jeppe C. Dyre. NVU perspective on simple liquids' quasiuniversality. *Physical Review E*, 87:022106, 2013.

[45] Weeks, John D. and Chandler, David and Andersen, Hans C. Role of Repulsive Forces in Determining the Equilibrium Structure of Simple Liquids. *The Journal of Chemical Physics*, 54(12):5237, 1971. doi: 10.1063/1.1674820. URL Link.

[46] Chandler, David and Weeks, John D. and Andersen, Hans C. Van der Waals Picture of Liquids, Solids, and Phase Transformations. *Science*, 220(4599):787, 1983. doi: 10.1126/science.220.4599.787. URL Link.

[47] Andersen, Hans C. and Weeks, John D. and Chandler, David. Relationship between the Hard-Sphere Fluid and Fluids with Realistic Repulsive Forces. *Phys. Rev. A*, 4:1597, Oct 1971. doi: 10.1103/PhysRevA.4.1597. URL Link.

[48] Nicholas P. Bailey and Ulf R. Pedersen and Nicoletta Gnan and Thomas B. Schrøder and Jeppe C. Dyre. Pressure-energy correlations in liquids. I. Results from computer simulations. *Journal of Chemical Physics*, 129:184507, 2008.

[49] U. R. Pedersen and N. P. Bailey and T. B. Schrøder and J. C. Dyre. Strong pressure-energy correlations in van der Waals liquids. *Phys. Rev. Lett.*, 100:015701, 2008. doi: 10.1103/PhysRevLett.100.015701.

[50] Nicholas P. Bailey and Ulf R. Pedersen and Nicoletta Gnan and Thomas B. Schrøder and Jeppe C. Dyre. Pressure-energy correlations in liquids. II. Analysis and consequences. *Journal of Chemical Physics*, 129:184508, 2008.

[51] Thomas B. Schrøder and Nicholas P. Bailey and Ulf R. Pedersen and Nicoletta Gnan and Jeppe C. Dyre. Pressure-energy correlations in liquids. III. Statistical mechanics and thermodynamics of liquids with hidden scale invariance. *Journal of Chemical Physics*, 131:234503, 2009.

[52] Nicoletta Gnan and Thomas B. Schrøder and Ulf R. Pedersen and Nicholas P. Bailey and Jeppe C. Dyre. Pressure-energy correlations in liquids. IV. 'Isomorphs' in liquid state diagrams. *Journal of Chemical Physics*, 131:234504, 2009.

[53] Thomas B. Schrøder and Nicoletta Gnan and Ulf R. Pedersen and Nicholas Bailey and Jeppe C. Dyre. Pressure-energy correlations in liquids. V. Isomorphs in generalized Lennard-Jones systems. *Journal of Chemical Physics*, 134:164505, 2011.

[54] Albrechtsen, Dan E. and Olsen, Andreas E. and Pedersen, Ulf R. and Schrøder, Thomas B. and Dyre, Jeppe C. Isomorph invariance of the structure and dynamics of classical crystals. *Phys. Rev. B*, 90:094106, Sep 2014. doi: 10.1103/PhysRevB.90.094106. URL Link.

[55] L. Bøhling and T. S. Ingebrigtsen and A. Grzybowski and M. Paluch and J. C. Dyre and T. B. Schrøder. Scaling of viscous dynamics in simple liquids: theory, simulation and experiment. *New Journal of Physics*, 14:113035, 2012.

[56] Bacher, AndreasK. and Dyre, JeppeC. The mother of all pair potentials. *Colloid and Polymer Science*, 292(8):1971, 2014. doi: 10.1007/s00396-014-3290-0. URL Link.

[57] Bacher, Andreas K. and Schrøder, Thomas B. and Dyre, Jeppe C. Explaining why simple liquids are quasi-universal. *Nature Communications*, 5:5424, 11 2014. doi: 10.1038/ncomms6424. URL Link.

[58] Veldhorst, Arno A. *Tests of the isomorph theory by computer simulations of atomic and molecular model liquids*. PhD thesis, Roskilde Universitet, 2014.

[59] Arno A. Veldhorst and Thomas B. Schrøder and Jeppe C. Dyre. Invariants in the Yukawa system's thermodynamic phase diagram. *Physics of Plasmas*, 22:073705, 2015.

[60] Ingebrigtsen, Trond S. and Schrøder, Thomas B. and Dyre, Jeppe C. Isomorphs in Model Molecular Liquids. *The Journal of Physical Chemistry B*, 116(3):1018, 2012. doi: 10.1021/jp2077402. URL Link.

[61] Ditte Gundermann, Ulf R. Pedersen, Tina Hecksher, Nicholas P. Bailey, Bo Jakobsen, Tage Christensen, Niels B. Olsen, Thomas B. Schroder, Daniel Fragiadakis, Riccardo Casalini, C. Michael Roland, Jeppe C. Dyre, and Kristine Niss. Predicting the density-scaling exponent of a glass-forming liquid from Prigogine-Defay ratio measurements. *NATURE PHYSICS*, 7(10):816, Oct 2011. doi: 10.1038/nphys2031.

[62] Roed, Lisa Anita and Gundermann, Ditte and Dyre, Jeppe C. and Niss, Kristine. Communication: Two measures of isochronal superposition. *Journal of Chemical Physics*, 139(10):101101, 2013. doi: 10.1063/1.4821163. URL Link.

[63] Wence Xiao and Jon Tofteskov and Troels V. Christensen and Jeppe C. Dyre and Kristine Niss. Isomorph theory prediction for the dielectric loss variation along an isochrone. *Journal of Non-Crystalline Solids*, 407:190, 2015. doi: 10.1016/j.jnoncrysol.2014.08.041. URL Link.

[64] L.D. Landau and E.M. Lifshitz. *Statistical Physics*. Pergamon, 1958.

[65] Rosenfeld, Yaakov. Relation between the transport coefficients and the internal entropy of simple systems. *Phys. Rev. A*, 15:2545, Jun 1977. doi: 10.1103/PhysRevA.15.2545. URL Link.

[66] Yaakov Rosenfeld. A quasi-universal scaling law for atomic transport in simple fluids. *Journal of Physics: Condensed Matter*, 11(28):5415, 1999. URL Link.

[67] Trond S. Ingebrigtsen and Lasse Bøhling and Thomas B. Schrøder and Jeppe C. Dyre. Thermodynamics of condensed matter with strong pressure-energy correlations. *Journal of Chemical Physics*, 136: 061102, 2012.

[68] Pedersen, Ulf R. Direct calculation of the solid-liquid Gibbs free energy difference in a single equilibrium simulation. *Journal of Chemical Physics*, 139(10):104102, 2013. doi: 10.1063/1.4818747. URL Link.

[69] Nicholas P. Bailey and Lasse Bøhling and Arno A. Veldhorst and Thomas B. Schrøder and Jeppe C. Dyre. Statistical mechanics of Roskilde liquids: Configurational adiabats, specific heat contours and density dependence of the scaling exponent. *Journal of Chemical Physics*, 139:184506, 2013.

[70] Bøhling, Lasse and Bailey, Nicholas P. and Schrøder, Thomas B. and Dyre, Jeppe C. Estimating the density-scaling exponent of a monatomic liquid from its pair potential. *The Journal of Chemical Physics*, 140(12):124510, 2014. doi: 10.1063/1.4869114. URL Link.

[71] Henderson, D. and Barker, J. A. Perturbation Theory of Fluids at High Temperatures. *Phys. Rev. A*, 1:1266, Apr 1970. doi: 10.1103/PhysRevA.1.1266. URL Link.

[72] Kang, Hong Seok and Lee, Choong Sik and Ree, Taikyue and Ree, Francis H. A perturbation theory of classical equilibrium fluids. *The Journal of Chemical Physics*, 82(1):414, 1985. doi: 10.1063/1.448762. URL Link.

[73] John E. Straub. Analysis of the role of attractive forces in self-diffusion of a simple fluid. *Molecular Physics*, 76(2):373, 1992. doi: 10.1080/00268979200101391. URL Link.

[74] Dor Ben-Amotz and George Stell. Reformulation of Weeks–Chandler– Andersen Perturbation Theory Directly in Terms of a Hard-Sphere Reference System. *The Journal of Physical Chemistry B*, 108(21): 6877–6882, 2004. doi: 10.1021/jp037810s. URL Link.

[75] Eskandari Nasrabad, Afshin. Thermodynamic and transport properties of the Weeks–Chandler–Andersen fluid: Theory and computer simulation. *The Journal of Chemical Physics*, 129(24):244508, 2008. doi: 10.1063/1.3041421. URL Link.

[76] Rodríguez-López, Tonalli and Moreno-Razo, J. Antonio and del Río, Fernando. Thermodynamic scaling and corresponding states for the self-diffusion coefficient of non-conformal soft-sphere fluids. *The Journal of Chemical Physics*, 138(11):114502, 2013. doi: 10.1063/1.4795118. URL Link.

[77] J.S. Rowlinson. The statistical mechanics of systems with steep intermolecular potentials. *Molecular Physics*, 8(2):107, 1964. doi: 10.1080/00268976400100141. URL Link.

[78] Dzugutov, Mikhail. A universal scaling law for atomic diffusion in condensed matter. *Nature*, 381(6578):137, 05 1996. doi: 10.1038/381137a0. URL Link.

[79] Agrawal, Rupal and Kofke, David A. Thermodynamic and structural properties of model systems at solid-fluid coexistence. *Molecular Physics*, 85(1):43–59, 1995. doi: 10.1080/00268979500100921. URL Link.

[80] Pedersen, Ulf R. and Schrøder, Thomas B. and Dyre, Jeppe C. Repulsive Reference Potential Reproducing the Dynamics of a Liquid with Attractions. *Phys. Rev. Lett.*, 105:157801, Oct 2010. doi: 10.1103/PhysRevLett.105.157801. URL Link.

[81] Berthier, Ludovic and Tarjus, Gilles. Nonperturbative Effect of Attractive Forces in Viscous Liquids. *Phys. Rev. Lett.*, 103:170601, Oct 2009. doi: 10.1103/PhysRevLett.103.170601. URL Link.

[82] Lasse Bøhling and Arno A Veldhorst and Trond S Ingebrigtsen and Nicholas P Bailey and Jesper S Hansen and Søren Toxvaerd and Thomas B Schrøder and Jeppe C Dyre. Do the repulsive and attractive pair forces play separate roles for the physics of liquids? *Journal of Physics: Condensed Matter*, 25(3):032101, 2013. URL Link.

[83] Lorenzo Costigliola, Thomas B. Schrøder and Jeppe C. Dyre. Freezing and melting line invariants of the Lennard–Jones system. *Phys. Chem. Chem. Phys.*, 18:14678, 2016. doi: 10.1039/C5CP06363A. URL Link.

[84] Ulf R. Pedersen, Lorenzo Costigliola, Nicholas P. Bailey, Thomas B. Schroder, and Jeppe C. Dyre. Thermodynamics of freezing and melting. *Nat Commun*, 7, 08 2016. doi: 10.1038/ncomms12386. URL Link.

[85] Sergei M Stishov. The thermodynamics of melting of simple substances. *Soviet Physics Uspekhi*, 17(5):625, 1975. URL Link.

[86] Cahn, Robert W. Materials science: Melting and the surface. *Nature*, 323(6090):668, 10 1986. doi: 10.1038/323668a0. URL Link.

[87] Oxtoby, David W. New perspectives on freezing and melting. *Nature*, 347(6295):725, 10 1990. doi: 10.1038/347725a0. URL Link.

[88] Cahn, Robert W. Materials science: Melting from within. *Nature*, 413 (6856):582, 10 2001. doi: 10.1038/35098169. URL Link.

187

[89] Ubbelohde, A R. *Melting and Crystal Structure*. Clarendon, London, 1965.

[90] D. C. Wallace. *Statistical Physics of Crystals and Liquids*. World Scientific, Singapore, 2002.

[91] Yu D Fomin and V N Ryzhov and V V Brazhkin. Properties of liquid iron along the melting line up to Earth-core pressures. *Journal of Physics: Condensed Matter*, 25(28):285104, 2013. URL Link.

[92] Stacey, F. D. and Irvine, R. D. Theory of Melting: Thermodynamic basis of Lindermann's Law. *Australian Journal of Physics*, 30:631, 1977.

[93] Frank D Stacey. Thermodynamics of the Earth. *Reports on Progress in Physics*, 73(4):046801, 2010. URL Link.

[94] Pedersen, Ulf R. and Hummel, Felix and Kresse, Georg and Kahl, Gerhard and Dellago, Christoph. Computing Gibbs free energy differences by interface pinning. *Phys. Rev. B*, 88:094101, Sep 2013. doi: 10.1103/PhysRevB.88.094101. URL Link.

[95] Khrapak, Sergey A. and Morfill, Gregor E. Accurate freezing and melting equations for the Lennard-Jones system. *Journal of Chemical Physics*, 134(9):094108, 2011. doi: 10.1063/1.3561698. URL Link.

[96] Ahmed, Alauddin and Sadus, Richard J. Solid-liquid equilibria and triple points of n-6 Lennard-Jones fluids. *Journal of Chemical Physics*, 131(17):174504, 2009. doi: 10.1063/1.3253686. URL Link.

[97] Mastny, Ethan A. and de Pablo, Juan J. Melting line of the Lennard-Jones system, infinite size, and full potential. *Journal of Chemical Physics*, 127(10):104504, 2007. doi: 10.1063/1.2753149. URL Link.

[98] Yaakov Rosenfeld. Additivity of melting curves. *Chemical Physics Letters*, 38(3):591, 1976. doi: 10.1016/0009-2614(76)80048-6. URL Link.

[99] Yaakov Rosenfeld. Universality of melting and freezing indicators and additivity of melting curves. *Molecular Physics*, 32(4):963, 1976. doi: 10.1080/00268977600102381. URL Link.

[100] Hansen, Jean-Pierre and Verlet, Loup. Phase Transitions of the Lennard-Jones System. *Phys. Rev.*, 184:151, Aug 1969. doi: 10.1103/PhysRev.184.151. URL Link.

[101] Hansen, Jean-Pierre. Phase Transition of the Lennard-Jones System. II. High-Temperature Limit. *Phys. Rev. A*, 2:221, Jul 1970. doi: 10.1103/PhysRevA.2.221. URL Link.

[102] Gilvarry, J. J. The Lindemann and Grüneisen Laws. *Phys. Rev.*, 102: 308, Apr 1956. doi: 10.1103/PhysRev.102.308. URL Link.

[103] Ross, Marvin. Generalized Lindemann Melting Law. *Phys. Rev.*, 184: 233, Aug 1969. doi: 10.1103/PhysRev.184.233. URL Link.

[104] Lindemann, F. A. The Calculation of Molecular Vibration Frequencies. *Physikalische Zeitschrift*, 11:609, 1910.

[105] Evans, Denis J and Morriss, Gary. *Statistical mechanics of nonequilibrium liquids.* Cambridge University Press, 2008.

[106] Daivis, Peter J. and Todd, B. D. A simple, direct derivation and proof of the validity of the SLLOD equations of motion for generalized homogeneous flows. *Journal of Chemical Physics*, 124(19):194103, 2006. doi: http://dx.doi.org/10.1063/1.2192775. URL Link.

[107] Evans, M.W. and Heyes, D.M. Combined shear and elongational flow by non-equilibrium molecular dynamics. *Molecular Physics*, 69(2):241, 1990. doi: 10.1080/00268979000100171. URL Link.

[108] Andrade, E.N. da C. Viscosity of Liquids. *Nature*, 128:835, 1931.

[109] Andrade, E.N. da C. XLI. A theory of the viscosity of liquids.—Part I. *The London, Edinburgh, and Dublin Philosophical Magazine and Journal of Science*, 17(112):497, 1934. doi: 10.1080/14786443409462409. URL Link.

[110] Andrade, E.N. da C. LVIII. A theory of the viscosity of liquids.—Part II. *The London, Edinburgh, and Dublin Philosophical Magazine and Journal of Science*, 17(113):698, 1934. doi: 10.1080/14786443409462427. URL Link.

[111] Felix Hummel, Georg Kresse, Jeppe C. Dyre, and Ulf R. Pedersen. Hidden scale invariance of metals. *Phys. Rev. B*, 92:174116, Nov 2015. doi: 10.1103/PhysRevB.92.174116. URL Link.

[112] Luo, Sheng-Nian and Strachan, Alejandro and Swift, Damian C. Vibrational density of states and Lindemann melting law. *Journal of Chemical Physics*, 122(19):194709, 2005. doi: 10.1063/1.1902948. URL Link.

[113] Vliegenthart, G. A. and Lekkerkerker, H. N. W. Predicting the gas–liquid critical point from the second virial coefficient. *The Journal of Chemical Physics*, 112(12):5364, 2000. doi: 10.1063/1.481106. URL Link.

[114] M Hasegawa and K Ohno. The dependence of the phase diagram on the range of the attractive intermolecular forces. *Journal of Physics: Condensed Matter*, 9(16):3361, 1997. URL Link.

[115] Ashurst, WT and Hoover, WG. Dense-fluid shear viscosity via nonequilibrium molecular dynamics. *Phys. Rev. A*, 11(2):658, 1975. doi: {10.1103/PhysRevA.11.658}.

[116] Woodcock, Leslie V. Equation of state for the viscosity of Lennard-Jones fluids. *AIChE Journal*, 52(2):438, 2006. doi: 10.1002/aic.10676. URL Link.

[117] Heyes, David M. Transport coefficients of Lennard-Jones fluids: A molecular-dynamics and effective-hard-sphere treatment. *Phys. Rev. B*, 37:5677, Apr 1988. doi: 10.1103/PhysRevB.37.5677. URL Link.

[118] Kaptay, G. A unified equation for the viscosity of pure liquid metals. *Zeitschrift fur Metallkunde*, 96(1):24, Jan 2005.

[119] Dabir S. Viswanath and Tushar Ghosh and Dasika H.L. Prasad and Nidamarty V.K. Dutt and Kalipatnapu Y. Rani. *Viscosity of Liquids: Theory, Estimation, Experiment, and Data.* Springer Netherlands, 1 edition, 2007.

[120] Stephan, K. and Lucas, K.,. *Viscosity of dense fluids.* Plenum Press New York, 1979. ISBN 030640320.

[121] Reif, F. *Fundamentals of Statistical and Thermal Physics.* McGraw Hill, Tokyo, 1965.

[122] Hildebrand, J H. Viscosity of dilute gases and vapors. *Proceedings of the National Academy of Sciences of the United States of America*, 73 (12):4302, 12 1976. URL Link.

[123] Chapman, Sydney and Cowling, T. G. (Thomas George). *The mathematical theory of non-uniform gases : an account of the kinetic theory of viscosity, thermal conduction, and diffusion in gases.* Cambridge : Cambridge University Press, 1939. Includes index.

[124] Yaakov Rosenfeld and Pedro Tarazona. Density functional theory and the asymptotic high density expansion of the free energy of classical solids and fluids. *Molecular Physics*, 95(2):141, 1998. doi: 10.1080/ 00268979809483145. URL Link.

[125] Baranyai, Andras and Evans, Denis J. Direct entropy calculation from computer simulation of liquids. *Phys. Rev. A*, 40:3817, Oct 1989. doi: 10.1103/PhysRevA.40.3817. URL Link.

[126] William Sutherland. LXXV. A dynamical theory of diffusion for non-electrolytes and the molecular mass of albumin. *Philosophical Magazine Series 6*, 9(54):781, 1905. doi: 10.1080/14786440509463331. URL Link.

[127] Einstein, A. Über die von der molekularkinetischen Theorie der Wärme geforderte Bewegung von in ruhenden Flüssigkeiten suspendierten Teilchen. *Annalen der Physik*, 322(8):549, 1905. doi: 10.1002/andp.19053220806. URL Link.

[128] von Smoluchowski, M. Zur kinetischen Theorie der Brownschen Molekularbewegung und der Suspensionen. *Annalen der Physik*, 326 (14):756, 1906. doi: 10.1002/andp.19063261405. URL Link.

[129] Lorenzo Costigliola, Thomas B. Schrøder and Jeppe C. Dyre. Communication: Studies of the Lennard-Jones fluid in 2, 3, and 4 dimensions highlight the need for a liquid-state 1/d expansion. *The Journal of Chemical Physics*, 144(23):231101, 2016. doi: 10.1063/1.4954239. URL Link.

[130] Maimbourg, T. and Kurchan, J. Approximate scale invariance in particle systems: a large-dimensional justification. *ArXiv e-prints*, March 2016.

[131] Heyes, D. M. The Lennard-Jones Fluid in the Liquid-Vapour Critical Region. *Computational methods in science and tecnology*, 2015. doi: 10.12921/cmst.2015.21.04.001. URL Link.

[132] Smit, B. and Frenkel, D. Vapor-liquid equilibria of the two-dimensional Lennard-Jones fluid(s). *The Journal of Chemical Physics*, 94(8):5663, 1991. doi: 10.1063/1.460477. URL Link.

[133] Potoff, Jeffrey J. and Panagiotopoulos, Athanassios Z. Critical point and phase behavior of the pure fluid and a Lennard-Jones mixture. *The Journal of Chemical Physics*, 109(24):10914, 1998. doi: 10.1063/1.477787. URL Link.

[134] Hloucha, M. and Sandler, S. I. Phase diagram of the four-dimensional Lennard-Jones fluid. *The Journal of Chemical Physics*, 111(17):8043–8047, 1999. doi: 10.1063/1.480138. URL Link.

[135] Smit, B. Phase diagrams of Lennard–Jones fluids. *The Journal of Chemical Physics*, 96(11):8639, 1992. doi: 10.1063/1.462271. URL Link.

[136] J.A. Barker and D. Henderson and F.F. Abraham. Phase diagram of the two-dimensional Lennard-Jones system; Evidence for first-order

transitions. *Physica A: Statistical Mechanics and its Applications*, 106 (1):226, 1981. doi: 10.1016/0378-4371(81)90222-3. URL Link.

[137] Coslovich, Daniele and Ikeda, Atsushi and Miyazaki, Kunimasa. Mean-field dynamic criticality and geometric transition in the Gaussian core model. *Phys. Rev. E*, 93:042602, Apr 2016. doi: 10.1103/ PhysRevE.93.042602. URL Link.

[138] Stillinger, Frank H. and Weber, Thomas A. Study of melting and freezing in the Gaussian core model by molecular dynamics simulation. *The Journal of Chemical Physics*, 68(8):3837, 1978. doi: 10.1063/1. 436191. URL Link.

[139] Stillinger, F. H. and Weber, T. A. Amorphous state studies with the Gaussian core model. *The Journal of Chemical Physics*, 70(11):4879, 1979. doi: 10.1063/1.437365. URL Link.

[140] Ikeda, Atsushi and Miyazaki, Kunimasa. Slow dynamics of the high density Gaussian core model. *The Journal of Chemical Physics*, 135 (5):054901, 2011. doi: 10.1063/1.3615949. URL Link.

[141] Ikeda, Atsushi and Miyazaki, Kunimasa. Thermodynamic and structural properties of the high density Gaussian core model. *The Journal of Chemical Physics*, 135(2):024901, 2011. doi: 10.1063/1.3609277. URL Link.

[142] Prestipino, Santi and Saija, Franz and Giaquinta, Paolo V. Phase diagram of softly repulsive systems: The Gaussian and inverse-power-law potentials. *The Journal of Chemical Physics*, 123(14):144110, 2005. doi: 10.1063/1.2064639. URL Link.

[143] Prestipino, Santi and Saija, Franz and Giaquinta, Paolo V. Phase diagram of the Gaussian-core model. *Phys. Rev. E*, 71:050102, May 2005. doi: 10.1103/PhysRevE.71.050102. URL Link.

[144] Prestipino, Santi and Saija, Franz and Malescio, Gianpietro. Anomalous phase behavior in a model fluid with only one type of local structure. *The Journal of Chemical Physics*, 133(14):144504, 2010. doi: 10.1063/1.3499830. URL Link.

[145] Stillinger, Frank H. Duality relations for the Gaussian core model. *Phys. Rev. B*, 20:299, Jul 1979. doi: 10.1103/PhysRevB.20.299. URL Link.

[146] Gnan, Nicoletta. *Viscous liquid dynamics in and out of equilibrium*. PhD thesis, Roskilde Universitet, 2010.

[147] Gnan, Nicoletta and Das, Gayatri and Sperl, Matthias and Sciortino, Francesco and Zaccarelli, Emanuela. Multiple Glass Singularities and Isodynamics in a Core-Softened Model for Glass-Forming Systems. *Phys. Rev. Lett.*, 113:258302, Dec 2014. doi: 10.1103/PhysRevLett. 113.258302. URL Link.

[148] Fomin, Yu. D. and Ryzhov, V. N. and Gribova, N. V. Breakdown of excess entropy scaling for systems with thermodynamic anomalies. *Phys. Rev. E*, 81:061201, Jun 2010. doi: 10.1103/PhysRevE.81.061201. URL Link.

[149] Søren Toxvaerd. Algorithms for canonical molecular dynamics simulations. *Molecular Physics*, 72(1):159, 1991. doi: 10.1080/ 00268979100100101. URL Link.

[150] OpenMP website http://openmp.org/wp/. URL Link.

[151] Valeria Molinero and Emily B. Moore. Water Modeled As an Intermediate Element between Carbon and Silicon. *The Journal of Physical Chemistry B*, 113(13):4008, 2009. doi: 10.1021/jp805227c. URL Link.

[152] Toxvaerd, Søren and Dyre, Jeppe C. Communication: Shifted forces in molecular dynamics. *The Journal of Chemical Physics*, 134(8):081102, 2011. doi: 10.1063/1.3558787. URL Link.

[153] Chialvo, A. A. and Debenedetti, P. G. On the use of the Verlet neighbor list in molecular dynamics. *Computer Physics Communications*, 60:215, 1990. doi: 10.1016/0010-4655(90)90007-N.

[154] Ariel A. Chialvo and Pablo G. Debenedetti. On the performance of an automated Verlet neighbor list algorithm for large systems on a vector processor. *Computer Physics Communications*, 64(1):15, 1991. doi: 10.1016/0010-4655(91)90046-N. URL Link.

[155] MBN Explorer: A universal program for multiscale simulation of complex molecular structure and dynamics. http://www.mbnexplorer.com/documentation/5-numerical-methods-interatomic-interactions/52-linked-cell-interaction-approach, June 2016. URL Link.

[156] Martyna, Glenn J. and Tobias, Douglas J. and Klein, Michael L. Constant pressure molecular dynamics algorithms. *The Journal of Chemical Physics*, 101(5):4177, 1994. doi: 10.1063/1.467468. URL Link.

[157] Leila Separdar and Nicholas P. Bailey and Thomas B. Schrøder and Saeid Davatolhagh and Jeppe C. Dyre. Isomorph invariance of Couette shear flows simulated by the SLLOD equations of motion. *Journal of Chemical Physics*, 138:154505, 2013.